

**Hoai Nga Le**

**A concept for  
nanoparticle-based photocatalytic treatment  
of wastewater from textile industry**

Dresden 2018

© Hoai Nga Le Selbstverlag

2018

01069 Dresden

Alle Rechte vorbehalten

Satz und Redaktion: Hoai Nga Le

Printed in Germany, 2018

# **A concept for nanoparticle-based photocatalytic treatment of wastewater from textile industry**

Von der Fakultät Maschinenwesen  
der Technischen Universität Dresden  
Zur Erlangung des akademischen Grades

**Doktoringenieur (Dr.-Ing.)**

genehmigte Dissertation

von

Master of Science in Chemical Engineering

**Le, Hoai Nga**

Tag der Einreichung: Sep 21, 2017

Tag der Verteidigung: Mar 22, 2018

Vorsitzender: Prof. Dr.rer.medic. H.-P. Wiesmann

Gutachter: Prof. Dr.rer.nat. G. Cuniberti

Prof. Dr.-Ing.habil. M. Stintz

Jun.-Prof. Dr.-Ing. S. Wießner

Mitglied: Prof. Dr.rer.nat. et Ing.habil. K. Eckert



Dedicated to

*Bố mẹ*

*&*

*các thầy cô Bộ môn Hóa Công*



## ACKNOWLEDGMENT

In the summer 2012, I put my first step in Germany, as a Ph.D. student and as a beginner in the field of nanotechnology. I never pictured me as a soldier in a scientific battle, whom actually I turned to be.

Firstly, I thank the scholarship program Erasmus Mundus – One More Step, the Graduate Academy of TUD and the Federal Ministry for Education and Research (BMBF) via the CLIENT/NaViTex project 02WCL1264A for the financial supports.

To the committee of my Ph.D. defense, I thank for the nice scientific discussion from multidisciplinary aspects.

To the Chair of Materials Science and Nanotechnology of TUD, I would like to thank Prof. Gianaurelio Cuniberti for providing me all the facilities to access the work. Many thanks to Grit, Nicole, Manu, Emanuel and Sylvi for helping me with all complicated documents. I thank Jochen Förster for the technical help, Supreeth Venkatraman, Hieu Le, Jackie Le, Yen Chia Feng, Sun Kim, and especially Felix Alscher for their experimental contributions.

To the research group Mechanische Verfahrenstechnik of TUD, I deeply appreciate Prof. Michael Stintz and other colleagues for welcoming me as their member. I was motivated to learn German with them (which is, as far as my understanding, one of the most difficult languages in the world). It does not go as expected, but more importantly, with them, I learned the values of German people and culture.

To Prof. Senentxu Lanceros-Méndez and the group Electroactive Smart Materials of University of Minho for hosting my internship. I hope this short time started a cooperation in the future.

To the Department of Chemical Engineering, Hanoi University of Science and Technology. I was educated and trained to be confident and conductive in working as an engineer. They always supported me from apart whenever I questioned.

To Dr. Nguyen Minh Tan, Mr. Steffen Johne, Dr. Ulrich Soltmann from the NaViTex project. Thanks for the nice work together in Germany and Vietnam. I am grateful for Mr. Cong Thanh Tran. We shared time doing the “hot” experiments (literally) in Danang under the heat of 50 °C.

My special thanks are to Dr. Klaus Kühn and Dr. Frank Babick. They are my worthy supervisors who never mind spending time and giving me not only scientific but intercultural lessons.

To my great colleagues, Leonardo Medrano Sandonas, Hagen Eckert, Pedro M. Martins, Sandro Kappert, Duy-Dung Phan, especially Sara Teixeira and Nadia Licciardello who are always kind and helpful. I have learnt a lot from them till the last months of my Ph.D. To Thomas Lehmann for solving a lot of difficulties to a foreign. To my friends, Carlito, Tommi, Nara, Phu-ong Duy, GN and Sara. To ‘Dresden Windschneiden’, ‘What is love’ (formerly ‘Beer’) and Welcome Center. To ones though I did not list here due to the limited space. We all shared full of

fun together, doesn't matter in/out of the office, and in/out of Dresden. Without them, I would not have enough strength and braveness to finish my work. Without them, I would not have as laughed, but I would not be as distracted.

Last but not least, the thesis credits my parents, my brother and his family. They worry about my study and my daily life even more than I do. Last few years, we haven't spent much time together, but for me, their support and their love from abroad are priceless.

And thank you, the very patient audience who read until the end of my endless acknowledgment.

Vielen herzlichen Dank!

*Xin chân thành cảm ơn!*

## SUMMARY

Industrial wastewater, such as the effluents from textile and garment companies, may contain toxic organic pollutants, which resist conventional wastewater treatment. Their complete and environmentally friendly degradation requires innovative technologies. Photocatalysis, an advanced oxidation process, can serve this purpose. Since 1972, when the photocatalytic activity of titanium dioxide was first noticed, photocatalysis has drawn the attention of scientists and engineers but it has not yet been widely applied in industrial practice. This is mainly related to the challenges of up-scaling from laboratory experiments to large production sites.

The main goal of this thesis is to develop a concept of nanoparticle-based photocatalysis for the treatment of wastewater. Ideally, process parameters should be adjustable and process conditions should be well-defined. These constraints are prerequisite for establishing process models and comparing the photocatalytic efficiency of different photocatalysts or for different pollutants. More importantly, the configuration should be scalable, in order to cover a wide spectrum of applications.

In response to these requirements, this thesis introduces a new reactor concept for photocatalytic wastewater treatment, which relies on finely dispersed photocatalysts as well as uniform and defined process conditions with regard to illumination and flow. The concept was realized in a photocatalytic setup with an illuminated flow reactor. The flow channel has a rectangular cross section and meanders in a plane exposed to two dimensional illumination. Crucial process parameters, e.g., volumetric flow rate and light intensity, can be adjusted in a defined manner. This facilitates the study on the photocatalytic degradation of different organic pollutants in the presence of various photocatalytic materials under arbitrary illumination.

The thesis provides a comprehensive description of the operational procedures necessary to run photocatalytic reactions in the experimental setup. It includes three main steps: i) dispersion of photocatalysts, ii) equilibration with respect to pollutant adsorption and iii) accomplishing the photocatalytic reaction. Samples are collected in a mixing tank for online or offline analysis. The proceeding decrease in the concentration of organic pollutant is used to assess the activity of the photocatalytic materials.

A particular focus lies on the first of these steps, the dispersion of photocatalysts, because it is ignored in most studies. Typically, photocatalysts are in an aggregated state. The thesis demonstrates that type, intensity and energy of dispersion exert a crucial influence on size and morphology of the photocatalyst particles and, thus, on their optical properties and, accordingly, macroscopic photocatalytic behavior. Apart from this, a proper dispersion is necessary to reduce speed of gravitational solid-liquid separation, at best, to prevent catalyst sedimentation and to avoid misleading results.

The photocatalytic performance was intensively investigated for the color removal of a model dye substance, methylene blue. Commercial titanium dioxide nanoparticles, widely explored in literature, were used as a photocatalyst. Their characteristics (size, morphology, stability

and optical properties) were determined. Photocatalytic experiments were carried out under UV irradiation. Influences of different factors, including the concentration of the photocatalyst, the concentration of the organic compounds, light intensity, optical pathlength and pH were examined. The degradation was quantified via the decrease of methylene blue concentration. This conversion is, however, an immediate result influenced by all process parameters, e.g., the volume, the light intensity, the optical pathlength. Hence, kinetic models on macroscopic and microscopic levels are established. Normalizations with respect to process conditions are proposed. The apparent reaction kinetics are traced back to volume- and intensity-related reaction rate constants, and the reaction rate constant at the illuminated surface of the reactor. Additionally, the model is modified to be used for time-variant UV intensities, as encountered for solar photocatalysis. These achievements allow for a comparison of the experimental results from different laboratories. Moreover, they are prerequisite for the translation of laboratory results into large scale plants.

Selected case studies for further applications are introduced. The photocatalytic degradation of different organic molecules (one antibiotic and two commercial dyes) with different photocatalytic materials (commercial nanomaterials and self-synthesized magnetic particles) under artificial or natural light sources was performed. Additionally, photocatalysis was studied in a realistic application. Preliminary tests with dye solutions of a textile company in Danang, Vietnam, impressively showed the feasibility of wastewater treatment by means of photocatalysis. Based on the reported capacity of wastewater in the current treatment plant of the company, the necessary process parameters were assessed. The rough estimation showed that photocatalysis can improve the working ability of the current wastewater treatment plant.

In conclusion, this thesis presents a concept for wastewater treatment by slurry photocatalysis. As the process conditions are adjustable and definable, the process can be ideally performed in laboratories for research purposes, where different materials need to be tested and the working volume can be lower than hundreds of milliliters. The photocatalytic configuration is expected to work with a capacity of hundreds of liters, although appropriate experimental evidences are reserved for further up-scaling studies.

## KURZFASSUNG

Industrielle Abwässer, wie solche der Textil- und Bekleidungsindustrie, können giftige organische Verunreinigungen enthalten, die durch konventionelle Abwasserbehandlung nicht beseitigt werden. Um einen vollständigen und umweltfreundlichen Abbau zu gewährleisten bedarf es neuer Technologien. Die Photokatalyse, eine Form der Erweiterten Oxidation (engl.: *advanced oxidation process*), entspricht den gewünschten Anforderungen. Sie ist seit 1972, dem Jahr als die photokatalytische Aktivität von Titandioxid entdeckt wurde, umfangreich untersucht worden. Allerdings findet sie in der industriellen Praxis kaum Anwendung. Das liegt im Wesentlichen an den Schwierigkeiten der Maßstabsüberübertragung vom Labor zu großtechnischen Anlagen.

Das übergeordnete Ziel der vorliegenden Dissertation besteht in der Entwicklung eines Konzeptes zur nanopartikel-basierten Photokatalyse in der Abwasserbehandlung. Idealweise sollten die Prozessparameter einstellbar und die Prozessbedingungen eindeutig definiert sein. Das ist notwendig, um Prozessmodelle zu entwickeln und die photokatalytische Effizienz von unterschiedlichen Photokatalysatoren oder für unterschiedliche Schadstoffe zu vergleichen. Außerdem sollte das Konzept eine skalierbare technische Umsetzung ermöglichen, damit sich ihm ein breites Anwendungsfeld eröffnet.

Die Dissertation antwortet auf diese Anforderungen mit einem Reaktorkonzept für die photokatalytische Abwasserbehandlung, das feindisperse Photokatalysatoren nutzt sowie einheitliche und definierte Prozessbedingungen in Bezug auf Beleuchtung und Strömung gewährleistet. Das Konzept wurde in einem photokatalytischen Versuchsstand umgesetzt, das einen Strömungsreaktor beinhaltet, dessen mäandrierender Strömungskanal einen rechteckigen Querschnitt besitzt und einer planaren Beleuchtung ausgesetzt ist. Die kritischen Prozessparameter wie Durchfluss und Lichtintensität sind definiert und einstellbar. Das ermöglicht vergleichende Untersuchungen zum photokatalytischen Abbau unterschiedlicher organischer Substanzen für unterschiedliche Photokatalysatormaterialien und beliebigen Beleuchtungsszenarien.

Ergänzend dazu, werden auch die zum Betrieb des photokatalytischen Versuchsstandes notwendigen Verfahrensschritte umfassend beschrieben. Sie beinhalten drei Schritte: i) die Dispergierung des photokatalytischen Materials, ii) eine Wartezeit zur Einstellung des Adsorptionsgleichgewichtes der organischen Schadstoffe und iii) die Durchführung der photokatalytischen Reaktion. Zur Offline- und Online-Analyse des Abbauprozesses werden aus einem Vorlagebehälter Proben gezogen. Die stetige Absenkung der Schadstoffkonzentration ermöglicht eine Quantifizierung der photokatalytischen Aktivität auf mikroskopischer Ebene.

Ein besonderes Augenmerk gilt der Dispergierung des Photokatalysators, weil dieser Prozessschritt in den meisten publizierten Studien ausgeblendet wird. Dabei handelt es sich bei Photokatalysatoren typischerweise um aggregierte Partikelsysteme, deren Größe und Morphologie entscheidend von der Art, Intensität und Energie der Dispergierung bestimmt

wird. Die vorliegende Arbeit zeigt, dass dementsprechend auch ein Einfluss auf die optischen Materialeigenschaften und folglich auf das photokatalytische Verhalten des Gesamtsystems besteht. In jedem Fall ist eine Katalysatordispergierung notwendig, um eine Schwerkraft induzierte Entmischung der Suspension zu verhindern und daraus resultierend Fehlinterpretationen der Versuchsergebnisse zu vermeiden.

Mit dem neuen Versuchstand wurde der photokatalytische Abbau vor allem an der Entfärbung eines Modelfarbstoffes (Methylenblau) untersucht. Als Photokatalysator wurde ein kommerzielles, nanostrukturiertes Titandioxid verwendet, das auch in anderen Studien zum Einsatz kam. Dessen morphologischen und optischen Kenngrößen wurden gemessen. Die photokatalytischen Experimente wurden regulär bei UV-Beleuchtung durchgeführt. Die Einflüsse diverser Faktoren, u.a. die Katalysatorkonzentration, die Farbstoffkonzentration, die Lichtintensität, die optische Weglänge und der pH-Wert, wurden untersucht. Die Kinetik der Abbaureaktion wurde zunächst unmittelbar aus dem Rückgang der Farbstoffkonzentration berechnet. Doch da das entsprechende Ergebnis von Prozessparametern, wie dem Reaktorvolumen, der Lichtintensität oder der optischen Weglänge, abhängt, wurde ein Modell entwickelt, dass die Kinetiken auf Mikro- und Makroebene miteinander verbindet. Es ermöglicht eine Normalisierung von Messdaten bezüglich verschiedener Messbedingungen. Das heißt, dass die beobachteten Reaktionsraten auf volumen- und intensitätsbezogene Reaktionskonstanten unmittelbar hinter dem Beleuchtungsfenster zurückgeführt werden. Darüber hinaus, wurde das Modell so modifiziert, dass es auch für Situation mit zeitlich veränderlicher Bestrahlungsintensität (z.B. Sonnenlicht) genutzt werden kann. Die Ergebnisse der Modellentwicklung erlauben nunmehr den Vergleich zwischen photokatalytischen Messdaten aus unterschiedlichen Laboren, sie sind aber auch Voraussetzung für die Übertragung von Versuchsdaten aus dem Labor auf großtechnische Anlagen.

In Form von Fallstudien werden mögliche Anwendungsszenarien betrachtet. Unter anderem wurde der photokatalytische Abbau von verschiedenen organischen Molekülen (ein Antibiotikum und zwei herkömmliche Farbstoffe) mit unterschiedlichen photokatalytischen Materialien (kommerzielle Nanomaterialien und selbsthergestellte Partikel) unter künstlichen und natürlichen Licht untersucht. Zudem wurde die Photokatalyse für einen realen Anwendungsfall eingesetzt. Machbarkeitstests mit Farblösungen einer Textilfabrik aus Danang (Vietnam) bestätigten die Wirksamkeit der photokatalytischen Abwasserbehandlung. Anhand des Abwasservolumens und der Kapazität des vorhandenen Klärwerkes der Fabrik wurden die notwendigen Prozessparameter abgeschätzt und der Nutzen einer Implementierung der Photokatalyse in das bestehende Abwasserbehandlungskonzept nachgewiesen.

Die vorliegende Dissertation präsentiert ein Konzept zur Abwasseraufbereitung durch Photokatalyse mit suspendierten Nanopartikeln. Aufgrund der definierten und einstellbaren Prozessbedingungen eignet sich dieses Konzept hervorragend für Forschungsaufgaben im Laborbereich, um z. B. unterschiedliche photokatalytische Materialien bei einem geringen Arbeitsvolumen zu testen. Das Konzept ermöglicht jedoch auch eine Umsetzung in großskaligen

Anlagen mit größeren Kapazitäten, gleichwohl entsprechende experimentelle Nachweise zukünftigen Studien vorbehalten bleiben.



# TABLE OF CONTENTS

Acknowledgment.....	v
Summary .....	vii
Kurzfassung .....	ix
Table of contents .....	xiii
List of figures.....	xvii
List of tables .....	xxi
Nomenclature .....	xxiii
1 Introduction .....	1
1.1 Motivation .....	1
1.2 Outline of the thesis .....	3
2 Fundamentals of photocatalysis.....	5
2.1 Photocatalysis.....	5
2.1.1 Photo excitation.....	5
2.1.2 Reaction pathway .....	6
2.1.3 Modified photocatalysts .....	7
2.2 Photocatalytic setups.....	9
2.2.1 Requirements .....	9
2.2.2 Reactors .....	11
2.3 Quantitative descriptions of photocatalysis.....	15
2.3.1 Influence of photocatalyst concentration and morphology .....	16
2.3.2 Influence of organic compounds.....	17
2.3.3 Influence of light intensity.....	18
2.3.4 Influence of other factors.....	19
2.3.5 Modeling .....	21
2.4 Challenge.....	23
3 A photocatalytic setup for research purposes .....	27
3.1 The experimental setup .....	27
3.1.1 Objectives .....	27

3.1.2	The setup .....	27
3.1.3	Design of a flow reactor .....	29
3.1.4	Illumination .....	32
3.1.5	Flow conditions .....	34
3.2	Operation.....	35
3.3	Determination of reaction rate constant.....	37
3.3.1	Assumptions.....	37
3.3.2	Heterogeneous reaction .....	38
3.3.3	Reactor model .....	39
3.4	Concluding remarks .....	41
4	Materials and experimental methods.....	43
4.1	Materials and their properties .....	43
4.1.1	Photocatalysts .....	43
4.1.2	Organic compounds.....	44
4.1.3	Others .....	47
4.2	Photocatalyst dispersion techniques.....	48
4.3	Analytical techniques .....	48
4.3.1	UV-VIS spectroscopy .....	49
4.3.2	Diffuse reflectance UV-VIS spectrometer .....	51
4.3.3	Photon correlation spectroscopy.....	52
4.4	Photocatalytic experiments.....	54
4.4.1	Procedure .....	54
4.4.2	Dispersion tests.....	56
4.4.3	Color removal of methylene blue .....	57
4.4.4	Selected case studies for applications of photocatalysis.....	60
5	Physical properties of P25 photocatalyst aggregates .....	63
5.1	Size and stability .....	63
5.1.1	Photocatalyst size .....	63
5.1.2	Stability of dispersed photocatalyst .....	67
5.2	Optical properties .....	68

5.2.1	Bandgap energy.....	69
5.2.2	Scattering .....	70
5.2.3	Transmittance, turbidity and extinction coefficient.....	70
5.2.4	Influence of aggregate size.....	74
5.3	Concluding remarks .....	76
6	Color removal of methylene blue in the designed photocatalytic setup .....	77
6.1	Process conditions.....	77
6.2	Preliminary tests.....	78
6.3	Uses of the reactor model .....	80
6.3.1	Verification of the model.....	80
6.3.1	Further discussion .....	82
6.3.2	Concluding remarks .....	85
6.4	Influential parameters on the photocatalytic performance .....	86
6.4.1	Suspension volume .....	86
6.4.2	Irradiance. The intensity-related reaction rate constant.....	87
6.4.3	Optical penetration. A modified model.....	89
6.4.4	High initial concentration of the organic compound .....	95
6.4.5	Acidic/basic property.....	99
6.4.6	Photocatalyst size .....	103
6.4.7	Concluding remarks .....	107
7	Towards applications of photocatalysis.....	111
7.1	Laboratory applications: Selected case studies.....	111
7.1.1	The volume-related reaction rate constant.....	111
7.1.2	Solar photocatalysis. The UV energy-dependent model .....	112
7.1.3	Photocatalysis with different nanomaterials.....	115
7.1.4	Photocatalysis for commercial dye substances.....	118
7.1.5	Concluding remarks .....	121
7.2	Industrial application in a textile company .....	122
7.2.1	Scenario in March 29 Textile-Garment Joint Stock Company.....	122
7.2.2	The CLIENT/NaViTex project.....	125

7.2.3	Challenges .....	130
7.2.4	An up-scaled photocatalytic reactor in a wastewater treatment system .....	131
7.2.5	Concluding remarks .....	141
8.	Conclusions and future work .....	143
8.1	Conclusions .....	143
8.2	Outlook.....	146
	References .....	147
	Appendix.....	167
A1.	Fundamentals of particle size .....	167
A2.	Characterization of P25 colloidal suspensions by photon correlation spectroscopy.... .....	169
A3.	Dispersion of P25 .....	173
A4.	UV-VIS absorbance of methylene blue .....	175
A5.	UV-VIS absorbance of Ciprofloxacin .....	181
A6.	UV-VIS absorbance of wastewater from Hachiba Company.....	182
	Scientific output.....	183
	<i>Curriculum vitae</i> .....	185

## LIST OF FIGURES

Figure 2.1	Scheme of a photocatalytic process.....	5
Figure 2.2	The number of scientific manuscripts with keywords "photocataly*" and "solar" .	7
Figure 2.3	A photocatalytic configuration .....	10
Figure 2.4	A batch reactor.....	11
Figure 2.5	A flow reactor .....	13
Figure 2.6	Illumination on the fluid layers in different flows .....	13
Figure 2.7	Configuration of a hybrid photocatalysis-membrane process .....	15
Figure 2.8	Factors influencing a photocatalysis.....	16
Figure 3.1	Scheme of the photocatalytic setup.....	29
Figure 3.2	The laboratory-scaled photocatalytic setup.....	29
Figure 3.3	Engineering drawing of the flow reactor .....	30
Figure 3.4	Engineering drawing of the flow reactor (cont.).....	31
Figure 3.5	Spectral intensity of the artificial UV lamp .....	33
Figure 3.6	Spectral intensity of the artificial visible lamp .....	34
Figure 3.7	Fluid velocity in the reactor .....	35
Figure 3.8	Fluids and concentrations of species in the photocatalytic system .....	37
Figure 3.9	Solution of the characteristic equation .....	41
Figure 4.1	UV-VIS absorbance spectrum of methylene blue .....	45
Figure 4.2	Dimerization of methylene blue .....	45
Figure 4.3	UV-VIS absorbance spectrum of ciprofloxacin .....	46
Figure 4.4	UV-VIS absorbance spectra of two commercial dyes .....	47
Figure 4.5	UV-VIS spectroscopy.....	49
Figure 4.6	Diffuse reflectance UV-VIS spectroscopy.....	51
Figure 4.7	Photon correlation spectroscopy .....	53
Figure 4.8	Procedure for photocatalytic experiments.....	55
Figure 5.1	SEM image of P25 aggregates.....	63
Figure 5.2	Ultrasonic dispersion of P25 suspension: Size characterization .....	64
Figure 5.3	Ultrasonic energy consumption.....	65

Figure 5.4	Ultrasonic dispersion of P25 suspension: The energy model .....	66
Figure 5.5	Stability test of dispersed P25.....	68
Figure 5.6	Diffuse reflectance UV-VIS spectroscopy of P25.....	69
Figure 5.7	UV-VIS absorption spectroscopy of P25 suspensions .....	71
Figure 5.8	UV-VIS absorption spectroscopy of P25 suspensions (cont.): Lower limitation of transmittance .....	72
Figure 5.9	UV-VIS absorption spectroscopy of P25 suspensions (cont.): Turbidity .....	73
Figure 5.10	Extinction coefficient of P25 suspensions.....	74
Figure 5.11	Influence of P25 particle size on the optical properties .....	75
Figure 6.1	Control tests of the photodegradation of methylene blue .....	78
Figure 6.2	Typical UV-VIS spectra of the photodegradation of methylene blue .....	80
Figure 6.3	Photocatalytic degradation of methylene blue.....	81
Figure 6.4	Reaction rate constants of photodegradation of methylene blue.....	82
Figure 6.5	Lower limitation of the methylene blue concentration .....	84
Figure 6.6	Influence of the suspension volume on the photodegradation of methylene blue .....	87
Figure 6.7	Influence of light intensity on the on the photodegradation of methylene blue .	88
Figure 6.8	Influence of the photocatalyst concentration on the photodegradation of methylene blue .....	90
Figure 6.9	Fluids and concentrations of species in the photocatalytic system (cont.).....	91
Figure 6.10	Influence of the photocatalyst concentration and optical pathlength on the photodegradation of methylene blue.....	93
Figure 6.11	Photocatalytic degradation with the high initial concentration of methylene blue .....	96
Figure 6.12	Influence of the initial concentration on the photodegradation of methylene blue .....	98
Figure 6.13	Influence of pH on the photodegradation of methylene blue.....	101
Figure 6.14	Influence of pH on the adsorption of methylene blue on the P25 photocatalyst .....	102
Figure 6.15	Influence of P25 aggregate size on the photodegradation of methylene blue .	104
Figure 6.16	Influence of photocatalyst aggregate size on the photodegradation of methylene blue.....	106

Figure 7.1	Conversion of methylene blue under visible illumination.....	112
Figure 7.2	Color removal of methylene blue under solar radiation.....	114
Figure 7.3	Photodegradation of methylene blue with commercial photocatalytic materials .....	115
Figure 7.4	Photodegradation of ciprofloxacin with magnetic nanoparticles .....	117
Figure 7.5	Color removal of Remazol Red RR dye under artificial UV/ visible light and solar light.....	119
Figure 7.6	Color removal of Everzol Navy ED dye under artificial UV/visible light and solar light .....	120
Figure 7.7	The NaViTex's pilot combined photocatalytic system.....	126
Figure 7.8	Photodegradation of colored solutions with the NaViTex's pilot combined photocatalytic system .....	127
Figure 7.9	The NaViTex's solar photocatalytic setup.....	128
Figure 7.10	Photodegradation of methylene blue with the NaViTex's solar photocatalytic setup .....	129
Figure 7.11	Photodegradation of wastewater from Hachiba Company with the NaViTex's solar photocatalytic setup .....	130
Figure 7.12	Photocatalysis introduced in a wastewater treatment plant .....	132
Figure 7.13	UV-VIS spectroscopy of highly colored (waste) water .....	134
Figure 7.14	Color removal efficiency with the high initial concentration of methylene blue	136
Figure 7.15	Color removal of Everzol Navy ED dye with a high initial concentration.....	136
Figure 7.16	The up-scaled photoreactor.....	138
Figure A 1	Graphical representation of particle size distribution of an assemble .....	167
Figure A 2	Correlogram of a sample measured by dynamic light scattering .....	169
Figure A 3	Effect of the particle concentrations on the transmittance and dynamic light scattering measurements .....	171
Figure A 4	Correlation of two dynamic light scattering instruments .....	172
Figure A 5	ULTRA-TURRAX® dispersion of P25 suspension: Size characterization.....	173
Figure A 6	Ultrasonic dispersion of P25 suspension: Size characterization (cont.) .....	174
Figure A 7	Ultrasonic dispersion of P25 suspension: Size characterization (cont.) .....	174
Figure A 8	Ultrasonic dispersion of P25 suspension: Stability test .....	175
Figure A 9	Calibration of methylene blue.....	178

Figure A 10 Effect of pH on the UV-VIS absorption spectra of methylene blue .....	179
Figure A 11 Calibration of ciprofloxacin .....	181
Figure A 12 UV-VIS absorbance of real wastewater from Hachiba Company (Danang, Vietnam) .....	182

## LIST OF TABLES

Table 3.1	Futures and technical solutions for a photocatalytic setup .....	28
Table 3.2	Specifications of the designed flow reactors.....	32
Table 3.3	Flow conditions.....	35
Table 4.1	UV-VIS spectroscopy of organic compounds.....	51
Table 4.2	Particle sizers used for the characterization of the dispersed photocatalysts ....	54
Table 4.3	Overview of experiments on the pre-treatment of the photocatalyst.....	57
Table 4.4	Overview of experiments on the color removal of methylene blue by photocatalysis .....	59
Table 4.5	Overview of experiments on applications of photocatalysis for wastewater treatment. ....	60
Table 5.1	UV-VIS absorption spectroscopy of P25 suspensions: Lower limitation of transmittance.....	73
Table 6.1	Lower limitation of the methylene blue concentration .....	85
Table 6.2	Influence of the initial concentration on the photodegradation of methylene blue .....	98
Table 6.3	Evolution of pH during the photodegradation of methylene blue.....	100
Table 6.4	Parameters of the kinetic model for the photodegradation of methylene blue	103
Table 6.5	Characteristics of the suspensions during the test with ultrasonic pre-treatment .....	105
Table 7.1	Technical regulation of textile wastewater in Vietnam .....	123
Table 7.2	Commercial dyes provided by Hachiba Company (Danang, Vietnam).....	124
Table 7.3	UV-VIS spectroscopy of highly colored (waste) water .....	135
Table 7.4	UV lamps for up-scaled photocatalytic setup.....	139
Table 7.5	Specifications of the up-scaled photoreactor.....	140
Table A 1	Effect of particle concentration on the dynamic light scattering measurements .....	170
Table A 2	Correlation of two dynamic light scattering instruments .....	172



# NOMENCLATURE

## ABBREVIATIONS

AOP	Advanced oxidation process
BET	Brunauer–Emmett–Teller model
BOD	Biological oxygen demand
Cipro	Ciprofloxacin
COD	Chemical oxygen demand
DLS	Dynamic light scattering
MB	Methylene blue
NP	Nanoparticle
PZC	Point of zero charge
SEM	Scanning electron microscopy
TEM	Transmission electron microscopy
UV	Ultraviolet radiation
VIS	Visible radiation
XRD	X-ray powder diffraction
WW	Wastewater

## SYMBOLS

### Capital letters

<i>symbol</i>	<i>significance</i>	<i>unit</i>
$A$	Area	$\text{m}^2$
$Abs$	Absorbance	–
$C_m$	Mass concentration of particles	$\text{g}/\text{m}^3$
$C_n$	Molar concentration of aqueous solution	$\text{mol}/\text{m}^3$
$C_{n,ini}$	Initial molar concentration of the organic substance	$\text{mol}/\text{m}^3$
$D$	Diffusional coefficient	$\text{m}^2/\text{s}$
$E_a$	Activation energy	J
$E_g$	Bandgap energy	eV
$E_v$	Energy density (of the ultrasonic dispersion)	$\text{J}/\text{m}^3$
$G_2(\tau)$	Autocorrelation function of the scattered intensity (in photon correlation spectroscopy)	–

$H$	Enthalpy	J
$I$	Light intensity	W/m <sup>2</sup>
$K$	Apparent reaction rate constant in a photocatalytic system	s <sup>-1</sup>
$K_{\text{ads}}$	Adsorption – desorption equilibrium constant	m <sup>3</sup> /mol
$L$	Optical pathlength	m
$N_p$	Number of particles	–
$P$	(Electric) power	W
$PDI$	Polydispersity index (of particle size distribution)	–
$Q$	Sum function of the size distribution	–
$R$	Universal gas constant	J/mol K
$R$	Reflectance	–
$Re$	Reynolds number	–
$S$	Surface area	m <sup>2</sup>
$T$	Absolute temperature	K
$T$	Transmittance	–
$V$	Volume	m <sup>3</sup>

Small letters

<i>symbol</i>	<i>significance</i>	<i>unit</i>
$a_R$	Activity factor (in a reactor)	–
$d_h$	Hydraulic diameter	m
$h$	Planck's constant	m <sup>2</sup> kg/s
$k$	Integrated reaction rate constant in a flow reactor	s <sup>-1</sup>
$k_B$	Boltzmann's constant	J/K
$k_r$	Intrinsic reaction rate constant	s <sup>-1</sup>
$n$	Moles of species	mol
$n$	Exponent	–
$\dot{n}$	Molar flow rate of species	mol/s
$p$	Perimeter	m
$p_d$	Dynamic pressure	N/m <sup>2</sup>
$q$	Modulus of the scattering vector	m <sup>-1</sup>
$q$	Density distribution function	–
$r$	Reaction rate	mol/m <sup>3</sup> s

$r_R$	Recombination rate	mol/m <sup>3</sup> s
$t$	Time	s
$u$	Velocity	m/s
$x_{\text{cum}}$	Intensity weighted mean size (of particle size distribution)	m
$x, y, z$	Cartesian coordinates	m

## Capital Greek letters

<i>symbol</i>	<i>significance</i>	<i>unit</i>
$\Gamma$	Decay rate of the correlation function (in photon correlation spectroscopy)	s <sup>-1</sup>

## Small Greek letters

<i>symbol</i>	<i>significance</i>	<i>unit</i>
$\alpha$	The order of magnitude	–
$\beta$	Extinction coefficient	m <sup>2</sup> /g
$\delta_{\text{opt}}$	Optical penetration	m
$\eta$	Degradation efficiency (in photocatalysis)	–
$\kappa$	Absorption coefficient	m <sup>2</sup> /g
$\lambda$	Wavelength	m
$\mu$	Dynamic viscosity	N s/m <sup>2</sup>
$\nu$	Light frequency	m <sup>-1</sup>
$\dot{v}$	Flow rate	m <sup>3</sup> /s
$\theta$	Surface coverage	–
$\theta$	Scattering angle	rad
$\rho$	Density	kg/m <sup>3</sup>
$\sigma$	Scattering coefficient	m <sup>2</sup> /g
$\tau$	Turbidity	m <sup>-1</sup>
$\tau$	Time interval (in photon correlation spectroscopy)	s
$g$	The stoichiometric coefficient of species	–

## Subscripts

<i>symbol</i>	<i>significance</i>
ad	adsorbed
aq	aqueous
R, T, M	reactor, tube, and mixing tank



# 1 INTRODUCTION

The term “photocatalysis” is intensively mentioned throughout this Ph.D. dissertation. This process is expectedly applied in water treatment. This study aims a concept for the treatment of textile industry wastewater by heterogeneous photocatalysis. In this chapter, the state of the art, the problem statement, the overview of the methodology and the organization of the dissertation are introduced.

## 1.1 MOTIVATION

The industry of textile and garment, which are inevitable products, drew a speedy growth, especially in Asian developing countries [1]. Worldwide, their market share increased from 36 % in 1990 to 58 % in 2011 worldwide. For instance, Vietnam had a market share of 2.5 % of the world exports (2008) [2], and was the 9<sup>th</sup> and 6<sup>th</sup> major exporter of textile and clothing, respectively (2014) [3]. Together with the growth of the garment economy, dyes are broadly consumed. The amount of synthetic dyes produced annually worldwide was estimated to be over  $7 \times 10^5$  tons (2013) [4]. Due to the inefficiency of the dyeing process, up to  $2 \times 10^5$  tons of dyes were lost to the effluents [4]. They have affected more and more seriously the environment [3]–[6]. Their toxicity together with their chemical stability makes it difficult to be degraded by the conventional wastewater treatments.

Therefore, modern wastewater treatments are required. It is essential that modern technology is cost-effective hence applied in developing countries, where a sustainable development attracts less attention. A wide range of modern techniques has been used, including adsorption, oxidation, microbiological or enzymatic decomposition. Among all, chemical oxidation is effective but its selectivity limits its applications. Advanced oxidation processes (AOPs) have received increasing attention as an alternative method [7]–[10]. Generated reactive free radicals are strong oxidizing agents (e.g., the superoxide radical  $O_2^{\bullet-}$  and the hydroxyl radical  $OH^{\bullet}$ ) that make AOPs non-selective to decompose organic solutes. These radicals are responsible for the oxidation, discoloration, mineralization and degradation of organic pollutants.

Among AOPs [11], photocatalytic oxidation has been applied successfully to the removal of recalcitrant pollutants [12]. The process was first introduced by Fujishima and Honda in 1972 [13]. The heterogeneous process is based on the interaction between photocatalytic materials and radiation with adequate energy to induce generation of electron-hole pairs [8], [23], [27]–[32]. Semiconductor nanoparticles are widely used as photocatalysts [14]–[16]. Usually, ultraviolet (UV) or near UV light can be utilized. To perform photocatalytic tests, key solutions [8] were focused: i) the utilization of new catalysts, including modified materials more effectively working under wide spectral illumination, or immobilized catalysts to enhance the recovery of the materials and avoid post treatment by filtration or sedimentation, ii) performances with harsh operational conditions, iii) design of efficient photoreactors, and iv) combination with other processes to enhance the efficiency.

45 years after photocatalysis was introduced for the first time, only a few industrial-scaled photocatalytic systems were presented. Two systems for water treatment were early installed at the National Solar Thermal Test Facility in Albuquerque, New Mexico, USA, and at Plataforma Solar de Almería, Spain [17]–[19]. For air purification, in 2015, a photocatalytic depollution performance was installed at the Leopold II tunnel in Brussels, Belgium [20], [21]. In fact, 29,095 papers on the topic “photocatalysis” had been published in open access journals within 1972–2012 (data are based on Thompson Reuters, <http://apps.webofknowledge.com>, accessed on 10-Sep-2017). Despite the numerous amount of researches, photocatalysis still meets a barrier when it comes to its applicability at large scale. It seems that, the studies of new materials (strategies i), and combined process (strategy iv) have been favored. Indeed, in 2015, it is the first time that a separated symposium of photocatalysis was organized in a conference. This event was held by the European Materials Research Society (the 2015 E-MRS Spring Meeting, Lille, France, May 2015). Most of the talks focused on photocatalytic materials development, while engineering studies were dispersedly presented. In May 2017, in the second occasion, the E-MRS again gathered scientists from the field (the 2017 E-MRS Spring Meeting, Strasbourg, France). Of all 15 sessions, new materials were intensively presented, while it was given only one session for the process performances and another for photoreactors.

A suitable photocatalytic reactor has become essential to fill in the gap between the laboratory studies and real applications. First, the photoreactor must ensure the engineering requirements of a reactor where process parameters are controllable and determinable. Second, an efficient interaction between light and fluid must be guaranteed [22], [23]. Third, the reactor must be scalable. A down-scale is needed to conduct experiments in different laboratories. An up-scale is necessary for further applications at industrial scale, or at least at pilot scale.

Facing these challenges, in this Ph.D. study, a photocatalytic setup was designed. Illuminated batch reactors widely used in other studies of materials development [6], [24], [25] are shown inappropriate. Instead, this work is based on the flow reactor prototype which was applied at the pilot scale [17]–[19]. An operational procedure is suggested. A reactor model for quantitative experimental results is introduced. To acquire comprehensive understanding of the designed setup, photocatalytic performance was tested with a model dye substance, methylene blue, and a widely used photocatalyst, commercial titanium dioxide nanoparticles. To test the ability for further applications, different photocatalytic materials and organic substances and different light sources (artificial or natural light) were used. At the end, a proposal of applying photocatalysis as one step in the effluent treatment system in a textile and garment company in Vietnam is given. It fulfills the concept of wastewater treatment by photocatalysis with nanoparticles. Detailed challenges are presented after the state of the art.

This Ph.D. study tackles various issues on the development of a scalable photocatalytic system which can be applied for wastewater treatment. Various ideas came up. In fact, with certain facilities, a limited time and a finite knowledge, only few of them were successfully conducted. For future work, the use of immobilized photocatalysts in the setup can be one

important application. Up-scaling can be done based on the connection between laboratories and reality which is introduced in this multidisciplinary study.

## **1.2 OUTLINE OF THE THESIS**

This dissertation is structured as follows:

Chapter 2: The state of the art is introduced. Based on reviewed literature, different aspects are considered, including photocatalytic materials used in research worldwide, pros and cons of photocatalytic reactors, influencing factors, and modeling. Detailed challenges are presented at the end.

Chapters 3 to 7 give a detailed description of the main findings and results of this thesis. The main results can be divided into four parts: 1) the design and realization of the reactor; 2) the experimental characterization of the materials used as photocatalysts; 3) the experimental and theoretical aspects of the photocatalytic performance; 4) the real application in a textile company in Vietnam. More in details, the chapters are divided as following:

Chapter 3: The chapter introduces the design of a new laboratory-scaled flow photocatalytic setup together with an operational procedure. A reactor model is established. This chapter actually shows the first main results of the dissertation.

Chapter 4: Materials, experimental and analytical methods are given.

Chapter 5: The characteristics of the photocatalytic materials used in this work are shown. This chapter represents the second part of the main experimental results of the thesis.

Chapter 6: Experiments are performed for a comprehensive understanding of the engineering photocatalysis. Theoretical aspects of a photocatalytic performance are discussed. The chapter is the third part of the main results of this work.

Chapter 7: Selected case studies aiming at laboratory applications are shown. Further experiments towards real applications in a textile company in Danang, Vietnam are presented. Data are discussed regarding a joint German-Vietnamese project. The results aim at practical aspects, and are the fourth main results of the thesis.

Chapter 8: Conclusions of the work are given. Ideas for further studies are suggested.



## 2 FUNDAMENTALS OF PHOTOCATALYSIS

### 2.1 PHOTOCATALYSIS

#### 2.1.1 Photo excitation

Photocatalysis is a heterogeneous process with a wide range of application. Various oxides with narrow bandgap such as  $\text{TiO}_2$ ,  $\text{ZnO}$ ,  $\text{SnO}_2$ ,  $\text{Fe}_2\text{O}_3$ ,  $\text{WO}_3$  or sulfides such as  $\text{CdS}$ ,  $\text{ZnS}$  are potential photocatalysts [14]–[16]. In these materials, free electrons are localized in the valence band. When the materials are irradiated with light, they will absorb photon energy ( $h\nu$ ) of greater than the bandgap (typically with the ultraviolet illumination) [6], [8], [25]–[31]. Electrons are excited and jump to the conduction band. The positively charge carriers left in the unfilled valence band are called holes. The photo excitation is described as Eq. (2.1) and shown in Figure 2.1.



The created electrons and holes move to the surface of the photocatalyst. They are trapped, or recombine at surface trapping sites.

The time scale for each step of photocatalytic mechanism can be summarized as [28], [32], [33]: electron–hole excitation time is few fs, trapped time is 100 fs–10 ns, and recombination time is tens ns. Consequently, the fast recombination restricts the application of photocatalysis [17], [31].

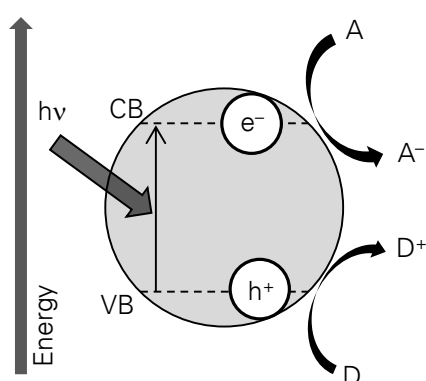


Figure 2.1 Scheme of a photocatalytic process, where  $h\nu$  is the photon energy, VB and CB are the valence and conduction band of the photocatalyst,  $e^-$  and  $h^+$  are the photo excited electrons and holes, A and D are electron acceptors and donors, respectively.

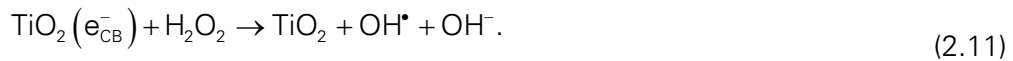
### 2.1.2 Reaction pathway

The photo induced electrons and holes react with electron acceptors or donors, respectively. The reaction of holes with electron donors can be performed via two mechanisms. The trapped holes either directly degrade organic compounds (so-called direct mechanism or hole mechanism, Eq. (2.2)) or react with surface hydroxyl groups in water to produce  $\text{OH}^\bullet$  radicals (the indirect mechanism or the radical mechanism, Eqs. (2.3)–(2.4)).



The dual reaction mechanism may happen where both hydroxyl group and the organic compound can act as electron donors, or reductants, which are oxidized [34]–[36]. Accordingly, the properties and products of reaction may be influenced. It is interesting that, like other AOPs, photocatalytic reaction are chain reaction sequences and the ideal final products are  $\text{CO}_2$  and water.

While hydroxyl groups or organic substances consume the holes, electron acceptors utilize the counter charge carriers, the electrons in the conduction band. Dissolved oxygen ( $\text{DO}$ ) is a primary electron acceptor since it involves the formation of other reactive oxygen species. As  $\text{DO}$  reacts with electrons, its presence is vital to maintain the electron-hole separation and to promote the photocatalysis [37]. The reaction pathway of  $\text{DO}$  was proposed [30], [38] as



The kinetics of  $\text{O}_2$  as well as the decay profile  $\text{O}_2^{\bullet-}$  was studied [30], [37], [39].

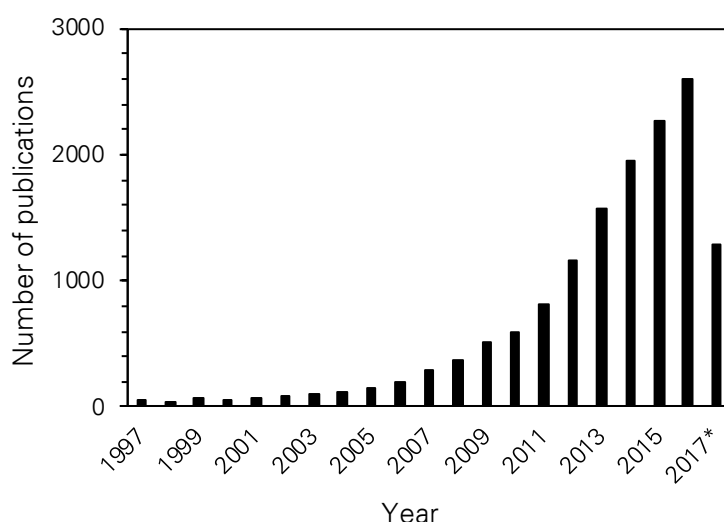
Other electron acceptors are  $\text{H}_2\text{O}_2$ ,  $\text{O}_3$  [39]. Note that  $\text{H}_2\text{O}_2$  can act a dual role not only to accept conduction band electron as an oxygen species, but also to generate hydroxyl radicals (Eq. (2.12)) [40].



### 2.1.3 Modified photocatalysts

Among photocatalytic materials, titanium dioxide  $\text{TiO}_2$  is very promising because of its chemical, biological inertness and especially its commercial availability [8], [26]. However, the large bandgap requiring UV irradiation for the activation is the main disadvantage. For  $\text{TiO}_2$ , to excite the electron-hole pair, an adequate energy of 3.0–3.2 eV appropriate to wavelengths of shorter than 410–387 nm is requisite [28], [33], [41]. Due to a small quantity of UV-radiation in the sunlight spectrum [17], [31],  $\text{TiO}_2$  can absorb only 2–5 % of solar energy. It limits the utilization of solar photocatalysis which has become the goal for industrial applications (Figure 2.2) [17], [23], [42], [43]. As previously presented (section 2.1.1), the fast recombination is the second main limitation of  $\text{TiO}_2$  photocatalysts. Critical solutions [8], [43] to overcome these drawbacks are the modification of the photocatalytic materials. There are three forms of modification [44].

In the bulk modification, dopant chemicals can be added to the bulk of the photocatalysts [44]. Doping is the technique to achieve this modification. Photocatalysts can be doped with different types of metals (including rare earth elements) or nonmetals [8], [46], [47]. The non-metallic dopants (nitrogen [48], [49] and carbon [50]) may localize electronic states above the valence band of the photocatalyst, thus narrowing the bandgap energy and extend the light absorption of photocatalysts to the visible range [46], [48]. It increases the photocatalytic response, or photoresponse of the materials. The presence of metals can also narrow the bandgap of photocatalysts and utilizes lower photon energy than pristine photocatalysts [46]. Moreover, metallic ion dopants prolong the lifetime of the charge carriers by trapping electrons, thus the



\* The data statistic was tallied throughout the first half of the fiscal year.

Figure 2.2 The number of scientific manuscripts with keywords "photocataly\*" and "solar" based on the data of Thompson Reuters [45]. The statistics was conveyed on June 2017.

counter carrier can reach the surface of the photocatalyst [51], [52]. Various metals can be listed, e.g., silver [53], [54], platinum [55], gold [56], iron [57], copper [58], chromium [59], magnesium [60] and tin [61]. Rare earth doping is another strategy to enhance photocatalytic activity. Rare earth elements belong to the f-block in the periodic table including lanthanides, as well as scandium and yttrium. Doping with rare earth elements can inhibit the phase transformation of titania photocatalysts from anatase to rutile [62], [63]. Note that, of three phases, anatase is the most active for photocatalytic purposes. Additionally, rare earth doped photocatalysts have an improved photocatalytic activity as lanthanide ions play the role of an electron acceptor and accelerate the electron-hole separation [64]–[67]. Attributed to a charge transfer transition between f-electrons and the conduction/valence band of titania, the bandgap of the photocatalyst is narrower [59], [64]–[67]. The red shift to longer wavelengths excites the catalyst in the visible light and makes the utilization more efficient.

Another modified photocatalyst group is nanocomposites [43], [44]. The materials consist of photocatalyst domains in contact with inert or photoactive compounds. Different strategies can be applied. Nanocomposites can be produced by depositing metals (Ag [68], [69] and Au [70]) on photocatalysts. Similar to the mechanism of metallic doped photocatalysts, the Fermi level of metals shift closer to the conduction band of the photocatalyst, which indicates a better separation of electrons and holes [44], [71]. Composites made of photocatalysts and some carbonaceous materials with high conductivity (graphene [72] and carbon nanotubes [73]) also have this property. Another strategy is coupling.  $\text{TiO}_2$  can be coupled with different semiconductors ( $\text{SnO}_2$  [74],  $\text{WO}_3$  [75], ZnO and CdS [76]). They have a similar bandgap to that of  $\text{TiO}_2$  where the energy state of the conduction band is lower and the valence band is either similar or lower. They act as an electrons and holes storages. Consequently, the inter-particle electron transfer from  $\text{TiO}_2$  to the other semiconductors can happen and prolong the lifetime of electrons and holes.

Surface modification is the other form to improve photocatalytic activity [44]. Since this section aims at the enhancement of photoresponse and the retard of electron-hole recombination, surface modification is briefly introduced. Accordingly, the physicochemical properties of photocatalysts can be varied [43]. Sol-gel preparation of silica or zirconia may control the crystallinity and help to achieve purer anatase phase [77]. The surface roughness of photocatalysts related the reflectivity and the efficiency of light absorbance [44] can be altered by doping photocatalysts with silver [78]. Adsorption capacity is one of the most dominant parameters affecting the photodegradation [44]. The deposition on nanoporous materials such as fractal-type morphology [79], nanofibrous architecture [80], nano hollow [81] structured may enlarge the surface area of photocatalysts. In addition, increasing the adsorption of dissolved oxygen enhances the charge carriers' separation [44]. As polytetrafluoroethylene (PTFE) has an affinity toward  $\text{O}_2$ , it can be chosen to produce the composite film to increase the local concentration of oxygen [82]. Other properties such as surface charge, surface hydrophilicity, and specificities (which is the selectivity toward certain toxic compounds) can be altered as well [44].

## 2.2 PHOTOCATALYTIC SETUPS

### 2.2.1 Requirements

A photocatalytic setup certainly ensures the engineering requirements. Additionally, the reactor must efficiently collect photon energy to perform the reaction.

#### Illumination

Illumination is an absolute requirement for a photocatalytic reaction. Regarding the light sources, the excitation of commercial photocatalysts required energy in the UV region of the electromagnetic spectrum. Artificial UV lamps can be employed. Mercury lamps are widely used. However they are costly and unfriendly to the environment [6], [31], whereas photocatalysis is expected to solve environmental problems. The substitution of these lamps by mercury-free UV source is a must strategy [31], [83]. Light-emitting diode (LED) [84], [85] or excimer lamps [86], [87] with a broad range of applications can be used. For the modified photocatalysts, which can utilize the visible light, sunlight has gained a great attention to researchers (Figure 2.2) [17], [23], [42], [43]. If the reactor design allows for an efficient light collection, solar photocatalysis can be performed even with commercial photocatalytic materials. Different types and technical issues of solar photocatalytic reactors have been investigated by the group of Malato in Plataforma Solar de Almería (PSA) in Spain [17]–[19]. The design was used for pilot scale photocatalysis.

Regarding the brightness, the flux density striking the illuminated surface should be taken into account. In photocatalysis, this characteristic is commonly referred as “intensity” and has the unit of  $\text{W/m}^2$  (which is actually the unit of irradiance in optics [88]). Light intensity in most current studies is lower than  $200 \text{ W/m}^2$ . In this range, the photocatalytic reaction rate is proportional to the light intensity [39], [41], [89]–[93]. The influence of light intensity is introduced in detail in section 2.3.3.

Optical penetration should be considered. In case of working with slurry photocatalysts, the turbidity of the suspension affects the radiation propagation [94], [95]. For this reason, the optical penetration is usually short [17], [19].

#### Flow

In continuous flow process with slurry photocatalysts, a mixing tank is required to disperse the photocatalyst in the fluid [8]. A good mixing should be performed to avoid sedimentation or re-agglomeration of photocatalysts [17], [19].

A pump is needed to supply the massive suspension into the system. The pump energy must be high enough to maintain the flow regime. Typically, in flow reactors of which length in reality can be hundreds meter and the retention time can last for hours, turbulence must be carried [17], [19].

Additionally, due to the non-uniformity of light intensity in different fluid layers inside the reactor (e.g., Figure 2.6 in section 2.2.2), the concentration gradients of organic substances cannot be avoided [95]–[97]. A strong mixing condition can help to lower this mass transport limitation.

### Post treatment

An integral step is entailed for the post-separation. One simple technique is the integration of coagulation, flocculation, and sedimentation steps, yet it is unable to recover the photocatalysts. Membrane filtration (micro- or nanofiltration [98]–[100]) is a practical solution (Figure 2.3). It not only handles products separation but also realizes the continuous mode of photocatalysis.

### Materials

Reactors must be stable enough to contain the mass of the catalyst and a large amount of liquid. Especially the illuminated side must be UV-transparent to receive radiation for photocatalyst activation. Other needs for chemical reactions must be guarded, e.g. the material must be pH-resistant depending on the pollutants to be treated and their (by-) products. Fluoropolymers such as PTFE (polytetrafluoroethylene), PVDF (polyvinylidene fluoride), FEP (fluorinated ethylene propylene), PFA (perfluoroalkoxy) and several types of glass such as borosilicate glass satisfy these requirements [17].

When working with solar light, to concentrate the light, a sun collector is needed [17]–[19]. Its surface must be polished and mirrored but, at the same time, anti-abrasive so that it can effectively reflect the solar light in various climatic conditions. A wavelength-selective reflective surface is needed since the reaction requires the high photon energy of UV light. Electro-polished anodized aluminum and organic plastic films with an aluminum coating are the two best fitting of these requirements.

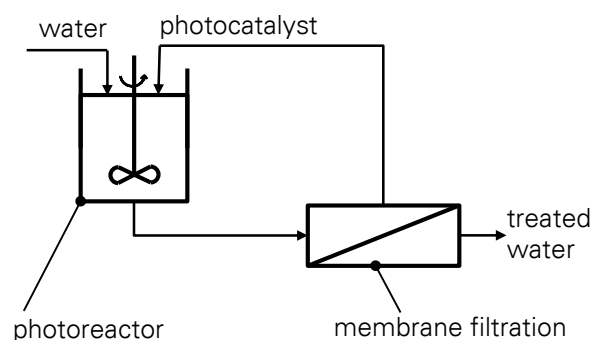


Figure 2.3 A photocatalytic configuration: a photocatalytic reactor integrated with a membrane filtration for continuous flow.

### 2.2.2 Reactors

This study concentrates on water treatment. Heterogeneous reaction occurs in solid-liquid systems. Depending on photocatalytic types, operational conditions and applications, compatible photocatalytic reactors are required [101]. Different types of reactor deal with well-stirred slurries, fluidized beds, packed beds and catalytic walls [102]. Since fixed photocatalysts reduce the active sites, enlarge the mass transfer limitation as well as restrict the photon penetration, the suspended photocatalysts are preferred [8], [31]. This section firstly introduces reactors for suspended and fixed photocatalysts. It is then followed by coupling processes of photocatalysis and post treatment.

#### Batch reactors for slurry photocatalysts

Most of the slurry photocatalysis have been implemented in illuminated batch reactors where a perpendicular or magnetic stirrer maintains the dispersion. A UV lamp (usually mercury lamp) housed in an inner quartz tube is immersed in the cylindrical axis of the reactor to generate the UV radiation for photocatalyst's excitation (Figure 2.4) [6], [24], [103]. Cooling water for thermal stabilization (optional) can be circulated in the quartz well. Gas electron acceptor (if needed) can be purged in the reaction container. The use of multiple lamps can enhance a more uniform distribution of light intensity [104]. Illuminations from the side, from the top or through a bottom optical window of the reactor are other variants of this reactor prototype [25].

When one uses laboratory-scaled batch reactors, e.g. flasks, the recirculation time is seconds, whereas the reaction time is minutes to hours [22]. The fluid parcel is considerably well-stirred. Every particle assumedly has the same averaged exposure to illumination and the system can be treated as a well-stirred reactor.

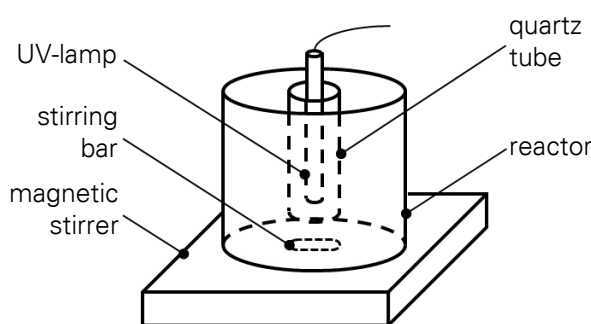


Figure 2.4 A batch reactor widely used in photocatalysis studies.

### Flow reactors for slurry photocatalysts

With this reactor type, photocatalysis is performed in a UV-transparent tube, which receives illumination from the side [12], [17], [18], [89], [97], [105]. Reactor diameter must be small enough to eliminate the non-illuminated space, but big enough to maintain the small pressure drop. The inner diameter is recommended to be in the range of 25–50 mm.

Flow reactors can be well applied for solar photocatalysis [17], [18]. A reflector based on solar thermal collectors is used to concentrate sunlight. Solar photocatalysis requires only a high-energy photon gathering, whereas heating plays no significant role, thus, the process identifies with medium-, and low- or non-concentrating systems. Parabolic trough collector is a medium-concentrating system. The tubular reactor (or absorber) is located in the focal line of a parabola to receive concentrated solar radiation from the parabolic reflective surface. The configuration demands an azimuth tracking mechanism to adjust the system direct to the solar irradiation angle which is costly. Additionally, the high concentrated irradiation of such concentrating systems causes a higher electron-hole recombination rate and decreases the photocatalytic property. The problems are negligible in compound parabolic collector, a low-concentrating system. This alternative has a reflective surface constructed by two parabolas thus indirect solar light is also reflected onto the absorber (Figure 2.5). Accordingly, this collector is less dependent on the solar irradiation angle. The complex design and the costly operation of the tracking device in parabolic trough collectors are avoided. The large scaled reactors for suspended photocatalysts were successfully employed.

In flow reactors, the interplay between incident photons and fluid elements is inextricably coupled and should be accounted [22]. While the irradiance profile essentially follows the Beer-Lambert law, the flow rate bears different fluid velocity profiles (Figure 2.6a and c), thus the absorbing species are spatially non-uniformly distributed. Ollis and Turchi [107] introduced a model to determine the reactant concentration for each single fluid element which depends on the distance to the illuminated wall, the axial distance, the velocity profile as well as the ratio between the diffusion rate and reaction rate (the Damkohler number).

In the laminar flow (Figure 2.6 a), the paraboloid flow by the radii causes non-uniform residence time for each fluid layer. The fastest velocity is in the middle of the slit whereas radiation traverses a half distance and is being extinguished. For an industrial performance, since the reactor tube is long, a turbulence must be guaranteed to avoid the sedimentation of the catalyst along the circuit [19]. The turbulence (Figure 2.6 c) allows for a uniform fluid over any cross section. This configuration is more efficient than the former.

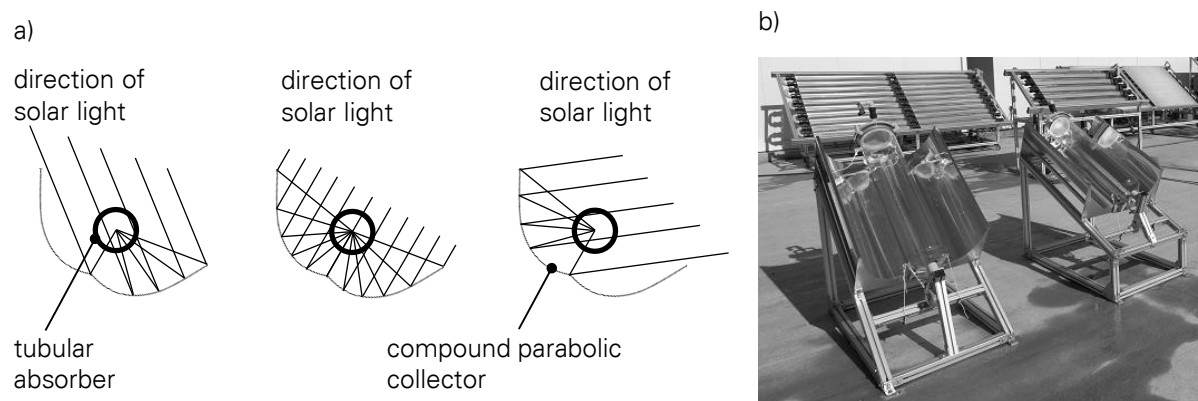


Figure 2.5 A flow reactor used for solar photocatalysis: a) Scheme and b) image of compound parabolic systems for water disinfection which were installed in the Plataforma Solar de Almería (2010) [106].

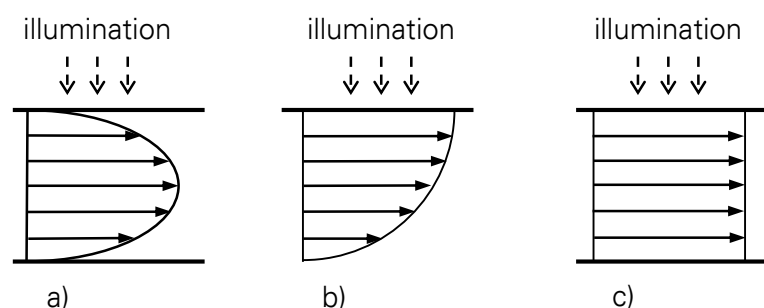


Figure 2.6 Illumination on the fluid layers in different flows: a) laminar flow, b) laminar falling film flow, and c) turbulent flow.

### Reactors for fixed photocatalysts

When using photocatalyst powders, dispersion is needed to homogeneously distribute photocatalyst particles in reactors. Additionally, the final separation of the catalyst from the treated stream is the main limitation of the process. Immobilization of photocatalyst on an inert support restrains the costly membrane filtration of the post-treatment [8], [83], [108]. A variety of conventional supports include mesoporous clays (zeolite, kaolinite) [103], [109] or polymers [84], [110], glass or steels [111].

Three main categories of reactors for fixed photocatalysts are glass plate reactors, wall reactors, and bed reactor. In fluidized bed reactors, beds were prepared by immobilizing photocatalysts on glass beads [112]. Silica gel can be used to enhance the fluidized quality [113], [114]. Recently, an innovation of fluidized reactors was reported via the utilization of a coupling photocatalytic membrane reactor [115] which is introduced in the next section. The biggest problem of bed reactors is light distribution. To avoid it, glass plate reactors or wall reactors are other options. In glass plate reactors, the photocatalyst coated on a glass sheet and water falls as a thin film top side down which is illuminated from the side [116]. The falling film

(Figure 2.6b) holds the great amount of efficient absorbing species, because the fastest flow at the illuminated wall receives the greatest radiation. Glass sheet can also be held on an inclined surface of the reactor and UV light was irradiated from the top [117]. The immobilized catalysts can be also placed on the bottom of the reactor [111], [117]. Instead of coating on a glass sheet, fixation on polymers can be employed as well [109], [118], [119]. These configurations, however, encounter the capacity problems and so far not a practical design for an up-scaling purpose. In wall reactors, photocatalysts are coated directly on the inner surface of a reactor [38], [114], [120], [121]. Both batch or flow reactor can be used.

There are other forms of immobilization. Photocatalysts entrapped balls or immobilized on cement beads were employed in a flow reactor [122]. Magnetic nanoparticles allowing for the recovery of the magnetized photocatalysts by an external magnetic field also have a great attention [123]–[125]. These materials provide the large surface area, which is unapproachable for conventional immobilized photocatalysts. The reaction was performed in batch reactors. In other techniques, catalysts can be coated on glass fibers or glass tubes [126], [127]. The reactor can be cylindrical where UV lamp is positioned in the center axis. The photocatalyst tubes [127] or coated fiberglass fabric [126] in a cylindrical form are placed in the space between the UV lamp and the reactor wall. For a better light distribution, the catalyst-coated optical fibers can be used. The fibers act a double role as a photocatalyst support and as a light distributing guide [128]. The photoreactor consists of glass tubes distributed between two baffles (similar to a tube bundle heat exchanger) [129], [130]. The free reactor volume is, however, small and arduous for up-scaling purposes.

The commercial performance for immobilized photocatalyst has not identified to date [17].

### **Coupling processes**

The combination of photocatalysis with other processes can be a solution to improve the photocatalytic efficiency and moreover allow for the performance of a large amount [31]. Here combined (simultaneous) processes, which are dissimilar from integrated (sequential) processes [99], [131], are mentioned. Combined processes may be divided into two main categories [132]. The photocatalysis can be coupled with other AOPs such as ozonation, ultrasonic irradiation, photo-Fenton reaction or electrochemical treatment to increase the number of generated radicals. The other is coupling with biological treatment, membrane filtration or physical adsorption which improves the efficiency of the overall process but does not affect the photocatalytic mechanism.

To solve the problem of photocatalyst post-separation and recovery which were questioned in the previous section, hybrid photocatalysis-membrane process can be employed [132], [133]. The coupling process includes three main units as shown in Figure 2.7a) [133], [134].

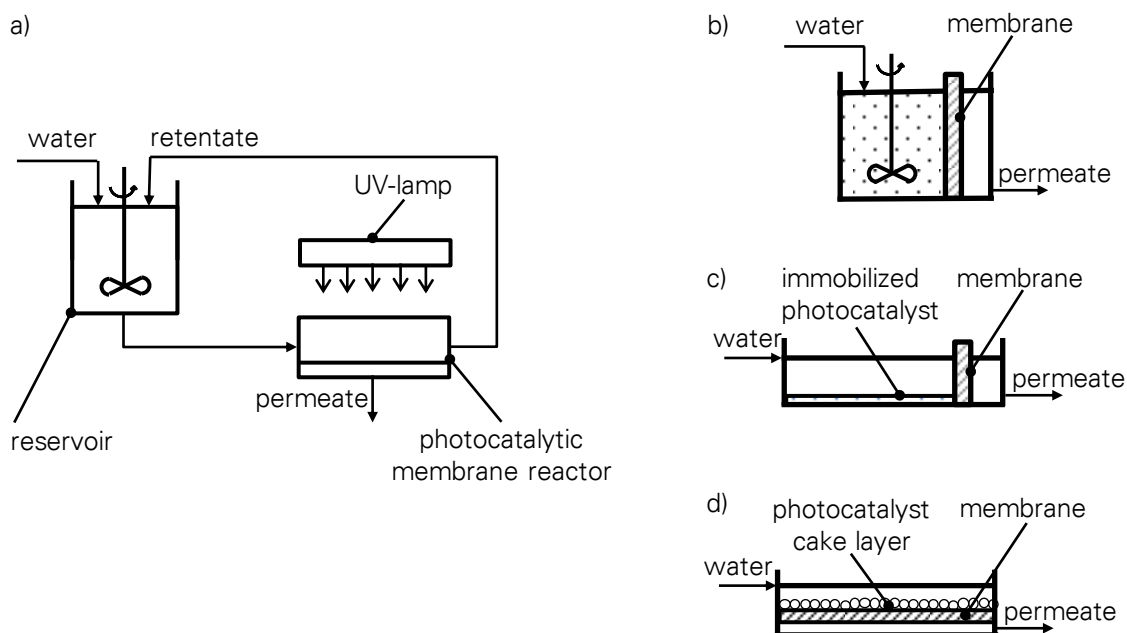


Figure 2.7 Configuration of a hybrid photocatalysis-membrane process: a) the whole system; and b–d) photocatalytic membrane reactors.

Water and photocatalyst are stored in the feed reservoir. Photocatalytic reaction occurs in the photocatalytic membrane reactor (PMR) illuminated by a UV lamp [135], [136]. Photocatalysts can be either colloidal (Figure 2.7b) or immobilized (Figure 2.7c and d). In slurry photocatalysis, the submerged membrane is used for the coupling filtration. When using fixed photocatalysts on an external support but not on membrane (Figure 2.7c), the membrane isolates the particles segregated from the immobilized layer due to the mechanical instability. A PMR can be also constructed by photocatalyst particles forming a cake layer beyond a microfiltration membrane (Figure 2.7d) [115]. The PMRs reduce the size of installation as well as help to control the residence time of the molecules in the reactor.

## 2.3 QUANTITATIVE DESCRIPTIONS OF PHOTOCATALYSIS

Application of photocatalysis requires the understanding of the process as well as of its operational parameters. A lot of authors have made their contributions to the effect of parameters [41], [89], [94], [101], [137], [138]. For the study purpose, influences on the slurry photocatalysis are discussed. Impact factors can be grouped into main categories (Figure 2.8):

- Photocatalyst which promotes the reaction;
- Reactants, in particular the organic compounds to be degraded and the electron acceptors to be oxidized;
- Light which is the driving force of the process, more specifically light wavelength and intensity;

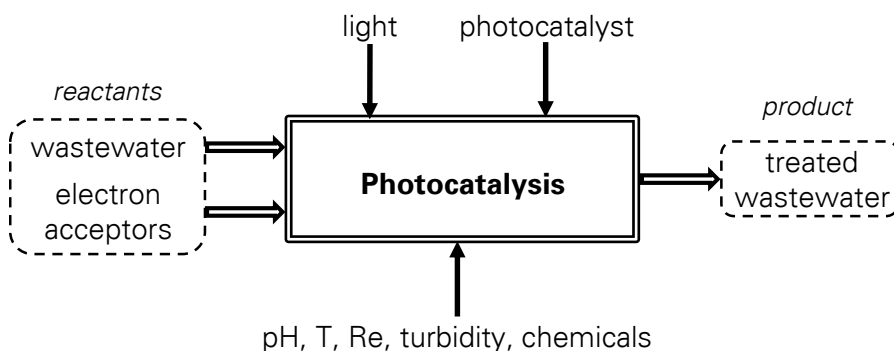


Figure 2.8 Factors influencing a photocatalysis.

- And other factors, such as acid-base property, thermal condition, flow regime, turbidity, and the appearance of other chemicals.

At the end of this sub-chapter, modeling of photocatalytic process is introduced. Light propagation, kinetic model and the evaluation of the reaction by photonic efficiency are mentioned.

### 2.3.1 Influence of photocatalyst concentration and morphology

#### Photocatalyst dispersion

Mechanical mixing is usually used to achieve homogeneity of slurry photocatalysts [8]. Dispersion with ultra-energy has some attention [24], [33], [36], [37], [137], [139]–[144]. However, the relation between dispersion related to the aggregated level [145] and the turbidity shortening the optical penetration [94], [95] was not reported.

#### Photocatalyst loading

In photocatalysis researches, the photocatalyst concentrations from few mg/l to few g/l were reported [12], [14], [26], [101], [105], [146]–[150].

Mostly, in a low range of photocatalyst concentration (below hundreds mg/l), the reaction rate increases along with the concentration due to the increase of surface area [12], [14], [40], [148], [149], [151]. It was claimed that the rate is proportional to the number of active sites of the photocatalyst [40], [152]. The reaction rate constant reaches a plateau or even decreases with ongoing increased photocatalyst concentrations [14], [148]–[150]. This phenomenon was usually noticed when the concentration is from hundreds mg/l to few g/l. It is explained with the high turbidity of the suspension and also with possible re-agglomeration, which consequently shorten the radiation propagation [94], [95]. Additionally, at high loading, the particles with the activated species adsorbed on their surface collide with the ground state particles (i.e., with no activated species on their surface) thus turn to be deactivated [146], [149], [153]. Moreover, the availability of the active sites on catalysts depends upon solute concentration which should be accounted. Diffusive limitations (external interfacial diffusion and even internal diffusion) may be another reason [95]–[97].

It is agreed that there is an optimum catalyst concentration. This value depends on types of contaminants, operation parameters as well as experimental setups [8], [26], [101], [105]. The assessment of photocatalyst concentration is more important when using flow reactors. Since an industrial reactor can be hundreds meter long, highly concentrated photocatalysts can cause the massive load.

### **Morphology of photocatalysts**

Various analytical methods can be employed to characterize photocatalysts. Most of them focused on the morphology of primary particles (or fundamental particles). They are structured by atomic or molecular bonding and cannot be separated into smaller particles except using an ultrahigh energy. Due to the synthetic process of photocatalysts, one rarely finds them as primary particles. Instead coalescence of primary particles by the tight bound or by the loose bound is formed. These so-called aggregate or agglomerate structures [154] have their properties differing from the primary particles. Scattering properties, as well as the degree of photons diffusion depends on the aggregate size and structure.

Certainly, the size of primary particles determines the specific surface area of photocatalysts which is related to the adsorption capacity and the reaction zone [44], [155]. Finer particles have a larger specific surface area and higher saturated absorbability [24], [156]. Dissimilarly, aggregates of different size can have the same BET surface [157]. It means that aggregate size has no effect on the surface area.

Particle size and morphology determine optical properties of the system [95], [156]–[160]. It is caused by the UV penetration influenced by particle size. It was also shown that particle size affects the lifetime of excited electrons and holes, and their recombination [146], [153], [159]. Additionally, shape and structure of photocatalysts affect the internal diffusion of light and organic concentration inter-particles [22], [95], [96], [142]. Experimentally, the reactivity of photocatalysts reduces as the aggregates become larger and denser [142], [145], [157], [161]. Finally, size affects the distribution and sedimentation of photocatalysts in the suspension, as well as decides the operation of post-treatment [98]–[100].

Notably, when a “particle size” is presented, depending on analytical methods, the shape of primary particles and structure of agglomerates or aggregates, different equivalent diameters can be mentioned [162]–[164] (see Particle size distribution in Appendix A1). It is necessary to inspect the used method so that one can acknowledge which property of the photocatalyst was introduced.

### **2.3.2 Influence of organic compounds**

Organic pollutants in wastewater (WW) can be diverse. Depending on the sources, some organic chemicals can have a higher concentration than in municipal WW. E.g., pesticides and fertilizers are introduced in WW from agriculture [165]. In the textile industry, WW consists of dye substances [4]. Pharmaceuticals from different drug classes mainly present in WW from

hospitals or pharmaceutical companies [166]. Different attempts have been performed to degrade such organic pollutants.

Photocatalytic pathway depends on the chemical structure of organic compound(s) in the water. As affecting the mass transfer between the bulk liquid and the photocatalyst [95]–[97], the organic substances also impact the photocatalytic conversion. In photocatalytic studies, adsorption is assumed to be equilibrated. It follows the Langmuir isotherm [8], [167]

$$\theta = \frac{K_{\text{ads}} C_n}{1 + K_{\text{ads}} C_n}, \quad (2.13)$$

where  $\theta$  is the surface coverage of the catalysts,  $K_{\text{ads}}$  is the adsorption constant and  $C_n$  is the molar concentration of the organic molecule in the aqueous solution.

Since the adsorption depends on the ratio between the amount of photocatalyst and the concentration of organic compounds, the reaction rate is altered by the initial concentration of the organic substance [91]. Profiles of the pollutants concentration in the bulk always present in the heterogeneous reaction [22], [91]. The increased concentration causes mass transfer. Organic compounds, intermediates and products obstructs the active reaction sites at the  $\text{TiO}_2$  surface [90], [101]. However, below a certain concentration of the photocatalyst, the mass transport is negligible [95]–[97]. Also the turbulent flow can diminish the mass transfer limitations in a flow reactor.

The shielding effect of organic substances is, of course, important. Depending on their properties, organic molecules can absorb UV or visible light. Typically for colored dye substances from textile wastewater when the initial concentration is high, more photons are absorbed by the dye molecules whereas fewer photons can reach the  $\text{TiO}_2$  surface [3], [4], [10], [38], [101], [168]. The limited UV penetration depth thus decreases the photodegradation.

Other consequences such as surface charge and pH are discussed later (section 2.3.4) together with the influence of the aqueous medium.

### 2.3.3 Influence of light intensity

Radiation, the driving force of photocatalysis, is a key factor in the process [101], [169]. In the field of photocatalysis, due to the large bandgap of photocatalysts, only radiation in the UV range or near UV range (for modified photocatalysts) is utilized. The effectiveness of light depends on its intensity [39], [41], [89]–[93].

In most photocatalytic studies, the intensity is lower than  $200 \text{ W/m}^2$ , and the dependence of the reaction rate on the light intensity is linear. The number of photogenerated electron-hole pairs on the photocatalyst surface governs the reaction rate. The higher radiant flux causing the larger number of charge carriers certainly explains the linear function.

Some work reported the photocatalytic performance at medium range (approx.  $250 \text{ W/m}^2$ ), where the reaction rate is proportional to the square root of the intensity. The electron-hole

recombination in a meanwhile competes for the excitation. The recombination rate  $r_R$  is presented as in [170]

$$r_R = k_R C_{e^-} C_{h^+} = k_R C_{e^-}^2, \quad (2.14)$$

where  $C$  is the concentration of the charge carriers, and  $k_R$  is the recombination rate constant. The transition to zero-order is noticed at the intense UV intensity due to the predominance of electron-hole recombination over the formation. Note that the recombination is exothermic. Thus, an extreme radiant flux should be considered, as it may overheat the catalyst and reduce the reusability of the catalyst. The influence of temperature is discussed later.

Exceptionally, in the very high range, the reaction rate is independent of the light intensity.

### 2.3.4 Influence of other factors

#### Electron acceptors

Electron acceptors (such as dissolved oxygen, hydrogen peroxide and ozone [30], [37], [39]) react with trapped electrons, thus trapped holes have a relatively long lifetime to initiate the radicals. In other words, the presence of electron acceptors promotes the electron-hole separation and retards the recombination [37]. However, at high concentrations of electron acceptors they occupy the surface of the photocatalyst, compete the adsorption of the organic pollutants and thus have an adverse effect. Additionally, as hydrogen peroxide  $H_2O_2$  and ozone  $O_3$  are not friendly to the environment, their use should be reduced.

#### Temperature

As a chemical reaction, the photocatalytic reaction rate constant depends on the temperature according to the Arrhenius' equation [170]

$$k = A e^{-\frac{E_a}{RT}}, \quad (2.15)$$

where  $E_a$  is the activation energy and  $A$  is the pre-exponential factor.

The adsorption of organic molecules on the photocatalyst surface is exothermic. At low temperature [8], [165] according to the Le Chatelier's principle, adsorption of reactants, intermediates and products is favored and limits the product desorption. On the contrary, at high temperature, the adsorption is disfavored and becomes the rate-determining step. The theory was experimentally proved [40], [171], [172]. Indeed, the adsorption constant complies with the van't Hoff's equation [170]

$$\frac{\partial(\ln K_{ads})}{\partial T} = -\frac{\Delta H}{RT^2}, \quad (2.16)$$

where  $\Delta H$  is the enthalpy of adsorption.

The solubility of oxygen, an electron acceptor, in water reduced by temperature [17] should be also considered. In photocatalytic performances, the temperature hardly affects the point of zero charge (PZC) of  $\text{TiO}_2$  colloids [173], [174] leading to no effect on the morphology of the photocatalysts.

Considering solar photocatalysis based on the mechanism of a solar thermal concentrator, photoreactors concentrate the heat of solar radiance [17], [18], [175]. Aiming at a photons activation, the photocatalytic systems require no heating and can be operated at room temperature. In addition, for wastewater treatments, the temperature of the process is intentionally operated at ambient conditions to avoid the loss of volatile organic compounds. Compound parabolic concentrators are employed of which concentrating factor is approx. 1 (one-sun collectors) and the temperature during the performance slightly intensifies up to 40 °C. In the summer, the temperature is higher, but the upper limitation to ensure the safety of the setup does not exceed 60–70 °C. In this not very extreme conditions [170], an insignificant role of the temperature was practically proved.

## pH

Photocatalytic degradation depends on the generation of hydroxyl radicals, which strongly depends on the pH of the solution [30], [91].  $\text{TiO}_2$  particles suspended are, as other metal oxides, well known to be surrounded by hydroxyl groups and to act as amphoteric materials [32], [39]. The surface titanol groups ( $>\text{Ti}-\text{OH}$ ) can undergo acidification or basification [26], [174], [176], [177] as



The pH of the solution defines the charging mechanism. By comparing the pH value with the PZC (that is the pH at zero net surface charge of the colloids), one can anticipate which are the predominant charges in solution. When the pH is lower than the PZC, the surface charge is positive, and inversely.

By defining the surface charge of the colloids, pH determines the stability of the suspension. In an unstable colloidal system, esp. when pH is approximate to the PZC, particles may adhere to others. The aggregates can successively increase in size. It causes the change of optical properties of the suspension [169], in particular, limitation of optical penetration. Sedimentation may undergo and, in the case of a long retention time in a reactor, cause the inhomogeneity of the suspension as well as the mass transfer limitation.

There is also a possibility that the position of conduction and valance bands of photocatalysts is pH dependent [178], [179]. In this case, the bandgap determining photon absorbance may be varied.

In targeted water, ionic organic molecules presence and their adsorption on photocatalysts depends on pH [174]. Methylene blue, as an example, is a cationic dye. The negative surface

charge of  $\text{TiO}_2$  at a high pH may intensify the adsorption of the contaminants as the result of the electrostatic attraction. One should stay aware of the decrease of the degradation rate attributing to the favored adsorption in the basic medium but not to the photocatalytic efficiency [180].

Last but not least, intermediates may be pH-sensitive [178], [181]. Individual studies on same systems (4-chlorophenol/ $\text{TiO}_2/\text{O}_2$  photosystem) but at varied pH were compared. Not only the temporal distribution but also the concentration of intermediates took place.

The influence of pH on the photocatalytic reaction was also explicitly quantified [16], [25].

### Impurities

In reality, wastewater contains numerous known and unknown substances. Chong *et al.* [8] reviewed the effects of presented ions and metals. The contaminants may occupy the active surface area of the photocatalyst, i.e. cause competitive adsorption of reactants or desorption of products. Chemical investigations showed either positive, neutral or even negative effects on the photo-reaction depending on different ions. Some of them should be noticed. For instance,  $\text{Ca}^{2+}$ ,  $\text{Mg}^{2+}$ , and  $\text{Zn}^{2+}$  cations decrease photo-mineralization;  $\text{Fe}^{2+}$  promotes the Fenton or photo-Fenton reaction, but fouls the catalyst surface;  $\text{Cl}^-$ ,  $\text{HCO}_3^-$ ,  $\text{CO}_3^{2-}$  anions compete for the degradation by consuming radicals and/or trapped holes; in contrast, oxyanion oxidants (e.g.,  $\text{ClO}_2^-$ ,  $\text{ClO}_3^-$ ,  $\text{S}_2\text{O}_8^{2-}$ ) consume the electrons and prevent the electron-hole recombination. Additionally, some contaminants cause negative effects on the optical properties of the water, i.e. shorten the UV penetration due to its turbidity or its irradiation absorbance.

## 2.3.5 Modeling

### Radiative transfer

In a heterogeneous photocatalysis, light interacts with photocatalysts and it can be absorbed or scattered.

The propagation of light  $I_\lambda$  traversing a medium by a distance of  $z$  follows the Bouguer-Lambert-Beer law (abbreviated to the Beer-Lambert law) [182]

$$dI_\lambda = -\beta_\lambda C_n dz, \quad (2.19)$$

where  $\beta_\lambda$  is the molar extinction coefficient at the wavelength  $\lambda$ , and  $C_n$  is the molar concentration of the substance in the medium.

For scattering systems such as heterogeneous photocatalysis, application of the law is limited as scattered light is not negligible [152], [183]. Its intensity depends on the number of particles, refractive indices of the medium, the volume of the particles, the wavelength and scattering angle. A complete radiative transfer equation (RTE) can be substituted [102], [184]. An RTE is written as a radiation transport balance. In general, due to a low temperature operation, the

radiation emission is negligible. The light conversion is actually the difference between the scattered, and absorbed parts; and extinction coefficient is the sum of absorption and scattering coefficients. In particular, the radiation at one specific point changes by a loss of photons by absorption, or by out-scattering, and a gain of photons by in-scattering as a result of multiple scattering in the space surrounding the point. To solve the RTE, absorption and scattering coefficients must be known. The RTE can render the intensity of specific points inside the reactor, which depends on reactor geometry. Eventually, the intrinsic reaction rate constant of the heterogeneous reaction is achievable. Details of formulation and solution of the model can be found in [102].

### Reaction rate constant

The overall photocatalytic reaction includes five steps [170]

1. Diffusion: reactants transfer from the bulk liquid to the catalyst surface through the boundary layer
2. Adsorption: the organic compounds adsorb on the surface of the catalyst
3. Photocatalytic reaction: reactants are oxidized or degraded by trapped electrons and holes, or by radicals on the surface of the photocatalyst
4. Desorption: the (intermediate) products desorb from the catalyst surface
5. Diffusion: the (intermediate) products transfer to the fluid phase

Langmuir-Hinshelwood kinetics is widely used to evaluate the conversion of photocatalysis [8], [22], [91]. In this model, diffusion is omitted, adsorption is assumed to be equilibrated, and photocatalytic reaction is the rate determining step. The reaction rate is written as

$$r = k_r \theta, \quad (2.20)$$

where  $\theta$  is the equilibrium surface coverage based on the Langmuir adsorption at the reactant concentration  $C_n$ . It can be written as

$$\theta = \frac{K_{\text{ads}} C_n}{1 + K_{\text{ads}} C_n}, \quad (2.21)$$

where  $K_{\text{ads}}$  is the adsorption equilibrium constant. The reaction rate accounting the light intensity dependence  $I$  is defined as

$$r = k_r \theta = k_{r0} I^\alpha \frac{K_{\text{ads}} C_n}{1 + K_{\text{ads}} C_n}, \quad (2.22)$$

where  $k_r$  is the reaction rate constant accounting the influence of light intensity  $I$ , and  $k_{r0}$  is the intrinsic reaction rate constant. The order of magnitude of irradiance is  $\alpha = 0.5-1$ . When the electron-hole formation dominates,  $\alpha = 1$ , and when the electron-hole recombination favors,  $\alpha = 0.5$  (section 2.3.3).

In the limit case, when  $K_{\text{ads}} C_n \ll 1$ , the denominator is approx. 1. As the consequence, the rate is rewritten as the pseudo first order model

$$r = -\frac{dC_n}{dt} = k_{r0} I^\alpha K_{ads} C_n = k_r K_{ads} C_n = k' C_n, \quad (2.23)$$

where  $k' = k_r K_{ads}$ . Integrating the equation renders

$$\ln \frac{C_n}{C_{n,0}} = -k' t, \text{ or } C_n = C_{n,0} e^{-k' t}. \quad (2.24)$$

The value  $k'$  is the so-called apparent reaction rate constant. It follows  $k' = k_r K_{ads} = k_{r,0} I^\alpha K_{ads}$  thus is linear to the magnitude irradiance  $I^\alpha$ . This parameter is widely used to quantify the photocatalysis.

### Photonic yield and efficiency

In photocatalytic researches, in addition to the reaction rate constant, the terms quantum and photonic yield/efficiency are popularly addressed but sometimes with misconception [152], [184].

*Quantum efficiency* (dimensionless) is defined as the amount of reactant consumed or product formed per the amount of absorbed photons [152]. It can also be defined as the reaction rate per the photonic flux (which is the rate of absorbed photons) [185]. Quantum efficiency is dimensionless, and is a “double kinetics” as the ratio of two rates.

In the heterogeneous photocatalysis, scattering is significant [152], [184]. The rate of incoming photons is different from the rate of absorbed photons. This value depends on the illumination and is known. The term *photonic efficiency* is used instead. It is the amount of reactant transformed or product formed per the amount of incident photons on the reactor cell.

The quantum efficiency of the heterogeneous system can be calculated via a *relative photonic efficiency* [152]. It is determined by comparing the initial rate of reactant degradation with that of phenol degradation. This substitution allows for an elimination of the reactor geometry, light wavelength and intensity, as well as other influencing parameters. Quantum efficiency of the solute is determined as the products of the relative photonic efficiency and the known quantum efficiency of phenol disappearance [152].

When mentioning to monochromatic excitation, i.e. at a specified wavelength, *quantum* or *photonic yield* is termed with the same meanings [184].

## 2.4 CHALLENGE

This chapter presents the state of the art in the field of photocatalysis. Basically, heterogeneous photocatalysis can be applied in a broad range of applications, e.g., wastewater treatment. Photocatalytic materials can be activated by radiation of an adequate photon energy. The reaction mechanism was presented. Among photocatalysts, titanium dioxide  $\text{TiO}_2$  nanoparticles have been widely explored in literature. These materials are commercially available, but they have a large bandgap and require a post-treatment after use to recover the nanoparticles.  $\text{TiO}_2$

based photocatalysts obtained by modification and immobilization of the nanoparticles on supports can overcome these drawbacks. The form of the photocatalysts, as well as other requirements (e.g., illumination, flow and post treatment), demand different reactors. In principle, batch or flow reactors can be employed. Coupling processes such as a photocatalytic membrane reactor is an alternative to avoid a post treatment. Photocatalysis is also influenced by various factors, such as the photocatalyst concentration and morphology, organic compounds, light intensity, pH, temperature, impurities, among others. The process can be quantified by a radiative transfer equation or a kinetic model.

However, since the first notice of photocatalytic activity of titanium dioxide in 1972, up to now, the application of photocatalysis in reality is still limited. There is an incomparability among photocatalytic reactors at different scales. It is due to insufficiently defined process conditions at lab scale, e.g., illumination and flow conditions in batch reactors. Also among a large variation of lab reactors, the disposition of the light source is difficult to scale up and ensure an efficient illumination of all the volume of a reactor. Last but not least, kinetic models were inappropriately used regardless of the reactor types and caused insufficient intrinsic reaction rate constants at the microscopic level.

Therefore, this Ph.D. thesis focuses on a concept for water treatment by photocatalysis aiming at a scalable photocatalytic setup. The configuration can be either down-scaled so that it suits different study purposes in different labs or up-scaled and applied in reality. Ideally, the data of different scaled work are comparable.

In this work, slurry photocatalysts were performed as photocatalyst powders are commercially available. Titanium dioxide, a commercial nanomaterial, is mostly tested. Since the catalyst is not composed of spherical primary particles, but it is in an aggregated state, it is necessary to investigate the influence of aggregation to avoid an unwanted decrease of the efficiency of the photocatalyst.

The design of a photocatalytic reactor was the prerequisite for this study. As photocatalysis is a complex process, many factors can affect the reaction. Unlike batch illuminated reactors, a flow reactor allowing for definable parameters (e.g., flow regime and uniform illumination) is necessary for on-going studies. Therefore, in this work, the photocatalytic setup was based on a flow reactor. Aforementioned, the reactor must satisfy the scalability, but also ensure research purposes. A reactor model, inevitably, must be established alongside the new design.

For a comprehensive insight of the photocatalytic process in the research reactor, it is necessary to study the influence of different process parameters. The goal of this thesis work is to eliminate different impacts which are available in a macroscopic photocatalysis, or at least give explanations of different phenomena. To compare with publications worldwide, the photocatalytic degradation of a model organic compound, methylene blue, was performed.

In this work, also the applicability of the reactor concept for different purposes was studied. Different photocatalytic materials and organic compounds, as well as the utilization of sunlight,

were tested. As this work especially aims the treatment of wastewater from textile industries, color removal of commercial dyes as a realistic scenario was studied. At the end, the integration of an up-scaled photocatalysis in a wastewater treatment is proposed.

The five following chapters go through all theoretical and practical investigations. Expectedly, this Ph.D. research brings a new sight in photocatalysis and fill in the gap between experimental studies and large-scaled work.



## 3 A PHOTOCATALYTIC SETUP FOR RESEARCH PURPOSES

### 3.1 THE EXPERIMENTAL SETUP

The key factor of this Ph.D. work is a photocatalytic performance in a configuration, where influential parameters can be determinable. This section introduces a photocatalytic setup used for research purposes. The designed system is a modification of the original setup first presented in 2015 [186].

#### 3.1.1 Objectives

As mentioned in the previous chapter, suspended photocatalysts are commercial available. Here, a new photocatalytic setup for slurry photocatalyst was designed. Desired features were specified. Technical solutions were proposed alongside as listed in Table 3.1.

#### 3.1.2 The setup

Based on the requirements, a photocatalytic setup was innovated [186]. Scheme of the process is shown in Figure 3.1. Experimental setup in the lab was photographed as shown in Figure 3.2.

Feed suspension including a dye substance and photocatalysts is contained in a container and kept mixed by a magnetic stirrer. The suspension is pumped into the reactor. The reactor cell consists of a meandering flow channel. In addition, the channel has rectangular cross section, which allows for a 2-dimensional UV illumination and thus ensures a roughly uniform UV intensity along the whole channel.

More details of the flow reactor are mentioned in section 3.1.3. The photocatalysis receives a steady-state illumination from a planar UV irradiator (section 3.1.4). Depending on the study purposes, artificial visible light (section 3.1.4) or sunlight can also be employed. In this case, the reactor was illuminated from the top and the reactor was placed on an inclined plane (approx. 30 °). The Micropump®132-665-316 pump operates the circulation of fluid in the process.

Table 3.1 Futures and technical solutions for a photocatalytic setup.

Features	Proposed technical solutions
<i>In general</i>	
G1 Though the design is for research purposes, the prototype must be scalable for other researches and further applications.	So far up-scaling batch reactors face the problem of light distribution. A flow reactor is one possible solution. Of two flow reactor configurations (Figure 2.6) [107], falling flow reactors enable a better use of light, however are not recommended because of the limitation of up-scaling. The tubular flow reactor would be chosen.
G2 Because a lab-scaled flow reactor is small, the retention time is short.	The length of the reactor must be maximized. The reactor consists of a meandering flow channel within the illuminated area.
G3	The flow must be circulated. Principal components of the setup are: a flow reactor illuminated by a light source (see also I2), a pump circulating the flow and a mixing tank storing the feed as well as connecting the reactor with the pump.
<i>Illumination</i>	
I1 The illuminated surface must be made of UV-transparent material.	UV-transparent Schott BOROFLOAT®33 glass is used.
I2 The radiation field must be definable. The radiation should be as homogenous as possible [184].	The UV illuminator is planar and the reactor is rectangular. The UV intensity distributed on the illuminated surface is thus measurable. Only reactor is illuminated, whereas other components are not.
I3 The reactor ensures an efficient photon collection [23].	The specific illuminated surface area (Eq. (3.1), section 3.1.3) is large. In particular, the width and length of the reactor are large, while the depth is small.
I4 Because of the short optical path-length [17], [19], non-illuminated space should be diminished [8].	The optical path (thickness) of the reactor is small.
I5 At best, photocatalytic performance is monochromatic. When employing polychromatic light, at least the spectrum must be known [184]. Additionally, the radiation should be steady [184].	The Philips 8-watt mercury fluorescent tubes were employed as the artificial UV irradiation. The UV spectrum and lifetime are specified [187].
I6 For research purposes, the light intensity can be varied.	The distance between the reactor and the artificial irradiation is adjustable to vary the light intensity on the illuminated surface.
<i>Flow regime</i>	
F1 For colloidal photocatalysis, mass transfer limitation [95] and sedimentation must be avoided [19].	A good mixing condition is ensured. The high flow rate is controlled by a pump.
<i>Others</i>	
O1 The reactor must be easily cleaned.	The design is as simple as possible. Thus the reactor is easily assembled.

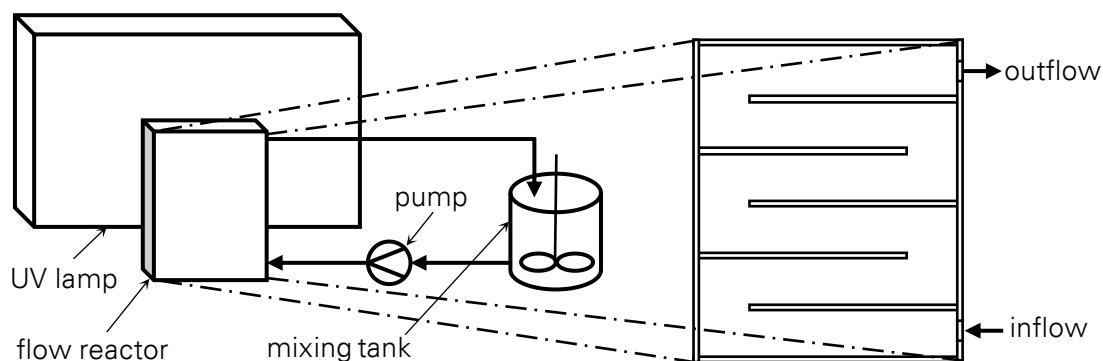


Figure 3.1 Scheme of the photocatalytic setup, including the UV lamp, the flow reactor, the mixing tank, and the pump. The flow reactor is zoomed in as shown in the right.

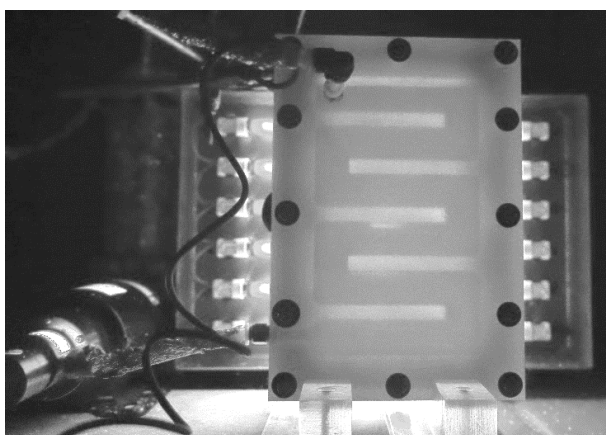


Figure 3.2 The laboratory-scaled photocatalytic setup including the pump (front left), the flow reactor (front right), the UV irradiator (behind), and the mixing tank (far behind). Visualization of the setup animated by Supreeth Venkatraman can be found in the URL: <https://www.youtube.com/watch?v=99TiM-UOLKo>.

### 3.1.3 Design of a flow reactor

The flow reactor prototype was originated as the one-side optical reactor [186]. The engineering drawing for the design can be found in Figure 3.3 and Figure 3.4. The illuminated window of the reactor is made from 3.3 mm UV-transparent Schott BOROFLOAT®33 glass. According to the manufacturer, the glass is more than 90 % UVA transmittance [188]. Our measurement showed that 92 % radiation with the wavelength of 365 nm can transmit through the 3.3 mm glass. Lately, both front and back sides of the reactor are made from glass. Thus the transmitted light intensity through the reactor is measurable.

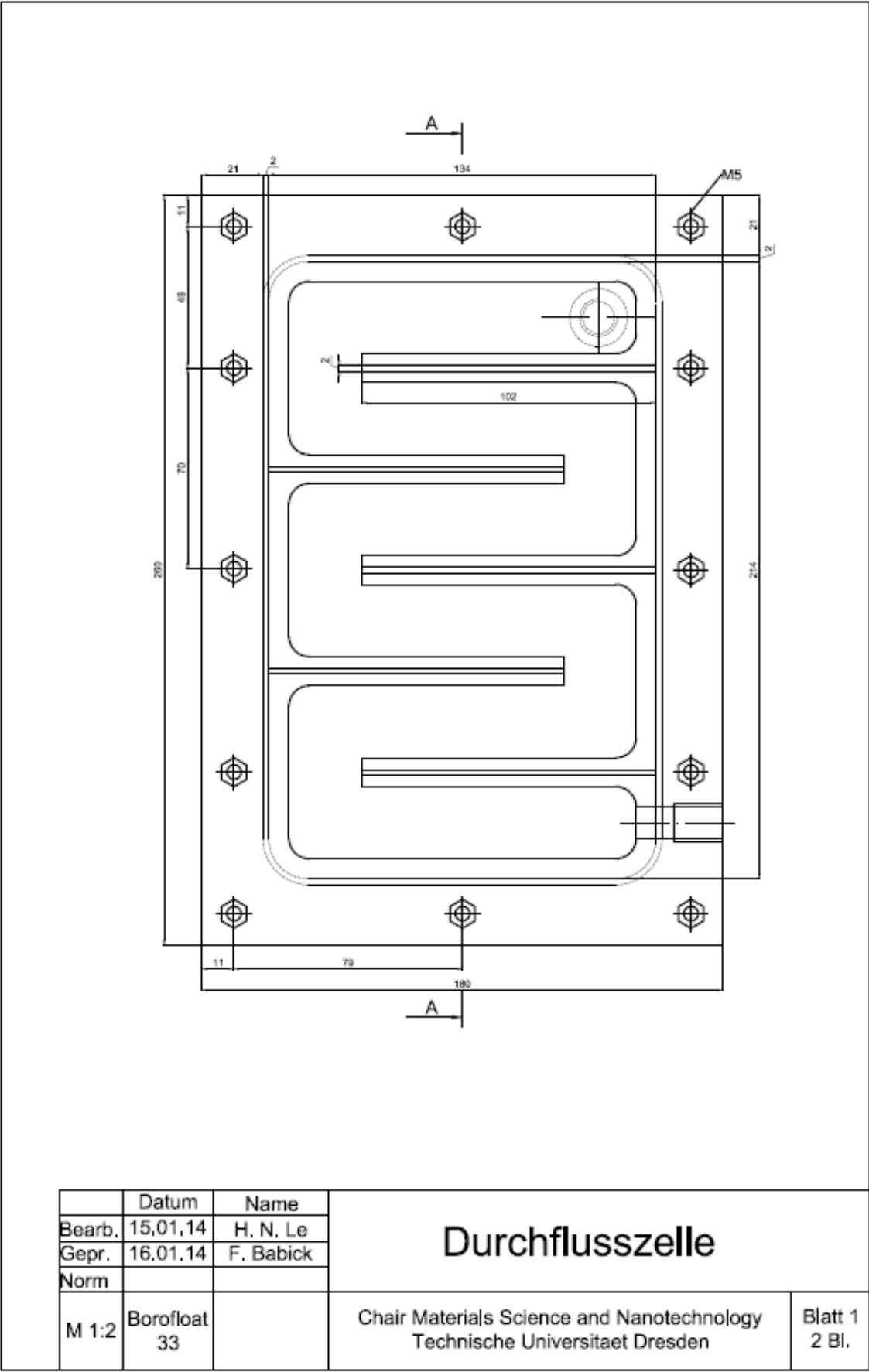


Figure 3.3 Engineering drawing of the flow reactor: The transverse section from the front view.

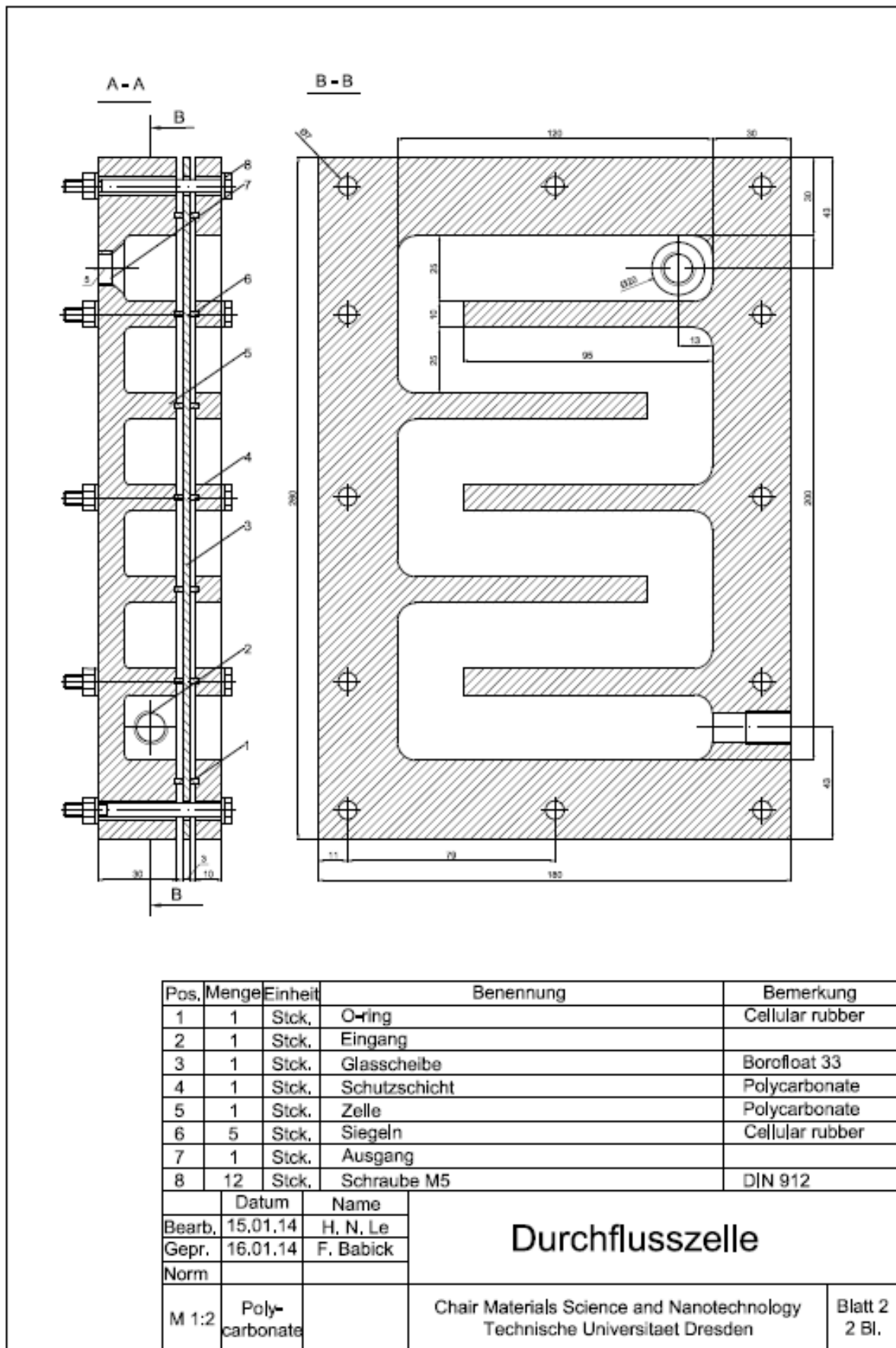


Figure 3.4 Engineering drawing of the flow reactor (cont.): The cross sections.

Table 3.2 Specifications of the designed flow reactors.

Reactor		R10	R15	R20
Reactor size	mm	260×180×27	260×180×33	260×180×38
Reactor volume	ml	206	318	411
Number of channels	-	6		
Channel size	mm	25×120×11	25×120×17	25×120×22
Optical path	mm	11	17	22
Specific illuminated surface area <sup>a</sup>	cm <sup>2</sup> /cm <sup>3</sup>	0.91	0.59	0.45

<sup>a</sup> Specific illuminated surface of the reactor  $S_v$  is the illuminated surface area  $S$  over the volume  $V$  as

$$S_v = \frac{S}{V}. \quad (3.1)$$

Three reactors, namely R10, R15 and R20, with different optical paths (11 mm, 17 mm and 22 mm) were fabricated. They would be chosen to suit the various study purposes. Table 3.2 presents main specifications of three flow reactors.

### 3.1.4 Illumination

The flow reactors receive radiation from an artificial UV or visible lamp, or from sunlight. Here, UV intensity of an artificial UV illumination is presented, followed by the brief introduction of the artificial visible and solar illumination.

#### Artificial UV lamp

The UV lamp constructed with six Philips 8-watt mercury fluorescent tubes was assembled by UMEX GmbH. The mode wavelength is 365 nm (Figure 3.5a) as reported by Koninklijke Philips N.V. Company [187], while the minimum and maximum wavelengths are 340 nm and 410 nm.

The UV lamp is center-aligned with the reactor. As the reactor is rectangular, light intensity on the illuminated surface is determinable. UV intensity was measured by a lux-meter PCE-UV34 which is sensitive to UVA and UVB. The maximum UV intensity was noticed at the center of the reactor, while the minimum intensity was at the edge. The UV intensity can be varied by adjusting the distance between the lamp and the reactor. Figure 3.5b shows the UV intensity profiles on the illuminated surface when the distance is 7 cm, 10 cm and 15 cm. The corresponding intensity range in these three cases are 13.7–25.5, 11.7–19.7 and 9.3–14.5 W/m<sup>2</sup>. The average intensity  $\bar{I}$  was calculated from the specific intensities at different coordinates ( $x$ ,  $y$ ) as

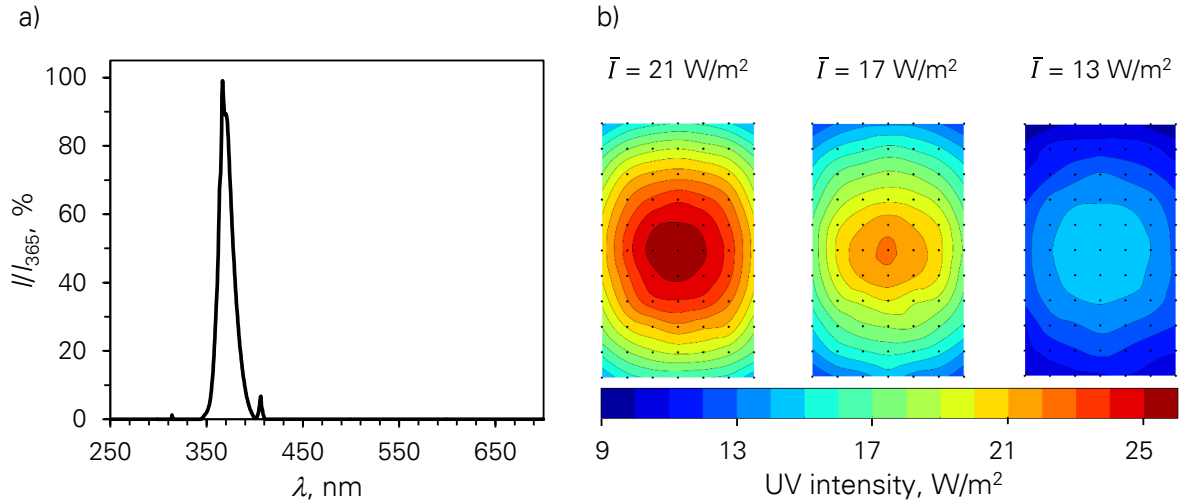


Figure 3.5 Spectral intensity of the artificial UV lamp: a) Relative intensity (which is the specific intensity over the intensity at 365 nm) vs. wavelength; and b) Intensity profile and average intensity on the illuminated surface of the reactor corresponding to three radiance levels [189].

$$\bar{I} = \frac{1}{S} \sum_{x,y} I(x,y) \Delta x \Delta y. \quad (3.2)$$

The average value in three cases are 20.8, 16.7 and 12.9 W/m<sup>2</sup>, respectively.

### Artificial visible lamp

The artificial visible light was irradiated by a simulator fabricated by Ingenieurbüro Mencke & Tegtmeyer GmbH. According to the company, the mode wavelength of the lamp is 650–700 nm (Figure 3.6a), and no UV light was recorded (also by the lux-meter PCE-UV34). Figure 3.6b shows the light distribution of the visible lamp of different wavelength ranges in comparison with visible light of solar spectrum.

In experiments, light intensity was monitored with the Susicontrol software (version 2.9.0) by a silicon irradiance sensor of the company, which is sensitive in the wavelength range from 300–1200 nm. The light intensity was approx. 98 W/m<sup>2</sup>.

### Natural solar light

For experiments with solar light, UV intensity was recorded every 30 s by the lux-meter PCE-UV34 and are shown along with the experimental data. No visible light was detected.

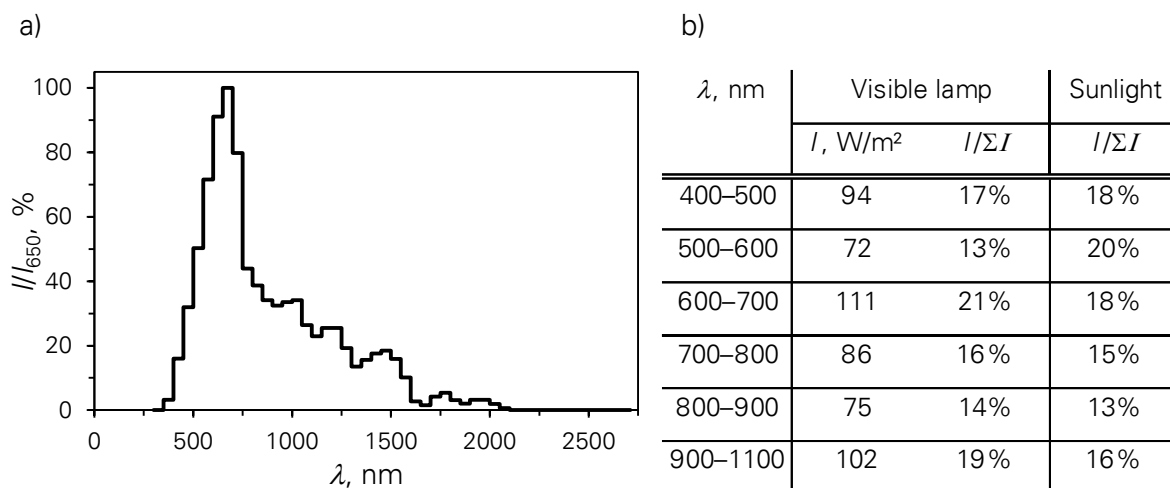


Figure 3.6 Spectral intensity of the artificial visible lamp: a) Relative intensity (which is the specific intensity over the intensity at 650 nm) vs. wavelength; and b) Comparison of intensity distribution between the lamp and sunlight.

### 3.1.5 Flow conditions

In the setup, fluid is circulated by a pump with a flow rate of 2.28 l/min. As all dimensions are known, flow conditions used in experiments are definable. In particular, equivalent hydraulic diameter  $d_h$  of the channel can be determined as

$$d_h = \frac{4A}{p}, \quad (3.3)$$

where  $A$  and  $p$  are the area section and the wetted perimeter of the channel, respectively. Retention time of the fluid elements in the reactor  $t_R$  follows

$$t_R = \frac{V_R}{\dot{V}}, \quad (3.4)$$

where  $V_R$  is the volume of the reactor and  $\dot{V}$  is the flow rate of the fluid. Reynolds number  $Re$  of the fluid in the reactor is defined as

$$Re = \frac{\rho u d_h}{\mu}, \quad (3.5)$$

where  $\rho$ ,  $\mu$  and  $u$  is the density, dynamic viscosity and velocity of the fluid, respectively. All determined data are presented in Table 3.3.

Table 3.3 Flow conditions used in this study.

Reactor		R10	R15	R20
Equivalent hydraulic diameter of the channel	mm	15	20	23
Retention time	s	5.41	8.35	10.81
Reynolds number (at 20 °C)	-	1770	1517	1356

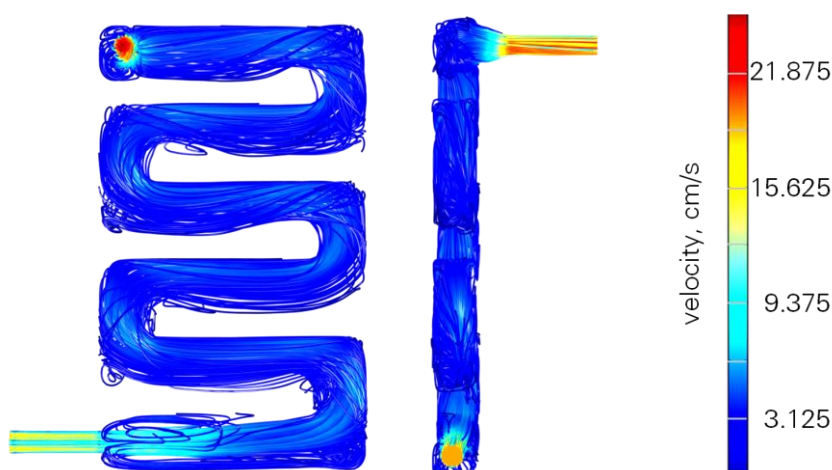


Figure 3.7 Fluid velocity in the reactor: Flow field simulation of the reactor R20 corresponding to the flow rate of 0.84 l/min and the Reynolds number of 500. The simulation with the finite element method of COMSOL Multiphysics® Modeling was operated by Hagen Eckert [192].

The Reynolds numbers (at 20 °C) for three reactors are respectively 1770, 1517 and 1356. Note that the cross section of the fluid is non-circular, the ratio between the length of channels and the diameter is small, as well as the fluid direction has U-turns. Indeed, by simulation, even with a one-third of the operating flow rate, eddies are obvious esp. in the entrance and exist, or when the fluid changes its direction (Figure 3.7), which imply a quasi-turbulence. The pressure drop does not guarantee to the laminar regime [190], [191].

Though the simulation has been run with the lower operating flow rate (0.84 l/min), it proved that flow in the reactor could be obtained.

## 3.2 OPERATION

Photocatalytic degradation of organic compound is performed in the presence of slurry photocatalyst. This subchapter introduces the operation of a photocatalytic test with the experimental setup. In general, one test includes three steps as followings:

### 1. Preparation of the slurry photocatalyst

Photocatalysts are dispersed into water then stored in the mixing tank. Different dispersion techniques can be employed.

### 2. Adsorption-desorption equilibrium

An organic compound is added into the prepared photocatalyst suspension. It is stored in the dark and kept under mixing. Due to the difference between concentrations of organic molecules in the bulk and on the photocatalyst surface, adsorption and desorption happen. The equilibrium is necessary. No photocatalytic reaction occurs since the suspension is kept in the dark.

As presented (section 2.3.5), an overall photocatalytic reaction includes five steps [170]: diffusion of the compounds to the catalyst surface, adsorption, photocatalytic reaction, desorption, and diffusion of intermediates and (by-) products to the bulk liquid. Under certain conditions (low particle concentration, strong mixing/turbulence), diffusion is negligible [95]–[97], [184]. Dissimilarly, sorption of organic molecules on the photocatalyst's surface happens during the reaction. The loss of target organic compounds is attributed not only to the photocatalytic reaction but also to the adsorption. This disturbing process [39], [193], [194] may mislead the evaluation of photocatalysis [185]. Therefore, a steady-state regime of the adsorption of the reactant on the catalyst needs to be achieved.

### 3. Photocatalytic degradation

The equilibrated system is then loaded into the illuminated flow reactor and circulated by the pump. According to the study purposes, different illumination conditions can be employed. While working with artificial illumination, the lamp should be turned on 10 min prior to the test for the stabilization of the light source.

At first, the reactor is covered to ensure that no reaction occurs while purging air inside reactor out and homogenizing the flow in the channels. Typically, it takes approx. 0.5–1 min.

Lately, the reactor is uncovered and the photocatalytic reaction (if happens) starts immediately under the illumination. Samples are collected in the mixing tank for online or offline analysis.

Here, the adsorption of the organic molecules on the inner walls of the reactor and of the other components was not visible when being observed, so it is assumed to be negligible. Another phenomenon should be taken into account. When starting the circulation, the flow properties is different from that in the previous step. Additionally, pH may change. Thus the adsorption-desorption equilibrium previously achieved may be broken. At best, the second equilibrium in the reactor should be carried out. However, to mimic the process in reality, this equilibrium is omitted. For theoretical investigations, control tests need to be done, where all the procedures of this step are performed similarly but in the dark.

After each experiment, the flow reactor needs to be dismantled and cleaned.

Details of each step are presented in chapter 4.

### 3.3 DETERMINATION OF REACTION RATE CONSTANT

Previously the determination of the apparent and intrinsic reaction rate constants in the photocatalytic setup was proposed [186]. Based on the assumptions (section 3.3.1), by inspecting the Langmuir adsorption (section 3.3.2), an improvement of the model is initiated (section 3.3.3). The fluids and the concentrations of the organic compound in the setup can be found in Figure 3.8.

#### 3.3.1 Assumptions

- There is no axial dispersion in the flow reactor, i.e., variations only exist along the length of the reactor. The mass balance is thus written as one-dimensional.
- Adsorption of the species on the catalyst surface is a rate-determining step only at high temperature (section 2.3.4). At ambient temperature, adsorption takes place instantaneously and is quasi-equilibrated.
- The reaction of the adsorbate is steady-state isothermal and it is the rate-determining step of the multistep heterogeneous reaction.
- During the photocatalytic reaction, desorption of intermediates or (by-) products competes with adsorption of the reagent on the photocatalyst. This assumedly has no big influence on the process, i.e. there is no change of the adsorption constant with respect to reaction time.
- Influence of mass transfer is inconsiderable since the particle concentration is small [95]–[97], while mixing is strong (section 3.1.5).
- In the mixing tank, the mixing is ideal.
- Since the lifetime of radicals is in nano-seconds [32], they exist in the reactor where the activation occurs under UV radiance. In the mixing tank and in tubes, no radical persists which means that no chemical reaction occurs.
- The volume of the suspension is assumedly unchanged during the the reaction.

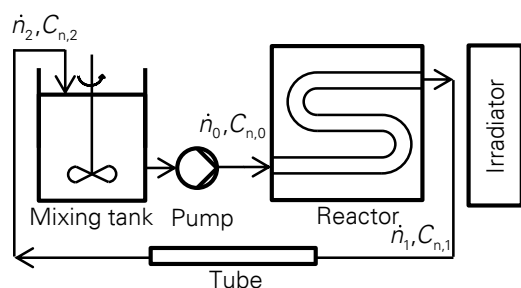
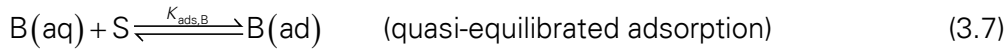
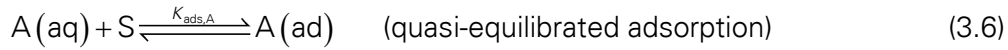


Figure 3.8 Fluids and concentrations of species in the photocatalytic system. The setup includes a mixing tank, a flow reactor illuminated by an irradiator, a pump and connecting tubes. The molar flow rate and the molar concentration of the organic compound are denoted as  $\dot{n}$  and  $C_n$ , respectively.

### 3.3.2 Heterogeneous reaction

The heterogeneous photocatalysis is a five-step process as mentioned in section 2.3.5. With the assumptions above, the multistep heterogeneous reaction can be simplified to two steps including an adsorption equilibrium and the rate-determining step (i.e., oxidation of adsorbed reactants). The reaction on the surface of the photocatalyst produces the most abundant intermediate. The transformation of the reactant is, thus, the rate-determining step, while the other steps have no kinetics significance [195].

The simple sequence for a bimolecular reaction is



where S is the photoadsorption center of a catalyst, A(aq) and A(ad) are the reactant in the aqueous solution and on the adsorbent surface, B(aq) is either hydroxyl groups OH<sup>-</sup> or holes and B(ad) is radicals on the photocatalyst surface. Eq. (3.7) actually describes the formation of the active species (hydroxyl radicals in the case of an indirect photocatalytic mechanism, or trapped holes in the case of a direct pathway) (Eqs (2.2) and (2.4), section 2.1.2).

The adsorption is assumedly equilibrated. The fractional surface coverage  $\theta_i$  of each species (or the number of adsorption sites occupied) is

$$\theta_i = \frac{K_{ads,i} C_{n,i}(aq)}{1 + K_{ads,i} C_{n,i}(aq)}. \quad (3.9)$$

where  $K_{ads,i}$  is the adsorption constant, and  $C_{n,i}$  is the molar concentration of the species i. Rate of the sequence is the rate of the reaction  $r$  and is determined as

$$r = k_r \theta_A \theta_B = \frac{k_r \theta_B K_{ads,A} C_{n,A}(aq)}{1 + K_{ads,A} C_{n,A}(aq)}, \quad (3.10)$$

where  $k_r$  is the reaction rate constant. Generally,  $\theta_B$  depends on the properties of the photocatalyst and the interfacial phenomena. In particular, it relates to the photoadsorption capacity (which is the maximum number of photoadsorbed entities to the number of surface sites [184]). It also depends on the properties and the flow phenomenon of the medium as well as the light phenomena. In one experiment, if all influential conditions (e.g., temperature, pH, electrical conductivity and light intensity) are kept unchanged during the experiment, for a certain amount of photocatalytic powder in a certain volume of aqueous solution, the value  $\theta_B$  is a constant. The reaction rate is, thus, a function of one variable  $C_{n,A}(aq)$

### 3.3.3 Reactor model

#### Materials balance in the flow reactor

Considering a volume element of species A in the plug flow reactor, the amount changes only by the reaction. The change of the molar flow rate is

$$d\dot{n}_{A,0} = \dot{v}dC_{n,A,0}, \quad (3.11)$$

where  $\dot{v}$  is the flowrate. The material balance is derived as [196]

$$\frac{d\dot{n}_{A,0}}{dV_R} = g_A r, \quad (3.12)$$

where the stoichiometric coefficient  $g_A$  is  $-1$ ,  $V$  is the volume,  $dV_R = \dot{v}dt_R$ ,  $t$  is the retention time, and the subscript R denotes the reactor. The photocatalytic reaction  $r$  is calculated as Eq.(3.10). Eq. (3.12) can be written as

$$\frac{dC_{n,0}}{dt_R} = -\frac{k_r \theta_B K_{ads,A} C_{n,A,0}}{1 + K_{ads,A} C_{n,A,0}}. \quad (3.13)$$

For a shorter display, let

$$k_r K_{ads,A} \theta_B = k. \quad (3.14)$$

Since the aim of this study focuses on only species A, in order to simplify all following equations, the subscript "A" is omitted. Eq. (3.13) becomes

$$dC_{n,0} \frac{1 + K_{ads} C_{n,0}}{k C_{n,0}} = -dt_R. \quad (3.15)$$

$$d(\ln C_{n,0}) + K_{ads} dC_{n,0} = -k dt_R. \quad (3.16)$$

The integrated equation is derived as

$$\int_{C_{n,0}(t-t_R)}^{C_{n,1}(t)} d(\ln C_{n,0}) + K_{ads} \int_{C_{n,0}(t-t_R)}^{C_{n,1}(t)} dC_{n,0} = -k \int_{t-t_R}^t dt_R, \quad (3.17)$$

$$\ln \frac{C_{n,1}(t)}{C_{n,0}(t-t_R)} + K_{ads} [C_{n,1}(t) - C_{n,0}(t-t_R)] = -kt_R. \quad (3.18)$$

Since  $K_{ads}$ ,  $k$  and  $t_R$  are constants, the solution for the mass balance in the reactor is

$$C_{n,1}(t) = f(C_{n,0}(t-t_R)). \quad (3.19)$$

#### Materials balance in the mixing tank and tubes

In the mixing tank, by assuming that the change of amount is due to the in- and outflows, and not due to the reaction, the material balance follows [196]

$$\frac{dn_0}{dt} = -\dot{n}_0 + \dot{n}_2, \quad (3.20)$$

$$\frac{dC_{n,0}}{dt} t_M = -C_{n,0} + C_{n,2}, \quad (3.21)$$

where  $n$  is the mole. In addition,

$$C_{n,2}(t) = C_{n,1}(t - t_T), \quad (3.22)$$

where the subscript T denotes the tubes. Eq. (3.21) is derived as

$$\frac{dC_{n,0}}{dt} t_M = -C_{n,0}(t) + C_{n,1}(t - t_T), \quad (3.23)$$

where the subscript M denotes the tank. Eq. (3.23) is a delay differential equation with one variable  $C_{n,0}(t)$ .

### The special case

When  $K_{\text{ads}} C_{n,0} \ll 1$ , Eq. (3.15) can be shortened as

$$\frac{dC_{n,0}}{C_{n,0}} = -K dt_R. \quad (3.24)$$

The mass balance in the flow reactor has one explicit solution

$$C_{n,1}(t) = C_{n,0}(t - t_R) e^{-K t_R}. \quad (3.25)$$

Eq. (3.23) is expanded as

$$\frac{dC_{n,0}}{dt} t_M = -C_{n,0}(t) + C_{n,0}(t - t_R - t_T) e^{-K t_R}. \quad (3.26)$$

The linear delay differential equation has the exponential solution  $C_{n,0}(t) = A e^{-K t}$ . The characteristic equation is

$$1 - K t_M = e^{K(t_R + t_T) - K t_R}. \quad (3.27)$$

Eq. (3.27) can be solved by looking for the intersection(s) of the straight line  $y = 1 - K t_m$  and the curve  $y = e^{K(t_R + t_T) - K t_R}$  (Figure 3.9). For positive  $t_M$  and  $(t_R + t_T)$ , there is a single intersection corresponding to a unique solution  $K$ , equaling to  $C_{n,0}(t) = A e^{-K t}$ . The boundary condition lets  $C_{n,0}(t = 0) = C_{n,\text{ini}}$ , so  $A = C_{n,\text{ini}}$ .

Eventually the degradation in the experimental setup follows the exponential law as

$$C_{n,0}(t) = C_{n,\text{ini}} e^{-K t}. \quad (3.28)$$

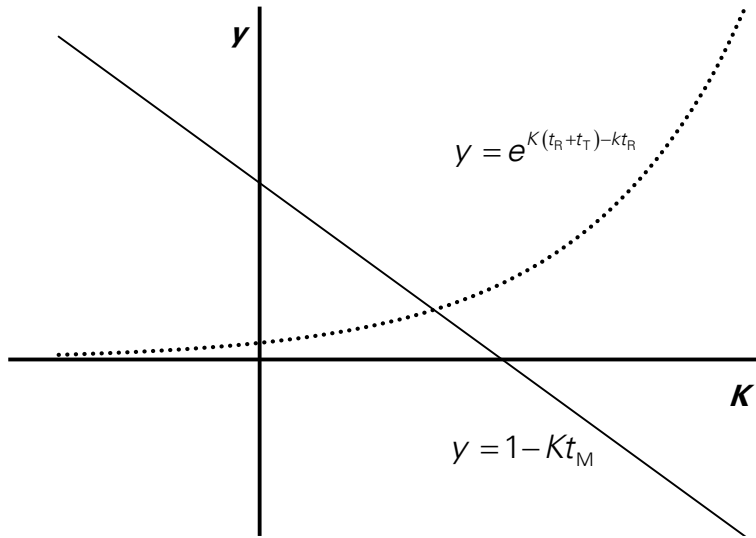


Figure 3.9 Solution of the characteristic equation (Eq. (3.27)).

The reaction rate constant  $K$  in the photocatalytic setup is determined by means of least square regression from experimental data  $(t, C_{n,0}(t))$ . Note that, the photocatalytic reaction occurs only in the flow reactor but not in the other components (i.e., the mixing tank, the tubes and the pump). Thus, the value  $K$  reflects the reaction rate constant at the macroscopic level, where phenomena happening in all components are taken into account. It is only an apparent reaction rate constant.

Additionally, it is possible to discover the integrated reaction rate constant  $k$  in the flow reactor. The value  $k$  defines the reaction rate constant at the microscopic level, counting only influential factors within the flow reactor and reflecting the true photocatalytic activity of the setup. It can be computed from the characteristic equation as follows

$$k = \frac{K(t_R + t_T) - \ln(1 - Kt_M)}{t_R}. \quad (3.29)$$

In the flow reactor, light intensity across the reactor extinguishes. For this reason, the value  $k$  is the average value of all specific reaction rate constants at specific points in the entire volume of the reactor. At best, one reference point, e.g., a point at the illuminated surface (or the window) of the reactor, should be fixed and the reaction rate constant at this point is employed. This is discussed in details in section 6.4.3.

### 3.4 CONCLUDING REMARKS

The chapter introduces a laboratory-scaled photocatalytic setup which was designed for research purposes. The configuration includes main components: an illuminated flow reactor, a mixing tank, a pump and connecting tubes. This design works with the suspended photocatalysts. Depending on study purposes, different illumination can be employed: artificial UV or

visible light, or sunlight. The flow channel meandering within the reactor has a rectangular cross section, thus allows for a 2-dimensional illumination. Operational conditions including light intensity and flow conditions, which were not commonly presented in other publications, are assessable in this study.

An operation procedure of a photocatalysis with the setup was given. Three main steps were listed, including the preparation of the slurry photocatalyst, adsorption-desorption equilibrium and photocatalytic degradation. Sample analysis can be done online or offline. Additionally, the simple construction makes the reactor easy to be cleaned after use.

These reasons above proved that the reactor type is recommended for studies at laboratory scale. Also, as all process parameters are accessible, with some modification, the prototype can be scalable and can suit different purposes.

To evaluate the process, a quantitative model was established. It is based on the Langmuir equilibrated adsorption. Material balances were written for each component. The combination derives a delay linear differential equation. Within assumptions, a shortened form which is mathematically solvable was procured. The apparent reaction rate constant of the entire system follows an exponential function and can be experimentally determined. It can be easily converted to the integrated photocatalytic reaction rate constant which is a characteristic of the flow reactor. It accounts the influences of flow, transport and light phenomena. These two parameters are distinct from the intrinsic reaction rate constant.

The reactors design was employed for all experiments in this study. Initially, the established reactor model was used for evaluating photocatalytic activity of the tests. If necessary, the derived forms (introduced alongside when being used) are the alternatives to adapt different study purposes.

## 4 MATERIALS AND EXPERIMENTAL METHODS

This chapter introduces materials and methods used for selected experiments which are categorized in two chapters 5–6 and subchapter 7.1. Exceptionally, in subchapter 7.2, some typical experiments of the NaViTex CLIENT project are introduced. Materials, experimental set-ups and methods are various. As they were used only for experiments shown in that subchapter but not in the other parts of this dissertation, they are introduced alongside of experimental data.

### 4.1 MATERIALS AND THEIR PROPERTIES

#### 4.1.1 Photocatalysts

In this work, four photocatalytic materials were employed, including commercial titanium dioxide Aeroxide®TiO<sub>2</sub> P25 and P90 (formerly Degussa P25 and P90) provided by Evonik, zinc oxide ZnO 90–210 nm purchased from IOLITEC GmbH, and self-synthesized magnetic particles. Their properties which are of main concern in the field of photocatalysis are here introduced.

##### Titanium dioxide TiO<sub>2</sub> P25

The properties of commercial titanium (IV) oxide Aeroxide®TiO<sub>2</sub> P25 are well-known [197]. The primary particle size determined by SEM is  $25 \pm 3$  nm [166]. The specific surface area is  $56 \text{ m}^2 \text{ g}^{-1}$  [166].

P25 consists of an approx. 80/20 w/w anatase/rutile mixture. Bandgap energy, the crucial property of a photocatalyst, differs between these two crystal modifications [33]. The bandgap energy values of P25 were reported to be between 2.98 eV and 3.37 eV [66], [198]–[200], corresponding to the wavelength range of 400–368 nm.

Another important property of photocatalytic materials is the isoelectric point (IEP), which is the pH at the zero zeta potential. The IEP reflects the acid-base properties of the catalyst surface. The IEP of P25 is in the range of 6–6.8 (pH unit) [201], depending on the electrolytes' concentration obtained by different measurement techniques [39], [176], [202], [203]. Note that the IEP of other types of TiO<sub>2</sub> varies due to the different phase anatase/rutile ratio [173].

##### Titanium dioxide TiO<sub>2</sub> P90

Commercial titanium (IV) oxide Aeroxide®TiO<sub>2</sub> P90 has the primary particle size of 14 nm (determined by TEM [197]). The specific surface area is  $90 \pm 20 \text{ m}^2 \text{ g}^{-1}$  [197]. Titania P90 consists of 90/10 w/w anatase/rutile mixture and has the bandgap energy similar to that of P25 (3.40 eV corresponding to the wavelength of 365 nm) [198].

### Zinc oxide ZnO

ZnO has the bandgap energy of more than 3.1–3.4 eV, corresponding to the wavelengths of shorter than 400–365 nm [204], [205]. The photocatalytic activity of ZnO was reported to be higher than that of TiO<sub>2</sub> [147], [166], [204]. However, the photodecomposition under irradiation limits application of ZnO [16]. In this work, ZnO has the primary size of  $251 \pm 83$  nm and the BET surface area of 5.23 m<sup>2</sup>/g [110].

### Magnetic particles Fe<sub>3</sub>O<sub>4</sub>/SiO<sub>2</sub>/TiO<sub>2</sub>

The magnetic particles Fe<sub>3</sub>O<sub>4</sub>/SiO<sub>2</sub>/TiO<sub>2</sub> were produced in our laboratories according to Teixeira et al. [125].

In general, photocatalyst magnetic nanoparticles (NPs) has two main layers: the magnetic NP as a core and the photocatalyst (e.g., TiO<sub>2</sub>) on the outer layer. By applying an external magnetic field, it is easy to separate the NPs from the aqueous solution. A passive layer can be optionally inserted between these primary layers to protect the core from oxidization and photo-dissolution. It also obstructs the electron-hole recombination centers.

The magnetic particles were synthesized by sol-gel method. The magnetite core (Fe<sub>3</sub>O<sub>4</sub>) was first prepared by co-precipitation. Afterwards the magnetic nanoparticles were coated with silica (SiO<sub>2</sub>). Finally, nanoparticles were immobilized by sol-gel method on the surface of the Fe<sub>3</sub>O<sub>4</sub>/SiO<sub>2</sub> particles. Synthesized samples were calcined at 500 °C. The BET surface area was reported to be 19 m<sup>2</sup>/g. No primary particle size or bandgap was reported for this kind of synthesis. However, with the same synthesis but with 600 °C calcination, the particle size is  $293 \pm 81$  nm as estimated by SEM image analysis, while the bandgap energy is 2.8 eV, calculated according to the modified Kubelka-Munk function (section 4.3.3). Other characteristics like zeta potential, XRD pattern and magnetic properties can be found in [125].

## 4.1.2 Organic compounds

In this study, photocatalytic degradation of various solutions was performed. The used organic compounds were methylene blue (Merck KGaA), ciprofloxacin (Sigma-Aldrich, Inc.) and two commercial dyes, Everzol Navy ED and Remazol Red RR (March 29 Textile-Garment Joint Stock Company, Danang, Vietnam, section 7.2.1). Optical properties of these substances which are important in the field of photocatalysis are presented.

### Methylene blue

Methylene blue (MB) (C<sub>16</sub>H<sub>18</sub>ClN<sub>3</sub>S.3H<sub>2</sub>O) is a thiazine dye. Since the first reports on UV-induced decomposition of MB in the presence of an inorganic semiconductor in 1969, MB has been employed as a model dye substance for examining photocatalytic activity [6], [43], [180], [206], [207].

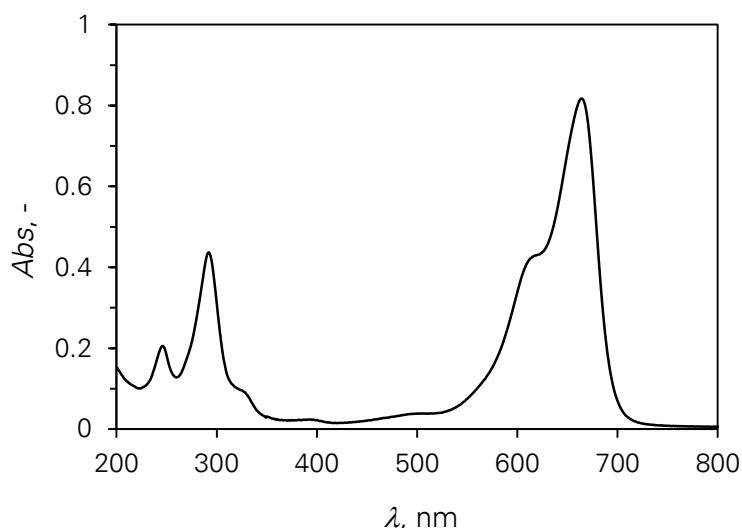


Figure 4.1 UV-VIS absorbance spectrum of methylene blue. The methylene blue solution with a concentration of  $10.31 \mu\text{M}$  was measured with a cuvette of 10 mm optical pathlength by means of a Varian Cary 100 Bio UV-VIS spectrometer.

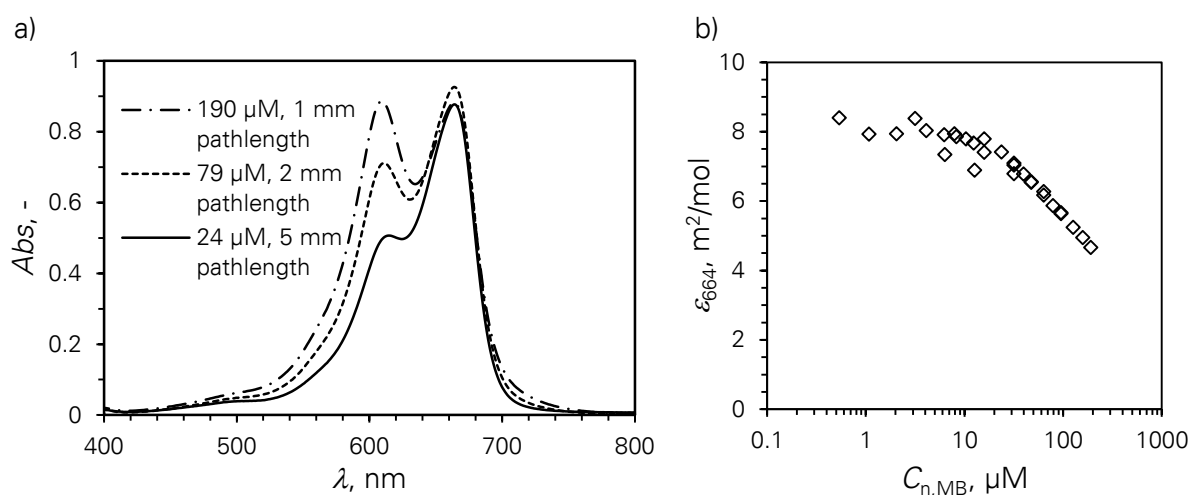


Figure 4.2 Dimerization of methylene blue (MB): a) Absorbance spectra of MB solutions with high concentrations of 24, 79 and  $190 \mu\text{M}$ , which were measured with different cuvettes of 5, 2 and 1 mm pathlength by means of a Varian Cary 100 Bio UV-VIS spectrometer; and b) Decadic molar extinction coefficient of MB at 664 nm  $\epsilon_{664}$  vs. concentration  $C_{n,MB}$ . Here the value  $\epsilon_{664}$  is the apparent molar extinction coefficient and dissimilar from the true molar extinction coefficient (Appendix A4).

In this study, MB was used for photodegradation. The photocatalytic pathway is known as photocatalyzed N-demethylation [25], [143]. Also the degradation of this dye substance is time-saving for implementing numerous experiments in this study.

Note that when studying the photocatalysis, the organic compound should not absorb the light used for the photoexcitation [85], [208], [209]. In other words, the compound should enable the optimal use of light for the photocatalytic performance. In the experimental setup, a UV

lamp with the mode wavelength by energy of 365 nm was employed. At this wavelength, MB does not show absorption (Figure 4.1), which means that it does not affect the UV light penetration in the aqueous suspension.

In this study, the desired initial concentration of MB in most of the experiments was kept at the moderate values of 10–13  $\mu\text{M}$  [24], [25], [207], [210]. A part of this study focuses on the variation of the initial concentration of MB (section 6.4.4) of up to 130  $\mu\text{M}$ . Note that, dimerization occurs at MB concentration higher than 7  $\mu\text{M}$  [211]. The dimerization can be observed in the UV-VIS absorbance spectrum of MB solutions, where a second peak at approx. 610 nm appears next to the main peak at 664 nm (Figure 4.2a). Indeed, the molar extinction coefficient decreases with the increasing concentration of dye (Figure 4.2b). The influence of dimerization of MB on the UV-VIS spectroscopy is discussed in Appendix A4.

### Ciprofloxacin

Ciprofloxacin (Cipro) [212], [213] is a quinolone antibiotic. Because of its stability in water, it has become ubiquitous in pharmaceutical effluents. This antibiotic is toxic and harmful to living organisms. It can be used as a model pollutant when studying the photocatalytic treatment of wastewater from hospitals [210].

In this study, Cipro ( $\geq 98\%$ , molecular weight of 331.34 g/mol) from Sigma-Aldrich, Inc. was used to indicate the photocatalytic activity of the photocatalyst magnetic nanoparticles. Its UV-VIS absorbance spectrum is shown in . The absorbance peak is at 277 nm. Dissimilar to methylene blue, a 12.1  $\mu\text{M}$  Cipro solution with a 10 mm optical pathlength absorbs approx. 5 % light of 365 nm.

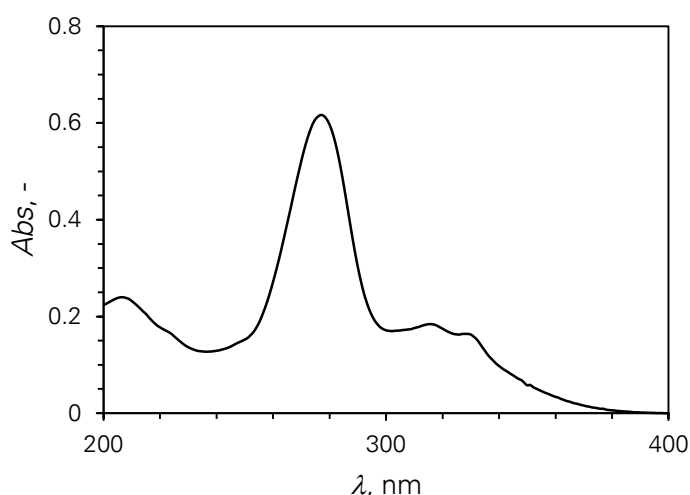


Figure 4.3 UV-VIS absorbance spectrum of ciprofloxacin (Cipro). The 12.1  $\mu\text{M}$  Cipro solution was measured with the 10 mm optical pathlength cuvette by means of a Varian Cary 100 Bio UV-VIS spectrometer.

### Commercial dye substances Everzol Navy ED and Remazol Red RR

The Everzol Navy ED dye contains the functional group of  $-\text{SO}_2\text{CH}_2\text{CH}_2-$  [214], while the azo dye Remazol Red RR contains the azo group of  $-\text{N}=\text{N}-$  [215].

These two commercial reactive dyes were provided by March 29 Textile-Garment Joint Stock Company, Danang, Vietnam (section 7.2.1). The names were given by the company. The powders may consist of mixtures of various components and the purity is not guaranteed. Due to the study purpose, discoloration was focused. For this reason, the absorbance of the solutions analyzed by UV-VIS spectroscopy were used to evaluate the data. The absorbance spectra of Everzol Navy ED and Remazol Red RR are shown in . Their maxima are observed at approx. 520 nm and 600 nm, respectively. When being tested with a 10 mm cuvette, the 52 mg/l red dye and 31 mg/l navy dye solutions absorbed 48 % and 33 % light at 365 nm, which means that shielding effect occurs during the test.

In this work, 25–30 mg/l dye solutions were discolored (section 7.1.4). Exceptionally, a high concentration of the Navy dye of 250 mg/l was also degraded (section 7.2.4.2).

### 4.1.3 Others

#### Water

Water was purified by an Astacus membraPure system. The ultrapure water was required to prepare suspensions and the solutions of organic compounds with defined ionic background.

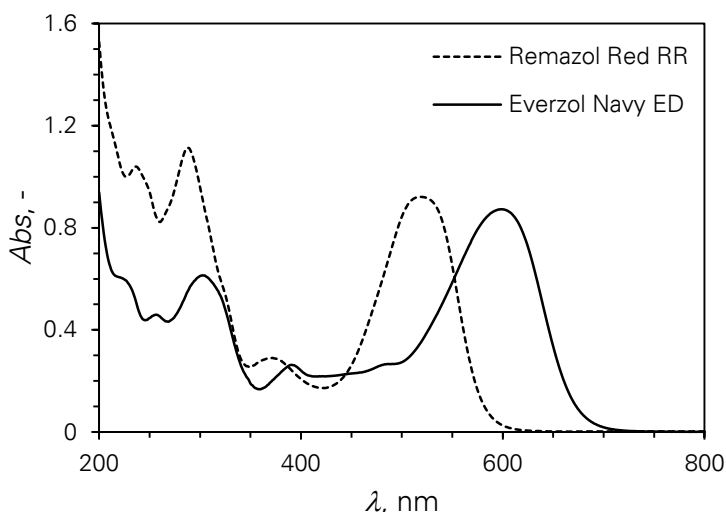


Figure 4.4 UV-VIS absorbance spectra of two commercial dyes: The 31 mg/l Everzol Navy ED and 52 mg/l Remazol Red RR solutions were measured with the 10 mm optical pathlength cuvette by means of a Varian Cary 100 Bio UV-VIS spectrometer.

## Air

In the experimental setup, the mixing tank is an open tank. Dissolved gases (noticeably CO<sub>2</sub> and O<sub>2</sub>) in the system can influence the properties of the suspension. Dissolved carbon dioxide forms the carbonic acid or bicarbonate. These weak acids change the pH of the system. Meanwhile, dissolved oxygen acts as an electron acceptor (section 2.1.3). The amount of gases was kept unchanged by maintaining the same stirring speed and the same form of the mixing tank.

## Chemicals used for pH adjustment

The acidity of the suspension was adjusted by HCl or NaOH. Sodium hydroxide (VWR BDH Prolabo® Chemicals) was dissolved to have 0.01 M solution. Hydrochloric acid, ACS reagent, 37 % (Sigma-Aldrich) was diluted to 0.01 or 1 M. A certain amount of these acid/base was added to the suspension to have the desired pH.

## 4.2 PHOTOCATALYST DISPERSION TECHNIQUES

P25 is a nanostructured material, which is composed of aggregates and agglomerates in the size range of 100 nm up to 100 µm, depending on the mechanical treatment that the material has experienced. In order to study the influence of the aggregated state in a defined manner, adequate dispersion techniques are required. Two methods were tested.

The P25 suspensions were dispersed by a T25 digital ULTRA-TURRAX® device (disperser S25N-25F). In this work, the rotation speed of 21 500 ppm was tested corresponding to an energy of 40 W.

High intensity ultrasound is another technique. Suiting the purpose of experiments, one of two ultrasonic processors was chosen, including Hielscher UP100H (sonotrode MS7, 7 mm diameter) and Topas UDS751 (sonotrode S7, 7 mm diameter). Generating power was measured by the power meter Voltcraf® Energy Logger 4000.

This part of this study is a cooperation with the research group Mechanical Process Engineering of TU Dresden.

## 4.3 ANALYTICAL TECHNIQUES

This subchapter introduces the characterization of P25 particles (as powder samples or in suspensions). Photon correlation spectroscopy, UV-VIS spectroscopy, and diffuse reflectance UV-VIS spectroscopy were used. The wavelengths used in these methods are in the UV and visible range (from 200–800 nm). As the dimension of the semiconductor particles is in the nano-scale and, therefore, smaller or comparable to the wavelength used, generally the light is absorbed or scattered. The interaction between the particles and the light can be determined, including transmittance, reflectance, and scattering. Depending on the used theories, characteristics such as the bandgap energy, the Kubelka-Munk function (which is clarified

later), the extinction coefficient, the intensity-weighted harmonic mean size, and the polydispersity of P25 can be achieved.

### 4.3.1 UV-VIS spectroscopy

UV-VIS spectrometer is a widely used instrument in laboratories. In this work, a Varian Cary 100 Bio UV-VIS spectrometer was used to determine the transmittance of photocatalyst suspensions as well as to measure the molar concentration of the organic molecules.

#### Transmittance of suspensions

This technique was used to measure the transmittance of the colloidal P25 suspensions [216]–[218]. It is the ratio of the transmitted radiant flux to the incident radiant flux (Figure 4.5). The principle of the method obeys the Beer-Lambert law. The (napierian) transmittance of light  $T$  is determined as

$$T_{\lambda} = \frac{I_{\lambda}}{I_{\lambda,0}} = e^{-\beta_{\lambda} C_m z} = e^{-\tau_{\lambda} z}, \quad (4.1)$$

where  $I_{\lambda}$  and  $I_{\lambda,0}$  is the transmitted and incident light intensity,  $z$  is the optical pathlength,  $C_m$ ,  $\tau_{\lambda}$ , and  $\beta_{\lambda}$  are the mass concentration, the turbidity of the suspension, and the extinction coefficient of the material, respectively. These values are related to each other as

$$\beta = \tau / C_m. \quad (4.2)$$

Seven particle concentrations in the range of 0.01–1 g/l were analyzed. The UV-VIS spectra were scanned in the wavelength range of 200–800 nm. For different purposes, transmittances and related optical properties at specific wavelengths are discussed: 340 nm, 365 nm and 410 nm (corresponding the minimum, the mode and the maximum wavelengths of the UV lamp, section 3.1.4), additionally, 410 nm and 387 nm (corresponding to the minimum [28], [33], [41] and maximum values of commonly reported  $\text{TiO}_2$  bandgap [28], [33], [41]), and 633 nm (corresponding to the wavelength of the red laser beam used in the photon correlation spectroscopy, section 4.3.3).

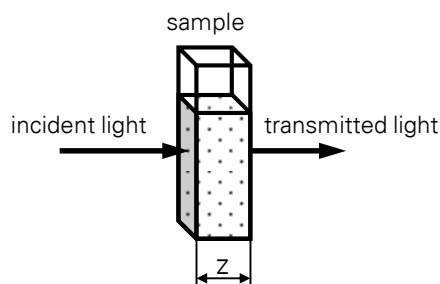


Figure 4.5 UV-VIS spectroscopy: transmittance.

### Absorbance of the organic compounds

In experiments, the color removal of dyes (methylene blue (MB), Everzol Navy ED and Remazol Red RR) and the degradation of ciprofloxacin (Cipro) was observed. UV-VIS spectroscopy is a practical analysis method for the quantitative determination of these organic substances based on the Beer-Lambert law (Eq. (2.19)). Absorbance of the solutions was measured with the Varian Cary 100 Bio UV-VIS spectrometer. The scanning range is 400–800 nm for dyes, and 200–400 nm for Cipro. Depending on the concentration ranges, 4 cuvettes were alternatively used. Low concentration samples (0–15  $\mu\text{M}$  for MB and Cipro, 25–30 mg/l for commercial dyes) were measured with the 10 mm cuvette, whereas 5, 2 and 1 mm cuvettes were used for higher concentration samples (25–125  $\mu\text{M}$  for MB and 250 mg/l for the Navy dye). The absorbance peak was used to quantify the organic compounds.

In order to determine the molar concentration of MB, a calibration curve is needed. According to ISO 10678:2010(E) and DIN 52980 [219], [220], the molar extinction coefficient at 664 nm is 7.4028  $\text{m}^2/\text{mol}$ . However, when increasing the concentration (exceed 7  $\mu\text{M}$ ), the dimerization of MB occurs (Figure 4.2) [211]. For this reason, the linear function of absorbance by MB concentration is invalid, especially with high concentrations. Instead, the calibration counting the dimerization follows

$$C_{n,\text{MB}} = \frac{2K}{\epsilon_{664}^2 L^2} E_{664}^2 + \frac{1}{\epsilon L} E_{664}, \quad (4.3)$$

where  $C_{n,\text{MB}}$  is the concentration of MB,  $K$  is the dimerization equilibrium constant,  $\epsilon_{664}$  is the true molar extinction coefficient of MB at 664 nm, and  $E_{664}$  is the napierian absorbance of MB through an optical pathlength  $L$  and related to the decadic absorbance by  $E_{664} = \text{Abs}_{664} \ln(10)$ . It was found that  $\epsilon_{664} = 1.9 \times 10^4 \text{ m}^2/\text{mol}$  and  $K = 3.58 \text{ m}^3/\text{mol}$ . Details of the calibration can be found in Appendix A4.

For Cipro, the calibration curve was determined as

$$C_{n,\text{Cipro}} = 24.00 \text{Abs}_{277} + 0.13, \quad (4.4)$$

where  $C_{n,\text{Cipro}}$  is the concentration of Cipro, and  $\text{Abs}_{277}$  is the decadic absorbance of Cipro through an optical pathlength of 10 mm. More details can be found in Appendix A5.

For Everzol Navy ED and Remazol Red RR dyes, absorbance peaks at 600 and 520 nm were used to evaluate the discoloration, respectively. No calibration was done.

All information for UV-VIS measurement of organic substances is presented in Table 4.1.

Table 4.1 UV-VIS spectroscopy of organic compounds.

Organic molecules	Color of the solution	Scanning range, nm	Absorbance peak at wavelength $\lambda$ , nm	Calibration curve
Methylene blue	blue	400–800	664	Eq. (4.3)
Everzol Navy ED	navy	400–800	600	Eq. (4.4)
Remazol Red RR	red	400–800	520	–
Ciprofloxacin	colorless	200–400	277	–

### 4.3.2 Diffuse reflectance UV-VIS spectrometer

The method was used to determine the ratio of the absorption coefficient to the scattering coefficient of the P25 semiconductor. Diffuse reflectance UV-VIS spectroscopy is also an empirical method to determine energy bandgap of the sample [199], [221], [222].

The powder was compressed then measured with a Shimadzu UV-2501 PC UV-VIS spectrometer. The thickness of the compressed sample must be large enough so that light cannot penetrate the solid samples but is absorbed or scattered. The ratio of the reflected radiant flux to the incident radiant flux is so-called reflectance. It includes two components: specular reflection (or symmetrical reflection) and diffuse reflection (or scattering) (Figure 4.6). The instrument is coupled with an integrating sphere, and BaSO<sub>4</sub> was used as a standard white board (or a reference). The diffuse reflectance  $R_{\infty}$  spectra was recorded. It is actually the ratio of the reflectance of the sample to that of the white board. In this study, only absolute but no other reflectance is referred, the subscript “ $\infty$ ” is omitted and the symbol  $R$  is used as the substitution.

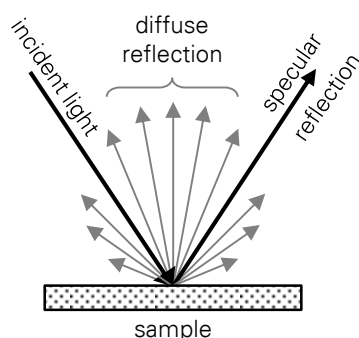


Figure 4.6 Diffuse reflectance UV-VIS spectroscopy: Specular and diffuse reflection.

The method offers a great advantage to determine the bandgap energy of the semiconductors [221]. The reflectance can be transformed to the Kubelka-Munk function  $F(R)$  through the Kubelka-Munk theory. It is the ratio of absorption coefficient  $\kappa$  to scattering coefficient  $\sigma$  at a specific wavelength and can be determined as [222]

$$\frac{\kappa}{\sigma} = \frac{(1-R)^2}{2R} = F(R). \quad (4.5)$$

Additionally, the Tauc equation is written as

$$(\kappa \times h\nu)^{1/n} = A(h\nu - E_g), \quad (4.6)$$

where  $h$  is the Planck's constant,  $\nu$  is the light frequency,  $A$  is a proportional constant,  $E_g$  is the bandgap energy, and  $n$  denotes the nature of the sample transition. When the scattering coefficient  $\sigma$  is assumed to be a constant (actually, it usually increases with the decreased wavelength),  $F(R)$  is proportional to the absorption coefficient  $\kappa$ . Eq. (4.6) can be expressed as

$$[F(R) \times h\nu]^{1/n} = A(h\nu - E_g). \quad (4.7)$$

The value  $[F(R) \times h\nu]^{1/n}$  is called the modified Kubelka-Munk function. It can be plotted as the function of energy of the incident light  $E = h\nu$  (the Tauc plot). By extrapolating  $[F(R) \times h\nu]^{1/n}$  to 0, the found energy is considered as the bandgap energy.

This work addressed the cooperation with other colleagues and with the Electroactive Smart Materials group of the University of Minho.

### 4.3.3 Photon correlation spectroscopy

For nano colloidal assemblies, photon correlation spectroscopy (also known as dynamic light scattering (DLS)) can be used to characterize the size distribution [154], [162], [218], [223]–[226]. The technique is based on the measurement of the scattered light (Figure 4.7).

Theoretically, the dispersed particles are in continuous Brownian movement, and the scattered intensity  $I(t)$  fluctuates along with time. The time autocorrelation function  $G_2(\tau)$  of the scattered intensity is determined as

$$G_2(\tau) = \langle I(t) \times I(t + \tau) \rangle, \quad (4.8)$$

where  $\tau$  is the time interval, and the symbol  $\langle \dots \rangle$  refer to an average value of the product  $I(t)$  and  $I(t + \tau)$ .

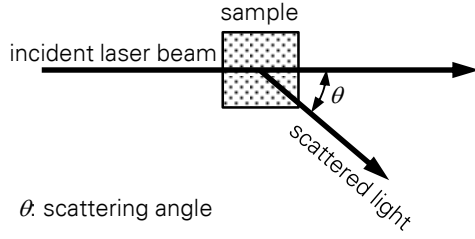


Figure 4.7 Photon correlation spectroscopy: Scattering geometry

For a large number of particles, the correlation function is an exponential function of the time difference

$$G_2(\tau) = A(1 + Be^{-2\Gamma\tau}), \quad (4.9)$$

where  $A$  and  $B$  are the baseline and intercept of the correlation function, respectively. The decay rate  $\Gamma$  is related to the diffusion coefficient  $D$  as

$$\Gamma = Dq^2. \quad (4.10)$$

The modulus of the scattering vector  $q$  is the function of the refractive index of dispersant  $n$ , the wavelength of the incident light  $\lambda$  and the scattering angle  $\theta$

$$q = \frac{4\pi n}{\lambda} \sin \frac{\theta}{2}. \quad (4.11)$$

Particle size can be calculated from the Stokes-Einstein equation

$$d_h = \frac{kT}{3\pi\eta D}, \quad (4.12)$$

where  $d_h$  is the hydrodynamic diameter,  $k$  is the Boltzmann's constant,  $T$  is the absolute temperature, and  $\eta$  is the viscosity.

In this work, DLS measures the intensity fluctuation of the scattered light. The immediate results of DLS measurement are the scattering intensity-weighted distribution functions. By means of the correlation function, the diffusion coefficient can be determined. The intensity-weighted harmonic mean size  $x_{\text{cum}}$  was extracted. To show the broadness of the size distribution, polydispersity index  $PDI$  was collected. Note that these parameters are physical values corresponding to both hydraulic and optical properties of the colloids (see also Appendix A1). Fundamentals of DLS can be found in Appendix A2.

Two particle sizers, Malvern HPPS-ET and Zetasizer Nano S90, were employed. The HPPS-ET was used in the early stage of this study with the cooperation with the research group Mechanical Process Engineering of TU Dresden. Some of the specifications of each instrument specified by the manufacturer are shown in. Data achieved by two instruments are correlated as presented in the Appendix A2.

Table 4.2 Particle sizers used for the characterization of the dispersed photocatalysts.

Specifications	HPPS-ET	Nano S90
Scattering angle, °	173	90
Laser		
beam	red	red
wavelength, nm	633	633
Measurement position, mm	-1	4.65

## 4.4 PHOTOCATALYTIC EXPERIMENTS

### 4.4.1 Procedure

Photocatalytic degradation tests involve 3 steps as generally introduced in subchapter 3.2. In the study, the operations were as follows:

#### 1. Preparation of the slurry photocatalyst

A desired amount of photocatalysts was dispersed in ultrapure water. Different techniques were tested, including mixing by a magnetic stirrer, an ULTRA-TURRAX® device or an ultrasonic processor (section 4.4.2). The particle characteristics were analyzed with samples collected at the beginning and the end of this step.

#### 2. Adsorption-desorption equilibrium

The dispersed suspension was placed in a mixing tank in the dark. The tank is open beakers. The same form of the beakers were used to ensure the same amount of incorporated air in the suspension which could act as electron acceptors (sections 2.1.1 and 2.3.4). The use of aluminum foil to cover the glassware avoided the interference of light (if possible) with the suspension. The desired volume of stock solution of the organic compound was then added into the suspension and the adsorption-desorption equilibrium started. Magnetic stirring during equilibrium prevented the suspension from re-agglomeration or sedimentation.

When working with a low initial concentration of organic compounds (10–15 µM for methylene blue and ciprofloxacin, 25–30 mg/l for commercial dyes) and using photocatalyst concentrations of 0.03–10 g/l, a 30 min dark adsorption-desorption can reach the equilibrium [25]. When studying the high initial of the organic compound (25–125 µM for methylene blue and 250 mg/l for the commercial Navy dye), an extended period of dark experiments was necessary to ensure a (near) equilibrium. Experimentally, the 90 min equilibrium was performed.

If necessary, HCl or NaOH was added to adjust pH of the suspensions.

### 3. Photocatalytic degradation or control tests

Experiments were performed as described in subchapter 3.2. Photocatalytic tests were done under artificial UV or sunlight. Control tests were done in the dark. Exceptionally, to verify the photosensitivity of dyes under visible light, control tests were conducted with the artificial visible light.

For experiments with UV illumination, UV intensities at the illuminated surface of the reactor were measured before each experiment series by the lux-meter PCE-UV34. The average intensity  $\bar{I}$  was determined as Eq. (3.2). During the individual test, the light intensity of a reference point  $I_{\text{ref}}$  was recorded to check the stability of light through the experiment. The correlation with the computed average intensity was done as

$$\bar{I} \propto I_{\text{ref}}. \quad (4.13)$$

For experiments with sunlight, the intensity is homogeneous on the entire illuminated surface. However, the intensity is chronologically changed by weather conditions. UV intensity was measured every 30 s by the lux-meter. No UVC or visible light was measured as it is out of the sensitivity range of the lux-meter. When conducting experiments with visible lamp, the visible intensity was monitored by the software.

The interference of illumination with the mixing tank and tubes can intensify the computed light intensity. To avoid it, aluminum foil was used to cover these components.

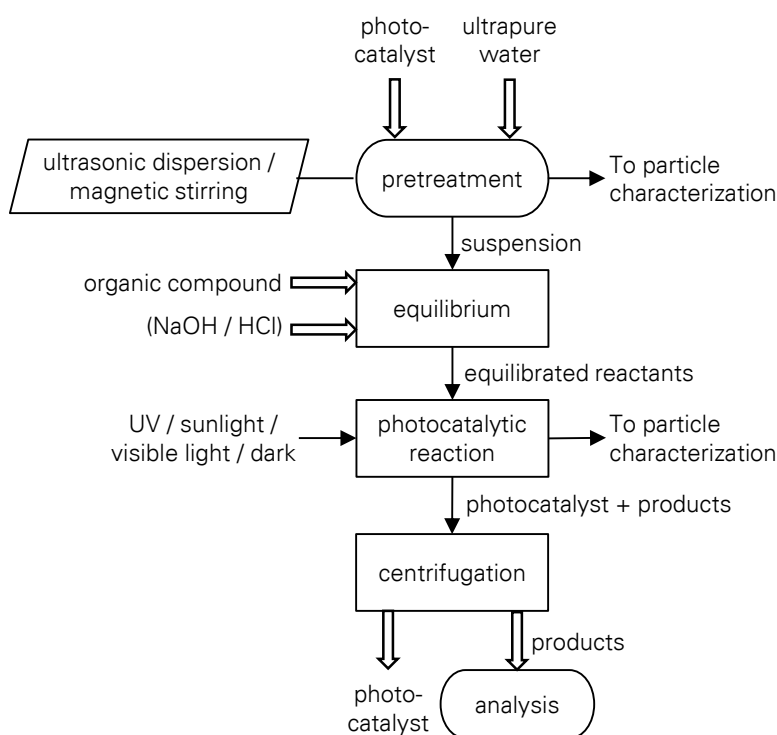


Figure 4.8 Procedure for photocatalytic experiments.

During experiments, samples were taken from the mixing tank each desired interval. Offline analysis was done by UV-VIS spectroscopy. As the samples were in a suspension state, centrifugation was used to separate the solid-liquid. The samples were put in the centrifuge Eppendorf 5417 for 40 min with the rotation speed of 14000 rpm. The temperature was set to be similar to the ambient conditions, in particular, 25 °C in summers, and 20 °C in winters. The supernatants were taken out for analysis.

When pH was adjusted in experiments, pH of the fluid in the mixing tank was noted with the pH meter (pH 100 VWR).

If necessary, at the beginning and at the end of this step, particle characterization was performed to check the changes during the test.

shows the entire procedure of experiments.

#### **4.4.2 Dispersion tests**

Experiments aimed at a study on the pre-treatment of the photocatalysts, including:

- comparison of two dispersion techniques by an ULTRA-TURRAX<sup>®</sup> device and an ultrasonic processor;
- a detailed study on the ultrasonic dispersion with the consideration of energy consumption;
- stability of dispersed suspensions with/without the appearance of methylene blue (MB), one organic compound;
- and the influence of the aggregate size on the optical properties and the photocatalytic activity of P25.

Depending on the experiment purposes, three dispersion methods were used: agitating by a conventional magnetic stirrer, high-performance dispersion by a T 25 digital ULTRA-TURRAX<sup>®</sup> disperser, and ultrasonication by a Topas UDS751 and a Hielscher UP100H. The particle concentration was set to be 1 g/l. Suspension volumes were varied from 20–1800 ml. The power during the dispersion time was recorded by the power meter Voltcraft<sup>®</sup> Energy Logger 4000. Samples were taken as the desired interval for analysis.

Selected experiments regarding dispersion technique are listed in Table 4.3. In subchapter 5.2.4 the influence of dispersion on the optical properties is discussed, whereas the impact of ultrasonic dispersion on the photocatalytic reaction of MB is presented in subchapter 6.4.6.

Table 4.3 Overview of experiments on the pre-treatment of the photocatalyst.

$m_{\text{P25}}$ , g	$V_{\text{H}_2\text{O}}$ , ml	Disperser	Power <sup>a)</sup> , W	$t_{\text{dispersion}}$ , min	Others	Data <sup>b)</sup>
purpose: choosing a dispersion technique						
0.20	200	Hielscher	30	52	-	5.1.1
0.21	200	Ultra Turrax	40	60		A3
purpose: an energy concept of ultrasonic dispersion						
0.22	200	Hielscher	10	90	-	5.1.1
0.20	200	Hielscher	30	52		
0.24	200	Topas	33	51		
0.20	200	Topas	70	36		
1.00	1000	Topas	97	32		
1.80	1800	Topas	97	48		
purpose: stability test						
0.20	200	Topas	60	60	stability test: 4 weeks	A3
0.05	50	Magnetic stirrer	-	-	with/without MB stability test: 3 days	5.1.2
0.05	50	Topas	52	4		
purpose: effects on optical properties						
0.02	20	Magnetic stirrer	-	-	stock suspension was then diluted to have the desired particle concentrations	5.2.3
0.02	200	Hielscher	40	0–32		5.2.4
purpose: effects of ultrasonic dispersion on photocatalytic reactivity						
0.04	40	Topas	20	0–4	-	6.4.6

<sup>a)</sup> Data show the average values in the dispersion period<sup>b)</sup> Experimental data are presented in the mentioned sections

### 4.4.3 Color removal of methylene blue

In chapter 6, all scientific investigations of photocatalysis in the designed illuminated flow reactor are presented. To compare results with other publications, widely used  $\text{TiO}_2$  P25 was used as the photocatalyst, and the model dye substance methylene blue (MB) was used as the target organic molecule.

#### Preliminary tests

The first preliminary test C1 is to inspect if MB is a photosensitizer. The MB solution was illuminated under UV light. No photocatalyst powder was added.

The second preliminary test C2 is to study the adsorption of MB on the photocatalyst during the photocatalytic reaction. The equilibrated MB and P25 system (after the adsorption-desorption equilibrium in the dark, section 4.4.1) was loaded into the reactor. The experiment was done in the dark.

The third preliminary test is to check if color removal of MB occurs in the presence of P25 photocatalyst under UV illumination following the procedures introduced in section 4.4.1.

Three preliminary tests are compared and photocatalytic ability of P25 for degradation of MB will be concluded.

### **Variation of process conditions**

To inspect the influential parameters on the photocatalysis, process conditions were varied, including: i) the photocatalyst concentration; ii) the initial concentration of MB; iii) the suspension volume; iv) the UV intensity; v) the optical thickness; vi) pH; and vii) the aggregation state of the photocatalyst.

i-iii) These conditions were achieved by altering the amount of P25 powder, the volume of water, or the volume of MB stock solution.

iv) UV intensity can be altered by changing the irradiation. In this study, UV intensity was adjusted by changing the distance between the UV lamp and the reactors, or by adding transparent films on the illuminated window.

v) Varying optical thickness were obtained by using different reactors, corresponding to the thickness of 11, 17 or 22 mm (see also section 3.1.3).

vi) pH was changed by adding a desired amount of HCl or NaOH.

vii) Different aggregation states were obtained by varying ultrasonic energy of the dispersion.

Photocatalytic experiments were carried out following the operational procedures in section 4.4.1. For experiments with varying pH or the MB initial concentration, in addition to the photocatalytic tests, control tests were done with the same procedure but in the dark.

Experimental plan is summarized in Table 4.4.

Table 4.4 Overview of experiments on the color removal of methylene blue by photocatalysis.

Materials			Process conditions				Notes	Data <sup>b)</sup>
P25	MB	Volume	Equilib- rium du- ration	Reac- tor	UV intensity <sup>a)</sup>	Reaction duration		
g/l	μM	ml	min	-	W/m <sup>2</sup>	min		
purpose: preliminary tests								6.2
0	11	400	-	beaker	15–16 <sup>c)</sup>	60	Control test C1	
1	124	400	90	R10	0	150	Control test C2 in dark	
0.3	11	1000	30	R20	19	60	Photocata- lytic test	
purpose: verifications of the reactor model, influence of the suspension volume								6.3.1 6.4.1 & 7.1.1
0.3	10–11	600, 800, 1000, 1400, and 2400	30	R20	18–21	30–60	Suspension volume was varied	
purpose: influence of UV intensity								6.4.2
0.1	10	600	30	R20	6–20	30–60	Intensity of incident light was varied	
purpose: influences of optical penetration								6.4.3
0.03, 0.1, 0.3 and 1	9–10	600	30	R10, R15, R20	26	40	Photocatalyst concentration was varied; Each experi- ment was done in three reactors	
purpose: influence of initial concentration of MB								6.4.4 & 7.2.4
0.1, 0.2, 0.5 and 1	13, 24, 51, and 123	400	90	R10	22	30, 60, 120 or 180	Initial concen- tration of MB was varied	
					0		Control tests in dark	
purpose: influences of pH								6.4.5
0.1	13	400	30	R10	24	40	pH = 3–10	
					0		Control tests in dark	
purpose: influences of aggregate size								6.4.6
0.1	13	400	30	R10	24.9	40	photocatalyst size was var- ied ( $x_{cum}$ = 243–469 nm); pH was set to be 5	

<sup>a)</sup> Data show the average values of all photocatalytic experiments<sup>b)</sup> Experimental data are presented in the mentioned sections<sup>c)</sup> The maximum intensity on the illuminated surface of the beaker

#### 4.4.4 Selected case studies for applications of photocatalysis

Chapter 7 introduces selected case studies for further photocatalytic applications. Different materials including TiO<sub>2</sub> P90, ZnO, and the synthesized magnetic particles were employed as photocatalysts. Here, not only lab chemicals (methylene blue (MB) and ciprofloxacin (Cipro)), but also commercial dye substances (Remazol Red RR and Everzol Navy ED) were used for degradation tests. Artificial UV or natural solar light were used for photocatalytic tests, while artificial visible light was employed for control tests.

Details and parameters of each test can be found in Table 4.5.

Table 4.5 Overview of experiments on applications of photocatalysis for wastewater treatment.

Materials			Process conditions				Notes	Data <sup>a)</sup>	
Photocatalyst	Organic substance	Volume	Equilibrium	Reactor	Illumination	Reaction duration			
purpose: solar photocatalysis									7.1.2
TiO <sub>2</sub> P25 0.1 g/l	MB 4 mg/l (13 μM)	600 ml	30 min	R10	solar light, cloudy day $I_{UV} = 2.4\text{--}19.7$ W/m <sup>2</sup> $I_{UV,ave} = 5.2$ W/m <sup>2</sup>	60 min	Photocatalytic test		
					solar light, sunny day $I_{UV} = 7.1\text{--}35.0$ W/m <sup>2</sup> $I_{UV,ave} = 23.6$ W/m <sup>2</sup>	50 min <sup>b)</sup>			
					artificial visible light $I_{VIS} \approx 100$ W/m <sup>2</sup>	60 min	Control test		
purpose: photocatalysis with different nanomaterials									7.1.3
TiO <sub>2</sub> P90 0.01–10 g/l	MB 3.3 mg/l (10 μM)	600 ml	30 min	R20	artificial UV light $I_{UV,ave} = 27.7$ W/m <sup>2</sup>	30, 40 or 60 min <sup>b)</sup>	Commercial NPs		
ZnO 0.1–3 g/l	MB 3.3 mg/l (10 μM)	600 ml	30 min	R20	artificial UV light $I_{UV,ave} = 27.2$ W/m <sup>2</sup>	15 min <sup>b)</sup>			
Fe <sub>3</sub> O <sub>4</sub> / SiO <sub>2</sub> / TiO <sub>2</sub> 1 g/l	Cipro 5.0 mg/l (15 μM)	500 ml	30 min	R10	artificial UV light $I_{UV,ave} = 16.7$ W/m <sup>2</sup>	120 min <sup>b)</sup>	Self-synthesized magnetic NPs		

<sup>a)</sup> Experimental data are presented in the mentioned sections

<sup>b)</sup> Duration to degrade more than 90 % of the initial concentration

Table 4.5 (cont.) Overview of experiments on applications of photocatalysis for wastewater treatment.

Materials			Process conditions				Notes	Data <sup>a)</sup>	
Photo-catalyst	Organic substance	Vol- ume	Equi- librium	Reac- tor	Illumination	Reaction duration			
purpose: photocatalysis for commercial dye substances									7.1.4
TiO <sub>2</sub> P25 0.3 g/l	Remazol Red RR 31 mg/l	600 ml	30 min	R10	solar light, sunny day $I_{UV} = 29.1\text{--}37.4$ W/m <sup>2</sup> $I_{UV,ave} = 33.7$ W/m <sup>2</sup>	60 min <sup>b)</sup>	Photo- catalytic test		
					artificial UV light $I_{UV,ave} = 20.8$ W/m <sup>2</sup>	60 min			
					artificial visible light $I_{VIS} \approx 100$ W/m <sup>2</sup>	60 min	Control test		
TiO <sub>2</sub> P25 0.3 g/l	Everzol Navy ED 24–29 mg/l	600 ml	30 min	R10	solar light, cloudy day $I_{UV} = 3.4\text{--}17.9$ W/m <sup>2</sup> $I_{UV,ave} = 8.6$ W/m <sup>2</sup>	40 min	Photo- catalytic test		
					artificial UV light $I_{UV,ave} = 20.8$ W/m <sup>2</sup>				
					artificial visible light $I_{VIS} \approx 100$ W/m <sup>2</sup>		Control test		
purpose: preliminary test for up-scaling purpose									7.2.4
TiO <sub>2</sub> P25 1 g/l	Everzol Navy ED 250 mg/l	400 ml	90 min	R10	artificial UV light $I_{UV,ave} = 24.6$ W/m <sup>2</sup>	300 min	Photo- catalytic test		
					dark		Control test		

<sup>a)</sup> Experimental data are presented in the mentioned sections<sup>b)</sup> Duration to degrade more than 90 % of the initial concentration



## 5 PHYSICAL PROPERTIES OF P25 PHOTOCATALYST AGGREGATES

TiO<sub>2</sub> P25 is a commercial material and its characteristics have been widely reported. The material is manufactured at industrial scale, thus the homogeneity of product in different stocks is not guaranteed. The characterization of the material in individual study is necessary.

The commercial materials are typically in an aggregated state (Figure 5.1). While the primary particle has the mean size of  $25 \pm 3$  nm [166], the fractal-like aggregates are in sub-micron scale [79], [227], [228]. Depending on the aggregated degree, the properties of the P25 may change. This chapter discusses this topic. Only characteristics which have important effects on photocatalysis, such as size, optical characteristics and stability, are of interest.

### 5.1 SIZE AND STABILITY

#### 5.1.1 Photocatalyst size

Results in this section were previously published [186].

##### Dispersion technique

P25 nanoparticles are usually in an aggregated state. Since the aggregates are tightly bound, high-performance dispersing devices are required to disintegrate the aggregates. A dispersion technique is required to disintegrate P25, and to vary the aggregate size.

ULTRA-TURRAX® device can produce strong shear force which provides a better dispersion compared to conventional mechanical mixing. The device works based on the rotor-stator

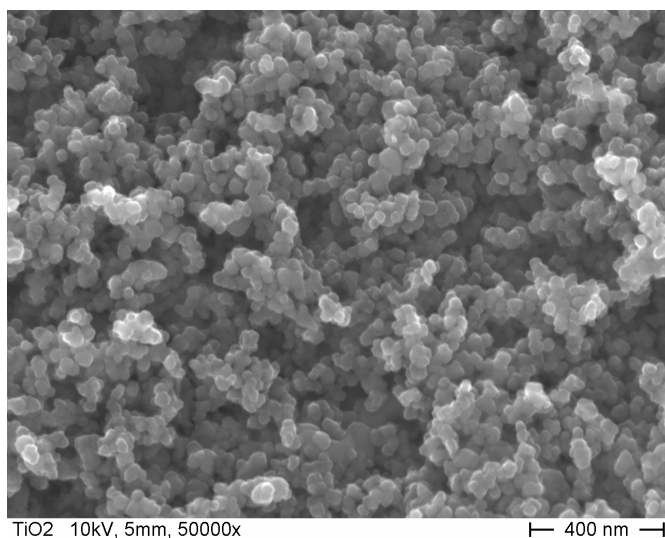


Figure 5.1 SEM image of P25 aggregates. Image credit to Annegret Benke.

principle [229]. The rotor is operated at a high speed within a stationary stator. Suspension moves both axially and radially between the gaps of the rotor-stator. The high speed of the rotor and the small gap can produce a strong shear force, thus facilitate a better dispersion. However, the shear force is ineffective to disintegrate P25. The data is presented in Appendix A3. It indicates that the P25 aggregates are structured by tight bonds and require ultra-high energy performance, such as ultrasound.

Ultrasonication is well applied in materials science because of its wide range of chemical and physical consequences [230]. The main mechanism of ultrasound in liquids is the acoustic cavitation. Formed bubbles and jets are collapsed and generate local heat and high pressure, thus produce surface damage at interfaces of multiphase systems, or/and make ultrasonic stirring much highly intense than mechanical agitation. The initial test is to find out if ultrasound can usefully disperse the P25 suspension. A rather low electric power of 30 W was applied by using the Hielscher device. A 200 ml volume of 1 g/l P25 suspension was dispersed within a period of 40 min and the P25 size was characterized by the dynamic light scattering (DLS) instrument (Figure 5.2).

Prior to the dispersion, the P25 has the size  $x_{cum}$  of  $416 \pm 24$  nm. The value measured by DLS is the intensity-weighted harmonic mean size of the entire body. It is far different from the size characterized by image analyses (Figure 5.1), which is the diameter corresponding to the projected area of the primary particles. For this reason, in the test, the P25 size of sub-microns was found. In a meanwhile, the polydispersity index  $PDI$  is  $0.544 \pm 0.062$ . It implies that DLS is not suitable to measure such a highly polydispersed population, yet it indicates a broad distribution of the aggregates.

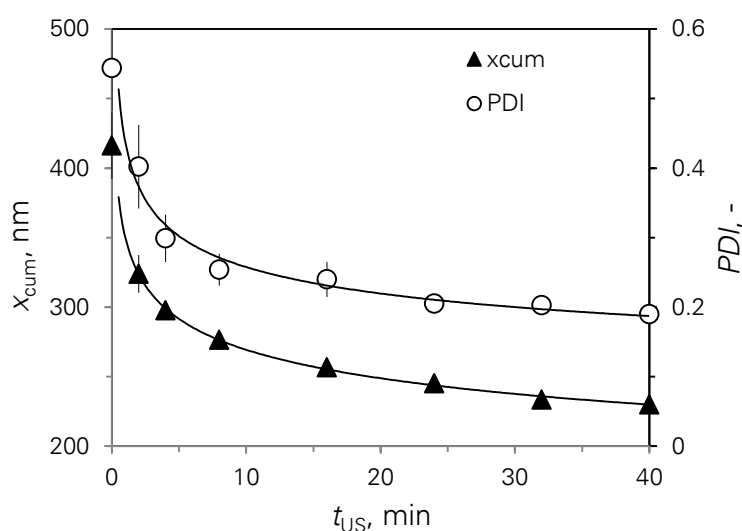


Figure 5.2 Ultrasonic dispersion of P25 suspension: Size characterization. A 200 ml P25 suspension of 1 g/l was dispersed with 30 W ultrasonication by the Hielscher processor. Aggregate size and polydispersity index of P25 colloidal suspensions measured by the Malvern Nano S90 dynamic light scattering instrument were shown along with the dispersion time.

During the ultrasonic dispersion,  $x_{cum}$  and  $PDI$  reduced. After a short dispersion of 2 min,  $x_{cum}$  of  $324 \pm 14$  nm and  $PDI$  of  $0.402 \pm 0.060$  were achieved. The lower  $PDI$  shows the narrower distribution which can be well measured by DLS. After the period of 40 min, the aggregate size  $x_{cum}$  of  $230 \pm 3$  nm and the  $PDI$  of  $0.190 \pm 0.023$  were obtained. These data prove that the ultrasonication can be an effective dispersion technique.

The decrease of  $x_{cum}$  and  $PDI$  obeys the power law. It also means that the decay rate at the beginning is speedy, while later it becomes slower. It seems to have a critical value of  $x_{cum}$ , where a long dispersion time has no more effectively disintegrating effect.

The reports of correlogram and size distribution by intensity before and after the dispersion can be found in Appendix A3.

### Energy concept

Ultrasonication is considered as a high energy consuming technique. In this work, power was inspected. Different power was adjusted by altering generating amplitudes (20–100 %) and the immersion level of the sonotrodes (2.0–5.5 cm), depending on the suspension volumes (Figure 5.3). Since the Hielscher device can generate ultrasound corresponding to the low electric power of 8–23 W, it was preferably used for the dispersion of a small volume. With the big volume of dispersed suspension (up to 5 l in the test), the efficient dispersion requires a higher energy up to 154 W which was achieved by the Topas device.

Here, the energy density of the dispersion was considered. It is the product of the electric power  $P$  and the dispersion time  $t$  divided by the suspension volume  $V$ , i.e.  $E_v = P \frac{t}{V}$ . Different volumes of the P25 suspension were tested [186]. The decay of P25 aggregate size is a power function of the energy density (Figure 5.4) as

$$x_{cum} \propto E_v^{-(0.13 \rightarrow 0.14)} \quad (5.1)$$

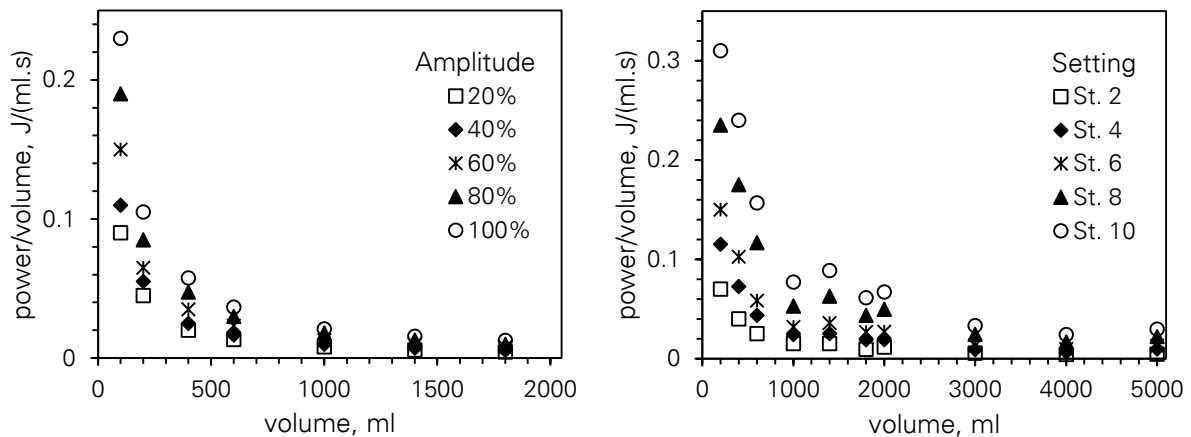


Figure 5.3 Ultrasonic energy consumption in a certain volume of water by using the ultrasonic processors (left) Hielscher UP100H and (right) Topas UDS751.

The data are in agreement with the energy concept [231], [232]. The exponent of Eq. (5.1) quantifies the efficiency of the dispersion. Small values suggest the requirement of a high energy to achieve a good dispersion. In this work, the exponent values of 0.142 and 0.134 for the Hielscher and Topas processors were obtained, respectively. This result means that an energy density of factor 170 is necessary to halve the P25 aggregate size. For instance, a dispersion time of 30 min is required to achieve the half size of colloids in one liter suspension when generating an ultrasonic power of 100 W. In this study, the real electric power consumption was measured, which is non-identical to the ultrasonic energy generated into the suspension. Thus, energy consumption of the two devices is dissimilar, noticed by the deviation of the two lines in Figure 5.4. In any event, this energy density concept is applicable for academic researches and economic estimation.

From the practical point of view, highly concentrated suspensions can be dispersed by means of ultrasonication, then be diluted to have the desired photocatalyst concentration of hundreds mg/l. With this procedure, ultrasonic dispersion can be realized as a pre-treatment step prior to the photocatalytic reaction. In this study, the maximum volumes of 1.8 and 5 liter, in case of with and without P25, respectively, were dispersed. It shows a promising application at a pilot scale. The next subchapter discusses further the impact of aggregate size on the photocatalyst properties.

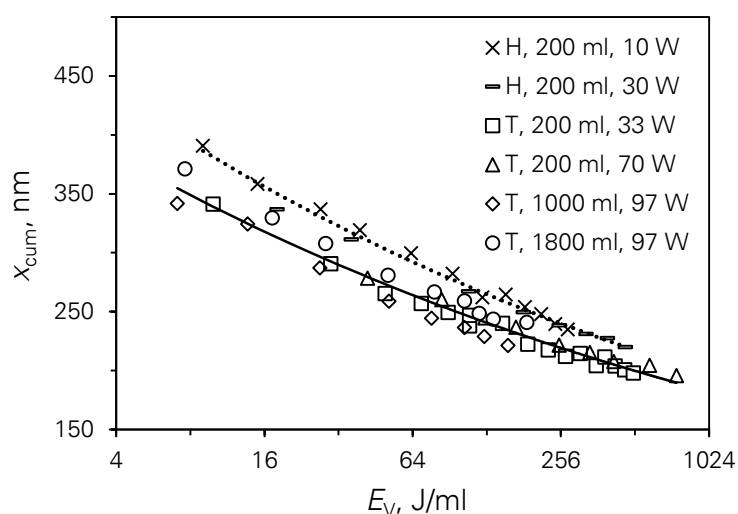


Figure 5.4 Ultrasonic dispersion of P25 suspension: The energy model. The 200–1800 ml suspensions of 1 g/l were dispersed with 10–97 W ultrasound by two ultrasonic processors, Hielscher UP100H (denoted by “H”) and Topas UDS751 (denoted by “T”). Dot and solid lines show power functions of aggregate size by energy density achieved by Hielscher and Topas processors, correspondingly. Aggregate size were measured by the Malvern HPPS-ET dynamic light scattering instrument and the correlation with Malvern Nano S90 was done (Appendix A2). Horizontal axis is in logarithmic scale.

### 5.1.2 Stability of dispersed photocatalyst

As mentioned in the previous section, P25 aggregates are structured by tight bonds. By ultrasonication, these bonds, to some extent, can be broken, and aggregates can be disintegrated. Due to the surface charge of the colloids, they can attract each other and re-aggregation probably occurs. Depending on the aggregate level, the fractal-like aggregates [79], [227], [228] may have different properties. This fact is to be discussed later in section 5.2.4. For this reason, the dispersity state of the suspension should remain as constant as possible for study purposes. Furthermore, a flow reactor at an industrial scale may be as long as hundreds of meters. Re-aggregation or/and sedimentation of the photocatalyst can cause the change of catalyst loading along the axial reactor [97]. This section discusses the stability of the dispersed photocatalyst.

Prior to the stability test, 50 ml P25 suspensions of 1 g/l were dispersed with two dispersion methods, which are conventional mixing by a magnetic stirrer, and ultra-mixing by assisted ultrasound (section 2.3.1). As the adsorption of the organic substance on the P25 may change its surface charge, and affect the aggregation of the colloids, suspensions with and without methylene blue (MB) were prepared.

The suspensions have pH of approx. 4.6–4.8. The conductivity of water was approx. 0.06  $\mu\text{S}/\text{cm}$ . No conductivity of suspensions was measured. The dispersed suspensions were kept in ambient conditions at which temperature was approx. 20 °C. The stability test was performed within 3 days. No pH value or conductivity was recorded, however, as shown in Appendix A3, there might have no significant change during the 3 day test. A weak mixing by a magnetic stirrer was applied before each analysis for the sampling purpose. Figure 5.5 shows the changes in the aggregate size  $x_{\text{cum}}$  and the polydispersity index  $PDI$ .

The conventional mixing shows the unstable suspensions with or without MB. Within 4 days, a deviation of the size of 57–62 nm was noticed, whereas  $PDI$  fluctuates by 0.05–0.09. It is in agreement with other work of our group [233], where at this pH, the interpolated zeta potential of P25 is approx. 22–26 mV.

Being dispersed with ultrasonication, the suspension without MB was stable. In particular,  $x_{\text{cum}}$  is  $221 \pm 2$  nm, and  $PDI$  is  $0.19 \pm 0.01$ . The results of the stability test over 4 weeks can be found in Appendix A3. Interestingly, even with the appearance of MB, the stability is likely unchanged. The values  $x_{\text{cum}}$  and  $PDI$  fluctuate in the range of 219–233 nm and 0.18–0.19, respectively. In this test, P25 is positively charged [26], [174], [176], [177], [233]. As MB is a cationic dye, when it is adsorbed on P25, it may promote the repulsive force among colloids. Thus aggregation is avoided. Here, only suspensions of P25 and MB were tested. No other organic substances were experimented. However, one should consider the possible change by other dyes, especially the anionic dyes, which can negatively affect the stability of the suspension.

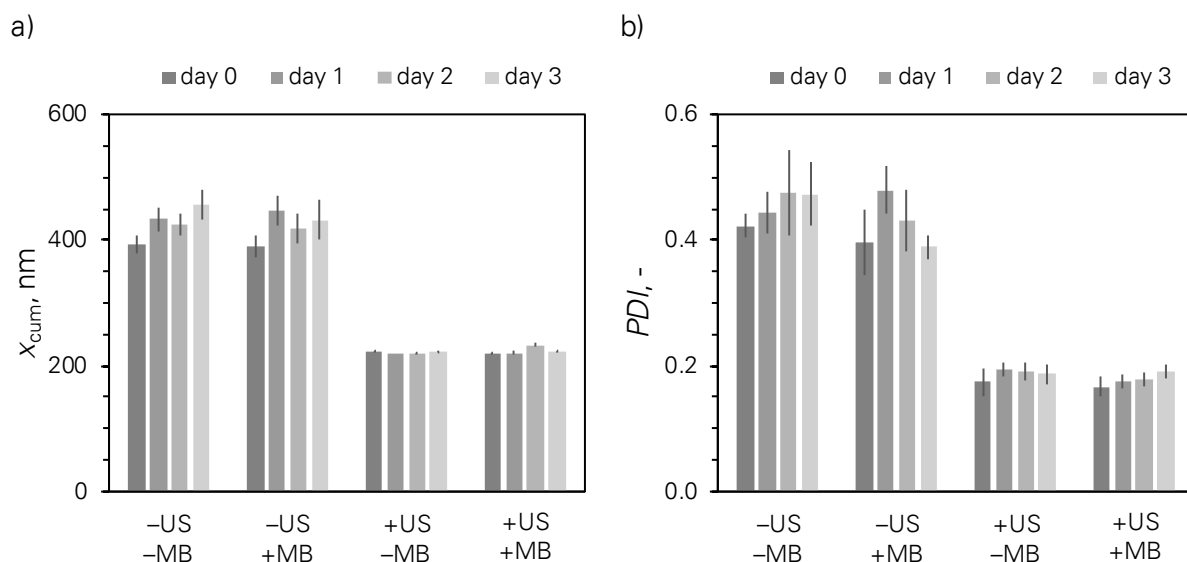


Figure 5.5 Stability test of dispersed P25: a) aggregate size ( $x_{cum}$ ), and b) polydispersity index ( $PDI$ ). The 50 ml P25 suspensions of 1 g/l were dispersed either by a magnetic stirrer (-US) or by the Topas ultrasonic processor (52 W, 4 min) (+US). The stability test was performed with/without methylene blue (+MB/-MB) in ambient conditions.

In reality, few hours after the dispersion, a sedimentation of the conventionally mixed P25 samples was visible to the naked eye. On the contrary, no sedimentation of ultrasonic-dispersed samples was observed. As mentioned early in this subchapter, sedimentation can induce problems during the operation of the industrial flow reactor. Also the harsh working conditions (such as the appearance of different chemicals, electrolytes, salts, intermediates or (by-) products of real water) can intensify the sedimentation. Regularly, the fluid must be well mixed which requires a high pumping energy [19]. In this subchapter, ultrasonic dispersion was proposed as an alternative.

In this study, most suspensions have P25 concentrations of 0.1–0.3 g/l and pH of around 5.5–6.0 corresponding to zeta potential of 5–12 mV [233]. A concept of ultrasonic dispersion to avoid the instability of the suspension is necessary. Due to the working conditions, a short dispersion of 0.5–1 min by the Hielscher disperser with the energy of 10–30 W was used, otherwise size was characterized for controlling or at least experiments were always repeated to check the reproducibility. Exceptionally, experiments to examine the impact of ultrasonic dispersion on photocatalytic activity were done with the Topas processor.

## 5.2 OPTICAL PROPERTIES

In this study, P25 was used as a photocatalyst for the color removal of dye substances under illumination. Optical properties are, thus, one of the most significant concerns. In such a heterogeneous system, light can be absorbed, scattered, or emitted. Typically, photocatalysis is

performed at ambient temperature, i.e. room temperature under artificial illumination, or outside temperature under sunlight, thus radiation emission is negligible. The photon energy of absorbed light or elastic scattering light activates the photocatalysts. Bandgap energy corresponding to the absorbed wavelength were determined by a diffuse reflectance UV-VIS spectrometer [199], [221]. Unused light penetrating was measured by a conventional UV-VIS spectrometer [183], [217]. Turbidity, as well as extinction coefficient, were accessed by using the Beer-Lambert law within the validity range.

### 5.2.1 Bandgap energy

By a diffuse reflectance UV-VIS spectrometer, the reflectance of the photocatalyst powder was measured (Figure 5.6a). The Kubelka-Munk function  $F(R)$  was converted (Eq. (4.5), section 4.3.2). The modified Kubelka-Munk function  $[F(R) \times h\nu]^{1/n}$  can be used to determine the bandgap energy of the semiconductor (Eq. (4.7), section 4.3.2). For P25, it is suggested that  $n = 2$  (the indirect allowed transition) [199]. The function  $[F(R) \times h\nu]^{1/2}$  was plotted as the function of energy (Figure 5.6b). The bandgap energy was found to be 3.1 eV (Figure 5.6b) and is in agreement with other works, where P25 was reported to have the bandgap of 2.98–3.37 eV [66], [198]–[200]. Correspondingly, radiations with the wavelength of shorter than 400 nm can activate P25.

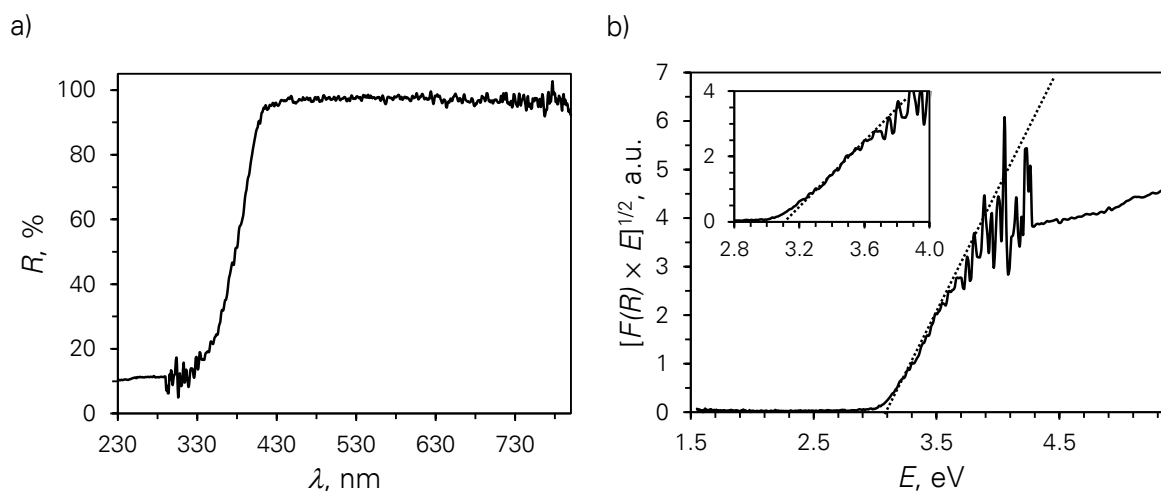


Figure 5.6 Diffuse reflectance UV-VIS spectroscopy of P25: a) The reflectance spectra, and b) The modified Kubelka-Munk function.

### 5.2.2 Scattering

By means of diffuse reflectance UV-VIS spectroscopy (the previous section), the Kubelka-Munk function  $F(R)$  which is the ratio of absorption coefficient  $\kappa$  to scattering coefficient  $\sigma$  [222] can be determined. For P25 powder this value at the wavelength of 365 nm is 0.6. The data were compared with other researches [200], [233]. Accordingly, the interpreted value  $\kappa$  over  $\sigma$  at 365 nm was found in an extensive range, from 0.25 to 1.2. Note that Kubelka-Munk function is an empirical method to determine the bandgap but not the scattering. In any event, back scattering seems to be weighty and should be taken into account when studying suspensions.

In this work, only extinction coefficient in the heterogeneous system (i.e., suspension) was determined (see the following section), but no scattering was measured. However, literature study shows that scattering is significant, while absorption is minor at 365 nm [183], [234]. The extinction coefficient  $\beta$ , the absorption coefficient  $\kappa$  and the scattering coefficient  $\sigma$  of P25 suspensions were obtained in independent measurements. These values at the wavelength of 365 nm are 5.51 cm<sup>2</sup>/g, 0.08 cm<sup>2</sup>/g and 5.41 cm<sup>2</sup>/g, respectively. Accordingly, the ratio of absorption coefficient to scattering coefficient is 1.6 %, and the absorption extinction is only 2 % of the extinction coefficient.

### 5.2.3 Transmittance, turbidity and extinction coefficient

UV-VIS absorption spectroscopy of P25 suspensions is shown in Figure 5.7a. There is difference among spectra of different samples at any wavelength. It is because particles absorb or scatter light.

In the visible range, as already discussed in the previous section, P25 particles do not absorb light. Here, only scattering happens as the result of interaction between visible light and aggregates of hundreds nm. It was claimed that the scattering intensity  $I_{\text{sca}}$  of a dilute aggregate suspension system is proportional to the volume concentration  $C_v$  of particles [235]

$$I_{\text{sca}} \propto C_v q^{-d_f} \propto C_v \lambda^{-d_f} \quad (5.2)$$

where  $d_f$  is the fractal dimension of the aggregates,  $q$  is the scattering factor, and  $\lambda$  is the wavelength. Experimentally, the transmittance decreases with the increased mass concentration of the photocatalyst. The high turbidity of the suspensions of higher than 0.5 g/l even caused the complete extinguishment of visible light through a 10 mm optical pathlength.

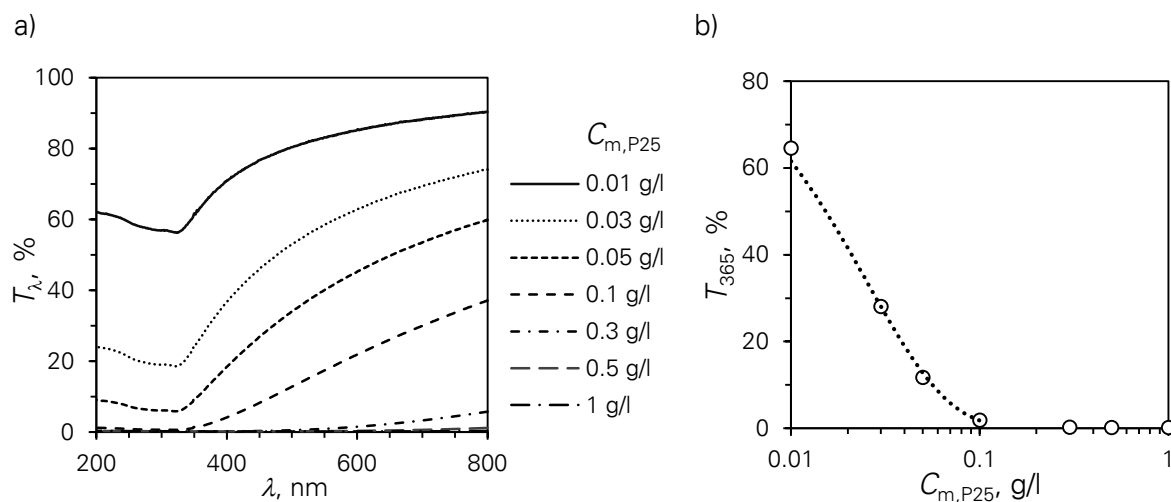


Figure 5.7 UV-VIS absorption spectroscopy of P25 suspensions: a) Transmittance spectra; and b) Transmittance at the wavelength of 365 nm. Seven particle concentrations of 0.01–1 g/l were used. Transmittances were measured with the 10 mm optical pathlength cuvette.

For each sample, the transmittance in the UV range is significantly lower than that in the visible range. Take a comparison of the 0.01 g/l and 0.03 g/l samples as an example. The gap between two curves within the entire visible range is rather constant. The slightly wider gap in the UV can be affiliated to the light absorption of the photocatalyst. The data are in agreement with literature, where P25 were proved to absorb the photon energy of light shorter than 416–368 nm (corresponding to 2.98–3.37 eV) [66], [198]–[200]. The lowest transmittance is observed at approx. 320 nm which agrees with the data obtained by the diffuse reflectance spectroscopy in this work (Figure 5.6a). The impact of the wavelength lower than 320 nm on the transmittance spectra is weak, which is dissimilar with Eq. (5.2). It was caused by the domination of absorption over scattering.

Figure 5.7b shows the transmittance at 365 nm, which is the mode wavelength of the used UV lamp in the photocatalytic experiments [187]. Data well fit with the Beer-Lambert law (Eq. (2.19)) indicated by the curve when the transmittance is, not surprisingly, higher than a threshold. Due to the lower limitation of the used UV-VIS spectrometer, the very low transmittance was not distinguished. A critical value of transmittance, thus, should be defined.

To determine the validity range, extinction coefficient of total 21 runs was computed at certain wavelengths. Theoretically, extinction coefficient depends only on the properties of material, thus are identical irrespective of either particle concentration or optical pathlength. Experimental data are shown in Figure 5.8.

When the transmittance is high enough, as shown in the right side of the figure, extinction coefficients slightly fluctuate; whereas data are significantly scattered when the transmittance is small, shown in the left side. Table 5.1 shows the average extinction coefficients  $\beta_\lambda \pm \Delta\beta_\lambda$  when the lower limitation of transmittance was set from 0.001–10 %.

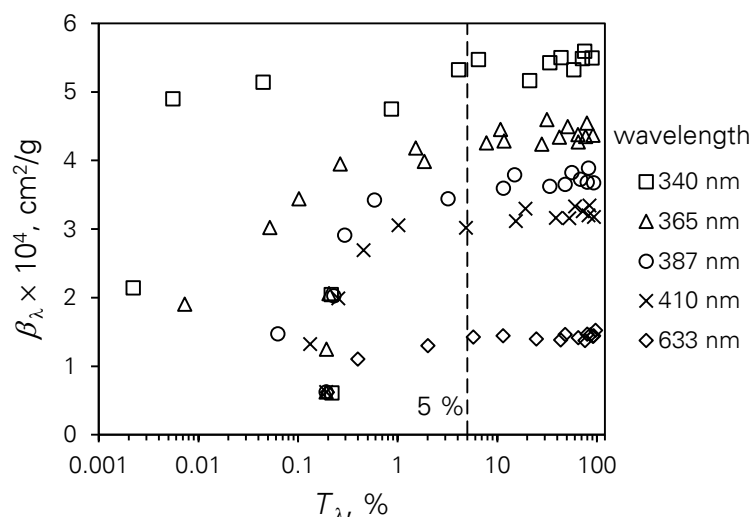


Figure 5.8 UV-VIS absorption spectroscopy of P25 suspensions (cont.): Lower limitation of transmittance. Seven particle concentrations of 0.01–1 g/l were used. Transmittances were measured with the 2, 5 and 10 mm optical pathlength cuvettes. Extinction coefficient was computed at five wavelengths: 340, 365, 387, 410 and 633 nm.

It can be noticed that data have high precision with  $T_\lambda \geq 1\text{--}10\%$ , shown by  $\Delta\beta_\lambda = 3\text{--}7\%$ . Deviations are usually larger than 20 % with  $T_\lambda \geq 0.001\text{--}0.1\%$ . It also means that 1–10 % can be reasonably chosen as the critical value. Considering data shown in Figure 5.8, this work fixed the lower transmittance limitation of 5 % for further computations.

To investigate the nature of P25 photocatalyst, extinction coefficient needs to be determined. Since the extinction coefficient is a constant at a given wavelength, transmittance for each particle concentration must be an exponential function of optical pathlength (Eq. (4.1), section 4.3.1). Data are presented in Figure 5.9a. Seven particle concentrations of 0.01–1 g/l were used, however, the transmittances of 0.5 g/l and 1 g/l samples are lower than the critical threshold (5 %) thus not shown. Figure 5.9b shows the relation between turbidity and particle concentration. Extinction coefficient was found to be  $4.28 \times 10^4 \text{ cm}^2/\text{g}$  (Eq. (4.2)). The high coefficient of determination ( $R^2 > 0.999$ ) affirms the accuracy of the values computed by means of the Beer-Lambert law.

Table 5.1 UV-VIS absorption spectroscopy of P25 suspensions: Lower limitation of transmittance. Extinction coefficient of P25 suspensions  $\beta_\lambda \pm \Delta\beta_\lambda$  at wavelength  $\lambda$  were computed with varied critical threshold.

critical thresh- old	$\lambda$ nm	$\beta_\lambda \times 10^4$ cm <sup>2</sup> /g	$\Delta\beta_\lambda \times 10^4$		critical thresh- old	$\lambda$ nm	$\beta_\lambda \times 10^4$ cm <sup>2</sup> /g	$\Delta\beta_\lambda \times 10^4$	
			cm <sup>2</sup> /g	-				cm <sup>2</sup> /g	-
0.001%	340	4.54	1.09	24%	1%	340	5.42	0.21	4%
	365	3.67	0.93	25%		365	4.34	0.26	6%
	387	3.14	0.78	25%		387	3.69	0.23	6%
	410	2.77	0.63	23%		410	3.20	0.21	6%
	633	1.36	0.17	12%		633	1.43	0.10	7%
0.01%	340	4.67	0.96	20%	5%	340	5.43	0.20	4%
	365	3.76	0.84	22%		365	4.38	0.22	5%
	387	3.14	0.78	25%		387	3.72	0.20	5%
	410	2.77	0.63	23%		410	3.23	0.17	5%
	633	1.36	0.17	12%		633	1.44	0.09	6%
0.1%	340	4.64	0.98	21%	10%	340	5.44	0.18	3%
	365	3.79	0.81	21%		365	4.39	0.21	5%
	387	3.22	0.70	22%		387	3.72	0.20	5%
	410	2.77	0.63	23%		410	3.23	0.17	5%
	633	1.36	0.17	12%		633	1.44	0.09	6%

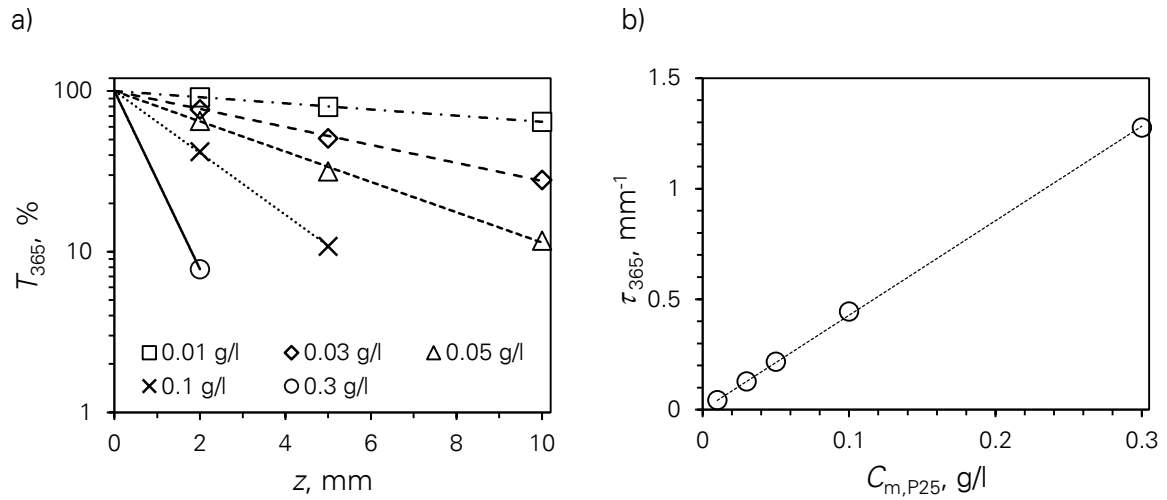


Figure 5.9 UV-VIS absorption spectroscopy of P25 suspensions (cont.): Turbidity. a) Transmittance  $T$  vs. optical pathlength  $z$ ; and b) Turbidity  $\tau$  vs. particle concentration  $C_m$ . Five particle concentrations of 0.01–0.3 g/l were used. Samples were measured with the 2, 5 and 10 mm optical pathlength cuvettes. Data at the wavelength of 365 nm were inspected.

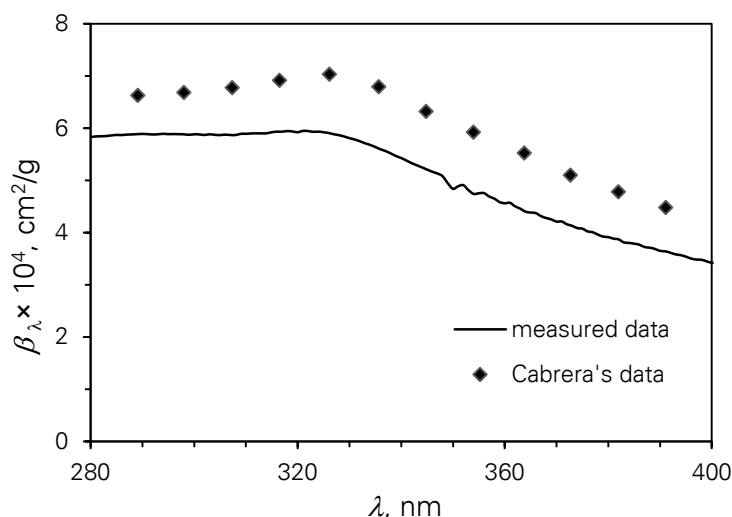


Figure 5.10 Extinction coefficient of P25 suspensions. The data determined in this study ("measured data") were compared with the works of Cabrera *et al.* [183].

The extinction coefficients at other wavelengths were compared with the work of Cabrera *et al.* [183] (Figure 5.10). It is shown that the measured values are lower than those of the reference study. Note that in the reference data, the primary particle size determined by SEM is 30–90 nm, while the secondary particle size measured by laser light scattering instrument is 700 nm. In this study, the primary and secondary particle sizes are  $25 \pm 3$  nm [166] and  $382 \pm 12$  nm (section 5.1.1), respectively. The bigger sizes certainly affect the extinction coefficient of the suspension. This topic is discussed in the following section. Additionally, Cabrera *et al.* assumed the aggregates as spherical particles that do not reflect the nature of pyrogenic P25 [197]. Such nanopowder is, indeed, fractal [79], [227], [228], and scattered light may internally diffuse within the aggregate structure. Also the use of an integration for the UV-VIS spectrometer to minimize the amount of in- and out- scattering might contribute to the difference of the compared data.

## 5.2.4 Influence of aggregate size

Results in this section was previously published [186].

Generally, the gross photocatalyst may experience an internal light diffusion within the aggregate structure. This section discusses if the aggregated state of the P25 photocatalyst impacts the optical properties. Ultrasonic dispersion was used to vary the P25 aggregates. The intensity-weighted harmonic mean size  $x_{\text{cum}}$  measured by dynamic light scattering characterizes the aggregate size. It is a physical parameter which reflects the optical property of the photocatalyst measured by means of the dynamic light scattering (section 4.3.3). As a P25 entity is in an aggregated state, and certainly not spherical (Figure 5.1), the value  $x_{\text{cum}}$  is actually an equivalent diameter and it differs from the diameter of the primary particle.

Figure 5.11 shows the influence of aggregate size of 234–343 nm on the optical properties.

In the visible range, no change of transmittance is observed, while there is a dissimilarity of data in the UV range (Figure 5.11a). Note that, light can be either scattered or absorbed by the UV light, but there is no absorption in the visible range (of which photon energy is smaller than the bandgap energy of the photocatalyst). Therefore, the change of the data in the UV range can be attributed to light absorption. The extinction coefficient (Figure 5.11b) shows the obvious change of the optical property. In the visible range (exampled at the wavelength of 633 nm), the extinction coefficient remains constant. In the UV range (data at 365 nm were compared), extinction coefficient increases with the decreased photocatalyst size. A decrease of transmittance by 15 % and 20 % corresponding to an increase of extinction coefficient by 34 % and 49 % was observed, respectively. This can be achieved by dispersing with 60 and 385 J/ml ultrasonic energy. As expected, the result indicates a more efficient use of light by the finer aggregates of the photocatalyst. The effect on the photocatalytic activity is discussed in subchapter 6.4.6.

On the other hand, without ultrasonic dispersion, to increase the turbidity of suspension by 50 %, an increase of particle concentration by the same factor (Eq. (4.2)) is required. Here, ultrasonic dispersion can be the substitution. It results in material saving. Consequently, energy for loading materials as well as operation cost of the post-treatment can be saved.

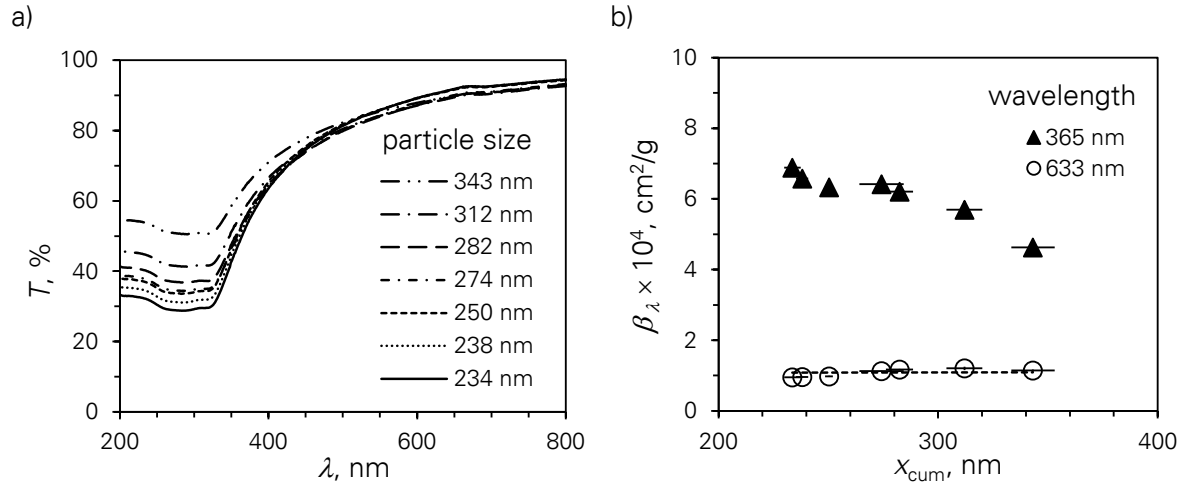


Figure 5.11 Influence of P25 particle size on the optical properties : a) the transmittance spectra, and b) the turbidity at the wavelengths of 633 nm and 365 nm.

### 5.3 CONCLUDING REMARKS

SEM shows that the P25 particles have the primary size of  $25 \pm 3$  nm. By dynamic light scattering analysis, it was confirmed that fractal-like P25 experiences aggregation of sub-microns. It is possible to disintegrate P25 aggregates by ultrasonic dispersion, however, the aggregate size  $x_{cum}$  smaller than 200 nm is impractical as it requires too high ultrasonic energy. The polydispersity index *PDI* of 0.2 shows that the homogeneity of the aggregate size can be improved by ultrasonication. During the dispersion, the decrease of  $x_{cum}$  and *PDI* along with the energy density follows the power law, which is in agreement with the energy concept. Though the studied volume is only at laboratory scale, but the validity for the maximum volume of 1.8 l suggests that the concept can be applied at pilot scale.

Depending on the concentration of the particle, pH can be changed and affect the stability of the suspension. In this work, the 1 g/l dispersed suspension in the presence of methylene blue was stable during 3 days. The suspension of finer aggregate without methylene blue was stable within 4 weeks, which is meaningful for further application in reality. Also the fine aggregates show no sedimentation during hours.

The optical properties of photocatalyst particles were studied. By diffuse reflectance UV-VIS spectroscopy, the bandgap energy of used P25 was found to be 3.1 eV, corresponding to the wavelength of 400 nm. It means that when using the artificial UV light with the wavelength of 340–410 nm (section 3.1.4), it is expected that photocatalytic reaction happens. Additionally, the back scattering of the materials is significant, shown by the Kubelka-Munk function, which is the ratio between the absorption coefficient and the scattering coefficient. By a UV-VIS spectrometer, one of the most common laboratory instruments, the interaction of particles and UV light was investigated. When the transmittance is higher than the critical threshold of 5 %, the Beer-Lambert law is well applied. Transmittance as well as extinction coefficient were discussed in parallel. At the low concentration of particles (hundreds mg/l), UV can effectively penetrate, thus make utilization of the catalyst. However, for the concentrations of few g/l, light penetration is restricted. It suggests an upper limitation of photocatalyst concentration. Depending on the optical pathlength, one should choose an optimal particle concentration so that catalysts can effectively absorb light.

Optical properties and the degree of aggregation are intrinsically coupled. Due to the specifications of the experimental setup, transmittance at 365 nm was studied. Experimentally, the transmitted light through fine photocatalyst suspensions of the same optical pathlength diminishes. It suggests that the finer aggregates of fractal-like photocatalysts more efficiently absorb UV light and consequently, induce a better photocatalytic activity.

## 6 COLOR REMOVAL OF METHYLENE BLUE IN THE DESIGNED PHOTOCATALYTIC SETUP

The photocatalytic activity of  $\text{TiO}_2$  P25 photocatalyst introduced in chapter 5 is here presented. This chapter shows the investigation of photocatalytic degradation of methylene blue (MB), a model dye substance, under UV illumination.

The first subchapter presents the process conditions of the experiments, which satisfy the assumptions used for the reactor model. Secondly, the preliminary tests, including the control tests and one photodegradation, are introduced to examine the presence of the photocatalytic reaction in experiments. Afterwards, the verification of the reactor model is presented. The use of the established kinetics is then discussed. Pros and cons are showed. In subchapter 6.4, the influences of different process conditions on the photocatalysis are presented, including the suspension volume, the light intensity, the photocatalyst concentration, the optical penetration, the initial concentration of the organic compound, and the pH of the suspension. The last section shows the investigation of the influence of the photocatalyst size modified by ultrasonic dispersion on the photocatalytic activity of P25. It is also the closing for scientific findings of chapter 6.

### 6.1 PROCESS CONDITIONS

In this subchapter, the experimental conditions, which are related to the assumptions in subchapter 3.3.1, are discussed.

The concentration of the photocatalyst as well as of the dye substance decide the period which is needed to achieve the adsorption-desorption equilibrium. Prior to the photocatalytic tests under UV illumination, a 30 min and 90 min mixing in the dark for low (9–13  $\mu\text{M}$ ) and high (25–125  $\mu\text{M}$ ) concentrations of methylene blue (MB) was carried out, respectively. This step is sufficient to achieve the adsorption-desorption equilibrium [25]. The adsorption of MB on P25 is thus considerably equilibrated and the reaction is the rate-determining step of the heterogeneous reaction.

During the reaction under illumination, the emission of electrons is negligible [102], [184]. The electron-hole recombination is dominated by the formation [39], [41], [89]–[93], thus the exothermal heat is insignificant. The increase of the temperature of the suspension is mainly because of the heat emitted from the artificial UV lamp. In the experiments, the temperature increased by 2–3 °C (from 21 to 24 °C) after 30 min under illumination. The reaction is considered as an isothermal process.

It was claimed that when photocatalyst concentration is lower than 1 g/l and a good mixing is operated (in particular, Reynolds number is higher than 1700), mass transfer restrictions are non-existent [97], [184]. Except the study on the photocatalyst concentration, in the other

experiments, the mass concentration of photocatalyst was intentionally kept minimum. It also helps to reduce the inactivation of the catalyst in such short UV penetration systems [184]. In this study, the experimental performances were done with three different flow cells of the same reactor prototype (section 3.1.3). Reynolds number was found to be 1356–1770 (section 3.1.5). However due to the structural geometry of the reactor, eddies are obvious especially with the in- and out-flows and in the corners of channels (Figure 3.7). As the result of the quasi turbulence, mass transfer limitations can be excluded. Additionally, the strong mixing effect in the reactors can mitigate the accumulation of catalyst at the window of the reactor.

As the lifetime of radicals is few nano-seconds, they persist only under illumination. Only the flow cell was exposed to the UV light, whereas the other parts of the setup were covered by aluminum foil to avoid the interference with illumination. Therefore, the reaction occurs only in the reactor.

During 30–180 min photocatalytic reaction (depending on the initial concentrations of MB), 1.4 ml samples were collected at regular time intervals for analysis. The total withdrawn volume of nine samples is 12.6 ml. Of the total suspension volume, the change of 1–2 % during the reaction was assumed to have no effect on the photocatalytic process.

## 6.2 PRELIMINARY TESTS

The photosensitization of methylene blue (MB) under UV illumination (control test C1) and the adsorption of MB in the photocatalytic system after equilibrium (control test C2) were tested.

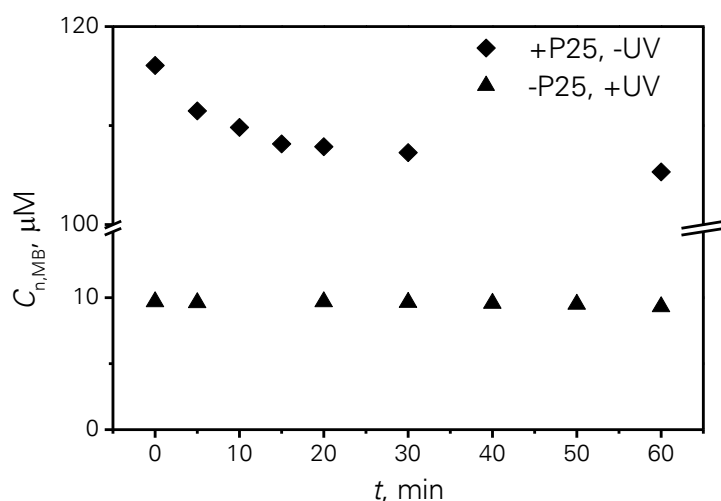


Figure 6.1 Control tests of the photodegradation of methylene blue (MB). Sample “-P25, +UV”: control test of 11 μM MB in the absence of P25 in a beaker under UV illumination. Sample “+P25, -UV”: control test of 124 μM MB in the presence of 1 g/l P25 in reactor R10 in the dark.

In the control test C1, 11  $\mu\text{M}$  MB solution was exposed to the UV light in the absence of photocatalyst. In this test, the mode wavelength of the UV lamp is 365 nm (section 3.1.4). At this wavelength, there is no interaction between MB and the electromagnetic radiation (Figure 4.1). For this reason, in the control test C1, the concentration of MB remained unchanged during the test (Figure 6.1, series “-P25, +UV”).

The second control test was conducted in the presence of P25 in the dark. The high concentrations of MB (124  $\mu\text{M}$ ) and P25 photocatalyst (1 g/l) were used to test the effect of adsorption. Prior to the reaction, the suspension was kept under stirring in a beaker in the dark for 90 min to achieve an equilibrium. After that, the suspension was loaded into the reactor, but no light was illuminated. As explained in subchapter 3.2, MB may be adsorbed on the inner walls of the reactor and other components of the setup. Additionally, due to the strong mixing in the setup (which is dissimilar to that in the beaker), the adsorption of MB on the P25 surface more or less depends on the tendency at which pH increases or decreases. In this study, the adsorption of MB on the walls of the setup is ignored and the influence of flow regime is not considered. Further study on the impact of pH is discussed in section 6.4.5. Experimentally, in the control test C2, the concentrations of MB slightly decreases (Figure 6.1, series “+P25, -UV”). After 30 min, the color was removed by 8 %. In the next 30 min, the color was removed by 1 %. The extension of time to 120 min caused a total loss of 10 % (not shown in the figure). It proves that even with a high concentration of MB, less than 10 % MB was adsorbed on P25 after the equilibrium prior to the test, and adsorption during the run in the photocatalytic setup is negligible.

The additional test was done in the presence of P25 under UV illumination. As P25 used here has the bandgap of 3.1 eV corresponding to 400 nm (section 5.2.1), it was expected to show the photocatalytic activity under the UV illumination of 340–410 nm of the UV lamp. The UV-VIS spectra of MB samples in the presence of P25 and at different times of UV irradiation are shown in Figure 6.2. The decrease of the characteristic absorption peaks of MB (at 664 nm) along with the reaction time shows that the photodegradation of the dye occurred. The degradation is caused by neither photosensitization nor adsorption (proved by the control tests), but it is truly attributed to the photocatalytic activity of P25 under UV illumination. In addition to the decrease of absorption intensity, the peak shift from 664 nm to 640 nm is observed in the UV-VIS spectra. This blue shift [143] is caused by the degradation of MB to new molecules [25], [236].

In the experiment, the volume of the suspension was a bit high (1 liter) compared to other laboratory-scaled experiments as well as other photocatalytic assays in this thesis. The discoloration is slow (which is discussed in section 6.4.1). However, after 60 min reaction, MB was bleached by 92 % showing that the reactor, in these working conditions, can practically decompose MB.

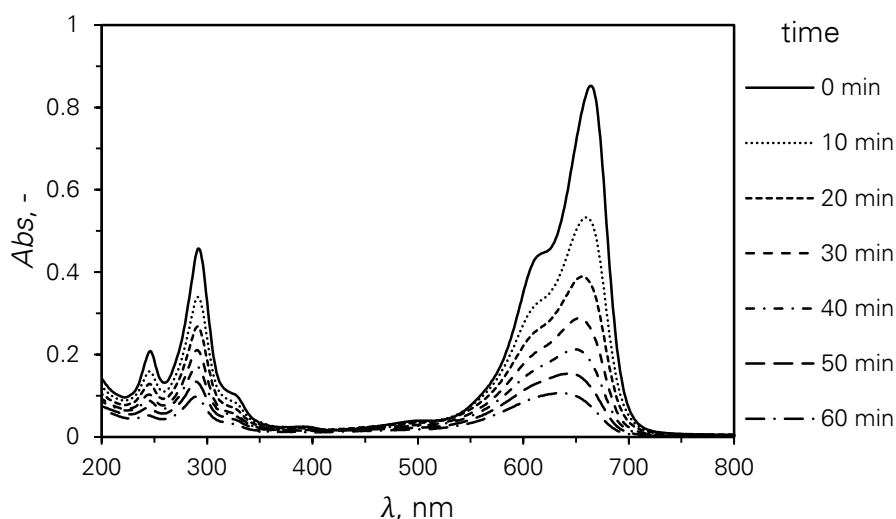


Figure 6.2 Typical UV-VIS spectra of the photodegradation of methylene blue (MB) at different experiment times. The color removal of 1 l MB solution of 11  $\mu\text{M}$  with 0.3 g/l P25 was performed in reactor R20 under UV illumination (the average intensity on the illuminated surface was 19  $\text{W}/\text{m}^2$ ).

### 6.3 USES OF THE REACTOR MODEL

To quantify the photocatalytic reaction, a reactor model is crucial. According to the reactor model introduced in subchapter 3.3, the apparent degradation rate constant in the entire photocatalytic setup  $K$  can be determined from the experimental data as Eq. (3.28) and the (integrated) photocatalytic reaction rate constant in the flow reactor  $k$  can be calculated as Eq. (3.29).

The verification of the reactor model with experimental data is introduced in this subchapter. The uses of the model is then discussed. Pros and cons are evaluated at the end.

#### 6.3.1 Verification of the model

The reactor model is validated by experiments with varied suspension volume while keeping the other influential parameters unchanged, e.g., light intensity, flow condition, the concentration of the photocatalyst, the initial concentration of methylene blue (MB). When varying the volume of reactant suspensions in experiments but using the same photocatalytic setup, only suspension volume in the mixing tank  $V_M$  was varied, whereas the suspension volumes in the flow reactor  $V_R$  and in the tubes  $V_T$  maintained constant. In essence, the increase of this unilluminated space in the photocatalytic setup  $V_2$  lowers the apparent degradation rate constant  $K$  in the entire system. On the contrary, as the process conditions in the flow reactor were fixed, an increase of the suspension volume in the mixing tank  $V_M$  has no contribution to the reaction. The integrated photocatalytic reaction rate constant  $k$  in the flow reactor is expected to remain unchanged.

Experiments were done with a set of five different suspension volumes. The decays of MB were observed during the reaction (Figure 6.3). With the smallest amount of suspension (600 ml), 90 % color was removed after 30 min. Experiments with the increased volume of 800 and 1000 ml required the longer reaction time of 40 and 60 min to achieve the same removal efficiency, respectively. For the high volume of 1400 and 2400 ml, the color bleaching of 40 % and 20 % were obtained after 60 min. It shows that the increase of reactant volume lowered the degradation of the entire setup.

In any event of the suspension volume, the conversions of MB are an exponential function of time, which are in agreement with the reactor model (Eq. (3.28)):

$$C_{n,MB} = C_{n,MB,ini} e^{-(0.016 \rightarrow 0.075)t} \quad (6.1)$$

The coefficients of determination of higher than 0.98 support the validity of exponential decay and thus of the first order kinetics. The values  $K = 0.016\text{--}0.075 \text{ min}^{-1}$  quantify the reaction rate in the entire photocatalytic setup. High values obtained with the small suspension volumes mean a rapid degradation, and inversely. The value can be also initiated to find the required duration  $t_\eta$  to achieve a desired color removal efficiency ( $\eta$ )

$$t_\eta = \frac{-\ln(1-\eta)}{K} \quad (6.2)$$

In experiments, the required time to acquire the 90 % color removal are  $t_\eta = 143\text{--}30 \text{ min}$ , corresponding to  $K = 0.016\text{--}0.075 \text{ min}^{-1}$ .

To determine the reaction rate constant in the flow reactor  $k$ , Eq. (3.29) was used. Though the irradiance in the experiments was kept unchanged, in reality it slightly fluctuated. To exclude the influence of light as well as to compare with data from other works, the constants  $K_{I25}$  and

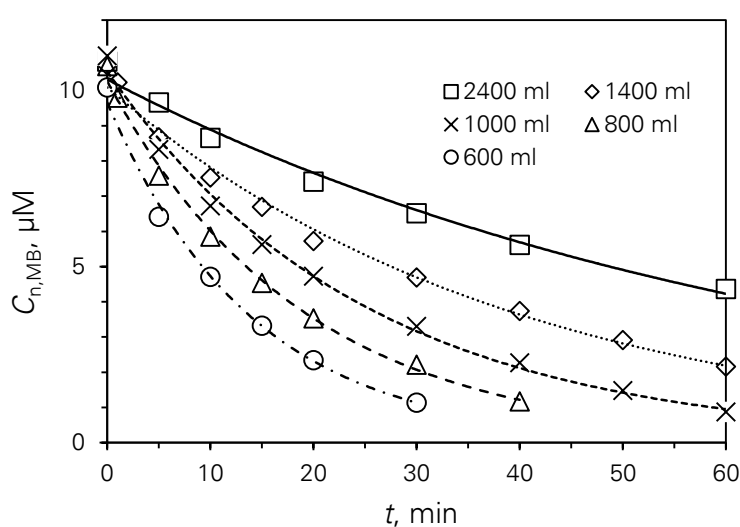


Figure 6.3 Photocatalytic degradation of methylene blue (MB): Color removal of 600–2400 ml MB solution of 10–11  $\mu\text{M}$  with 0.3 g/l P25 in reactor R20 under UV illumination (the average intensity on the illuminated surface was 18–21  $\text{W/m}^2$ ). Curves show the exponential fits.

$k_{125}$  were normalized (which are discussed in section 6.4.2). The data are shown in Figure 6.4. As predicted, the integrated reaction rate constant  $k$  deviates within the upper and lower bands (Figure 6.4) and yields an average value of  $0.120 \pm 0.009 \text{ min}^{-1}$ . This result supports the hypothesis of the model. The reactor model can eventually be used for further studies with the designed setup.

### 6.3.1 Further discussion

#### Deviation of the reactor model

In heterogeneous photocatalysis, adsorption constant is an important parameter which affects the reactor model (Eq. (3.28), section 3.3.2).

In this study, suspensions of  $\text{TiO}_2$  P25 and methylene blue (MB) were tested. To determine the adsorption constant, the change of the adsorption of MB on P25 in the dark should be studied [25]. In reality, MB concentration was analyzed by a UV-VIS spectrophotometer. The presence of P25 particles induces the scattering thus P25 must be separated from the collected suspensions. The separation with different syringe filters was tested, of which membranes are made of cellulose acetate (CA) (VWR and Rotilabo® syringe filters), nylon, polyvinylidene difluoride (PVDF) or regenerated cellulose (RC) (Rotilabo® syringe filters). However, there is a loss of 33–98 % of MB after filtering. It means that the use of these membranes is not suitable. Instead, a centrifuge was employed (section 4.4.1). To obtain the complete sedimentation of P25, a duration of 40 min was required. Unfortunately, this period is long enough

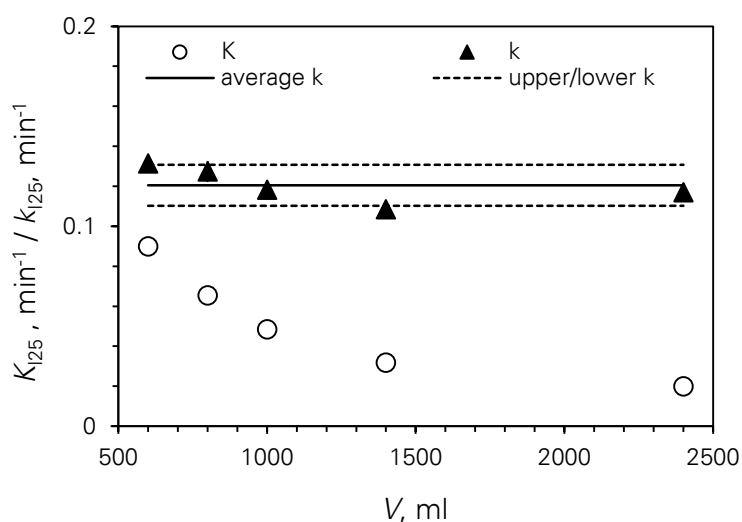


Figure 6.4 Reaction rate constants of photodegradation of methylene blue (MB): Color removal of 600–2400 ml MB solution of 10–11  $\mu\text{M}$  with 0.3 g/l P25 in reactor R20 under UV illumination (the average intensity on the illuminated surface was 18–21  $\text{W/m}^2$ ). The apparent reaction rate constants in the photocatalytic setup  $K_{125}$ , and the integrated reaction rate constants in the flow reactor  $k_{125}$  vs. the suspension volume  $V$ . Lines show the linear fit of  $k_{125}$  together with the 95 % confidence interval bands.

to achieve the equilibrium. Practically, adsorption of MB on P25 can be studied but it requires an alternative separation method or analysis procedure. Here, adsorption was not studied, and consequently, adsorption constant was not determined.

In this section, the adsorption constant of  $6.25 \times 10^3 \text{ M}^{-1}$  reported in the literature [25] is used for a brief estimation. The reactor model (Eq. (3.28), section 3.3.3) can be solved with the shortened form (Eq. (3.24)). It is the particular case of assuming  $K_{\text{ads}} C_{\text{n,MB}} \ll 1$ , where  $K_{\text{ads}}$  is the adsorption constant, and  $C_{\text{n,MB}}$  is the molar concentration of MB taken from the mixing tank. To ensure the assumption,  $K_{\text{ads}} C_{\text{n,MB}}$  should be lower than 1 % (or at least, 10 %). As a result, MB concentration should be lower than 1.6  $\mu\text{M}$  (or at least, 16  $\mu\text{M}$ ). However, in this study, the initial concentrations of MB were 10–123  $\mu\text{M}$ . It means that the assumption is limited and the shortened form has a restriction. Instead, the full form of Eq. (3.18) should be used. The reaction rate constant  $k$  is a total amount of two values

$$k = k_1 + k_2, \quad (6.3)$$

where

$$k_1 = -\frac{1}{t_R} \ln \frac{C_1(t)}{C_0(t - t_R)}, \quad (6.4)$$

and

$$k_2 = -\frac{1}{t_R} K_{\text{ads}} [C_1(t) - C_0(t - t_R)]. \quad (6.5)$$

Accordingly, the reaction rate constant is determined as the sum of one exponential function (Eq. (6.4)) and one linear function (Eq. (6.5)). The gain by the amount  $k_2$ , eventually, makes the apparent degradation in reality faster than in the shortened form. It explains that the raw experimental data in the early stage of the photocatalytic test are usually lower than the exponential fits (Figure 6.3). Even though, the exponential relation works (Figure 6.3) and the simplification of the model as Eq. (3.28) and Eq. (3.29) is applicable for the evaluation of the photocatalytic test.

#### Other limitation of the reactor model

When using the simple reactor model, another point should be noted. The model is established for the “disappearance” of the original organic compound. The influence of the intermediates and (by) products was not considered. In reality, the produced intermediates or (by) products occupy the photocatalyst coverage and cause the decrease of the amount of active centers on the photocatalyst surface. Depending on the interaction between these species and the photocatalyst surface, the value  $K_{\text{ads}}$  is not constant but varied during the reaction, thus makes the assumption fail. This fact is discussed in section 6.4.4.

### Lower limitation of the methylene blue concentration in photocatalytic tests

The concentration of MB in photocatalytic tests were measured by means of UV-VIS spectroscopy. When the absorbance peak is lower than approx. 0.05, the sensitivity of the reactor is low and it affects the accuracy of the data. Additionally, the conversion of MB concentrations follows an exponential function. As the characteristic of the function, the curve is asymptotic when the reaction time becomes infinite (which is impractical). The concentration should be, thus, higher than a critical value to assure the regression.

Figure 6.5 shows an example of one photocatalytic test. Basically, the degradation obeys an exponential function. Thus, the plot in the logarithmic scale should express a linearity. The data were plot with different reaction time of 20–60 min, corresponding to the final concentration of 0.87–0.15  $\mu\text{M}$ . When the MB concentration is very low (e.g., from 30 min onwards), the plots are deviated from the data (Table 6.1). In this work, the lower limitation corresponding to  $C_n/C_{n,\text{ini}}$  of 5 % was chosen as the critical value.

### “End” of a photocatalytic test

For different study purposes, experiments were performed with the variation of operational parameters leading to a wide range of results. With fast reactions, the value  $C_n/C_{n,\text{ini}}$  reached 5 % after a short duration of 30–40 min. This lower critical value of MB concentration was chosen as the end of the test. On the contrary, slow reactions took longer. The experiments were ended after collecting 8 samples at suitable time intervals. This total number of samples are enough for exponential regressions. Additionally, the changes of total sampling volumes by less than 2 % ensure the assumption (section 3.3.1), and the time-saving is reasonable for numerous experiments.

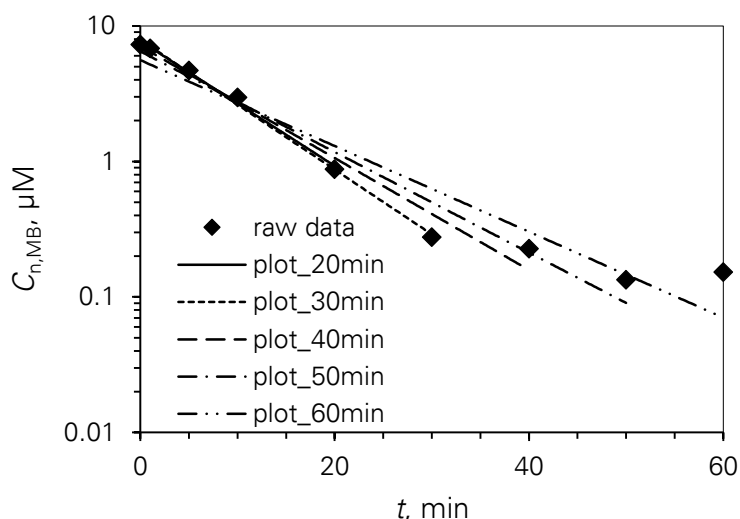


Figure 6.5 Lower limitation of the methylene blue concentration: Color removal of 600 ml MB 7.3  $\mu\text{M}$  with 0.1 g/l P25 photocatalyst in reactor R15 under UV illumination (the average intensity on the illuminated surface was 26  $\text{W}/\text{m}^2$ ). Exponential function was plotted with different reaction duration. Numerical results are shown in Table 6.1.

Table 6.1 Lower limitation of the methylene blue concentration. Graphical results were shown in Figure 6.5. Parameters of the exponential plots were computed with different ending concentrations, including the coefficient of determination  $R^2$ , the apparent reaction rate constant in the setup  $K$ . The values  $\Delta$  show the differences between the experimental and regressed data  $C_n$  and  $C_{n,comp}$ .

$t$ min	$C_n$ $\mu\text{M}$	$C_n/C_{n,ini}$ -	$C_n(t) = C_n^* e^{-Kt}$				
			$R^2$ -	$C_n^*$ $\mu\text{M}$	$K$ $\text{min}^{-1}$	$C_{n,comp}$ $\mu\text{M}$	$\Delta(C_{n,comp}-C_n)$ -
0	7.288	100%	-	-	-	-	-
1	6.820	94%	-	-	-	-	-
5	4.678	64%	-	-	-	-	-
10	2.960	41%	-	-	-	-	-
20	0.875	12%	0.994	7.714	0.106	0.926	6%
30	0.276	4%	0.997	7.869	0.110	0.290	5%
40	0.227	3%	0.975	7.087	0.095	0.159	30%
50	0.134	2%	0.966	6.479	0.086	0.088	34%
60	0.153	2%	0.925	5.583	0.073	0.070	54%

### 6.3.2 Concluding remarks

The reactor model was established based on the first order reaction of organic molecules. Experiments with methylene blue (MB) showed that the MB concentration versus reaction time approximately substantiates an exponential relation.

To ensure the accuracy of the exponential function, the use of low molar concentration of organic compound (approx.  $C_n \leq 0.01-0.1 K_{ads}$ ) is recommended. The maximum value depends on the adsorption of the organic molecules on photocatalysts in the setup and, in particular, the nature of the materials, the properties of the medium and the process parameters. However, this value is determined by the nature of the targeted water and is not an arbitrary value. Thus, the deviation of the model may happen. Here, the macroscopic reactor model suffices. With the known operating process conditions, reaction rate constants in the photocatalytic setup as well as in the flow reactor can be determined. These two non-identical values are adequate for an understanding of the photocatalytic process. Optionally, if one knows the adsorption constant and the surface coverage of the active holes/radicals, the intrinsic reaction rate constant can be also determined.

The reactor model can be used for experiments in a setup including an illuminated flow reactor combined with a non-illuminated reservoir. Such setup is popular in reality and the model has a broad range of application.

## 6.4 INFLUENTIAL PARAMETERS ON THE PHOTOCATALYTIC PERFORMANCE

In this subchapter the main factors of a photocatalytic process are discussed. The first section is related to the last subchapter, where the influence of suspension volume is presented. To activate a photocatalyst, an adequate photon energy supported by a light source is required. The second section analyzes the influence of illumination on the photodegradation of methylene blue. As the concentration of photocatalyst affects the total active surface area and decides the optical penetration, it is then discussed. Later, the initial concentration of the organic substance which influences the adsorption-desorption on the photocatalyst is introduced. Afterwards, the effects of pH, which is a property of wastewater and also an important factor of a photocatalysis, are introduced. The last section approaches the influence of the photocatalyst aggregate size.

### 6.4.1 Suspension volume

Experimental data in section 6.3.1 show the influence of the suspension volume on the apparent reaction rate constant in the photocatalytic setup. With the same reactor, a high suspension volume increased the non-illuminated space and reduced the degradation rate constant. An explicit relation can be determined from the characteristic equation (Eq. (3.27)). The first order approximation for Taylor series gives  $e^{K(t_R+t_T)-kt_R} = 1 + K(t_R + t_T) - kt_R$ . The equation can be rewritten as

$$K = \frac{kt_R}{t_M + t_R + t_T}, \text{ or } K = kV_R \frac{1}{V}. \quad (6.6)$$

When the value  $k$  is a constant (as only one reactor was used, and all process conditions were kept the same), the degradation constant is inversely proportional to the suspension volume. Figure 6.6 shows the fit of experimental data. Here, the intensity-related reaction rate constants  $K_{I25}$  and  $k_{I25}$  were computed (section 6.4.2). The slope, which is the product of the degradation constant and the inverse volume  $k_{I25} V_R$  is  $0.0516 \pm 0.0015 \text{ l}^{-1} \text{ min}^{-1}$ . As the volume of the reactor is 411 ml, the reaction rate constant in the flow reactor was  $0.126 \text{ min}^{-1}$ , which matches the value found in section 6.3.1,  $k_{I25} = 0.120 \pm 0.009 \text{ min}^{-1}$ .

The linear fit has a high coefficient of determination. It assures that the value  $k$  in the flow reactor is a constant. This calculation can be, thus, used as the second verification of the model.

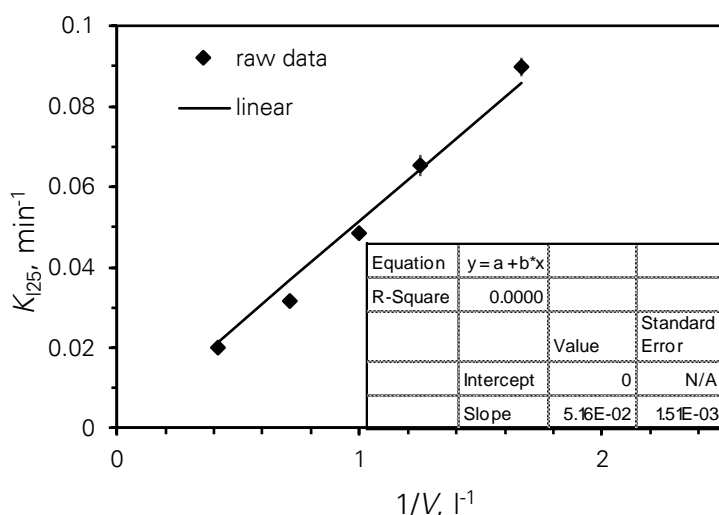


Figure 6.6 Influence of the suspension volume on the photodegradation of methylene blue (MB): Color removal of 600–2400 ml MB solution of 10–11  $\mu\text{M}$  with 0.3 g/l P25 in reactor R20 under UV illumination (the average intensity on the illuminated surface was 18–21  $\text{W}/\text{m}^2$ ). The apparent reaction rate constant in the photocatalytic setup  $K_{125}$  vs. the inverse reactant volume: raw data, and the linear fit with the 95 % confidence interval bands.

### 6.4.2 Irradiance. The intensity-related reaction rate constant

Results in this section were previously published [189].

#### Influence of the incident light

Generally, influence of intensity  $I$  on the reaction rate constant  $k$  can be written as

$$k \propto I^\alpha, \quad (6.7)$$

where  $\alpha$  is the exponent and is 1, 0.5 or 0 corresponding to  $I$  of lower than 200  $\text{W}/\text{m}^2$ , approx. 250  $\text{W}/\text{m}^2$  or higher, respectively. For an utilization of sunlight which is a cost-saving option, the average intensity is reported to be 20–30  $\text{W}/\text{m}^2$  and not exceed 55  $\text{W}/\text{m}^2$  in a sunny location [12], [26], thus  $\alpha$  should be approx. 1.

In this study, the intensity of UV light in a low range (6–20  $\text{W}/\text{m}^2$ ) was tested. As all experiment conditions were kept unchanged, the value  $K_{\text{ads}}$  and the intrinsic reaction rate constant  $k_r$  in Eq. (3.14) are constant. The (integrated) reaction rate constant in the flow reactor  $k$  is, thus, proportional to the surface coverage of the active species ( $\theta_b$ ). As the intensity is low, the formation of electron-hole dominates the recombination (section 2.3.3) and is proportional to the number of photons of incident radiation. As consequence, the integrated reaction rate constant  $k$  is a linear function of UV intensity. When associating with the condition boundary, the reaction rate constant is zero when no illumination is conducted. shows the influence of the UV intensity on the (integrated) photocatalytic reaction rate constant. The linearity was

fitted when the intercept was set to be zero. Results have a high coefficient of determination ( $R^2 = 0.998$ ) and confirm the theory. The result is also in agreement with other studies, where photocatalytic reactions in flow reactors were studied and the reaction rate constant was shown to be proportional to the UV intensity [12], [26], [89], [236]. Note that in this section, only intensity on the illuminated surface was accounted. In reality, light is attenuated along with the optical depth. The impact of optical penetration is discussed later in section 6.4.3.

### The intensity-related reaction rate constant

The finding above allows for a normalization of the experimental result  $k$  to the used intensity  $I$ . It originates the intensity-related reaction rate constant  $k_{\text{Iref}}$  corresponding to a reference intensity  $I_{\text{ref}}$  as

$$k_{\text{Iref}} = k \frac{I_{\text{ref}}}{I}. \quad (6.8)$$

The value  $k_{\text{Iref}}$  is used to exclude the influence of light intensity. The reference intensity  $I_{\text{ref}}$  can be an arbitrary value within the linear range of  $k(I)$ , i.e., lower than  $200 \text{ W/m}^2$  [39], [41], [89]–[93]. Since this study aimed at the application under solar illumination, the average UV intensity of solar light of  $25 \text{ W/m}^2$  was chosen as the reference value. For further discussion, the normalized value  $k_{25}$  is used to interpret the experimental data.

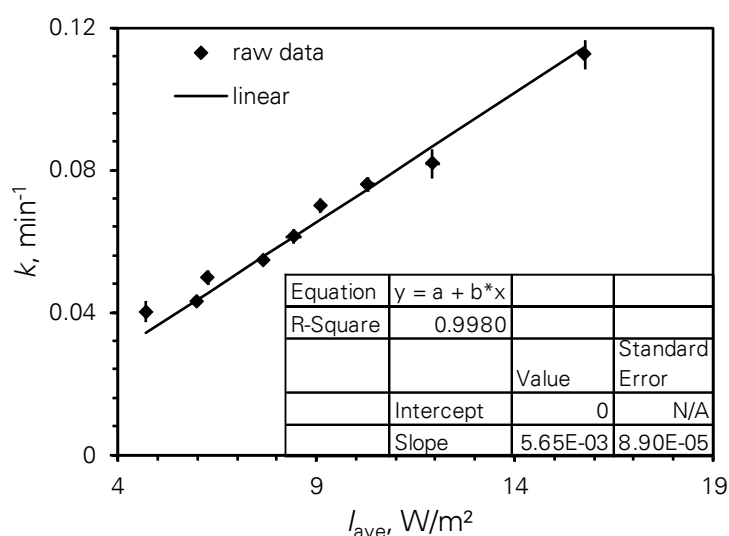


Figure 6.7 Influence of light intensity on the on the photodegradation of methylene blue (MB): Color removal of 600 ml MB solution of  $10 \mu\text{M}$  with  $0.3 \text{ g/l}$  P25 in reactor R20 under UV illumination (the average intensity on the illuminated surface  $I_{\text{ave}}$  was  $6\text{--}20 \text{ W/m}^2$ ). The reaction rate constant in the flow reactor  $k_{25}$  vs. the light intensity: raw data, and the linear fit.

### 6.4.3 Optical penetration. A modified model

In the previous section, the influence of light intensity was presented. In this section, the change of light within the bulk suspension is discussed. Due to the scattering and absorption by photocatalyst particles, light is attenuated along with the optical pathlength of the flow reactor. This optical phenomenon is also affected by the concentration and morphology of photocatalysts, i.e., size and structure. The influence of photocatalyst concentration is focused in this section, whereas the influence of photocatalyst morphology is presented later in section 6.4.6.

Color removal of methylene blue (MB) was performed in the presence of TiO<sub>2</sub> P25 photocatalyst. P25 concentration was varied in the range of 0.03–1 g/l. Optical pathlength was tested in three flow reactors (R10, R15 and R20) with different thicknesses (11, 17 and 22 mm, respectively). The shielding effect of the organic substances occurs but can be excluded, since the artificial illumination has the mode wavelength of 365 nm, at which MB molecules does not absorb light. Raw experimental data were previously reported [237].

#### Influence of photocatalyst concentration

When there is one photocatalyst particle in the system, it fully adsorbs the organic molecules. In a real photocatalyst suspension, many particles exist in the suspension and the fractional surface coverage  $\theta_{MB}$  (dimensionless) is low

$$\theta_{MB} = \frac{\Gamma_{MB}}{\Gamma_{MB,sat}} = \frac{K_{ads} C_{n,MB}}{1 + K_{ads} C_{n,MB}}, \quad (6.9)$$

where  $K_{ads}$  is the adsorption constant (m<sup>3</sup>/mol),  $C_{n,MB}$  is the molar concentration in the bulk solution (mol/m<sup>3</sup>), and  $\Gamma_{MB}$  is the surface concentration (mol/m<sup>2</sup>) of MB. The subscript “sat” denotes the saturation. The moles of MB adsorbed on the P25 photocatalyst  $n_{ads}$  (mol) is related to the mass concentration  $C_{m,P25}$  (g/m<sup>3</sup>) as

$$n_{ads} = C_{m,P25} S_{a,P25} V_{\Sigma} \theta_{MB} \Gamma_{MB,sat}, \quad (6.10)$$

where  $S_{a,P25}$  is the specific surface area (m<sup>2</sup>/g) of P25 photocatalyst and  $V_{\Sigma}$  is the total volume (m<sup>3</sup>) of the suspension. Generally, the increased photocatalyst concentration increases the number of the active sites on the suspensions. When the particle concentration is low, light penetrates and is absorbed in the whole volume of the suspension (section 5.2.3). In consequence, the integrated reaction rate constant  $k$  is expected to increase with the catalyst concentration  $C_{m,P25}$  [40], [147], [152]. To some extent, the increased mass concentration induces more dominant scattering and light phenomena become more challenging to be accessed [42], [183]. At high concentration of photocatalysts, there is the loss of photons in the system. It is caused by reflection of light out of the reactor which is related to the back scattering. Thus,  $k$  may decrease at high  $C_{m,P25}$ .

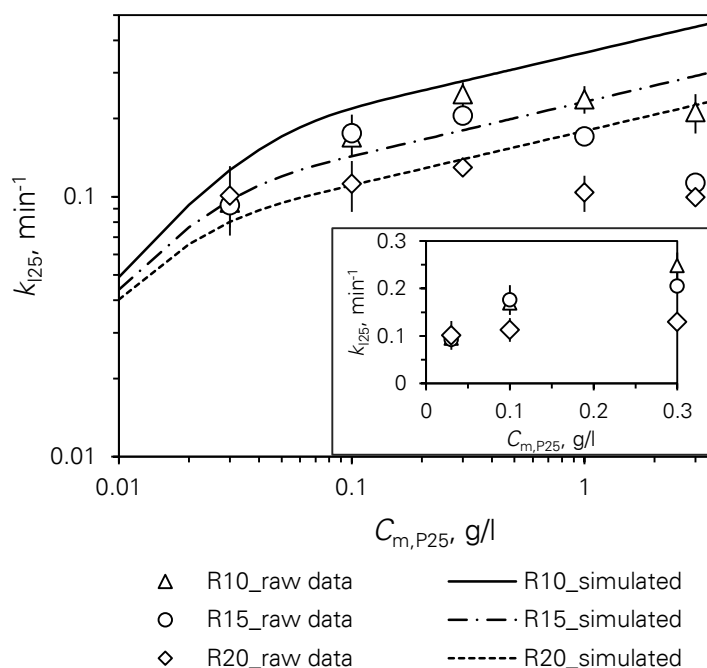


Figure 6.8 Influence of the photocatalyst concentration on the photodegradation of methylene blue (MB): Color removal of 600 ml MB solution of 9–10  $\mu$ M with different concentrations of P25 in three reactors R10, R15 and R20. The average intensity of UV illumination on the illuminated surface was 26 W/m<sup>2</sup>. The reaction rate constant in the flow reactor  $k_{125}$  vs. the P25 concentration  $C_{m,P25}$  is shown, experimental data were compared with the simulated data. The inset shows the data in the low range of concentration in normal scale.

The theory was proved by experimental results, shown in Figure 6.8. When the photocatalyst concentration was lower than 0.3 g/l, the reaction rate constant increased with the increased photocatalyst concentration (Figure 6.8). In contrast, when the concentration was higher than 0.3 g/l, the reaction rate constant decreased. The very high catalyst dose has an extreme turbidity. It hinders the optical penetration of UV light into the suspension [95]. In the experiments, the transmittance through the suspensions with different optical pathlengths (shown in Figure 5.9) proved this theory. The simulated data in the figure are discussed later.

### The modified reactor model

For further explanation of the decreased optical penetration by the turbid suspension, the influence of the optical pathlength of the reactors on the photocatalytic reaction was inspected. In this study, three reactors R10, R15 and R20 have rectangular cross-sectional channel meandering within a vertical plane facing the illumination. Their optical pathlengths are 11 mm, 17 mm and 22 mm, respectively.

Radiation across the channel depends only on the optical depth and can be extinguished in the rear of the reactors. The concept of active-inactive volumes of the reactors is derived. These abstract spaces are separated by an imaginary vertical plane (Figure 6.9). It is at a certain

distance  $L_{\text{active}}$  from the illuminated surface, where the transmittance of light reaches a critical threshold. The ratio

$$a_R = \frac{L_{\text{active}}}{L_R} \quad (6.11)$$

is the so-called activity factor of the reactor. This value is different depending on the thickness of the reactor  $L_R$ .

As discussed in section 5.2.3, when the particle concentration is lower than 0.3 g/l, turbidity of suspensions is proportional to the concentration (Figure 5.9). It was also shown that, depending on the particle concentration and optical pathlength, the linear function is invalid when transmittance is lower than 5 % (Figure 5.8). For this reason, the value 5 % was chosen as the lower transmittance, i.e. when the transmittance is lower than this critical value, light is considered to be extinguished. At the wavelength of 365 nm, the found extinction coefficient is  $4.28 \times 10^4 \text{ cm}^2/\text{g}$ . Accordingly, the optical penetrations  $\delta_{\text{opt}}$  are 24 mm, 7 mm and 2 mm for the particle concentrations of 0.03 g/l, 0.1 g/l and 0.3 g/l, respectively. When  $\delta_{\text{opt}} < L_R$ , it means that the reactor has the active volume in the front and the inactive volume in the rear. The separated plane is at  $L_{\text{active}} = \delta_{\text{opt}}$  and the activity factor is lower than 1. When  $\delta_{\text{opt}} \geq L_R$ , it means that the entire volume of the reactor is active, the maximum values are achieved, where  $L_{\text{active}} = L_R$  and the activity factor is 1.

A modified model was established based on the original reactor model (section 3.3.3), including the penetration of light inside the reactor, which is characterized by the activity factor.

In the active volume of the reactor, the change of the studied species is

$$\frac{d(a_R \dot{n}_0)}{d(a_R V_R)} = - \frac{k C_{n,0}}{1 + K_{\text{ads}} C_{n,0}}. \quad (6.12)$$

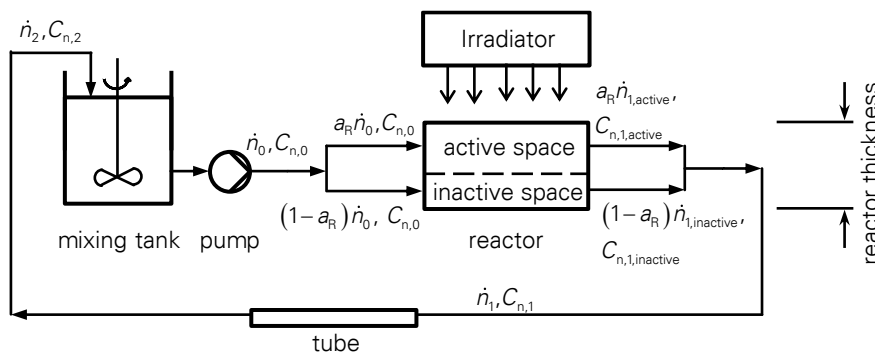


Figure 6.9 Fluids and concentrations of species in the photocatalytic system (cont.). The setup includes a mixing tank, a flow reactor illuminated by an irradiator, a pump and connecting tubes. The reactor is considered to have active and inactive volumes. The molar flow rate and the molar concentration of the species are denoted as  $\dot{n}$  and  $C_n$ , respectively.

The activity factor is a constant and can be omitted in the left side of the equation. The solution can be generated as Eq. (3.15). In the limit case, the concentration is written as the exponential function  $C_{n,1,\text{active}}(t) = C_{n,0}(t - t_R)e^{-kt_R}$  as Eq. (3.25).

In the inactive volume of the reactor, no reaction takes place. The concentrations of the inlet and outlet flows are related by the residence time

$$C_{n,1,\text{inactive}}(t) = C_{n,0}(t - t_R). \quad (6.13)$$

The fluid going out of the reactor includes the fluids from active and inactive volumes. Its concentration is

$$\begin{aligned} C_{n,1}(t) &= a_R C_{n,1,\text{active}}(t - t_R) + (1 - a_R) C_{n,1,\text{inactive}}(t - t_R) \\ &= C_{n,0}(t - t_R) [a_R e^{-kt_R} + (1 - a_R)]. \end{aligned} \quad (6.14)$$

No reaction occurs in the mixing tank or the tubes. The change of the amount in the mixing tank is due to the in- and out fluids as Eq. (3.20), and that in the tubes is due to the residence time as Eq. (3.22). The modified form of Eq. (3.26) is

$$\frac{dC_{n,0}}{dt} t_M = -C_{n,0}(t) + C_{n,0}(t - t_T - t_R) [a_R e^{-kt_R} + (1 - a_R)]. \quad (6.15)$$

The linear delay differential equation can be solved as described in section 3.3.3. The conversion of the organic substance follows the exponential function  $C_{n,0}(t) = C_{n,\text{ini}} e^{-kt}$  as Eq. (3.28). The reaction rate constant of the photocatalysis in the reactor is

$$k = -\frac{1}{t_R} \ln \left[ \frac{1 - K t_M}{a_R e^{K(t_T + t_R)}} - \frac{1 - a_R}{a_R} \right]. \quad (6.16)$$

When the activity factor is 1, the modified model returns the original model as Eq. (3.29).

### The reaction rate constant at the illuminated surface

The reaction rate constant is actually an average parameter. Indeed, as light across the reactor attenuates, each fluid vertical layer receives a correspondent illumination  $I_z$ . The specific reaction rate constant  $k_z$  of the fluid layer  $z$  is defined as

$$k_z = k_0 \frac{I_z}{I_0} = k_0 T_z = k_0 e^{-\beta z C_m}, \quad (6.17)$$

where  $k_0$  refers to the reaction rate constant at the illuminated surface of the reactor  $z = 0$ ,  $T$  is the transmittance,  $\beta$  is the extinction coefficient and  $C_m$  is the particle concentration. The reaction rate constant can be calculated as

$$k = \frac{1}{L_R} \int_0^{L_{\text{active}}} k_z dz = k_0 \frac{L_{\text{active}}}{L_R} \frac{1 - T^*}{-\ln(T^*)}, \quad (6.18)$$

where  $T^*$  is the transmittance through an active optical pathlength  $L_{\text{active}}$ . The value  $T^*$  can be chosen as the lower limitation of transmittance, i.e., 5 % as discussed. For a certain photocatalytic system, the turbidity of the suspension is known, thus  $L_{\text{active}}$  can be determined. The value  $k_0$  is derived as

$$k_0 = k \frac{L_R}{L_{\text{active}}} \frac{-\ln(T^*)}{1-T^*}. \quad (6.19)$$

With each photocatalyst concentration, the reaction rate constant at the illuminated surface is independent from the optical depth and thus identical. Experimental data (Figure 6.10a) confirm this theory. The scattering of the data is due to the fluid properties in three reactors. E.g., the lateral mixing of the flow induced the mixing among layers.

The average values for individual concentrations of three reactors were found (Figure 6.10b). The value  $k_{0,125}$  was expected to be proportional to the concentration in this low range [40], [152]. However, experimental data show a power law

$$k_0 = A(C_{m,P25})^\alpha. \quad (6.20)$$

The process parameter  $A$  is 19.60. The exponent is 1.29 and slightly higher than 1. It can be affiliated to the radial mixing. The back scattering in the system may also positively intensify the light at the illuminated surface. However, in the context of this study, this relation allows for an optimization of the data.

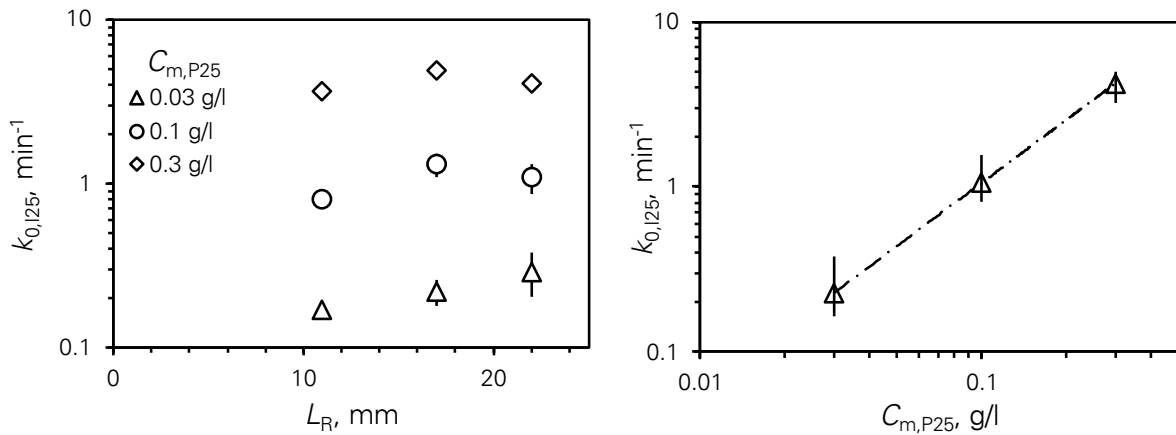


Figure 6.10 Influence of the photocatalyst concentration and optical pathlength on the photodegradation of methylene blue (MB): The reaction rate constant on the illuminated surface of the reactors  $k_{0,125}$ . Data were interpreted from experiments shown in Figure 6.8. a) Values of experiments with three photocatalyst concentrations  $C_{m,P25}$  in three reactors with different thickness  $L_R$ ; and b) The average values vs. the photocatalyst concentration.

## Optimization

In this study, the reactors were designed for research purposes. In following discussion, they are called the “research reactor”. To define the intensity of light across research reactors, the cross section of the flow channel is rectangular. In reality, a flow reactor is tubular. If light is illuminated on one side, e.g., from the top, the *inner diameter* of the tubular reactor is equal to the thickness of the research reactor. If light is illuminated on the total surface area of the flow channel, e.g. the solar photocatalytic reactor with the parabolic compound concentrator [12], [17], [18], [89], [97], [105], the *radius* of the tubular reactor is equal to the thickness of the research reactor. In any event, this dimension should be optimized to ensure the active space in the reactor. In addition, optimization of photocatalyst concentration should be done, in order to achieve fast photocatalysis performance while material- and operation-cost saving is ensured.

Eq. (6.19) and gives the formula of the reaction rate constant

$$k = A(C_{m,P25})^\alpha \frac{1 - e^{-\beta L_R C_{m,P25}}}{\beta L_R C_{m,P25}}. \quad (6.21)$$

The relation allows for the prediction of the reaction rate constant when the process conditions are known. Figure 6.8 shows the simulated data in comparison with the experimental results. Note that the optimization can be utilized only in the validity range of the Beer-Lambert law. In this study, the upper photocatalyst concentration to ensure the validity is 0.3 g/l. Therefore, only experimental data in this range can be used for the evaluation.

To look for the optimum value of the photocatalyst concentration, the partial differentiation by concentration is calculated

$$\frac{\partial}{\partial C_{m,P25}}(k) = \frac{A}{\beta L_R} (C_{m,P25})^{\alpha-2} \left[ (\alpha-1)(1 - e^{-\beta L_R C_{m,P25}}) + \beta L_R C_{m,P25} e^{-\beta L_R C_{m,P25}} \right]. \quad (6.22)$$

The value is always positive. Therefore, the value  $k$  monotonically increases with the increased photocatalyst concentration. The optimal concentration should be chosen as the upper value as 0.3 g/l. This optimal concentration is in good agreement with other works where organic compounds were degraded in either an illuminated batch or flow reactor [17], [148]–[150].

On the other hand, the partial differentiation by reactor thickness helps to find out the optimal value of the optical pathlength

$$\frac{\partial}{\partial L_R}(k) = \frac{A}{\beta} (C_{m,P25})^{\alpha-1} \times \frac{1 - e^{-\beta L_R C_{m,P25}} (1 - \beta L_R C_{m,P25})}{(L_R)^2}. \quad (6.23)$$

For  $\text{TiO}_2$  suspensions, typically the extinction coefficient  $\beta$  at the UV wavelength is approx.  $1 - 10 \times 10^4 \text{ cm}^2/\text{g}$ . The particle concentration is less than 1 g/l. The flow reactors usually have the optical depth of dozens of millimeters. Thus, the value  $e^{-\beta L_R C_{m,P25}} (1 - \beta L_R C_{m,P25})$  is higher

than 1 and the partial differentiation is negative. It means that the reaction rate constant monotonically increases with the decreased optical depth. One should choose the optimal optical pathlength as the lower boundary. Note that the small diameter of flow channels increases the fluid velocity, leads to the increase of pressure drop. It makes the small diameter impractical. The lower boundary of 10 mm is, thus, suggested as the optimal thickness of the reactor. It is compiled with data from other studies, where the optimal radius of the reactor are 10–25 mm [17], [19].

### **Practical remarks**

The simulated and experimental results show that the optimal concentration of P25 is 0.3 g/l. A larger amount has the negative effects from both theoretical and practical aspects. Indeed, increasing the photocatalyst loading induces the material cost. When using the commercial nanoparticles (NPs), such as  $\text{TiO}_2$  and  $\text{ZnO}$ , the energy bandgap is rather large, the UV light is required to provide adequate photon energy. To shorten the bandgap and make use of the visible radiation in solar light, the commercial photocatalysts are modified (section 2.1.3). To the best of my knowledge, these novel nanomaterials for photocatalytic uses have been not produced at industrial scale yet. The saving of material, hence, reduces the synthesis cost.

Additionally, less photocatalysts reduce the mass of the suspension. Energy consumption for loading the fluid with a pump is lower. Moreover, the use of NPs needs a post-treatment to separate the solid part from the supernatant. A decrease of used materials leading the operating cost of the post treatment to be more economical is, thus, very important.

Last but not least, for the experimental setup design, the weight of the flow reactor, which can be as long as hundreds meter, should be considered. The small diameter not only reduces the weight of the setup, but also ensures the efficient use of the illumination. The large diameter is useless, but has the lower pressure drop. In this study, cost estimation has not been done. The optical thickness of 10 mm is sufficient to achieve the highest photocatalytic degradation.

### **6.4.4 High initial concentration of the organic compound**

This part of the study focuses on the photocatalysis with the high initial concentrations of the organic substance. Here, methylene blue (MB) was discolored, of which concentrations are 2, 5 and 10-time higher than the commonly used one. It also aims at the fact that in industrial application of textile wastewater, the dye concentration is usually high. Raw experimental data were previously presented [238].

While diluted MB solutions can be easily analyzed by UV-VIS spectroscopy with common cuvettes of which optical pathlength is 10 mm, concentrated MB solutions require measurement with short optical pathlength cuvettes. All calibration curves determined with 1, 2 and 5 mm cuvettes as well as the calibration formula can be found in section A4 of the Appendix.

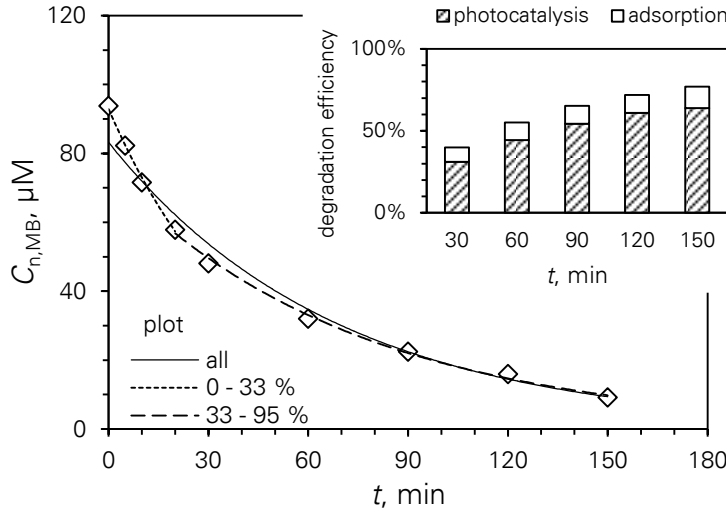


Figure 6.11 Photocatalytic degradation with the high initial concentration of methylene blue (MB): Color removal of 400 ml MB solution of 93.8  $\mu\text{M}$  with 1 g/l P25 in reactor R10 under UV illumination (the average intensity on the illuminated surface was 22  $\text{W}/\text{m}^2$ ). The evolution of MB concentration  $C_{n,\text{MB}}$  was plotted along with the experiment time  $t$  by exponential fits within the “all” degradation, or within “0–33 %” and “33–95 %” degradation. The inset shows the color removal efficiency by adsorption and by photocatalytic reaction.

Figure 6.11 shows the experiment result with 1 g/l  $\text{TiO}_2$  P25 and approx. 110  $\mu\text{M}$  MB which is the highest MB concentration in this study. After a 90 min adsorption-desorption equilibrium in the dark, 14 % MB was adsorbed on P25 photocatalyst. The initial concentration of MB in the photocatalytic test was 93  $\mu\text{M}$ .

Prior to the test, MB and P25 were stored in a mixing tank and kept stirring in dark condition. A period of 90 min can ensure the adsorption-desorption equilibrium of MB [25]. In fact, during the control test (which was also in the dark, but suspension was loaded and run through the channel of the reactor), there was an adsorption of 9 % after the first 30 min (shown in the inset of the figure). The strong mixing in the setup certainly impacted the mass transfer and increased the adsorption, especially at the beginning. From 30 to 150 min, more 4 % MB was adsorbed.

During the degradation test under UV illumination, the color removal occurred due to both adsorption and photocatalytic reaction. To exclude the adsorption effect, the concentration of MB by photocatalytic reaction was calculated as

$$C_{n,\text{MB}} = C_{n,\text{degradation}} - C_{n,\text{adsorption}} \quad (6.24)$$

where  $C_{n,\text{adsorption}}$  and  $C_{n,\text{degradation}}$  are the molar concentrations of MB in the control test and in the degradation test, respectively.

By assuming the adsorption constant of MB on P25  $K_{\text{ads}}$  an unchanged value, the reactor model (Eq. (3.28)) could be used for a determination of the reaction rate constant. In reality,

during reactions, MB was degraded, while intermediates or products were generated. These formed molecules occupied the adsorption sites of the photocatalyst. In other words, the vacant sites were covered not only by MB but also by the produced compounds. Though adsorption-desorption equilibrium was achieved prior to the photocatalytic test, there was always a competition between the adsorption-desorption of MB and that of the intermediates and (by-) products [90], [101]. As the results, the value  $K_{\text{ads}}$  changes along with the reaction time and the assumption above is only valid to a certain extent. This effect makes the exponential fit of the reactor model deviate from the experimental data.

For a low initial concentration, the deviation was also observed (Figure 6.3), but not remarkable. Dissimilarly, here, the MB concentration is high and this phenomenon is obvious. A scattering of the experimental data from the exponential plot of the entire test duration (the continuous line of the plot “all” in Figure 6.11) was observed. There seem to be two phases of the experiment. At the beginning, the amount of MB adsorbed on the photocatalyst is saturated after the equilibrium and abundant. The adsorbed MB is strongly degraded, and the decay rate is fast, shown by the raw data under the plotted line. In the second stage, the number of products is larger. The desorption of the products to the bulk restricts MB to transfer to the catalyst surface. The reaction is slower, indicated by the raw data above the line. For this reason, the division of the entire duration into two phases allows for the much better exponential fits.

In this study, the turning point of two phases was chosen at which the photocatalytic efficiency reaches 33 %. The degradation rate constant at the beginning  $K_1$  is higher than that at the end of the test  $K_2$  (Figure 6.11). These two values are 0.024 and 0.014  $\text{min}^{-1}$ , respectively. It proves the argument above about the change of reaction rate constant during the test.

Data of the other experiments were analyzed in the same way. The intensity-related reaction rate constants in two phases  $k_{1,125}$  and  $k_{2,125}$  are compared in Figure 6.12. Further discussion deals with the reaction rate constant in the first phase as it is less influenced by the intermediates or (by-) products.

With a same catalyst concentration, the number of generated products increases with the increased MB initial concentration. They obstruct the active site at the catalyst surface. It lowers the adsorption constant and consequently, the reduced reaction rate constant is observed. This trend was clearly observed by experimental data as shown in Figure 6.12.

With a same initial MB concentration, the use of the higher amount of the photocatalyst undoubtedly results in a larger surface area of the catalyst. It explains the ongoing increase of the reaction rate constant with the increased catalyst amount even when the P25 concentration is lower than 0.5 g/l. When the catalyst concentration is 0.5–1 g/l, the reaction rate constants in both phases slightly increases or reaches a plateau. It is a bit different from the finding in section 6.4.3, where the optimal concentration of photocatalyst of 0.3 g/l was claimed. Here, not only turbidity of the catalyst suspension but also adsorption of the organic

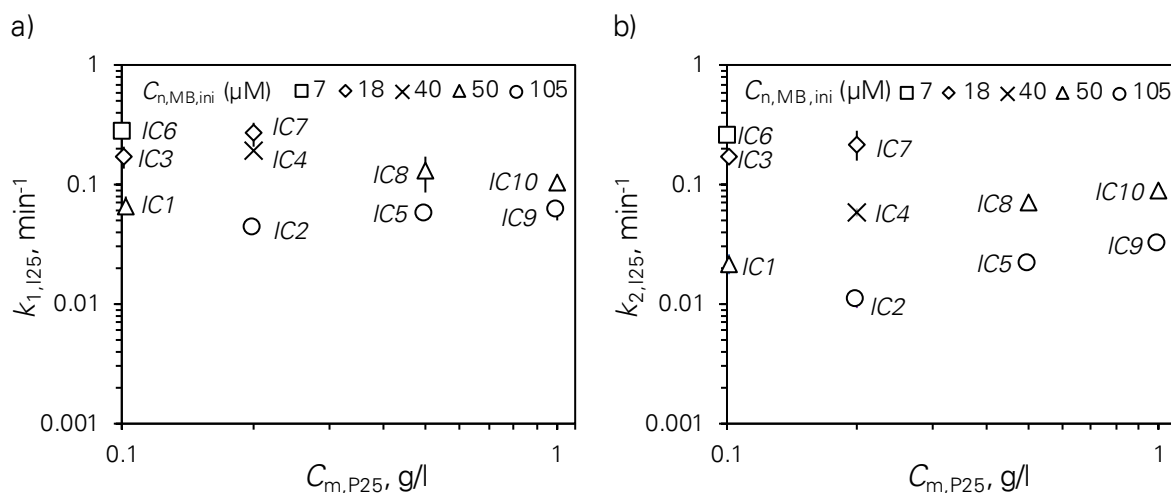


Figure 6.12 Influence of the initial concentration on the photodegradation of methylene blue (MB). Color removal of 400 ml MB solution (7, 18, 40, 50 and 105  $\mu\text{M}$ ) with  $\text{TiO}_2$  P25 (0.1, 0.2, 0.5 and 1 g/l) in reactor R10 under UV illumination (the average intensity on the illuminated surface was 22  $\text{W}/\text{m}^2$ ). Ten experiments (IC1–IC10) were done. More details can be found in Table 6.2. The intensity-related reaction rate constant in the flow reactor a) in the first phase  $k_{1,I25}$  and b) in the second phase of the degradation  $k_{2,I25}$  vs. the photocatalyst concentration  $C_{m,P25}$ .

Table 6.2 Influence of the initial concentration on the photodegradation of methylene blue (MB). The table shows the numerical results corresponding to the graphical results in Figure 6.12. The intensity-related reaction rate constant in the first phase  $k_{1,I25}$  and in the second phase of the degradation  $k_{2,I25}$  are compared.

Experiment	$C_{m,P25}$ g/l	$C_{n,MB,ini}$ $\mu\text{M}$	$C_{m,P25}/C_{n,MB,ini}$ g/mol	$k_{1,I25}$ $\text{min}^{-1}$	$k_{2,I25}$ $\text{min}^{-1}$
IC1	0.1	50	2004	$0.067 \pm 0.011$	$0.022 \pm 0.004$
IC2	0.2	105	1896	$0.042 \pm 0.003$	$0.011 \pm 0.001$
IC3	0.1	18	5445	$0.170 \pm 0.036$	$0.171 \pm 0.002$
IC4	0.2	40	5013	$0.192 \pm 0.000$	$0.058 \pm 0.004$
IC5	0.5	105	4740	$0.057 \pm 0.005$	$0.021 \pm 0.002$
IC6	0.1	7	13799	$0.269 \pm 0.009$	$0.252 \pm 0.107$
IC7	0.2	18	10889	$0.270 \pm 0.058$	$0.219 \pm 0.060$
IC8	0.5	50	10020	$0.130 \pm 0.043$	$0.071 \pm 0.004$
IC9	1.0	105	9481	$0.060 \pm 0.010$	$0.031 \pm 0.002$
IC10	1.0	50	20040	$0.104 \pm 0.002$	$0.090 \pm 0.007$

molecules affected the process. To exclude the effect of the adsorption as much as possible, only experiments of the same ratio of P25 to MB were compared (Table 6.2). Of each ratio (experiments IC3–IC5, or IC6–IC9), the reaction rate constant reaches the maxima at 0.2 g/l P25. Not surprisingly, the reaction rate constant with 0.5 or 1 g/l P25 is lower than that with 0.1 or 0.2 g/l P25. The high turbidity restricted the penetration of light and the optical influence is more important. It agrees with the results discussed in section 6.4.3.

### 6.4.5 Acidic/basic property

In previous experiments, it was preferred to use the original pH of the suspensions, which is 4–6 depending on the P25 photocatalyst concentration. In wastewater treatment, the influence of pH is important as pH is varied in a wide range of values. Especially, in textile companies, depending on the type of dye substances, the processing is altered, pH of wastewater can be as high as 10–12. Based on this reality, the impact of pH on the photocatalytic reaction was studied. In this section, color removal of methylene blue (MB) by photocatalysis is discussed where the pH was adjusted in the range of 3–10 by adding NaOH or HCl. As pH has no effect on the UV-VIS absorbance of MB (Appendix A4) [239], MB concentrations were analyzed with UV-VIS spectroscopy. Experimental work was contributed by Hieu Le.

#### Evolution of pH during experiments

It is reported that pH may change during the photocatalysis [181]. In the experiments, the decrease of pH was observed when pH was higher than 6, which is the pH of the suspension without pH adjustment. When circulating the suspension in the setup, due to strongly mixing by stirring in the mixing tank and by quasi-turbulent flow in the flow reactor, CO<sub>2</sub> in the air was incorporated and dissolved into the aqueous system. The formation of HCO<sub>3</sub><sup>−</sup> and H<sub>2</sub>CO<sub>3</sub> decreases pH during the photocatalytic tests. The maximum change was observed with pH of 9.5–10, where pH at the end of the tests was 6.9–8.4. In all cases, after the first 10 min, pH was relatively stabilized, which might be due to the likely saturation of CO<sub>2</sub> absorbed in the system. The minor drops after that might pose the different chemical functional groups of the intermediates/products [8]. The change of pH during experiments can be found in Table 6.3

#### Influence of pH on photocatalysis

Theoretically, the photocatalyst is excited by photon energy and the electron-hole formation is pH independent. However, holes react with hydroxyl group, of which formation is certainly influenced by pH, to form hydroxyl radicals. In a basic medium, the concentration of OH<sup>−</sup> is higher than in a neutral or acidic medium. Consequently, the increased concentration of radicals under illumination leads to a higher reaction rate constant. Experimentally, reaction rate constant increases with increasing pH (a), which agrees with other researches [25], [40]. The observed change can be assigned to the hydroxylation of the P25's surface due to the presence of OH<sup>−</sup>.

Another reason can be attributed to the adsorption of MB on the surface of photocatalysts. It is known that the PZC of P25 is 6–6.8 [201]. When pH is higher than 6, P25 is negatively charged, and inversely. As MB is a cationic dye, it is favorably adsorbed on negative surfaces, whereas positively charged surfaces counteract MB adsorption due to electrostatic repulsion. It was confirmed by the experiments in the dark, shown in . Exceptionally, at pH 3, slight desorption was observed. Initially, MB was added and its concentration was 13.2 μM. After 30 min adsorption-desorption equilibrium, MB concentration was 12.8 μM. During the test,

the concentration slightly increased and reached 13.3  $\mu\text{M}$  at the end of the test. It explains the very low reaction rate constant of experiment 1 and 2 (Table 6.3 and Figure 6.13).

In reality, the pH of the dye solutions can be high. The presence of hydroxyl groups promotes the photodegradation of the solutions. Additionally, the increased adsorption of the cationic dyes supports the color removal. However, desorption of the (by-) products which makes recovery of photocatalysts more problematic should be concerned.

Table 6.3 Evolution of pH during the photodegradation of methylene blue (MB): Color removal of 400 ml MB solution of 13  $\mu\text{M}$  with 0.1 g/l P25 in reactor R10 under UV illumination. 15 experiments were done (experiment 1–15). pH was adjusted to have a desired value (labelled “-30”). Photocatalyst was added into the solution. After 30 min adsorption-desorption in a mixing tank, pH was then measured (labelled “-0”). The suspension was then loaded into the covered reactor and circulated for the homogeneity of flow and pH was measured (labeled “+0”). The reactor was then uncovered for the photocatalytic test and pH was measured every 10 min (labelled “10”, “20” and “30”). Experiment 5 was done without pH adjustment.

Experiment	pH at time $t$ (min)					
	-30	-0	+ 0	10	20	30
1	2.9	3.0	3.2	3.2	3.1	3.1
2	3.0	3.0	3.1	3.0	2.9	3.0
3	3.9	3.9	3.9	4.0	4.1	4.1
4	4.4	4.4	4.6	4.7	4.8	4.8
<b>5</b>	<b>5.9</b>	<b>5.5</b>	<b>5.8</b>	<b>5.8</b>	<b>5.9</b>	<b>5.9</b>
6	7.2	6.0	5.7	5.6	5.7	5.7
7	7.3	6.0	6.1	6.1	6.2	6.2
8	8.3	6.3	6.3	6.4	6.4	6.4
9	8.3	6.3	6.3	6.2	6.3	-
10	8.5	6.3	6.3	6.2	6.0	5.9
11	9.5	8.1	7.9	7.5	7.2	6.9
12	9.5	6.6	6.5	6.7	6.8	6.9
13	9.6	9.3	9.0	8.5	8.2	7.7
14	9.8	9.3	8.9	-	-	7.1
15	10.0	9.7	9.4	8.9	8.1	8.4

### Parameters of the reactor model

When considering the indirect photocatalytic pathway, the hydroxyl groups in water react with trapped holes and form hydroxyl radical, which degrade the MB molecules. Eqs. (3.6)–(3.8) can be rewritten as follows



where  $K_{\text{rad}}$  is the constant of radical formation and  $K_{\text{ads}}$  is the adsorption constant. The integrated reaction rate constant  $k$  in Eq. (3.14) is derived as

$$k = k_r K_{\text{ads}} \theta_{\text{OH}} = k_r K_{\text{ads}} \frac{K_{\text{rad}} C_{\text{n,OH}^-}}{1 + K_{\text{rad}} C_{\text{n,OH}^-}}, \quad (6.28)$$

where  $\theta_{\text{OH}}$  is the fractional surface coverage of hydroxyl groups and  $k_r$  is the intrinsic reaction rate constant. The equation can be rewritten as

$$\frac{1}{k} = \frac{1}{k_r K_{\text{ads}}} \left( \frac{1}{K_{\text{rad}}} \frac{1}{C_{\text{n,OH}^-}} + 1 \right). \quad (6.29)$$

As adsorption is pH dependent, the value  $K_{\text{ads}}$  is not constant in Eq. (6.29) and  $1/k$  is a complicate function of  $C_{\text{OH}^-}$ .

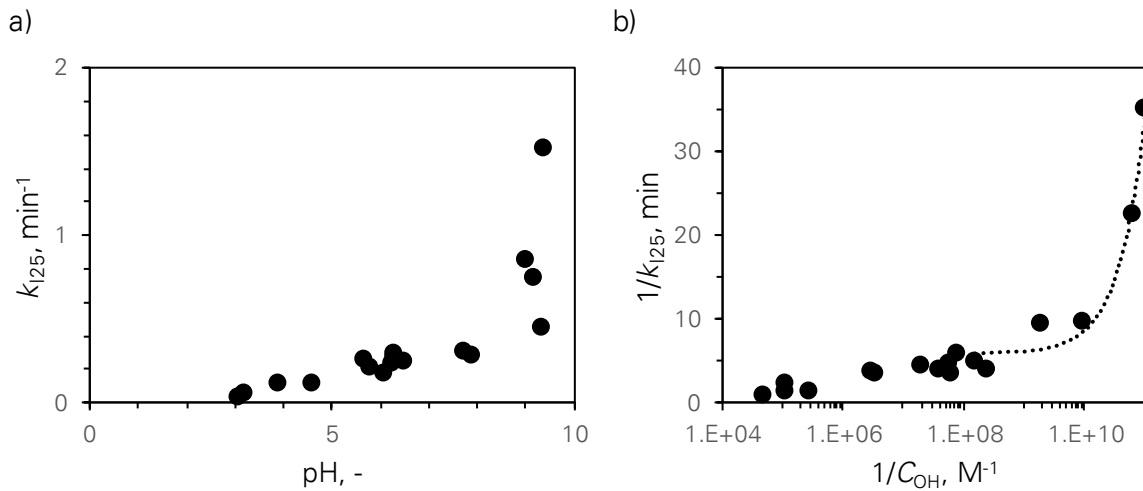


Figure 6.13 Influence of pH on the photodegradation of methylene blue (MB): Color removal of 400 ml MB solution of 13  $\mu\text{M}$  with 0.1 g/l P25 in reactor R10 under UV illumination. The average intensity on the illuminated surface was 24  $\text{W}/\text{m}^2$ . a) Reaction rate constant  $k_{125}$  vs. pH; and b) Inverse reaction rate constant vs. inverse concentration of  $\text{OH}^-$ .

Depending on pH, the color removal of MB in the presence of P25 with high pH is actually caused by both photocatalytic reaction and adsorption. E.g., when the P25 concentration is 0.1 g/l and the MB initial concentration is 13  $\mu\text{M}$ , P25 itself can adsorb up to 40 % MB when pH is 9.3 (). With the same experimental conditions, when pH is lower than 6, only less than 5 % of MB was adsorbed, the influence of pH on the adsorption can be eliminated and approximately,  $K_{\text{ads}}$  is a constant. With this assumption, Eq. (6.29) means that the inverse reaction rate constant is a linear dependence of the inverse concentration of hydroxyl groups. The function also fits the experimental data (b), where the relation was found as

$$\frac{1}{k_{125}} = 3 \times 10^{-10} \frac{1}{C_{\text{n,OH}^-}} + 5.8371 \quad (6.30)$$

with the coefficient of determination higher than 0.97. A system of equations can be derived from Eqs. (6.29)–(6.30)

$$\begin{cases} \frac{1}{k_r K_{\text{ads}}} = 5.8371 \\ \frac{1}{k_r K_{\text{ads}}} \frac{1}{K_{\text{rad}}} = 3 \times 10^{-10} \end{cases} \quad (6.31)$$

Once  $K_{\text{ads}}$  corresponding to each pH is found (as discussed in section 2.1.2),  $k_r$  and  $K_{\text{rad}}$  can be determined. E.g., with the adsorption constant of MB of  $6.3 \times 10^3 \text{ M}^{-1}$  [25], the other parameters can be determined (Table 6.4).

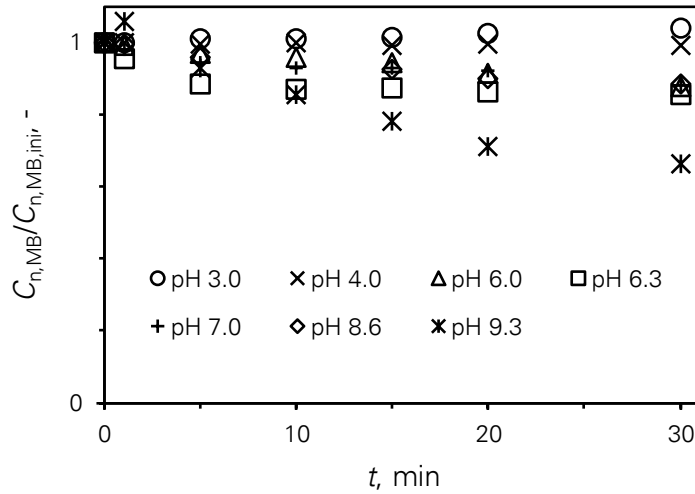


Figure 6.14 Influence of pH on the adsorption of methylene blue on the P25 photocatalyst. Adsorption tests of 400 ml methylene blue solution of 13  $\mu\text{M}$  with 0.1 g/l P25 in reactor R10 in the dark. Concentration conversion with regard to time with varied pH.

Table 6.4 Parameters of the kinetic model for the photodegradation of methylene blue with pH &lt; 6.

Description	Parameters	Unit	Value
Adsorption constant of MB *	$K_{\text{ads}}$	l/mol	$6.3 \times 10^3$
Intrinsic reaction rate constant	$k_r$	min <sup>-1</sup>	$2.7 \times 10^{-5}$
Radical formation constant	$K_{\text{rad}}$	l/mol	$1.9 \times 10^{10}$

\* The used value of the adsorption constant was taken from literature [25].

Note that, for photocatalysis, two reaction pathways can happen (section 2.1.2), where hydroxyl groups or organic compounds react with the trapped holes. In this work, only indirect mechanism (the former) was accessed. Additionally, the surface charge on the nanocolloids was not taken into account. The simple calculation above can be used only for a practical consideration. Further insights should be performed to obtain a full understanding of the influence of pH on the photocatalysis.

#### 6.4.6 Photocatalyst size

As discussed previously in subchapter 5.2.4, P25 photocatalysts are fractal-like aggregates and the degree of aggregation has a big effect on the optical properties of the photocatalyst. The aggregate size can be varied by ultrasonic dispersion. The extinction coefficient increased by 50 % corresponding to the decreased aggregate size from 343 nm to 234 nm. This suggested the improvement of the absorption properties of the aggregates. In this section, color removal of methylene blue (MB) was used to inspect the change of photocatalytic activity of P25 when varying the aggregate size.

##### Preliminary tests

The preliminary tests were to define the suitable photocatalyst concentration for the study on the influence of aggregate size on photocatalysis. Three photocatalyst concentrations were tested, including 0.03 g/l, 0.1 g/l and 1 g/l. First the catalyst was dispersed by ultrasonication, then equilibrium was carried in the dark and color removal of MB was tested in reactor R20. The intensity-related reaction rate constant (section 6.4.2) was computed. Data were shown in Figure 6.15.

In the tests with 1 g/l photocatalyst [186], originally the P25 photocatalyst has the aggregate size of 374–391 nm. When applying ultrasonication to the suspensions, the aggregate size can reduce to 245–250 nm, depending on the level of energy generated. In the photodegradation of MB, an increase of reaction rate constant by approx. 20 % was obtained. Here, the high concentration is very turbid (section 5.2.3). It was estimated that only 3 % of light with

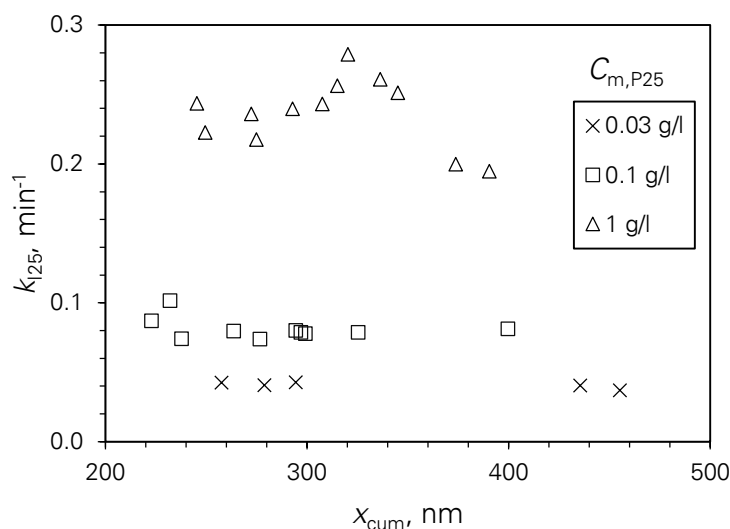


Figure 6.15 Influence of P25 aggregate size on the photodegradation of methylene blue (MB): Color removal of 600 ml MB solution of 10  $\mu$ M in reactor R20 under UV illumination. The average intensity on the illuminated surface was 16–18 W/m<sup>2</sup>. Three photocatalyst concentrations were used, including 0.03 g/l, 0.1 g/l and 1 g/l. Intensity-related reaction rate constant  $k_{125}$  vs. aggregate size  $X_{cum}$ .

the wavelength of 365 nm can transmit through a 1 mm pathlength. Due to the short optical penetration, in these performances, while employing the reactor R20 with 22 mm thickness, most of the space of the reactor is inactive (section 6.4.3). It explains that the effect of ultrasonication on the photocatalytic activity is only 20 % though extinction coefficient increased by 50 %. In addition, the photocatalytic performance of the disintegrated photocatalysts (245–345 nm) is faster than that of original aggregates (374–391 nm) but is not distinct among each other. It can be attributed to the high turbidity.

With the low concentration of 0.03 g/l, by ultrasonic dispersion, the aggregate size decreased from 455 nm to 258 nm and the extinction coefficient increased by 25 %. At this low concentration, 5 % of light can penetrate a pathlength of 15–18 mm. Here, reactor R20 with the optical path of 22 mm was used. However, due to the radial mixing in the flow channel, all particles may absorb light, which makes the entire volume of the reactor active (section 6.4.3). Indeed, by using the light intensity meter PCE-UV34, 7 % of light could pass through the reactor. For this reason, no change of reaction rate constant was observed.

The photocatalyst concentration of 0.1 g/l is a bit lower than the optimal concentration (0.3 g/l, as shown in section 6.4.3), thus a differentiation of reaction rate constant by aggregate sizes was expected. Here, the aggregate sizes were varied in the range of 400–223 nm. Extinction coefficient increased by 27–37 %. Correspondingly, the active pathlength was found to be 6.0–7.6 mm. The reaction rate constant increased by 25 %. The results suggest that this concentration is suitable for testing the influence of aggregate size. However, the use of a thick reactor (reactor R20) diminished the effect, thus, the use of a thin reactor (reactor R10) was

recommended for further test. Also, the reaction rate constant at the illuminated surface (section 6.4.3) which can exclude the impact of optical pathlength was suggested to analyze experimental data.

### Experimental results

Experiments were carried out in the thin flow cell (reactor R10). As discussed, the 0.1 g/l photocatalyst concentration was used. To restrict the re-aggregation of the photocatalyst, the pH was set to be 5.0. It was achieved by adding an amount of 100–400  $\mu$ l HCl 0.01 M into the suspensions.

In most experiments, at the beginning and at the end of the test, pH slightly fluctuated in the range of 5.0–5.3 (Table 6.5). Uncertainly, with the finest photocatalysts, there was an increase of pH from 4.6 to 5.1. It induced a re-aggregation, where  $x_{cum}$  increased from 236 nm to 314 nm and from 250 nm to 356 nm. *PDI* also increased from 0.21 to 0.23. Additionally with the gross photocatalysts of 465–473 nm, after 40 min test, the aggregate size decreased to 359–360 nm and *PDI* decreased from 0.44–0.46 to 0.33–0.34. When inspecting the extinction coefficient, not surprisingly, it increased by approx. 50 %, from 20 cm<sup>2</sup>/g to 31 cm<sup>2</sup>/g. It is expected that the photocatalytic performance also increased.

Table 6.5 Characteristics of the suspensions during the test with ultrasonic pre-treatment: Color removal of 400 ml MB solution of 11–12  $\mu$ M with 0.1 g/l P25 in reactor R10 under UV illumination. 12 experiments were done. The aggregate size  $x_{cum}$ , the polydispersity index *PDI*, pH and extinction coefficient at 365 nm  $\epsilon_{365}$  were determined at 0, 10 and 40 min. Photocatalysts of two first experiments were mixed by a magnetic stirrer but not dispersed by ultrasonication.

$x_{cum}$		<i>PDI</i>		<i>pH</i>			$\epsilon_{365}$
at 0 min	at 40 min	at 0 min	at 40 min	at 0 min	at 10 min	at 40 min	at 0 min
nm		-		-			cm <sup>2</sup> /g
<b>473</b>	<b>359</b>	<b>0.44</b>	<b>0.33</b>	<b>5.0</b>	<b>5.2</b>	<b>5.1</b>	<b>21</b>
<b>465</b>	<b>360</b>	<b>0.46</b>	<b>0.34</b>	<b>4.9</b>	<b>5.0</b>	<b>5.0</b>	<b>20</b>
343	359	0.34	0.29	5.3	5.4	5.3	27
340	340	0.34	0.28	5.1	5.2	5.1	26
325	318	0.30	0.26	5.0	5.3	5.2	26
323	302	0.34	0.26	5.0	5.4	5.2	28
306	302	0.29	0.26	5.0	5.3	5.2	27
300	-	0.28	-	5.1	5.1	5.0	28
282	296	0.24	0.24	5.6	5.5	5.4	29
278	292	0.24	0.25	5.3	5.3	5.2	30
250	356	0.20	0.20	4.6	5.0	5.1	29
236	314	0.21	0.23	5.4	5.5	5.6	31

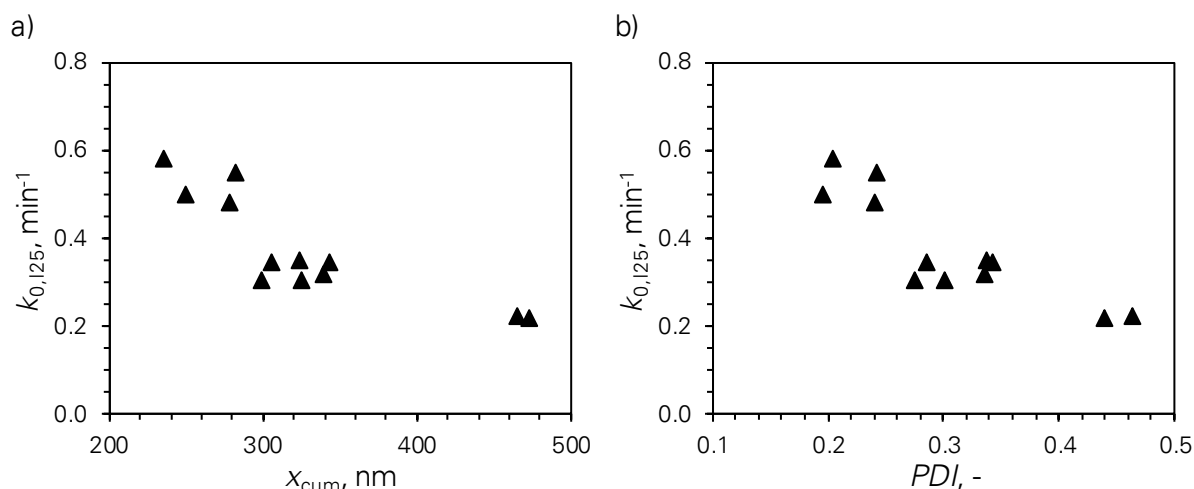


Figure 6.16 Influence of photocatalyst aggregate size on the photodegradation of methylene blue (MB): Color removal of 400 ml MB solution of 11–12  $\mu$ M with 0.1 g/l P25 in reactor R10 under UV illumination. The average intensity on the illuminated surface was 25 W/m<sup>2</sup>. Graphs show the intensity-related reaction rate constant on the illuminated surface  $k_{0,125}$  vs. a) aggregate size  $x_{cum}$ , and b) polydispersity index  $PDI$ .

Figure 6.16 shows the change of the reaction rate constant on the illuminated surface with respect to the varied catalyst aggregate size. The finer aggregates allow for higher reaction rate constants. In particular, an increase of the reaction rate constant by 2.5 times was obtained when disaggregating the photocatalysts from 473 nm to 236 nm.

Since ultrasonic dispersion disintegrates the smaller cluster aggregates, the total specific surface area of the photocatalyst insignificantly changes [240]. The increase of reaction rate constant is not attributed to the surface area of the fractal-like aggregates.

The interaction between light and particles is of great importance. The gross aggregates of up to sub-microns induce the shielding effect when interacting with UV light of which wavelength is less than 400 nm, i.e., light is restricted to penetrate a long distance and reach the neighbor photocatalysts behind. It was confirmed that the extinction coefficient increases with the decrease of the aggregate size (section 5.2.4 and Table 6.5). From a microscopic inspection, depending on the position of the photocatalyst, there may have an internal obscuration and light diffusion within the bulky structures is obstructed. As already known, in nano-photocatalyst systems, light is scattered. Within the internal structure of big aggregates, scattered light is easily captured and the elastic scattering is utilized to activate the neighbors. In this sense, the larger aggregates have a positive effect. To balance the advantages and the disadvantages, a model accounting light interacting with structural photocatalyst is needed. To the best of my knowledge, in the studies of the radiative transfer [102], [184], photocatalysts were considered as single spherical particles, which does not reflect the nature. Here, with the outcome, from the theoretical aspect, it should be aware that the aggregation has a big influence on the photocatalysis.

The interaction between the organic compounds and photocatalyst also contributes to the change of the reaction rate constant. For the P25 aggregates, the external mass transfer is negligible [97]. However, due to the light penetration restriction within the aggregates, the concentration profiles always present, which causes the internal mass transfer [96]. In principle, due to the diffusion path, the organic molecules and the intermediates or (by-) products easily reach the surface of a fine photocatalyst aggregate. Indeed, the adsorption constant was reported to depend on the size of photocatalysts [155]. Consequently, the smaller P25 photocatalysts achieved by ultrasonic dispersion allows for a faster color removal of MB.

More importantly, by disintegrating the photocatalyst with ultrasonication, the reaction rate constant can be boosted by 2.5 times. The average reaction rate constant in the entire flow reactor  $k_{125}$  is  $0.165 \text{ min}^{-1}$  and even higher than the maxima with the optimal catalyst concentration of  $0.3 \text{ g/l}$  (section 6.4.4). Obviously, ultrasonic pre-treatment can be considered as a technique to enhance the photocatalysis while ensuring the material saving. Consequently, the operating cost of the post treatment by membrane filtration reduces. Together with the energy concept introduced in section 5.1.1, it is possible to estimate the electric consumption of ultrasonic dispersion. A comprehensive cost estimation of the whole process, including ultrasonic pre-treatment, photocatalysis, and post-treatment should be studied, then one can decide if it is ambitious to apply ultrasonic dispersion to enhance the photocatalytic activity at pilot scale.

Last but not least, these findings recommend that gross photocatalysts have much lower photocatalytic activity. As the results, a suitable photocatalyst dispersion technique is necessary to homogenize and stabilize the properties of particles as well as to prevent the sedimentation of photocatalysts in real applications.

### 6.4.7 Concluding remarks

In this subchapter, the influence of different parameters on the color removal of methylene blue (MB) was examined. Depending on the study purposes in each part, an appropriate assessment of the experimental data was employed. It must be assured that photocatalysis is a complex process, which is influenced by operating conditions.

Experimental data with the varying suspension volume were introduced in the previous subchapter for the validation of the reactor model. Here, by another interpretation, an explicit relation was given, in particular, the inversely proportional dependence of the apparent reaction rate constant of the photocatalytic setup  $K$  on the volume were given.

The influence of UV light intensity, the driving force of a photocatalysis, was inspected. As expected, in the low range of intensity, as the electron-hole formation prevails over the recombination, it is proportional to the number of incoming photons. It explains the linear relation between the reaction rate constant of the flow reactor  $k$  and the light intensity at the illuminated surface. The intensity-related reaction rate constant was then derived, which can be used to compare with the data of tests of various intensities. The normalized reaction rate

constant with respect to the average intensity of the solar light of  $25 \text{ W/m}^2$   $k_{125}$  was introduced. This value was used for most discussion of this study.

The following results showed the study on the optical penetration. As light across the reactor attenuates, not all volume of the reactor is illuminated. In particular, in the front, where light can penetrate, photocatalyst is activated. Dissimilarly, in the rear, light is extinguished, and this space is considered as an inactive volume. For example, less than 5 % of light can penetrate an optical pathlength of 24 mm, 7 mm and 2 mm for the particle concentrations of 0.03 g/l, 0.1 g/l and 0.3 g/l, respectively. The value  $k_{125}$  is actually an average value of all specific reaction rate constants within the reactor. The concept of the reaction rate constant at the illuminated surface  $k_0$  was derived, and the original model was appropriately modified. This aimed at an understanding of the effect and a prediction of the photocatalytic reaction. Three reactors with the optical thickness of 11, 17 and 22 mm were used, and the photocatalyst concentration was varied from 0.03–3 g/l. In the low range of photocatalyst concentration where scattering is negligible, the simulated data are in fair agreement with the experimental data. It was optimized that the concentration of P25 photocatalyst is 0.3 g/l and the optical thickness is 11 mm. Since this part of the study focused on the optical properties, the pressure drop induced in such thin reactor was not discussed. For up-scaling purpose, this issue should be accounted to minimize the loss of energy.

In this subchapter, the influence of the reactant's concentration was also introduced. With high initial concentrations, the adsorption constant of the reactant is unsteady during the photocatalytic reaction. It is caused by the competition between the adsorption and desorption of the reactants and intermediates/products on the surface coverage of photocatalyst. To find out the parameters of the kinetic model, the adsorption constant must be simplified as a constant value. Experimental data showed that, when dividing the entire photocatalytic reaction into two stages (the beginning, phase 1, and the end, phase 2, corresponding to 0–33 %, and 33–95 % degradation, respectively), the experimental data are well fit to the exponential function of the reactor model. The results suggested that instead of inspecting the initial reactant concentration, the ratio between the photocatalyst and the reactant concentrations is a more important parameter.

Additionally, the influence of pH was described. In principle, the increase of pH allows for a larger number of hydroxyl groups, which certainly increases the number of hydroxyl radicals. It was confirmed by the experimental data. It can be also explained by the change of the adsorption of the organic molecules on the photocatalyst surface. As MB is a cationic dye, the adsorption is favored at pH of higher than PZC of P25, at which P25 is negatively charged. The impact was confirmed by experiments in the dark or under UV illumination. Generally, the photocatalytic degradation of MB increases at the increased pH. Indeed, pH higher than PZC promotes the adsorption and the reaction rate constant is much higher. Exceptionally, when pH is 3, desorption occurs, thus the reaction rate constant of the photocatalytic test is very low. When considering only indirect reaction pathway (section 2.1.2), the reactor model was

then adapted with respect to the concentration of hydroxyl groups. Once the adsorption constant is determined, intrinsic reaction rate constant can be defined.

The last section showed the study on the influence of the photocatalyst aggregate size. Aggregated state was varied by ultrasonic dispersion. The physical properties were previously discussed in subchapter 5.2.4. In the preliminary tests in reactor R20, only a slight enhancement of photocatalytic reaction rate constant was observed since light was extinguished in this thick reactor. Thus, the thin reactor (R10) was employed. The influence of process conditions as UV intensity, optical penetration and pH was eliminated by using the results in sections 6.4.2, 6.4.3 and 6.4.5. The enhancement of the photocatalytic activity by ultrasonic pretreatment was confirmed. Experimentally, the reaction rate constant on the illuminated surface increased 2.5 times. The result is even higher than the maximum reaction rate constant obtained with the conventional mixing with the optimal catalyst concentration (0.3 g/l), which is 3-time higher than the used one here (0.1 g/l). It was explained by the interaction between the catalyst particles with light as well as organic molecules. Both macro- and microscopic issues were interpreted.

Other practical aspects should be attended. In this work, though pH was adjusted to stabilize the photocatalyst colloids, the re-aggregation was detected after a 40-min reaction. When the photocatalyst aggregates are bigger, the photocatalytic activity reduces. In an up-scaled application, where the reactor can be hundreds meter long and the retention time can last few hours, the re-aggregation along with time is definitely problematic. Thus, ultrasonication, or at least an efficient dispersion, is necessary to minimize this aging problem. In addition, the turbulent flow must be considered to avoid the sedimentation caused by further re-aggregation.

It must be assured that photocatalysis is a complex process, which is influenced by operating conditions. This subchapter introduces a comprehensive view on the field of photocatalysis. For further studies and application, one should consider the weighting factor of each parameter and decide the most suitable operating conditions.



## 7 TOWARDS APPLICATIONS OF PHOTOCATALYSIS

Based on the photocatalytic degradation concept, which are discussed in the previous chapters, selected case studies aiming at laboratory applications are introduced in subchapter 7.1. Different photocatalytic materials were studied and the color removals of commercial dye solutions were examined under solar light. The high initial concentration of dye solution was also tested.

In the second subchapter, an application of photocatalysis for a specific case in textile industry is introduced. This Ph.D. study was inspired by the CLIENT/NaViTex project. The project aimed at the treatment, by means of photocatalysis, of wastewater coming from two textile companies in Danang, Vietnam. Some results within the project period are here introduced. They are also the challenges of this thesis. From both scientific and technical considerations, at the end, the possibility of using photocatalysis in a simulated up-scaled reactor for wastewater treatment is discussed.

### 7.1 LABORATORY APPLICATIONS: SELECTED CASE STUDIES

In this subchapter, photocatalysis in the designed reactors was examined with different materials. First experiments show the photocatalytic activity of different photocatalysts, including the novel materials. Various organic compounds were used, including the commercial dye substances from Hachiba Company, Danang, Vietnam (section 7.2.1). As the evaluation of these tests, photocatalytic reaction rate constants were determined according to Eq. (3.28) and (3.29) (section 3.3.3), and the normalization to light intensity was calculated according to Eq. (6.8) (section 6.4.2). Solar photocatalysis, which is the trend for applications, was tested. To exclude the weather conditions, the kinetic model by light energy consumption is proposed.

#### 7.1.1 The volume-related reaction rate constant

In most of experiments in this study, photocatalytic tests were done with a volume of 400 or 600 ml. However, depending on purposes, the volume can be varied. For lab-scaled studies, experiments usually have a small volume of less than 100 ml. It depends on the experimental conditions, such as the amount of photocatalysts, the capacity of setup, the volume of collected solutions. At larger scale, dozens of liters of water are treated. As the research reactor is scalable, a normalization by volume can be delivered. As the apparent reaction rate constant is inversely proportional to the total volume (Eq. (6.6), section 6.4.1), it can be derived as

$$K_{V_{\text{ref}}} = K \times \frac{V_{\text{ref}}}{V}, \quad (7.1)$$

where the apparent reaction rate constant  $K$  corresponds to the volume  $V$  tested in this work, and  $K_{Vref}$  corresponds to a reference volume  $V_{ref}$  of the compared study. The value  $K_{Vref}$  is called the volume-related reaction rate constant in the photocatalytic setup.

### 7.1.2 Solar photocatalysis. The UV energy-dependent model

Experiments in the previous chapter show good performance of photocatalytic degradation with P25 under artificial UV illuminated by a mercury lamp. Mercury-free UV source is a critical solution to perform an environmental-friendly process. Solar photocatalysis has attracted a great attention in this field.

This section presents the solar photocatalysis for the discoloration of methylene blue (MB) in the designed photocatalytic setup.

#### Color removal of methylene blue under visible light

It is noted that,  $\text{TiO}_2$  can experience photo-induced hydrophilic effect [33]. In particular,  $\text{TiO}_2$  is semi-hydrophilic under UV illumination, but turns to be hydrophilic under visible light. Water contact angle on an anatase film was reported to be around  $55^\circ$  and around  $5^\circ$  in two cases [33], respectively. The affinity toward water or organic solutions was enhanced. Experimentally,  $13 \mu\text{M}$  MB was mixed with  $0.1 \text{ g/l}$  P25 powder in the dark to achieve the adsorption-desorption equilibrium. The  $600 \text{ ml}$  suspension was then irradiated under artificial VIS light for  $60 \text{ min}$ . Though the adsorption-desorption equilibrium in dark was achieved before the test, more organic molecules were adsorbed on the surface of P25 when being exposed to visible light. A disappearance of  $28\%$  MB in the bulk liquid was obtained (Figure 7.1) Color was removed by  $19\%$  after the first  $30 \text{ min}$ . In the second half of the test, more  $9\%$  color was bleached.

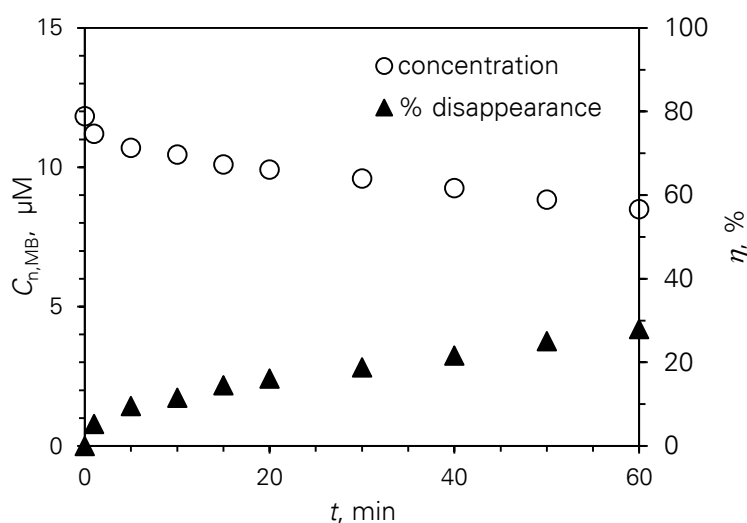


Figure 7.1 Conversion of methylene blue under visible illumination.  $600 \text{ ml}$  methylene blue (MB) of  $13 \mu\text{M}$  was tested with  $0.1 \text{ g/l}$  P25 under artificial visible light: The concentration of MB  $C_{n,MB}$  and the percentage of color removal  $\eta$  vs. time  $t$ .

Additionally, dye substances can be self-photosensitizers, i.e., self-degraded under illumination [85], [153], [208], [209], [241]. Dyes strongly absorb light in the visible range of the electromagnetic spectrum and therefore a charge transfer from the excited dye molecules to the conductance band of the photocatalyst may occur. It forms the unstable dye cation radical and an active species on the catalyst surface which can attack the unstable dye molecules or other molecules. Due to this self-sensitization mechanism, the discoloration can happen but it is not attributed to the photocatalytic reaction. For MB, the control test C1 (Figure 6.1) proved that it is not discolored by the used UV light. However, it was reported that MB itself experiences sensitization under visible light, [85], [208], [209]. Indeed, MB strongly absorbs visible light of 550–700 nm. It has one absorbance peak at 664 nm with one shoulder at 610 nm (Figure 4.1) [242], [243]. In the test, self-sensitization under visible light may happen and contribute to the loss of MB.

Supposedly the artificial visible light has no UV radiation and it was confirmed by the measurements with the UV intensity meter PCE-UV34. However, according to the manufacturer, there is a minor percentage of UV (3 %) in the spectra 3.1.4. This causes the photocatalytic reaction and cannot be excluded in this test.

### Solar photocatalysis of methylene blue

In these experiments, natural light was utilized. Dissimilar to the artificial UV, the solar light is spectral in both UV and visible ranges, and most of the energy is distributed in the visible range.

Two photocatalytic tests were individually carried out on a sunny day and a cloudy day (Figure 7.2). The finding in section 5.2.1 shows that P25 is activated by irradiation shorter than 400 nm. It means that visible light has no role in the photocatalytic reaction. UV intensity was recorded (Figure 7.2a). For the experiment on the sunny day, the average UV intensity was  $23.6 \text{ W/m}^2$  and the degradation of MB was very fast (Figure 7.2b). As shown in the inset, after 30 min, 92 % color was removed. On the cloudy day, UV light was weak, its average intensity was  $5.2 \text{ W/m}^2$ , and the color removal of MB was slow. The degradation efficiency is 53 % and 69 % corresponding to the degradation period of 30 and 60 min, respectively. In experiments with an artificial UV lamp, light intensity is stable during the illumination. The conversion of organic compound can be evaluated by the experiment time. Naturally, the solar light can be chronically changed according to weather conditions. The reactor model by time is no longer relevant to solar photocatalysis. Instead, an evaluation by the light energy consumption is required [105], [236]. As the reaction rate constant is proportional to UV intensity (section 6.4.2), the reactor model in section 3.3.3 can be rewritten as

$$C = C_{\text{ini}} e^{-KE}, \quad (7.2)$$

where the apparent reaction rate constant  $K$  in the photocatalytic setup is in inversed energy unit ( $\text{J}^{-1}$ ), and  $E$  is the light energy consumption (J). It is calculated from the recorded UV intensity  $I_i$  ( $\text{W/m}^2$ ) each time interval  $\Delta t$  (s) as

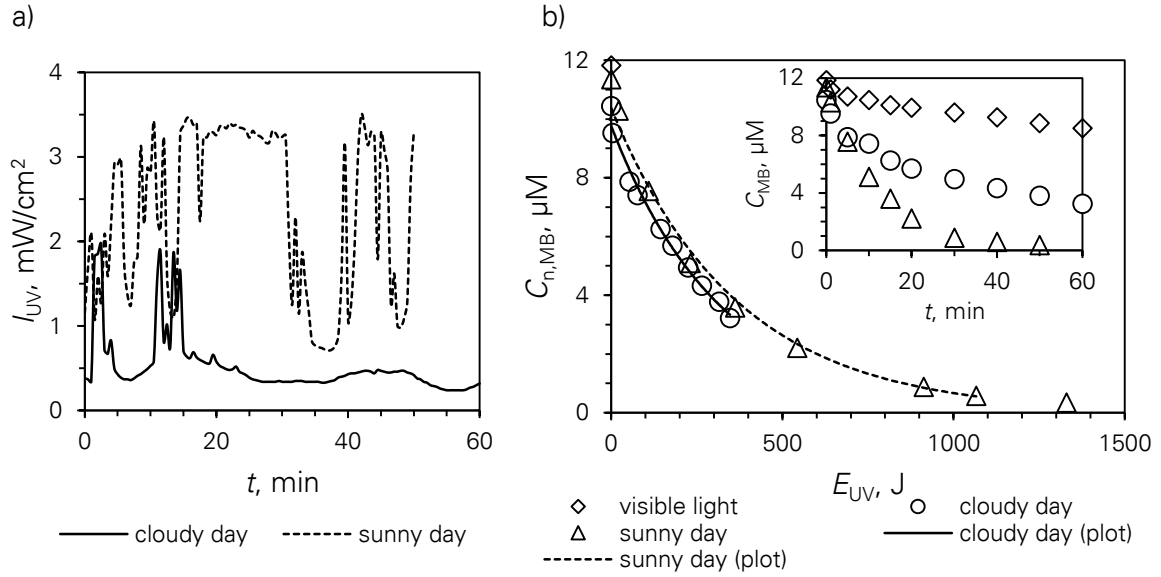


Figure 7.2 Color removal of methylene blue under solar radiation. a) UVA-B intensity recorded by the lux meter vs. experiment time; and b) 600 ml methylene blue (MB) of 13 μM was tested with 0.1 g/l P25 under sunlight or artificial visible light: Concentration of MB vs. UV energy consumption. The inset shows MB concentration vs. experiment time.

$$E = S \sum_i I_i \Delta t, \quad (7.3)$$

where  $S$  is the illuminated surface (m<sup>2</sup>).

The conversions of MB in two experiments were plotted by UV energy consumption (Figure 7.2b). As expected, the decay rate of two experiments is independent from the UV intensity and has a resemblance. Indeed, the UV energy-dependent model (Eq. (7.2)) yields the same reaction rate constant  $K$  of 3.10–3.17 kJ<sup>-1</sup>. It proves that the derivative model can be well-applied for solar photocatalysis.

For a comparison with experiments under artificial light in the previous parts, it is possible to convert the value  $K$  from the inversed energy unit (J<sup>-1</sup>) into the inversed time unit (min<sup>-1</sup>). By averaging the intensity with a reference value, Eq. (7.3) is rewritten as

$$E = S I_{ref} t. \quad (7.4)$$

The conversion can be initiated as

$$K \left[ \frac{1}{s} \right] = K \left[ \frac{1}{J} \right] \times S \left[ m^2 \right] \times I_{ref} \left[ \frac{W}{m^2} \right]. \quad (7.5)$$

For a normalization, the average UV intensity of solar light of 25 W/m<sup>2</sup> is used. Accordingly, the value  $K$  of 3.10–3.17 kJ<sup>-1</sup> is equivalent to 0.087–0.089 min<sup>-1</sup>. The values are similar to the data found from experiments of the same conditions in section 6.4.3, which is 0.082 min<sup>-1</sup>.

## Shielding effect

As shown in Figure 4.1, in the UV range, MB has 2 peaks at 292 nm and 246 nm. With the 10  $\mu\text{M}$  solution, at these two wavelengths, only 37 % and 62% light can transmit through 10 mm cuvette, it means that 63 % and 38 % light is shielded. The effect is weak (5 %) at 365 nm which is the mode wavelength of the UV light. The data show that shielding should be counted in the model.

### 7.1.3 Photocatalysis with different nanomaterials

To prove that the designed photocatalytic setup can work in different laboratories for various study purposes, experiments were conducted with different nanomaterials. Results of the tests with commercial  $\text{TiO}_2$  and ZnO nanoparticles and with self-synthesized nanoparticles are shown.

#### Commercial nanoparticles: $\text{TiO}_2$ P90 and ZnO

Color removal of methylene blue (MB) with three commercial photocatalysts were tested. Experiments were done in reactor R20. The intensity-related reaction rate constants (section 6.4.2) were determined and compared (Figure 7.3).

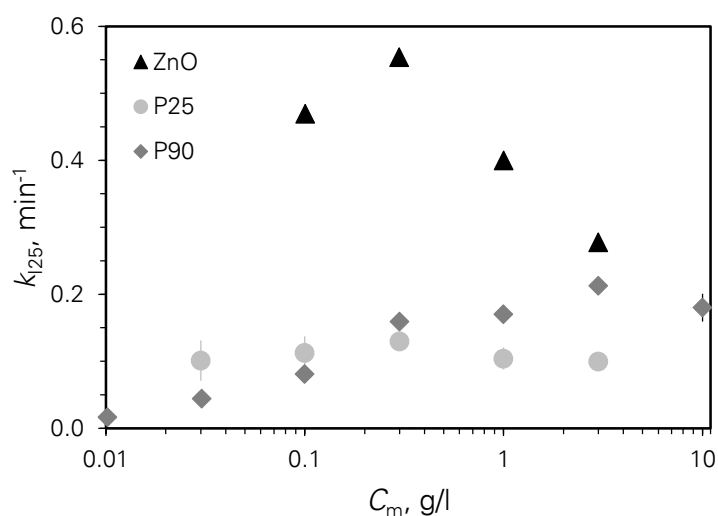


Figure 7.3 Photodegradation of methylene blue with commercial photocatalytic materials, including  $\text{TiO}_2$  P25,  $\text{TiO}_2$  P90 and ZnO. Color removal of 600 ml methylene blue (MB) of 10  $\mu\text{M}$  in reactor R20 under UV illumination (the average intensity on the illuminated surface was 26–28  $\text{W}/\text{m}^2$ ). The intensity-related reaction rate constant in the flow reactor  $k_{125}$  vs. mass concentration of photocatalysts  $C_m$ . Error bars of P25 and P90 series show the gap between minimum and maximum values of two repeated experiments. No repeated experiment with ZnO was done.

The highest reaction rate constants for  $\text{TiO}_2$  P25 and P90 are  $0.13$  and  $0.21 \text{ min}^{-1}$ , corresponding to the catalyst concentrations of  $0.3$  and  $3 \text{ g/l}$ , respectively. The difference can be explained by the morphology of these two materials. The primary size of P90 is  $14 \text{ nm}$  [197] and is smaller than that of P25, which is  $25 \pm 3 \text{ nm}$  [166]. It is followed by two consequences. Firstly, it leads to a higher specific surface area,  $90 \pm 20 \text{ m}^2/\text{g}$  compared to  $56 \text{ m}^2/\text{g}$ , respectively. It explains that the maximum reaction rate constant of P90 ( $0.21 \text{ min}^{-1}$ ) is higher than that of P25 ( $0.13 \text{ min}^{-1}$ ). Secondly, P90 suspension is less turbid than P25 suspension. Additional measurements indicate that UV light can penetrate more deeply in the P90 suspensions of the same concentration. It means that the active space in the reactor with P90 is larger than that with P25. In other words, P90 particles work more efficiently in the rear than P25 particles do. It results in the different optimum concentrations of photocatalysts. However, in the very low range of concentrations, the influence of turbidity is less important, instead, the role of energy bandgap becomes crucial. The different energy bandgaps of rutile and anatase were claimed, e.g. these values are  $3.0$  and  $3.2 \text{ eV}$  in a same report, respectively [33]. As P25 has a higher ratio of anatase/rutile ( $80/20 \text{ w/w}$  in comparison with  $90/10 \text{ w/w}$  for P90), the photocatalytic performance is better, shown by the experimental results. It was also reported that the recombination rate of electron-hole is different for anatase and rutile.

The reaction rate constants of ZnO tests lie in the higher range. The optimal reaction rate constant is  $0.55 \text{ min}^{-1}$ . The color removal of MB reached more than  $90 \%$  after  $10 \text{ min}$  of experiment. The data indicate that ZnO is more effective than  $\text{TiO}_2$ , which is in agreement with other researches [147], [166], [204]. Here, a comparison of ZnO and P25 is discussed [110]. The primary size of ZnO is much larger than that of P25,  $251 \pm 83 \text{ nm}$  with ZnO in comparison with  $25 \pm 3 \text{ nm}$  with P25. Correspondingly, the surface area of ZnO is much smaller than that of P25, i.e.,  $5.23 \text{ m}^2/\text{g}$  and  $56 \text{ m}^2/\text{g}$ , respectively. However, the reaction rate constant of ZnO is higher. Probably, the effect of size in this case is not as much important as the impact of optical properties. By using UV-VIS diffuse reflectance spectroscopy, it was shown that ZnO has a lower bandgap and absorbs light of shorter wavelengths ( $340 \text{ nm}$ , compared to  $380 \text{ nm}$  with P25), i.e., it has a broader absorbance. Neither recombination rate of electron-hole on the catalyst surface nor turbidity of the suspensions were compared. In addition, these materials have non-identical physical and chemical properties, thus the degradation pathways are dissimilar and contribute to the difference. Last but not least, when choosing photocatalytic materials, beside the reaction rate constant, other criteria should have an attention. For instance, in mineralization of ciprofloxacin [244], the photocatalytic materials remaining in aqueous solution after treatment caused the toxicity. It was proved that, while P25 is considered slightly toxic, ZnO is highly toxic. It showed the restriction of using ZnO for environmental applications.

#### **Self-synthesized nanoparticles: $\text{Fe}_3\text{O}_4/\text{SiO}_2/\text{TiO}_2$**

This work is a cooperation with Teixeira *et al.* [125]. In this test, ciprofloxacin (Cipro) was degraded with self-produced magnetic nanoparticle.

Generally, it was confirmed that after 30 min in the dark, the adsorption-desorption reaches the equilibrium. It was expected that the conversion of Cipro when being illuminated is attributed to the photocatalytic reaction. Experimental data are shown in Figure 7.4.

Due to the typical shape of the UV-VIS absorbance spectra of Cipro (notably at 240 nm and 300 nm) and the sensitivity of the used spectrometer, the absorbance peaks of lower than 0.05, corresponding to 1.3  $\mu\text{M}$  were not used for data processing. It was found that the apparent reaction rate constant  $K$  in the photocatalytic system is  $0.0146 \text{ min}^{-1}$  and the normalized reaction rate constant  $k_{125}$  in the reactor (section 6.4.2) is  $0.046 \text{ min}^{-1}$ . It means that Cipro can be degraded by 90 % after 50 min photocatalysis. When comparing the conversion of MB and Cipro of the same  $\text{TiO}_2$  P25 photocatalyst, the degradation of Cipro is faster but not much more than that of MB [210]. Accordingly, the experimental result can be modestly compared with the MB test in section 6.4.3. Here, the found reaction rate constant is rather low and equivalent to the test with 0.03–0.1 g/l  $\text{TiO}_2$  P25. The loss of the active surface area caused by immobilizing photocatalyst on magnetic particles can be the reason. The surface areas of the magnetic particles and pristine P25 are 56 and 19  $\text{m}^2/\text{g}$ , respectively. However, the use of magnetic particles is a means to avoid the post-recovery by membrane filtration. Here, an external magnetic field can be applied and the particles will be separated from the suspension. For this reason, magnetic particles are considered as a novel photocatalyst.

All results showed in this section are comparable regardless of commercial or self-synthesized photocatalysts, light intensity or working volume. It suggested that the flow reactor type can be well employed for a wide variety of research on new photocatalytic materials.

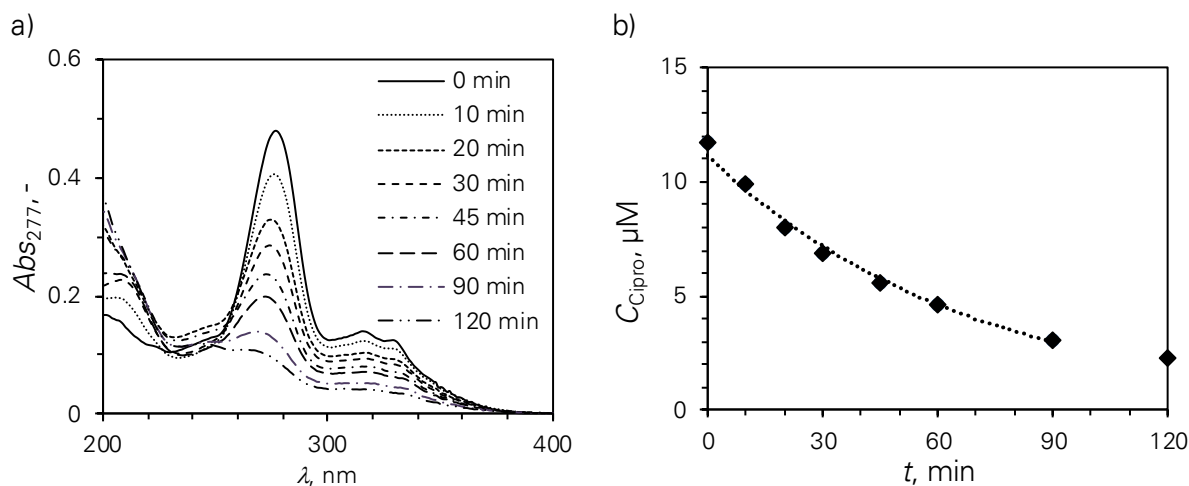


Figure 7.4 Photodegradation of ciprofloxacin with magnetic nanoparticles: 500 ml ciprofloxacin (Cipro) of 15  $\mu\text{M}$  was tested with 1 g/l self-synthesized  $\text{Fe}_3\text{O}_4/\text{SiO}_2/\text{TiO}_2$  [125]. The UV intensity on the illuminated surface was  $17 \text{ W}/\text{m}^2$ . a) The UV-VIS absorbance spectra of Cipro through 10 mm cuvette with different degradation time; b) The conversion of Cipro along with the reaction time.

### 7.1.4 Photocatalysis for commercial dye substances

In all previous experiments, methylene blue or ciprofloxacin was used. As shown in the UV-VIS spectra (Figure 4.1 and Figure 4.3), the absorbance at 365 nm, which is the mode wavelength of the UV lamp (section 3.1.4) is negligible, and no shielding effect has influence on the photocatalytic performance. Additionally, these substances used are purchased chemicals and their purity is high. However, these conditions are not guaranteed in reality. In this section, performance with two commercial dyes from Hachiba Company, Danang, Vietnam (section 7.2.1) is shown. Color removal was carried out with different light sources (artificial UV and VIS light, and natural sunlight). Because only qualitative aspect was focused, discoloration was quantified with UV-VIS spectroscopy by using a 10 mm cuvette [215] and no calibration was needed.

#### Dye Remazol Red RR

Experiments with the commercial dye Remazol Red RR was performed.

After 60 min under visible illumination, the absorbance decreases from 0.435 to 0.397, and the color was removed by 7 %. The test proves that the effect of adsorption and photosensitization under visible light are negligible (Figure 7.5a). With this result, it was expected that the adsorption in the dark has no big effect and the control test in the dark was skipped. No control test of only dye solution under UV (in the absence of photocatalyst) was carried out to test the self-sensitization under UV. It is because, in literatures, there is only claim of this phenomenon under visible light but not under UV [85], [153], [208], [209], [241].

When illuminating with artificial UV, a 70 % discoloration was obtained. It can be attributed to the photocatalytic reaction under UV. The average UV intensity was  $20.8 \text{ W/m}^2$ , which is a bit low compared to that of the average intensity of solar light ( $20\text{--}30 \text{ W/m}^2$ ).

With the outdoor experiment on a sunny day, the average measured UV intensity was  $30.7 \text{ W/m}^2$ , and color was removed by 93 % after 60 min.

To compare these experiments, the absorbance by the light energy consumption was shown (Figure 7.5b). The experimental data with the artificial illumination well fit the exponential function (Eq. (7.2)); whilst data with the solar light are deviated. There may have several reasons to explain this fact.

Firstly, the measured intensity is only of UVA and UVB (280–400 nm) since the used radiation meter has no sensitivity for UVC. For this reason, of the same recorded intensity value, the true UV intensity of solar light is stronger than that of the artificial lamp.

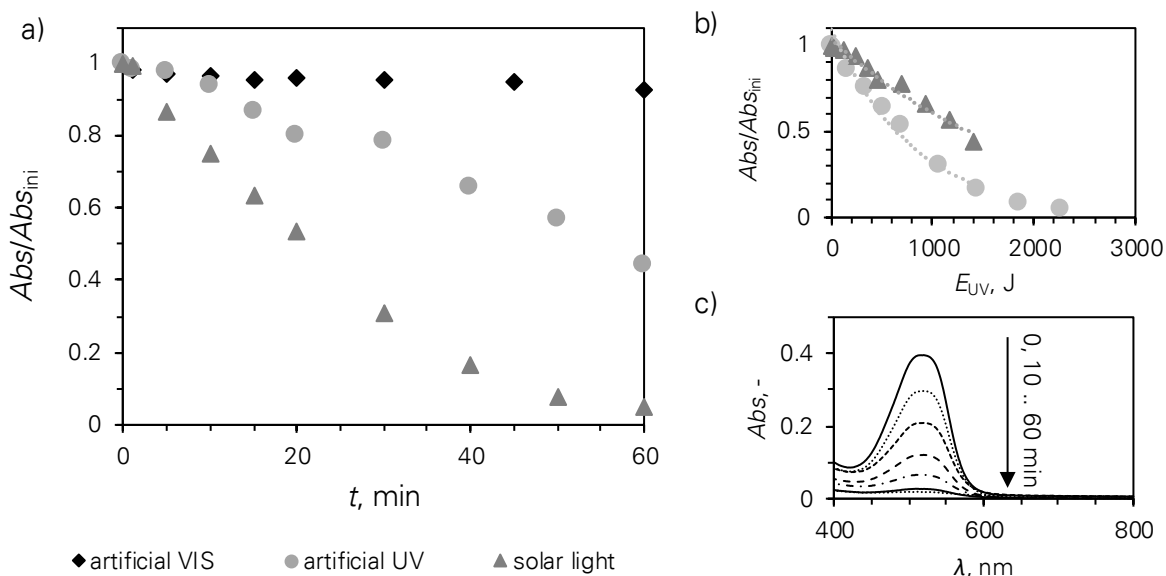


Figure 7.5 Color removal of Remazol Red RR dye under artificial UV/ visible light and solar light: The 600 ml dye solution of 31 mg/l was tested with 0.3 g/l P25 under artificial visible or UV light and sunlight. The average UVA-B intensities in three experiments were 0, 21 and 34 W/m<sup>2</sup>, respectively. Absorbance was measured with the UV-VIS spectrometer and with the 10 mm cuvettes. a) Evolution by time; b) Evolution by light energy consumption; and c) UV-VIS spectra of samples at 0, 10, and 60 min of the experiment under sunlight.

Secondly, shielding effect, which is not taken into account in the reactor model, contributes to the difference. As shown in , the Red RR dye strongly absorbs UV light, especially UVB and UVC. Some computation was performed with the 31 mg/l solution. At 365 nm, only 52 % light can transmit through a 10 mm cuvette. When the optical pathlength is 1 mm, 94 % light can transmit, while 6 % is shielded. The effect computed for 1 mm optical pathlength is 23 % and 30 % with 288 or 200 nm wavelength, respectively. While the artificial lamp has the mode wavelength of 365 nm (in the UVA range), the natural light has also UVB and UVC. It means that the restriction of UV penetration in the test with solar light is more important. This strong shielding effect in the UVB and UVC lifts the energy-dependent model of experiment with sunlight upon above that of experiment with artificial UV light.

Thirdly, the increase of temperature from 17 to 40 °C during the experiment on the sunny day may positively influence the degradation, especially at the end of the test.

And finally, as shown in Figure 7.5c), the absorption spectra are broad, spanning over 50 nm. It is caused by a number of vibrational levels resulting in the electronic absorption band. It may also be assigned to the mixture of the commercial dye substances. Either of them makes the UV-VIS spectroscopy not a precise measurement for these dye solutions. However, as introduced above, in this part of the study, a practical issue was aimed at, in particular the color removal. It needs to match the national regulation applied to the textile company. Therefore, this analysis method is applicable for the evaluation of the process.

Accordingly, the reaction rate constant in the photocatalytic setup  $K$  for the experiment with the artificial UV light is  $0.538 \text{ kJ}^{-1}$ . It is much lower than the value of  $1.224 \text{ kJ}^{-1}$  of the experiment with the solar light. The data were normalized to the average UV intensity of solar light. The computed values  $K_{125}$  are  $0.015$ , and  $0.034 \text{ min}^{-1}$ , corresponding to a required duration of 154 or 68 min for a 90 % color degradation under the average intensity.

### Dye Everzol Navy ED

Experiments with Navy ED dye were similarly performed. The results were analyzed in the same way. The graphical results are shown in Figure 7.6.

Under the artificial visible light, color was removed by 7 % (the absorbance peak decreases from 0.682 to 0.636). Like Red RR, Navy ED is not a photosensitizer under UV.

In the 60 min photocatalytic reaction, color was removed by 82 % and 67 % under the artificial UV light, and under sunlight of a cloudy day of which the average UV intensity was  $8.6 \text{ W/m}^2$ , respectively. The reaction rate constants  $K$  of the experiments with the UV lamp and with solar light are  $1.138$  and  $1.876 \text{ kJ}^{-1}$ , equivalent to the normalized values  $K_{125}$  of  $0.032$  and  $0.053 \text{ min}^{-1}$ , respectively. In other words, a 72 and 44 min reaction under the average intensity can obtain 90 % discoloration. The difference between these values is as discussed above.

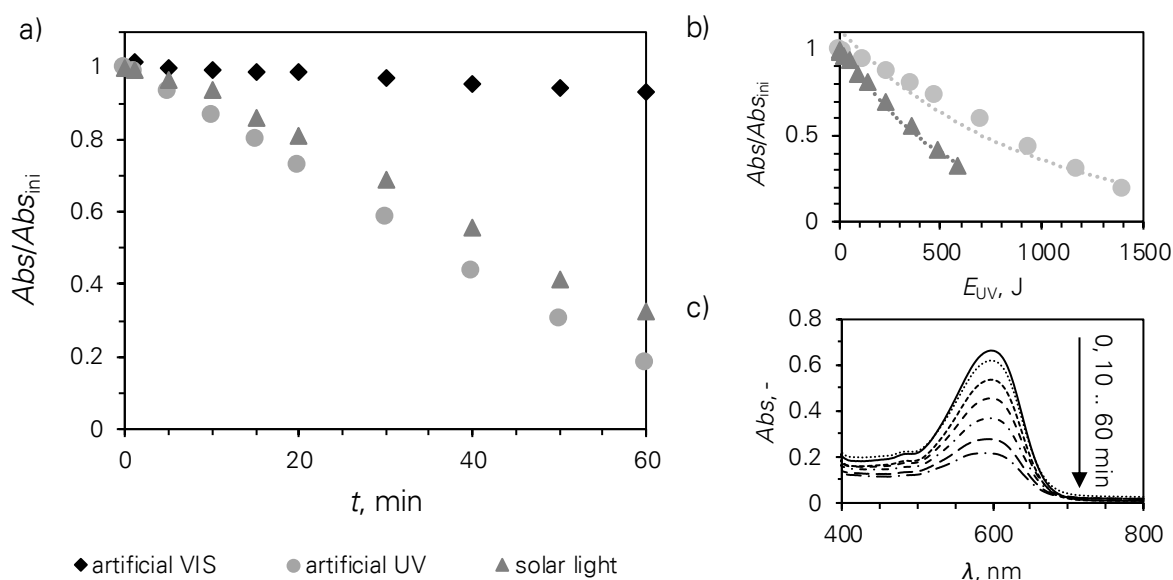


Figure 7.6 Color removal of Everzol Navy ED dye under artificial UV/visible light and solar light: The 600 ml dye solution of 24–29 mg/l was tested with 0.3 g/l P25 under artificial visible or UV light and sunlight. The average UVA-B intensities in three experiments were 0, 21 and  $9 \text{ W/m}^2$ . Absorbance was measured with the UV-VIS spectrometer and with the 10 mm cuvettes. a) Evolution by time; b) Evolution by light energy consumption; and c) UV-VIS spectra of samples at 0, 10, and 60 min of the experiment under sunlight.

Shielding effect was considered at 365 nm, 303 nm and 200 nm. Accordingly, 33 %, 76 % and 88 % light was shielded when penetrating through the total optical length of 10 mm, respectively. The corresponding data for 1 mm optical pathlength are 4 %, 13 % and 19 %.

### 7.1.5 Concluding remarks

In this subchapter, applications of photocatalysis were presented in different selected case studies.

Previously, the influence of testing volume on photocatalysis was shown (sections 6.3.1 and 6.4.1). The explicit relation was given by means of the reactor model (section 3.3.3). Based on the results, an elimination of the influence of volume for a comparison of different tests was rendered. The volume-related degradation rate constant was proposed.

As solar utilization is a trend of photocatalysis application, the subchapter introduces experiments under natural light. Color removals of methylene blue (MB) were examined. Though  $\text{TiO}_2$  P25 photocatalysts is not activated by visible radiation, the test under artificial visible lamp showed the loss of MB. It can be caused either by the photo-induced hydrophilic effect or by self-sensitization. It positively influences the degradation of MB under solar illumination. Sunlight utilization was tested on sunny and cloudy days. To omit the influence of the weather condition in the tests, the reactor model previously presented in subchapter 3.3 was adapted. Photosensitization, photo-induced hydrophilic effect and shielding effect were not accounted. Also the spectral light distribution was not interpreted. However, data computed by the UV energy consumption model are in good agreement with experimental data. A normalization to the average UV intensity of solar light was considered. The data are comparable with experimental results in chapter 6, where artificial UV was illuminated.

Different photocatalytic materials were compared, including commercial nanopowders (P25, P90, and ZnO), and self-synthesized magnetic particles. Depending on the used materials and the organic substances, the photocatalytic performance takes only few to dozens of minutes, which is quite fast, compared to other published data. Data were normalized to the average UV intensity of solar light. When using the optimal photocatalyst concentrations of P25, P90 and ZnO, the intensity-related reaction rate constant in the flow reactor  $k_{I25}$  are 0.13, 0.21 and  $0.55 \text{ min}^{-1}$ . It means that, a duration of 18, 11 and 4 min is sufficient for 90 % color removal of MB with P25, P90 and ZnO, respectively. With the 1 g/l magnetic particles, ciprofloxacin can be degraded by 90 % after 50 min. No optimization of the photocatalyst concentration was initiated, as the test was aimed at the possibility of utilizing the novel materials to overcome problems of post-treatment. All results are comparable and reproducible regardless of experimental conditions, e.g., light intensity, testing volume. They also show good performances of various photocatalysts in the photocatalytic flow reactor.

Red or navy solutions of two commercial dye substances from one textile company in Danang, Vietnam (section 7.2.1) were tested for the degradation. The P25 photocatalyst was used and its optimal concentration of 0.3 g/l was employed. Experiments were done under artificial UV,

artificial visible light and sunlight. The tests under visible light showed the loss of 7 %color after 60 min regardless of dye substances. Under artificial UV illumination or sunlight, the vanishing of color was observed. The reaction rate constants were found from the UV energy-dependent model. They were normalized to the average UV intensity of solar light. Accordingly, 90 % color can be removed after 68 and 44 min with the red and navy solutions, respectively. The findings suggest that solar photocatalysis is relevant for the degradation of colored WW from textile industry. However, it should be note that the shielding effect induced by these two dye molecules can be a problem when applying spectral illumination. For instance, up to 30 % or 19 % of light (200 nm) was shielded when transmit through 1 mm optical path-length of red and navy dyes, respectively.

## **7.2 INDUSTRIAL APPLICATION IN A TEXTILE COMPANY**

Earlier, photocatalytic application was tried at pilot scale for wastewater treatment in a textile company in Vietnam via the CLIENT/NaViTex project 02WCL1264A. After the 4-year project, there is still obstacle which hinders the photocatalytic application at industrial scale.

In the first section, the scenario of one textile company in Danang, Vietnam is presented. Selected results of the CLIENT/NaViTex project are shown and the limitation of current (semi) pilot photocatalytic setups in the company is discussed. The challenges is then introduced in the next section. The fourth section is the most important part of this subchapter, where the configuration of an industrial scaled photocatalytic reactor is proposed.

### **7.2.1 Scenario in March 29 Textile-Garment Joint Stock Company**

March 29 Textile-Garment Joint Stock Company (Hachiba) was found in 1976 in Danang, Vietnam. It manufactures towels, apparel and washing products. The company is also a supplier in the American, European and Japanese markets.

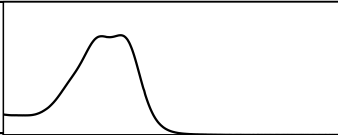
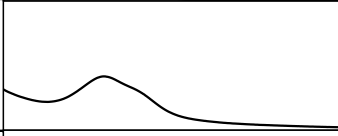
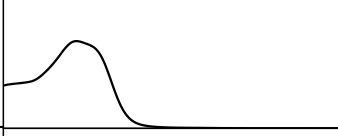
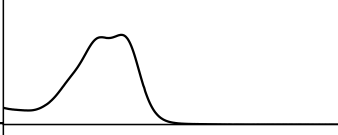
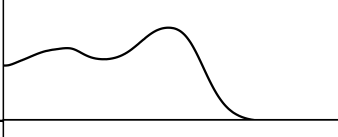

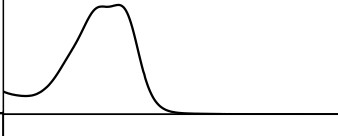
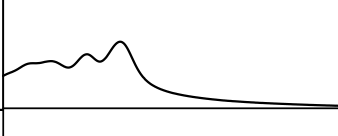
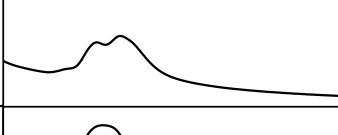
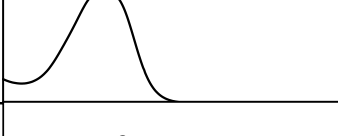
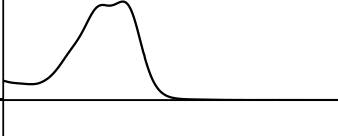

Typically, in textile companies, dyes are spread to the effluents. Wastewater (WW) after the dyeing and washing processes is usually dark. In Hachiba Company, the WW after processing was estimated to be 6–10 m<sup>3</sup>/day (said Mr. Tran Xuan Hoe, vice general director, in 2014). The current effluent treatment plant includes three main steps: mechanical separation, biotechnological treatment and sedimentation (section 7.2.4, Figure 7.12). However, treated WW does not fulfil the Vietnamese regulation of dye WW to be discharged Table 7.1. The most serious obstacle is that the complete discoloration is not achieved, especially in the case of strongly colored dyes, such as those listed in Table 7.2. In reality, when WW drains into the effluents of the industrial park, the company has to pay a fee for an extra treatment.

Table 7.1 Technical regulation of textile wastewater in Vietnam [245]. Wastewater satisfying upper limitations in column A (called wastewater type A in this thesis) can be discharged into domestic water. Wastewater with upper limitations in column B (called wastewater type B) must be treated.

No	Parameter	Unit	Upper limitations	
			A	B
1	Temperature	$^{\circ}\text{C}$	40	40
2	pH	-	6–9	5.5–9
3	Color index (pH = 7) for new plants	Pt-Co	50	150
	for current plants	Pt-Co	75	200
4	BOD <sub>5</sub> at 20 $^{\circ}\text{C}$	mg/l	30	50
5	COD for new plants	mg/l	75	150
	for current plants	mg/l	100	200
6	Total suspended solids	mg/l	50	100
7	Cyanide	mg/l	0.07	0.1
8	Chloride	mg/l	1	2
9	Cr <sup>6+</sup>	mg/l	0.05	0.1
10	Surfactants	mg/l	5	10

Regarding the regulation, color is determined by the Pt-Co measurement method (single point photometry). However, the UV-VIS spectra of different dye solutions in Table 7.2 show that they have a broad and various range of absorbance. For investigation in the next section, if possible, another concept for analysis, UV-VIS spectroscopy, was used to substitute this single point photometry.

Table 7.2 Commercial dyes provided by Hachiba Company (Danang, Vietnam). UV-VIS spectra with the horizontal axis of wavelengths scaled from 400 to 800 nm and the vertical axis of the absorbance scaled from 0 to 1 (dimensionless).

Dye powder	UV-VIS absorbance spectrum	
	Concentration mg/l	Spectrum
Cibacron Red S 2B	35	
Cibanon Red 2BM	45	
Entracion Orange F2R	34	
Entracion Red 3BF	35	
Everzol Black ED	33	
Everzol Navy ED	18	
Everzol Red ED-3B	37	
Indanthreen Orange GR	40	
Indanthreen Pink R	44	
Remazol Red RR	41	
Synozol Red HF-6BN	35	
Synozol Scarlet SHF-2G	40	

### 7.2.2 The CLIENT/NaViTex project

The CLIENT/NaViTex project 02WCL1264A (September 2012 – April 2016) is a cooperation project between the Federal Ministry of Education and Research (BMBF), Germany and the Ministry of Science and Technology (MOST), Vietnam. The project aimed at the “Water treatment in Vietnam using photocatalytic oxidation”.

The project was engaged with the current situation of two textile companies in Danang, Vietnam. One of two is March 29 Textile-Garment Joint Stock Company (Hachiba). The project mission is the integration of photocatalysis to enhance the conventional effluent treatment ability for discoloration. The WW satisfying wastewater type B (Table 7.1) is expected. Economically, the cost of operating photocatalysis should be less than the penalty required when the WW does not fulfil the eligible criteria.

The working plan was coordinated by the Institute for Research and Development of Natural Products (INAPRO), Hanoi University of Science and Technology. The photocatalytic materials were provided by Gesellschaft zur Förderung von Medizin-, Bio- und Umwelttechnologien e. V. (GMBU) and the photocatalytic setups were designed by UMEX GmbH Dresden. The wastewater samples used in the tests were collected from Hachiba Company. The experiments were mainly carried out in the Department of Science and Technology, MOST, Danang, Vietnam. The following subsections show selected experiments operated by the author within the framework of the project. More details or similar data can be found in reports elsewhere [246]–[248].

#### 7.2.2.1 Photocatalysis combined with hydrogen peroxide

##### *The pilot system*

The pilot photocatalysis system was designed by UMEX GmbH [248] and fabricated within the project. It consists of three main components: a photoreactor, a reservoir and a pump (Figure 7.7). The water to be treated is stored in a closed reservoir. There are two reservoir volumes, one is up to 20 l and other up to 2000 l. A centrifuge pump transports the water to the photoreactor with a flow rate of 39 l/min. The reactor has the inner diameter of 228 mm and the effective length of 560 mm. It can store approx. 17 l. The photocatalytic degradation takes place in this cylinder reactor. The mercury UV lamp housed in a quartz tube of 90 mm outer diameter is positioned in the center of the reactor. The lamp has a broad energy distribution range of 240–400 nm, the electric power of 2000 W and the radiance of 20–100 W/cm. With the addition of hydrogen peroxide  $\text{H}_2\text{O}_2$ , hydroxyl radicals are formed under UVC irradiation (wavelengths of 240–280 nm), and the degradation occurs. Optionally, immobilized photocatalyst prepared by GMBU [246] can be added, and the combined  $\text{H}_2\text{O}_2$  photocatalysis promotes the degradation. The photocatalytic material was prepared by dip coating 3D glass fiber fabric (Abstandsgewebe) in  $\text{TiO}_2$  sol (code K1297, K1295E and K1295G [246]), followed by drying and thermal treatment at 600 °C.

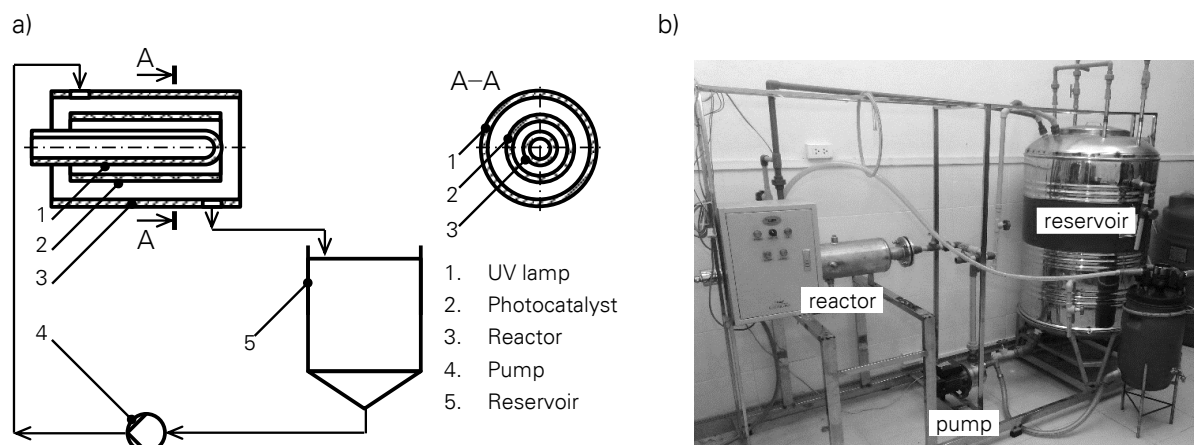


Figure 7.7 The NaViTex's pilot combined photocatalytic system: a) The diagram; and b) The setup in reality. Photo credit Steffen Johnne (UMEX GmbH).

#### *Color removal of methylene blue*

Degradation with hydrogen peroxide under UV illumination was tested for the color removal of 40 l methylene blue (MB) with a high initial concentration, 83  $\mu\text{M}$ . An amount of 20 ml commercial  $\text{H}_2\text{O}_2$  30 % was added to the solution prior to the test.

According to the Vietnamese regulation for dye wastewater (WW) (Table 7.1, color index (Pt-Co unit) is recommended to inspect the experimental results. This method is relatively precise with the red-orange color which absorbs light at 500 nm. However, in this test, the MB solution is blue, which is the complementary color of orange, i.e., the absorbance of MB 10  $\mu\text{M}$  at 500 nm is low (0.04 when measured with a 10 mm cuvette, see Figure 4.1). It means that the Pt-Co analysis has low sensitivity. Therefore, the UV-VIS absorbance at 665 nm of the samples was used in the analysis.

A short degradation with UV/ $\text{H}_2\text{O}_2$  of 6–10 min is able to completely remove the color of the solution (Figure 7.8a). The data suggest that this pilot system has a potential application in the treatment of the WW of the company.

#### *Color removal of real wastewater from Hachiba Company*

As mentioned, the current treatment plant of the company is unable to treat the highly colored wastewater (WW). Inquiries of strong colors of customers are usually refused, so the company can ensure the pale WW after treatment. For this reason, occasionally the WW is dark. As pH is typically high (10–12) and no microorganism exists, the WW was collected and stored for further tests. It was kept in ambient conditions and not exposed to direct sunlight. Before the experiments, all parameters were re-measured.

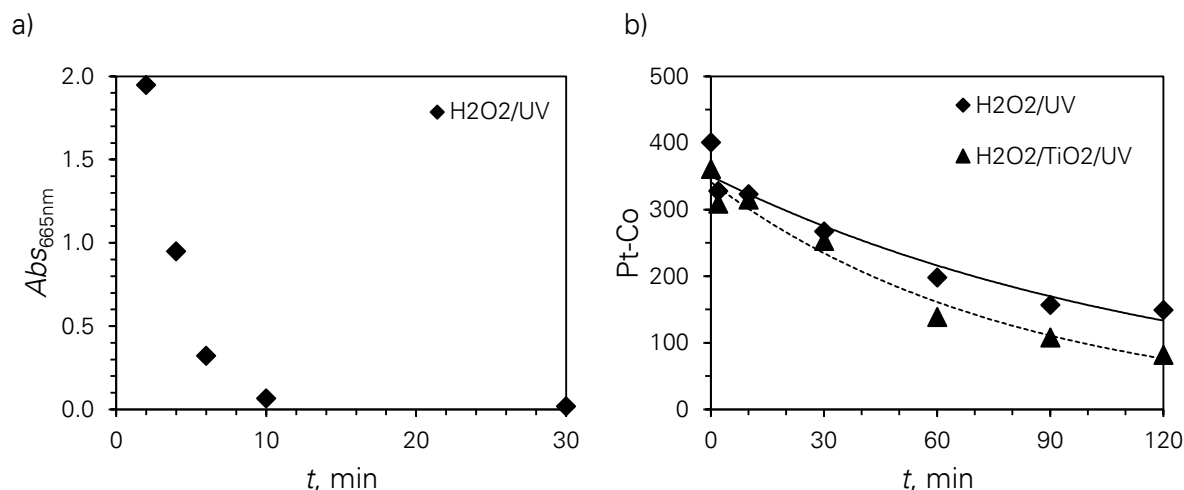


Figure 7.8 Photodegradation of colored solutions with the NaViTex's pilot combined photocatalytic system: a) 83  $\mu$ M methylene blue degraded with  $H_2O_2$  under UV and analyzed with a UV-VIS spectrometer; and b) Orange wastewater from Hachiba Company degraded with  $H_2O_2$  under UV (sample "H2O2/UV"), or with  $H_2O_2$  and  $TiO_2$  under UV (sample "H2O2/TiO2/UV") then analyzed with Pt-Co.

To have a model highly colored WW, a mixture of WW after dyeing (strongly colored) and after the entire treatment (lightly colored) was tested. In this experiment, WW after the dyeing and washing processes was collected in January 2015. The WW is dark orange and the color index is 4080 Pt-Co unit, measured according to the TCVN 6185:1996 method, which is equivalent to the ISO 7887:1985. BOD and COD measured at the collecting time are 1030 and 1737 mg/l, respectively. No visible suspended solids were observed after filtering. WW after the treatment plant was collected on June 04, 2015. The color index is 144 Pt-Co unit. BOD and COD are 13.8 and 25.1 mg/l. On the date of experiment (June 08–09, 2015), 2.4 l orange WW was mixed with 37.6 l pale WW. The color index of the mixture is 360–400 Pt-Co unit, which is twice as high as that of the WW type B. COD is approx. 240 mg/l. No BOD was measured.

Two experiments were done with and without the presence of the photocatalyst. An amount of 60 ml commercial  $H_2O_2$  50 % was added into the mixed WW in prior to each experiment. Experimental data are shown in Figure 7.8b. After 120 min, 63 % of the color was removed by  $H_2O_2$  under UV. With the addition of immobilized photocatalyst, the efficiency increases to 77 %. The reaction rate constants were found to be 0.483 and 0.749  $h^{-1}$ , respectively. This proves the improvement of the treatment by the addition of the photocatalyst. The corresponding color indices at the end of the tests are 149 and 82 Pt-Co unit and meet the requirement of the WW type B. Additionally, other properties of the obtained WW also meet the required characteristics. In particular, BOD after the photocatalytic treatment with and without the photocatalysts are 38 and 36 mg/l; while COD are 68 and 64 mg/l, respectively.

### 7.2.2.2 Solar photocatalysis

#### *The solar photocatalytic reactor*

Experiments were conducted with solar light using immobilized photocatalyst. N-modified TiO<sub>2</sub> (code K1297 [246]) coated on the aluminum ceramic (monolayer coating) was provided by GMBU (Figure 7.9) [246]. The photocatalytic sponges were placed inside a plate reactor fabricated by UMEX GmbH [248]. The reactor is split with 15 parallel channels. Water to be treated is pumped from the bottom, navigated by the split sheets and came out from the top of the reactor. The reactor can carry 7.7 l of aqueous solution. In the tests, the total tested volume was 15 l (including the solution in the tubes and the reservoir). The solution was circulated with a flow rate of 4 l/min. The reactor was placed on a fixed inclined plane of approx. 35–40 °. The illuminated area is 68 × 95 cm<sup>2</sup>.

#### *Color removal of methylene blue*

One of the preliminary tests is the color removal of methylene blue (MB). MB was dissolved in tap water to have the concentration of approx. 10 µM. No properties of tap water was reported. The photocatalytic test was carried out from 10:54 to 11:54 (local time) on June 09, 2015, at DOST Danang. It was partly cloudy. The temperature of the aqueous solution in the reservoir varied from 35 °C to 51 °C. The color removal along the treatment time can be observed by naked eyes (shown by the inset of Figure 7.10). The UV-VIS absorbance peaks at 664 nm were used for data analysis. After 1 h, the color was completely removed. The discoloration efficiency of 95 % and 97 % was found corresponding to the reaction time of 30 and 60 min, respectively. The photocatalytic reaction rate constant is 0.101 min<sup>-1</sup>. When considering the use of solar light, the method is potential, especially in strongly sunny regions like Danang, Vietnam.

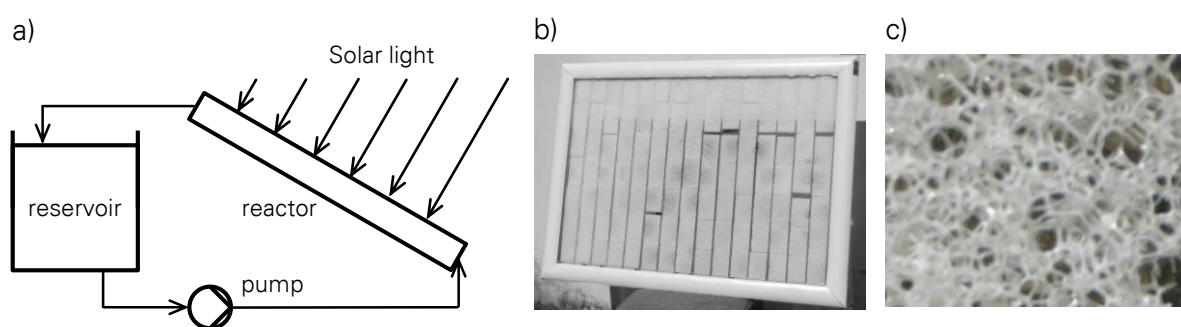


Figure 7.9 The NaViTex's solar photocatalytic setup: a) The diagram (the reactor is from the side view); b) Image of the reactor (from the front view); and c) The immobilized photocatalyst. Photo credit Steffen Johne, UMEX GmbH.

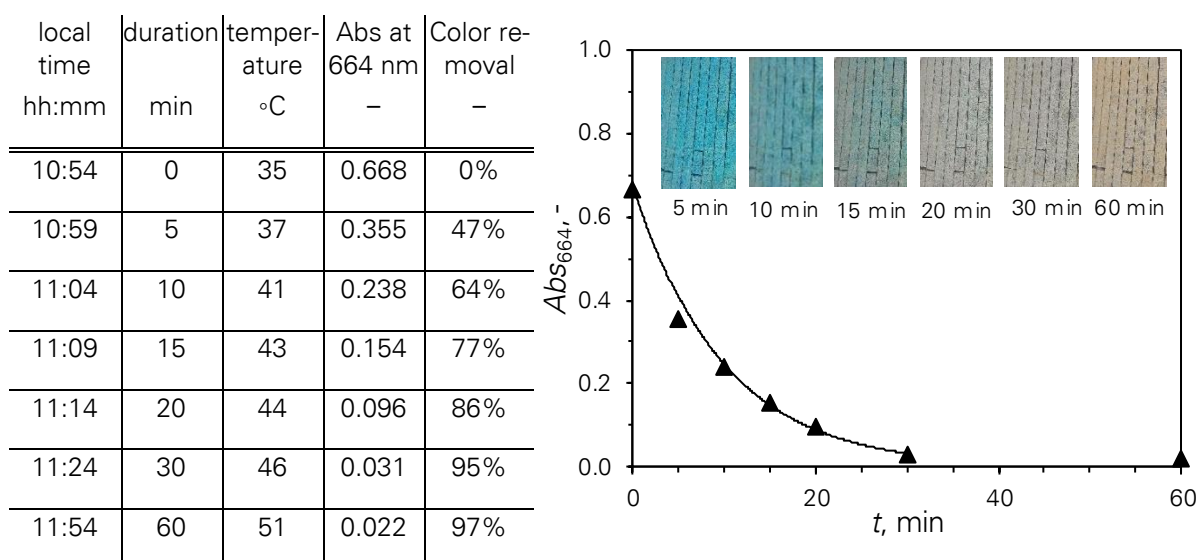


Figure 7.10 Photodegradation of methylene blue with the NaViTex's solar photocatalytic setup. The inset shows the pictures of the solution in the reactor along with the irradiation time.

#### *Color removal of real wastewater from Hachiba Company*

WW after dyeing and washing processes of Hachiba was collected on the June 01, 2015. The WW has the COD of 316.5 mg/l, the BOD of 16.2 mg/l, and the color index of 1595 Pt-Co unit. The WW were diluted 5 times with tap water to have 342 Pt-Co unit, which is 1.7 times as high as that of the target (for WW category B, see Table 7.1)

Experiments were carried out from 14:27 to 16:57 (local time) on June 10, 2015, at DOST Danang in a very sunny day. The UV index recorded by ASUS Zenphone 5 with ASUS Weather and Time Widget was 9/12. The temperature of the aqueous solution in the reservoir varied from 40 to 47 °C.

The control test was performed without photocatalyst. The WW was stored in an open tank illuminated by solar light. The color index at the end of the test was 382 Pt-Co unit, which is a bit higher than that at the beginning. It is caused by the evaporation of the solution in the hot and dry conditions. The result suggests that the colored WW is not self-degraded under solar illumination.

In the meantime, the solar photocatalytic test was taken place in the reactor. Through the startup process, water remaining from the previous experiment inside the reactor diluted the solution (from 382 to 244 Pt-Co unit). After a 5-min circulation of the flow for homogeneity, the color decreased over time. Figure 7.11 shows the data of the experiment. The photocatalytic reaction rate constant is  $0.109 \text{ h}^{-1}$ . The discoloration efficiency is 27 % after 2.5 h. The color index at the end is 250 Pt-Co unit, which is higher than the upper limitation of the Vietnamese standards. It is estimated that a value of 200 Pt-Co unit for WW quality B can be achieved by prolonging the photocatalysis to 4.5 h. In the real treatment plant, the combination with other methods (e.g. biological treatment) is recommended.

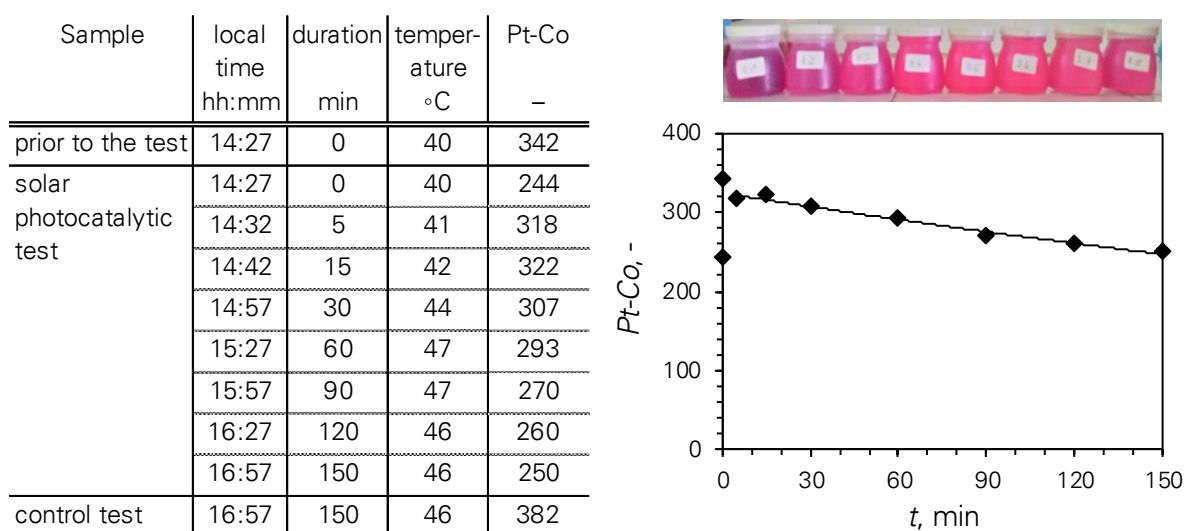


Figure 7.11 Photodegradation of wastewater from Hachiba Company with the NaViTex's solar photocatalytic setup. The upper right figure shows the color change of the collected solutions along with the irradiation time. Photo credit Cong Thanh Tran, INAPRO.

### 7.2.3 Challenges

In the first section of this subchapter, the scenario of March 29 Textile-Garment Joint Stock Company (Hachiba) in Vietnam was presented. Color removal in wastewater treatment is one of the biggest issues of the company. As indicated in the regulation of the government, treated water must satisfy observation analysis as well as ensure the pale color (Table 7.1).

Experimental results of the NaViTex project showed the promising application of photocatalysis for the treatment of dye polluted WW. Two photocatalytic setups were tested. Different types of water were treated, including methylene blue (MB) and real WW from the textile company. MB is a model textile dye and usually the discoloration of 10–20  $\mu\text{M}$  solution takes less than 1 h. Dissimilarly, a treatment of real WW requires a few hours. It means that the treatment in reality is more complex. Different techniques should be implemented, such as the use of slurry catalysts to ensure the large active site, the modification of photocatalysts, the strong light intensity, the reactor design and the combination with other processes.

The NaViTex project introduced two photocatalytic concepts.

The first system works based on the combination of  $\text{H}_2\text{O}_2$  under UV and photocatalysts. There is a potential application of such a pilot system. Though the cost estimation meets the requirement of the company, the use of the medium pressure lamp is not environmentally friendly and it should be accounted. Additionally, the disposition of the lamp is facing the problem of up-scaling. To some extent, the system can be considered to be applied in a small industrial plant and for treatment of highly colored water.

The second system works under solar illumination, which is the trend of photocatalytic applications. The conversion of MB in the NaViTex's solar photocatalytic setup can be roughly compared with that in the research reactor (chapter 3) because of the same reaction pathway. The reaction rate constant of the NaViTex's experiment was  $0.101 \text{ min}^{-1}$ , which is similar to the degradation with  $0.03 \text{ g/l TiO}_2 \text{ P25}$  catalyst in the research reactor under  $25 \text{ W/m}^2$  UV irradiation (section 6.4.3). The concentration of  $0.03 \text{ g/l}$  is very low. Not surprisingly it is because slurry photocatalysts exhibit a higher surface area than immobilized photocatalysts. In addition, the short retention time is a limitation. Further improvement of the reactor should be considered for an up-scalability.

## 7.2.4 An up-scaled photocatalytic reactor in a wastewater treatment system

As presented in previous sections, the flow reactor prototype with slurry photocatalysts can be the ideal solution for an industrial application. Here, in the first subsection, photocatalysis is proposed to be an additional step of the wastewater treatment system of Hachiba Company, Danang, Vietnam. Data of preliminary tests which were used as the input data for simulation are presented in the next subsection. Based on that, an up-scaled reactor is introduced.

### 7.2.4.1 Photocatalysis integrated within the wastewater treatment plant

Currently, Hachiba Company (section 7.2.1) operates a conventional wastewater (WW) treatment. Generally, the system includes these following steps: mechanical separation, neutralization, sedimentation and biological treatment (Figure 7.12). The WW after dye processing has concentrated color, high pH, high COD and BOD. This WW, labeled "WW type I", has a smaller capacity of  $6\text{--}10 \text{ m}^3/\text{day}$ . WW is then gathered with municipal WW thus its compositions are not controllable. It is treated with physical, chemical and biological methods. At the end of the treatment process, the WW, named "WW type II", has light color, neutral pH, low COD and BOD, but in a large amount.

In this work, slurry photocatalysis is proposed to be used in the current treatment plant as an integrated step. There may have two possibilities corresponding to two types of WW named above (Figure 7.12).

As shown in section 7.2.4.2, with strongly colored WW (WW type I, Figure 7.12), the photocatalytic reaction is slow. Although solar light can be utilized, in order to enhance the degradation rate, high UV intensity (section 6.4.2) supplied by an artificial lamp is suggested. The WW usually has high pH. This property is an advantage as it promotes the photocatalytic degradation of the cationic dyes (section 6.4.5). When anionic dyes are used, the pH of water should be adjusted to be acidic, because this supports the dye adsorption on the positively charged photocatalysts. Different materials should be endeavored to obtain the best photocatalytic activity (section 7.1.3). The photocatalyst loading should be optimized accounting the optical

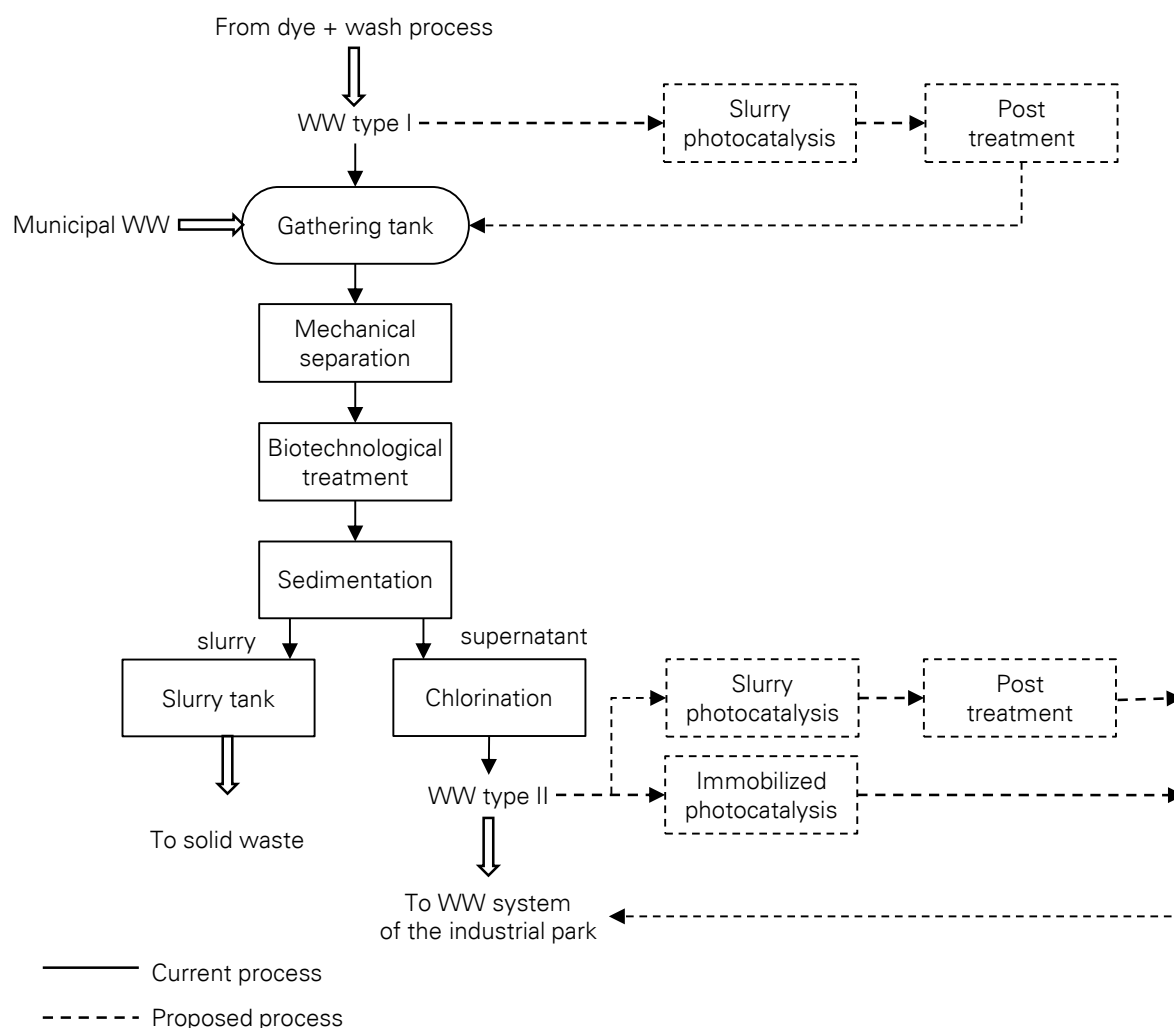


Figure 7.12 Photocatalysis introduced in a wastewater treatment plant.

penetration (section 6.4.3). Because of either turbidity of suspensions (section 6.4.3) or shielding effect of dye solutions (section 7.1.4), the optical path of the reactor should be small to ensure optical penetration. Any moderate or intense dispersion procedure that yields homogeneous, stable photocatalyst suspensions and avoids sedimentation should be used before loading the suspensions into the slurry reactors. Ultrasonic dispersion is a proper method to pretreat the photocatalysts (section 6.4.6). Dispersion can be performed at high catalyst concentration (1 g/l to 10 g/l). The combination of photocatalysis with other techniques is recommended to enhance the performance, e.g. the combined photocatalysis with  $\text{H}_2\text{O}_2$  (section 7.2.2). Membrane filtration can be the post-treatment to recover the photocatalyst. The operational cost must be estimated [100]. The alternative can be to use traditional separations, such as agglomeration by adjusting pH, coagulation with additives, integrated with sedimentation.

As WW type II has the light color, the treatment is not very complicated (section 7.1.4). In sunny regions, the utilization of sunlight (sections 7.1.2 and 7.1.4) can be an option. UV intensity can be intensified (section 6.4.2) by using the parabolic concentrator [17]. To take advantage of the visible light, modified photocatalysts should be used whose bandgap is narrowed. The immobilized photocatalyst on supports (section 7.2.2) can be a solution to overcome the technical and economical drawbacks of post-treatment, especially with a large amount of wastewater. The use of photocatalytic magnetic nanoparticles (section 7.1.3) is an alternative as they can be easily separated by an external magnetic field.

The treatment of WW with dark color (WW type I, Figure 7.12) is more problematic than with light color (WW type II, Figure 7.12). Hence, in next two subsections, preliminary tests and a simulated up-scaled photocatalytic reactor for this type of WW are introduced.

#### 7.2.4.2 Preliminary tests with strongly colored water

In this subsection, at first, the definition of strong color or high concentration of solutions is given. Then, photodegradation of highly colored solutions is presented. Methylene blue, a model dye substance, and commercial Everzol Navy ED dye from Hachiba Company were employed. As titanium dioxide P25 photocatalysts are commercial available, they were used in these tests. Color removal with P25 under UV illumination is reported.

##### *High concentrations*

In the test, methylene blue (MB) and Navy ED dye have the initial concentrations of 10 times as high as in previous tests. Samples were measured with a UV-VIS spectrometer and compared with wastewater (WW) from Hachiba Company in Danang, Vietnam (section 7.2.1). UV-VIS spectra of all samples were shown in Figure 7.13.

According to the Beer-lambert law, the absorbance  $Abs_\lambda$  of the solution at the wavelength  $\lambda$  measured through  $L$  optical pathlength is

$$Abs_\lambda = \varepsilon_\lambda L C_m, \quad (7.6)$$

where  $C_m$  is the mass concentration of solute in the analyzed solution. For WW, the samples were diluted by a dilution factor  $F_D$

$$F_D = \frac{C_{m,ini}}{C_m}, \quad (7.7)$$

and Eq. was rewritten as

$$Abs_\lambda = \varepsilon_\lambda L \frac{C_{m,ini}}{F_D} = \tau_{app,\lambda} L F_D. \quad (7.8)$$

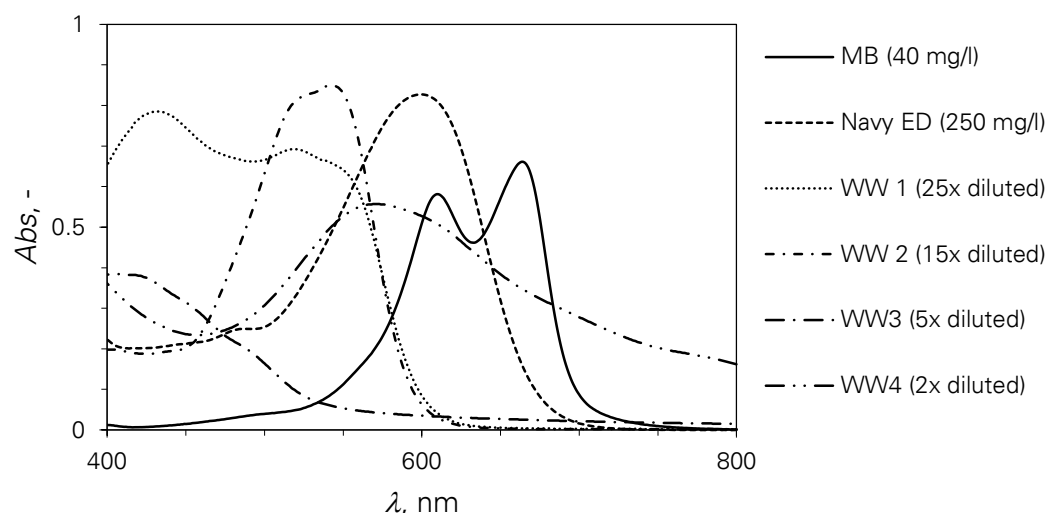


Figure 7.13 UV-VIS spectroscopy of highly colored (waste) water. UV-VIS absorbance spectra of 40 mg/l methylene blue (MB), 250 mg/l Everzol Navy ED dye solution, wastewater WW1 (25-time diluted), WW2 (15-time diluted), WW3 (5-time diluted) and WW4 (2-time diluted) which were collected from Hachiba Company (Danang, Vietnam) (section 7.2.1). MB and Navy ED were measured with 1 mm cuvette, WW1–4 were measured with 10 mm cuvette.

The value  $\tau_{app,\lambda} = \varepsilon_{\lambda} C_{m,ini}$  is called the apparent turbidity. There is a fact, when the concentration is high, dimerization can happen. This phenomenon was observed with MB molecules at 610 nm (Figure 4.1 and Appendix A4) [211]. This may happen with WW1 at approx. 500–600 nm (Appendix A6). Thus,  $\tau_{app,\lambda}$  is only an apparent value, which counts such phenomenon. However, it can characterize the color intensity of solutions.

The computed apparent turbidity is shown in Table 7.3. Accordingly, the color intensity of MB or Navy ED is a half of that of WW1 or WW2, and 6 times as high as that of WW4 and WW3, respectively. Note that, WW1 and WW2 have exceptionally dark color. WW's color is usually lighter, like WW3 and WW4. It is to say, though the used concentrations are not the highest concentration of the WW, the experiments approached a nearer fact.

#### *Experiments with methylene blue*

Different P25 photocatalyst amounts were used to examine the efficiency of the degradation of methylene blue under UV illumination. Accordingly, after 30 min of photocatalytic degradation, in all tests, color removal efficiency is higher than 50 %. With the lowest P25 concentration of 0.2 g/l, 70 % color was removed after 2.5 h (Figure 7.14).

The higher photocatalyst concentration of 0.5 g/l and 1 g/l helped to achieve approx. 85 % and 92 % discoloration after the same period. Accordingly, the intensity-related reaction rate constants in the flow reactor  $k_{2,l25}$  (sections 6.4.2 and 6.4.4) are 0.011, 0.021 and 0.031 min<sup>-1</sup>, corresponding to the P25 concentration of 0.2, 0.5 and 1.0 g/l. The promising results give an attention to the application of photocatalysis for textile wastewater treatment in reality.

Table 7.3 UV-VIS spectroscopy of highly colored (waste) water. Numerical results for Figure 7.13: Apparent turbidity  $\tau_{app,\lambda}$  at wavelength  $\lambda$  according to Eq. .  $C_m$  - mass concentration,  $F_D$  - dilution factor,  $\lambda$  - wavelength of absorbance peak,  $L$  - optical pathlength,  $Abs$  - absorbance peak, and  $\tau_{app}$  - apparent turbidity.

Sample	$C_m$ , mg/l	$F_D$ , -	$\lambda$ , nm	$L$ , mm	$Abs_{\lambda}$ , -	$\tau_{app,\lambda}$ , mm <sup>-1</sup>
methylene blue	40	1	664	1	0.661	0.66
Navy ED	250	1	610	1	0.883	0.88
wastewater WW1	na	25	433	10	0.785	1.96
wastewater WW2	na	15	543	10	0.850	1.28
wastewater WW3	na	5	402–408*	10	0.384	0.19
wastewater WW4	na	2	569–573*	10	0.557	0.11

\* WW3 and WW4 have a plateau peak in the mentioned wavelength

#### Experiments with Everzol Navy ED

Color removal of Everzol Navy ED is shown in Figure 7.15. The optimal concentration of P25 obtained in the previous part (1 g/l) was used. The control test was performed in the dark. The color remained unchanged (Figure 7.15), which proves that the adsorption-desorption reaches the equilibrium. It also demonstrates that the color change under artificial UV light is attributed to the photocatalytic reaction. During the test under UV illumination, the color was slowly removed and color removal efficiency reached 30 % after 5 h (Figure 7.15), which is much lower than that of the test with MB. Normalization to the average intensity of solar light (25 W/m<sup>2</sup>) was performed. The reaction rate constant in the photocatalytic setup  $K_{125}$  is 0.001 min<sup>-1</sup> or 0.057 h<sup>-1</sup>, while the reaction rate constant in the flow reactor  $k_{125}$  is 0.002 min<sup>-1</sup> or 0.111 h<sup>-1</sup>. These values were used as the input parameter for computation in the next subsection.

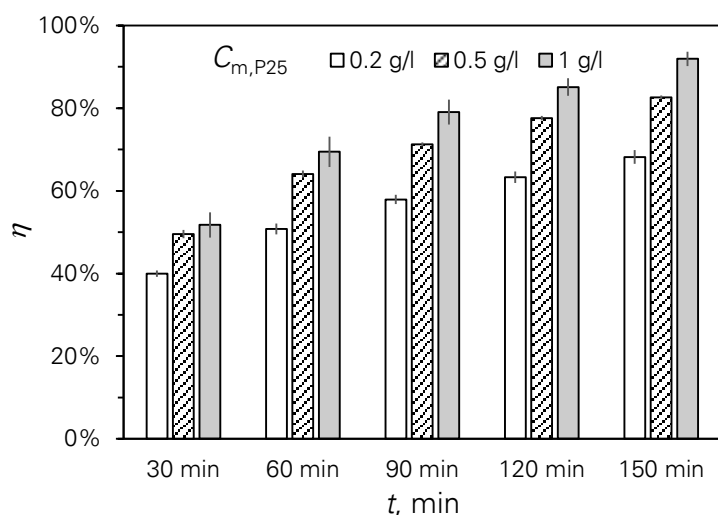


Figure 7.14 Color removal efficiency with the high initial concentration of methylene blue. Photodegradation of 400 ml MB solution of 40 mg/l with 0.2, 0.5 and 1 g/l P25 in reactor R10 under UV illumination (the average intensity on the illuminated surface was 22 W/m<sup>2</sup>).

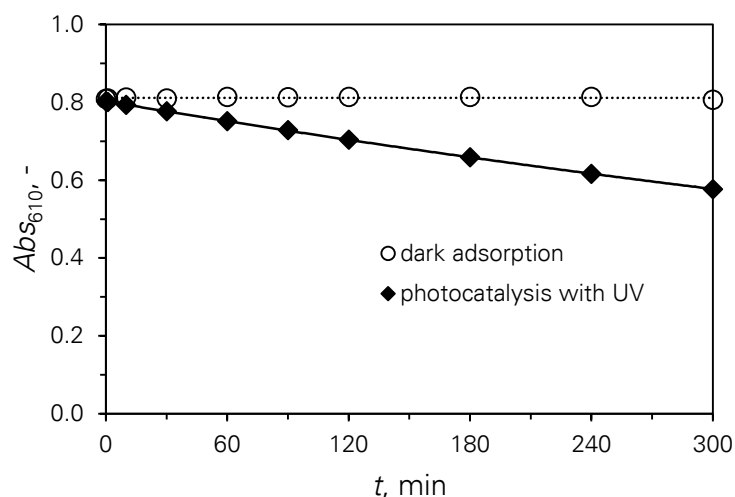


Figure 7.15 Color removal of Everzol Navy ED dye with a high initial concentration: Absorbance peak of samples measured with the 1 mm cuvette vs. experiment time. 400 ml dye solution of 250 mg/l was tested with 1 g/l P25 in the dark (labeled "dark adsorption") or under UV illumination (labeled "photocatalysis with UV", the average intensity on the illuminated surface was 25 W/m<sup>2</sup>).

#### 7.2.4.3 An up-scaled photoreactor

In this section, a simulated up-scaled photocatalytic reactor for strongly colored water is introduced. As discussed in subsection 7.2.4.1, the use of artificial UV lamp is necessary to supply high UV intensity. A flow reactor integrated with an UV lamp, named a "photoreactor", is presented. Simple computation was conducted to prove the up-scalability of the configuration of the flow reactor type.

*Definition of “photoreactor” within this thesis*

The photocatalytic setup at lab scale introduced in section 3.1.3 consists of a flow reactor and a UV lamp as individual components. An up-scaled reactor is a bit different. UV lamp should be housed in a close reactor to avoid eye contact for operators and workers. In other word, the up-scaled reactor is a reactor integrated with an UV lamp. In this work, this integration is called a “photoreactor”. For safety reasons, the lamps should be separated with the flow cells by walls to avoid the problem when the mercury lamps are broken. The wall material must be UV-transparent and it can be made of the same materials as that of the flow cell (which are discussed later).

The UV lamp can be arranged in a vertical row as the same design of the lab-scaled lamp. In this case, it is called a “UV lamp unit”. One photoreactor can have multiple lamp units (Figure 7.16).

The flow channel includes tubes which are aligned vertically. The channel units are placed in front of a UV lamp unit. As light can go through the gap between two near tubes, at least two rows of tubes should be dispositioned in a staggered array where three near tubes are arranged as triangular pitch, so tubes in the further row can make use of the UV light. It is the case for the outer flow channel units (next to the wall of the entire photoreactor, e.g. “Flow cell 1<sup>st</sup> unit” in Figure 7.16). In flow cell units between two UV lamp units, three rows can be arranged together and the illumination is ensured for all tubes (Figure 7.16). For instance, all surface area of the tube labelled “T2.3.4” in the “Flow cell 2<sup>nd</sup> unit” receives light from the 1<sup>st</sup> and 2<sup>nd</sup> UV lamp units. The surface area mainly receives light from the nearest lamp unit, in particular, from four lamps L2.3–L2.6, and also receives a minor part from the further lamp unit, lamps L1.4 and L1.5. Tubes in the middle row receive light equally from both UV units. In the figure, the tube “T2.2.3” receives the strongest light from lamps L1.3 and L2.3. It also receives light from very far lamps L1.1, L1.5, L2.1 and L2.5. Incoming lights from L1.2, L1.4, L2.2 and L2.4 also contribute. Certainly, the efficiency of illumination depends on the distance among lamps and tubes as well as their dimensions. This topic is discussed in the next sub-sections.

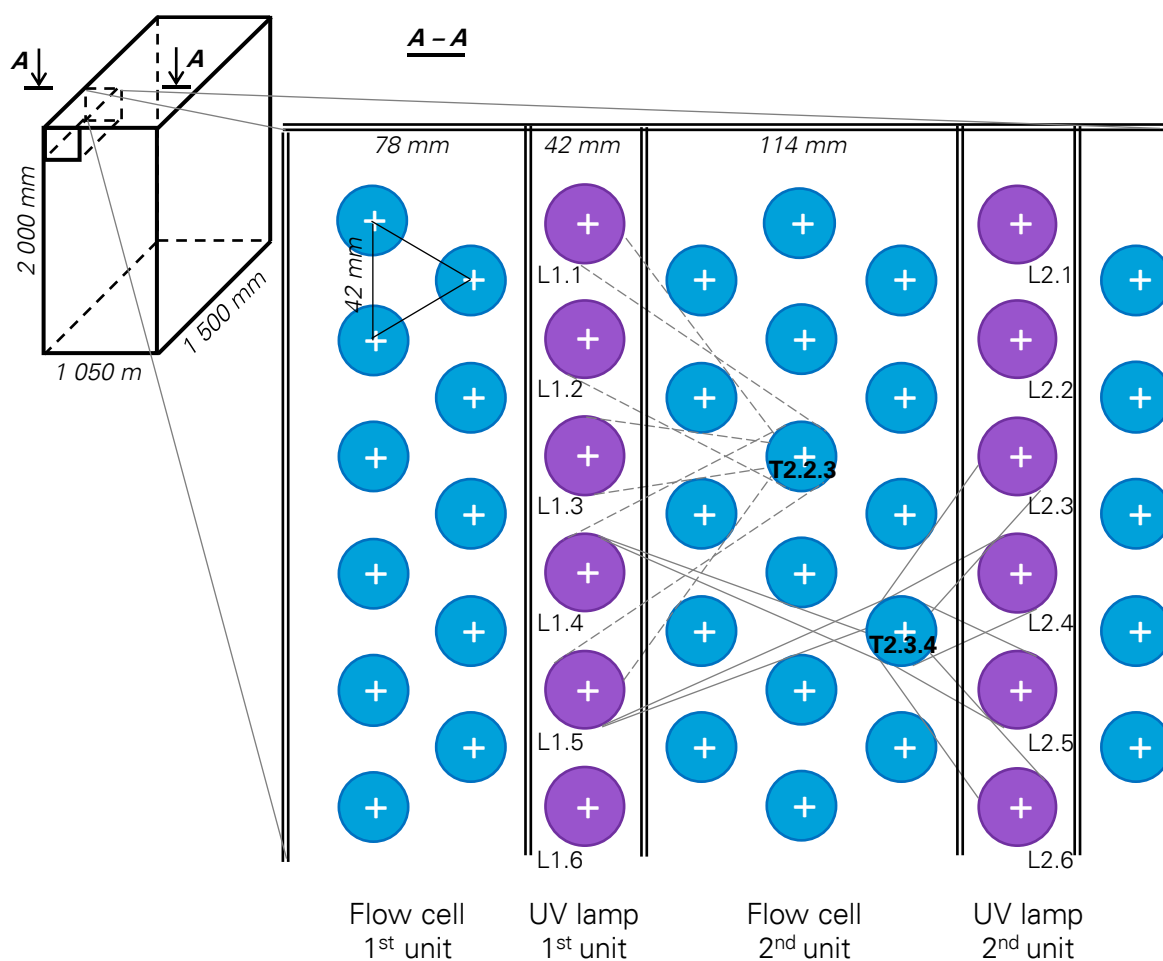


Figure 7.16 The up-scaled photoreactor: A proposed flow reactor of 365 liter for photocatalysis under artificial UV. A part of the reactor (top left) is zoomed out (right). The cross section (right) shows the dispositions of UV lamps (purple circles) and flow tubes (blue circles). Grey solid lines visualize the illumination from UV lamps to the tube T2.3.4, whereas grey dash lines visualize the illumination from the 1<sup>st</sup> UV lamp unit to the tube T2.3.4 (the illumination from UV lamps in the 2<sup>nd</sup> unit is similar and the symmetric lines are not shown).

#### UV lamp unit

The dimension of commercial UV lamp available in the market decides the dimension of the reactor. For example, in the lab setup (section 3.1.3), the length of the lamp is 302.5 mm, and of one flow channel length is 120 mm. The shorter length of the channel is to ensure the homogeneity of the UV intensity. In reality, to spare the operating room as well as to save the energy consumption of UV lamps, the length of the channel should be identical to that of the lamp. Long flow channels are preferred, so that of the same volume, fewer U-turn connectors, which induce pressure drop, are needed. For this reason, long lamp tubes were chosen. From the catalogue of Philips Koninklijke Philips N.V. Company, 5 lamps meeting this requirement were found. Important properties are shown in Table 7.4. Among all, TL-D 36W BLB 1SL/25 lamp bulb has some advantages, e.g., low electric power (36 W), light net weight (211 g), long

life time (approx. 500 days) and low mercury content (5 mg). The UV radiation is a bit low compared to the others. Another option can be TUV 36W SLV/6 bulb, of which electric power is similar to the former (36 W), net weight is lighter (135 g), lifetime is less (375 days), mercury content is lower (2 mg) but UV intensity is higher (15 W). Both of them have the same bulb diameter of 28 mm and efficient length of 1199.4 mm. These dimensions were used for computation.

#### *Flow cell units*

The tube material must be UV-transparent. Quartz or UV-transparent glass has good optical properties for photocatalysis. However, these fragile materials are not favored for assembly and operation. Instead, as mentioned in section 2.2.1, the use of polymer is an alternative. As specified by manufacturer (Adtech Polymer Engineering Ltd), FEP (fluorinated ethylene propylene) is UV-transparent. By a rough computation, it is known that 75 % UV can transmit a 1.6 mm thickness wall.

Here, the distance between two bulbs is chosen as 42 mm, i.e., the clearance and the pitch are 0.5 and 1.5 times as large as the outer diameter. The distance between bulb centers and inner walls is similar (42 mm), while the distance between the bulbs to the ceiling of the photoreactor is 118 mm. With this design, one UV lamp unit of 42×2000×1500 mm<sup>3</sup> can contain 42 bulbs in a row.

Table 7.4 UV lamps for up-scaled photocatalytic setup. Philips fluorescent lamps and their properties.

Product		F40T12/ BLACKLIGHT/48 BLB LF	TL-D 36W BLB 1SL/25	TL-D 95W HO SLV/25	TUV 36W SLV/6	TUV 75W HO 1SL/6
<i>General properties</i>						
Bulb diameter	mm	40.5	28	28	28	28
Total length	mm	1213.6	1213.6	1514.2	1213.6	1213.6
Efficient length	mm	1199.4	1199.4	1500	1199.4	1199.4
Net weight	g	310	211	233	135	135
Electric power	W	39	36	95	36	75
<i>UV properties</i>						
UV range	-	UVA	UVA	UVC	UVC	UVC
Mode wavelength	nm	365	365	250	250	250
UV radiation	W	9.6	9.5	22.5	15	25.5
<i>Others</i>						
Useful life	h	5000	12000	8000	9000	9000
Mercury content	mg	13	5	8	2	2

It is observed that some dyes strongly absorb near-UV wavelengths, e.g. Red 2BM, Orange F2R, Black ED, Orange GR, Pink R and Scarlet SHF-2G (Figure 7.13). When performing photocatalytic treatment, the shielding effect must be considered (section 7.1.4). To efficiently degrade these dyes, the optical pathlength of the photocatalytic reactor should be as short as possible (section 6.4.3). In the lab-scale experiments, the optical thickness of 11 mm of the reactor R10 is the optimal value. For an up-scaled reactor, tubes with the same optical path should be chosen. Note that, in the lab reactor, the cross section of the channel is rectangular, but in reality the channels are tubular. As shown in the previous subsection, all surface area of tubes can be illuminated, so the inner diameter of 22.2 mm equivalent with 11 mm optical path was chosen. The outer diameter of tubes is 25.4 mm. Each tube have the working length of 1200 mm (identical to the length of the UV bulb). It can contain 464 ml water.

Tubes are arranged as triangular pitch. Tube pitch is 42 mm (clearance is 16.6 mm). Distance from tube center to the wall splitting with the UV units is 21 mm, and to the wall of the reactor is 54 mm. The two outer flow cell units have a dimension of  $114 \times 2000 \times 1500 \text{ mm}^3$  and contain 83 tubes which are arranged in two rows. In each inner flow cell unit (between two UV lamp units), 124 tubes can be arranged in three rows. Its dimension is  $114 \times 2000 \times 1500 \text{ mm}^3$ .

A photoreactor with the width of approx. 1000 mm has 2 outer flow cell units, 5 inner flow cell units and 6 UV lamp units (total width =  $2 \times 114 + 5 \times 114 + 6 \times 42 = 1050 \text{ mm}$ ). The total number of tubes are  $2 \times 83 + 5 \times 124 = 786$ . The total working volume is 365 l. All specifications of the photoreactor can be found in Table 7.5.

Table 7.5 Specifications of the up-scaled photoreactor. Tubes and bulbs refer to the flow channel and the UV bulb, respectively.

		Outer flow cell unit	Inner flow cell unit	UV lamp unit
Dimension	$\text{mm}^3$	1050×2000×1500		
		114×2000×1500	114×2000×1500	42×2000×1500
Total volume	liter	365		-
Total number of bulbs/tubes	-	786		252
Bulb/tube inner diameter	mm	22.2		-
Bulb/tube outer diameter	mm	25.4		28
Bulb/tube length	mm	1199.4		1199.4
Volume of one tube	ml	464		-
Number of row	-	2	3	1
Bulb/tube pitch	mm	42	42	42
Number of bulbs/tubes in a row	-	42 or 41	42 or 41	42
Number of bulbs/tubes in a unit	-	83	124	42
Number of units	-	2	5	6

*Reaction rate constant*

In this study, a computation was attempted. The operational conditions were considered to be similar to those of the experiment presented in subsection 7.2.4.2, i.e., the organic compound Everzol Navy ED dye of 250 mg/l, the P25 photocatalyst of 1 g/l and no pH adjustment. The reaction rate constant in the lab-scaled flow reactor normalized to the light intensity of 25 W/m<sup>2</sup> is 0.111 h<sup>-1</sup>.

In reality, depending on the inquiry, dyeing and washing processes are operated only few times per month. With the capacity of 10 m<sup>3</sup>/day, it is possible to circulate the treatment of dye solution more than 3 times. In the flow reactor, the conversion of dye concentration follows an exponential function (Eq. (3.25)). The result computed for a 3-time circulation is  $C_n/C_{n,ini} = 11\%$ . It means that 90 % color of this dark solution can be bleached.

However, the presented data is only a rough estimation. Firstly, the flowrate of 10 m<sup>3</sup>/day or 7 l/min is low, Reynolds number is 5558 which means a transition of laminar and turbulent flow. For a long retention time, sedimentation may happen. The flow rate of 14 l/min can ensure a turbulence, however, in this work, the effect of flow regime has not been studied so this value is not used for computation here. Secondly, when increasing the reaction time, the intermediates and (by-) products compete the parents for the adsorption-desorption on the catalyst surface (previously discussed in section 6.4.4). It may make the reaction rate lower. Thirdly, light intensity was not considered in the computed data. Only average light intensity of sunlight was used for the normalization. However, as the UV lamps in the up-scaled setup have relatively high irradiance (compare to the lab-scaled UV lamp which is similar to UV of sunlight), they promote the reaction rate (section 6.4.2). Finally, shielding effect is not taken into account (section 7.1.4). These reasons make the experimental data different from the computed data. However, this computation proved that this photocatalytic configuration can be up-scaled for color removal of wastewater.

### 7.2.5 Concluding remarks

Based on all findings throughout the dissertation, in the last subchapter, photocatalyst was proposed to be used in a wastewater (WW) treatment plant. The scenario of wastewater treatment in March 29 Textile-Garment Joint Stock Company (Hachiba Company) in Danang, Vietnam was selected for this case study. The aim of photocatalysis is the discoloration of wastewater.

Two possibilities to introduce photocatalysis into the current treatment plant were discussed. Photocatalysis can be used to treat highly colored WW after dyeing and washing processes. It can be also the last step of the treatment, where light color needs to be removed. In any event, a flow reactor type is applicable. Artificial UV light with high intensity is recommended to treat dark WW, whereas sunlight can be utilized for treatment of light color.

Of two types of WW, the highly colored WW treatment is more complicated. An up-scaled reactor was proposed. For safety operation, UV lamp is integrated with a close reactor. This so-called photoreactor includes UV lamp units and flow channel units. In the UV lamp unit, long UV lamp bulbs of approx. 1 200 mm available in markets are aligned in one row. In the flow channel unit, FEP (fluorinated ethylene propylene) tubes are arranged as triangular pitch. Two or three rows can be dispositioned and make use of UV light. In the photoreactor of 1050×2000×1500 mm<sup>3</sup>, there are 6 UV lamp units composed of 252 bulbs and 7 flow channel units which can contain 365 l water.

Color removal efficiency was computed for the treatment of 10 m<sup>3</sup>/day dark wastewater of 250 mg/l Everzol Navy ED dye. This dye was provided by Hachiba Company and was reported to induce issues for the current WW treatment of the company. Based on the preliminary tests with 1 g/l commercial TiO<sub>2</sub> P25 photocatalyst under UV light equivalent to sunlight, the reaction rate constant was found for the system. This value was used in simulation of the 365-liter setup. Accordingly, photocatalysis can remove 90 % color in the wastewater. Though many influenced factors were not included in the computation (e.g., impact of pH, flow regime, intermediate and product molecules and shielding effect), the result show a promising application of photocatalysis in reality.

## 8. CONCLUSIONS AND FUTURE WORK

### 8.1 CONCLUSIONS

Color removal of wastewater is a crucial problem for textile industry. This issue has to be solved before draining the wastewater to effluents. In this thesis, a concept for wastewater treatment by photocatalysis was initiated. In particular, this work is dedicated to the color removal of textile wastewater under artificial or natural light. Generally, slurry photocatalysts were employed for this purpose. Facts and solutions, ideas and practice, computation and experiments shown in this work helped to achieve the study goals.

In chapter 8, motivation, goals and the main results achieved in this thesis are recalled. The detailed summaries are presented at the end of each chapter or subchapter.

It was shown (chapter 1) that together with the development of the textile industry, dye pollutants remaining in the effluents are more and more problematic. Conventional treatment techniques do not completely remove the strongly colored wastewater (WW). Recently, photocatalysis, one of the advanced oxidation processes, has been intensively studied for applications in WW treatment. Since 1972, when photocatalytic activity was first reported, there are approx. 29,000 papers on the topic "photocatalysis", but only a few industrial-scaled applications. The incomparability between laboratory studies and large-scaled practice causes the limit of photocatalysis.

Later (chapter 2), an overview of the state of the art and the fundamentals of photocatalysis were given. A detailed description of the factors and parameters (materials used, driving force, kind of reactor, etc.) that can influence the photocatalytic process was shown. Slurry photocatalysts have large surface area and therefore are very interesting materials to be used for such applications. Dissimilarly, immobilized photocatalysts can avoid the problem of post-treatment, but are not commercially available. UV or near UV light is necessary to activate the photocatalysts and act as the driving force of the photocatalytic process. Sunlight is environmentally friendly, but its UV intensity is low. In photocatalytic reactors, typically, light penetration is short and limits the use of illuminated batch reactors at a large scale. However, flow reactors can ensure an efficient light absorption. Also, process parameters in the flow reactors can be defined. Photocatalysis is a complex process, which is affected by many factors, e.g., photocatalyst and organic compound materials, catalyst concentrations and morphologies, light intensity and pH. Finally, the reaction rate constant is usually employed to compare the photocatalytic activity in the system.

Based on the state of the art, in the next five chapters (chapter 3–7), both theoretical and practical investigations were considered.

Firstly, the design of a photocatalytic configuration for slurry photocatalysis was presented as the key factor of this work. Unlike illuminated batch reactors which are commonly used in

other researches, the use of a flow reactor of which process parameters can be easily determined was introduced. Considering all the requirements for a photocatalytic reactor (e.g., illumination, flow, post treatment and materials), the new experimental setup was designed. It consists of three main components, including a flow reactor, an illumination source and a pump for circulating the suspension. Testing volume, flow conditions and light intensity are adjustable. Thus, the reactor is satisfactory for fundamental studies as well as different purposes in laboratories (e.g., experiments shown in chapter 6 and subchapter 7.1). The simple construction is also suitable for up-scaling purpose (subchapter 7.2).

The use of the Langmuir-Hinshelwood model in photocatalytic studies is arbitrary and it may lead to an insufficient distinction between the observed degradation kinetics (at macroscopic level) and the intrinsic reaction rate constant (at the microscopic level). Here, a reactor model was built to quantify the photocatalytic performance. This model is based on the heterogeneous reaction and the material balances in different components of the setup. Through mathematical equations, it is possible to determine the reaction rate constants which can characterize the photocatalytic activity. The model was verified by experiments. It was found that there is a dissimilarity between the apparent reaction rate constant in the entire photocatalytic setup and the reaction rate constant in the flow reactor. These findings are the tools used for experimental works.

A detailed operational procedure was given. Generally, a photocatalytic performance includes three steps: dispersion of photocatalyst, adsorption-desorption equilibrium of organic molecules on the photocatalyst, and photocatalytic reaction. The first step missing in most studies was inspected. Experimental results showed a big influence of dispersion technique on photocatalytic performance. The second step has not been experimentally studied but was engaged with the published work of other group. The third step was the center of the experimental work.

For academic purposes, titanium dioxide P25 was used as a photocatalyst. This nanopowder is a commercial product. The characteristics of the materials provided by the manufacturer may vary from one batch to another one. Therefore, important physical properties of P25 used in this work were investigated. To understand the activation of the photocatalyst, it was fundamental to determine the bandgap energy. Transmittance, turbidity, and extinction coefficient of the photocatalyst suspension are other notable optical properties. They were thoroughly discussed along the scattering phenomenon.

To access the key features of the photocatalytic performance in the new photocatalytic setup, color removal of methylene blue (MB) with P25 photocatalyst under UV light was studied. It is a popular testing pollutant for photocatalytic researches as suggested in the standard ISO 106789:2010. Experimentally, the use of the reactor model was verified. The impact of process parameters was, then, examined for the understanding of the photocatalysis. In particular, explicit relations of the reaction rate constants on testing volume or light intensity were given. Especially, the intensity-related reaction rate constant was presented. This parameter

is a normalization, which can exclude the impact of light intensity on a photocatalysis. Subsequently, the interaction between photocatalysts and light contributions to the optical penetration was examined. The reactor model was modified and the concept of reaction rate constant at the illuminated surface was introduced allowing for an elimination of optical depth of different reactors. The results were followed by an optimization of the photocatalyst concentration as well as the optical depth of the reactor. Other influenced conditions such as the initial concentration of MB and pH were explored. The reactor model was adapted for theoretical explanations of the experimental results. These results fulfilled a comprehensive insights of the photocatalytic performance.

Additionally, it is noticed that the P25 photocatalysts are in an aggregated state. The effect of photocatalyst aggregate size achieved by ultrasonic dispersion was discussed. The photocatalyst aggregate size and the stability of the suspensions were considered. Consequently, the aggregate size was demonstrated to have influence on the optical properties of the suspension. In the photocatalytic performance, it was proved that, when the photocatalyst aggregate size was smaller, the photocatalytic activity was enhanced. Hence, it was claimed that a suitable photocatalyst dispersion technique is necessary, as it can assure the stability of the suspension and the homogeneity of the photocatalyst aggregate size, which leads to the change of optical properties, thus the change of the photocatalytic reaction rate constant. A photocatalyst dispersion can also help to avoid sedimentation in a real application, where a flow reactor can be hundreds of meter long and the retention time can take up to several hours.

As examples of various laboratory applications, the experiments were put into different case studies. Experiments of different photocatalytic materials (commercial titanium dioxides P25 and P90 and zinc oxide) were compared. In addition, magnetic photocatalyst particles produced in our lab were tested. Different organic compounds were degraded, including three dyes (methylene blue, Remazol Red RR and Everzol Navy ED) and one antibiotic (ciprofloxacin). Different light sources were utilized, including artificial light sources. Of particular interest are the experiments made using sunlight which represent an important step in the direction of environmentally friendly applications. To exclude the influence of the testing volume of the suspension, the volume-related reaction rate constant was proposed. To eliminate time-variant light intensities, which are typical for the case of natural light source, the reactor model was transformed to a UV-dependent model. Ultimately, these results showed that the concept of the flow reactor suits a variety of applications in laboratories.

At the end, an industrial application was discussed. Aiming at a specific case, the photocatalytic treatment was applied for wastewater from one textile company in Danang, Vietnam. Earlier, photocatalytic reactors installed in the company within the German-Vietnamese CLIENT/NaViTex project worked at semi pilot or pilot scales. Here, in this work, the concept of a flow photocatalytic reactor was proposed for working at industrial scale. Preliminary tests and simulations were performed aiming at the treatment of strongly colored wastewater. The high dye concentration in such wastewater demands the use of high UV light intensity. Artificial UV lamps were recommended and the integration with the flow reactor in a so-called

“photoreactor” was suggested. A photoreactor of  $1050 \times 2000 \times 1500 \text{ mm}^3$  can contain 365 l water. With this industrial setup, the color removal of one textile dye from the company at high concentration can reach 90 %. Notably this result is a solution to upgrade the WW treatment plant of the company.

This Ph.D. work introduced a concept for the treatment of wastewater from textile industry by slurry photocatalysis. Operational procedure, influential factors and reactor models were given. The flow reactor prototype can suit various study purposes in laboratories and have a great potential for industrial applications. The contribution of this thesis can be a translation among studies of different scales. It is important to note that already some real industrial applications based on the findings of this thesis were performed and open the avenue for future up-scaled systems.

## 8.2 OUTLOOK

All shown results confirmed that photocatalysis is a key-process for applications of nanotechnology to environmental problems. To realize an efficient photocatalysis, the strategies that should be studied are the following: i) the development of catalytic materials, ii) the performance with real conditions, iii) the combined photocatalysis, and iv) the reactor design. This Ph.D. work solved the matters regarding strategies ii) and iv). Further studies are of special interest.

Regarding strategy i, new materials should be tested in the photocatalytic flow reactor type. Also, the use of immobilized photocatalysts is possible and should be tested. Regardless of material types, new photocatalysts should satisfy the physical and chemical resistances and the reusability. Very importantly, the materials must be able to be produced in a large amount.

Regarding strategy ii, influences of some other factors should be taken into account. For instance, shielding effect is of special interest. A number of organic molecules absorb UV light, which is the wavelength for excitation of photocatalysts. This means that the light propagation in the suspension must be described as a sum of photons absorption by the organic molecules and extinction by the catalyst particles. The extinction by catalyst particles remains constant during the photocatalytic reaction, while the photons absorption by organic molecules is not (this last factor is connected with the concentration of molecules in solution). This has not yet been taken into account in the model equations because it was irrelevant for the examined configurations. For the general case, this should be integrated into the model equations.

Regarding strategy iii, it is noted that, photocatalysis cannot alone solve the problem of industrial effluents. The combination with other processes is necessary. Also the pretreatment and post treatment of photocatalysts are necessary. Therefore, a comprehensive cost estimation is a need to successfully conduct photocatalysis.

Regarding strategy iv, up-scaling studies should be done and a real industrial photocatalytic treatment can be realized in the future.

## REFERENCES

- [1] E. Corovic, P. Jovanovic, and L. Ristic, "Current trends on the world textile market and the competitiveness of the Serbian textile industry," *Fibres Text. East. Eur.*, vol. 21, no. 5, pp. 8–12, 2013.
- [2] K. Goto, K. Natsuda, and J. Thoburn, "Meeting the challenge of China: The Vietnamese garment industry in the post MFA era," *Glob. Networks*, vol. 11, no. 3, pp. 355–379, 2011.
- [3] A. E. Ghaly, R. Ananthashankar, M. Alhattab, and V. V. Ramakrishnan, "Production, characterization and treatment of textile effluents: A critical review," *J. Chem. Eng. Process Technol.*, vol. 5, no. 1, pp. 1–19, 2014.
- [4] F. M. D. Chequer, G. A. R. de Oliveira, E. R. A. Ferraz, J. C. Cardoso, M. V. B. Zanoni, and D. P. de Oliveira, "Textile dyes: Dyeing process and environmental impact," in *Eco-friendly textile dyeing and finishing*, M. Günay, Ed. Rijeka: InTech, 2013, pp. 151–176.
- [5] E. Forgacs, T. Cserhádi, and G. Oros, "Removal of synthetic dyes from wastewaters: a review," *Environ. Int.*, vol. 30, pp. 953–971, 2004.
- [6] K. Rajeshwar *et al.*, "Heterogeneous photocatalytic treatment of organic dyes in air and aqueous media," *J. Photochem. Photobiol. C Photochem. Rev.*, vol. 9, pp. 171–192, 2008.
- [7] I. Carra, J. A. S. Pérez, S. Malato, O. Autin, B. Jefferson, and P. Jarvis, "Performance of different advanced oxidation processes for tertiary wastewater treatment to remove the pesticide acetamiprid," *J. Chem. Technol. Biotechnol.*, vol. 91, pp. 72–81, 2016.
- [8] M. N. Chong, B. Jin, C. W. K. Chow, and C. Saint, "Recent developments in photocatalytic water treatment technology: A review," *Water Res.*, vol. 44, pp. 2997–3027, 2010.
- [9] P. R. Gogate and A. B. Pandit, "A review of imperative technologies for wastewater treatment I: oxidation technologies at ambient conditions," *Adv. Environ. Res.*, vol. 8, pp. 501–551, 2004.
- [10] I. K. Konstantinou and T. A. Albanis, "TiO<sub>2</sub>-assisted photocatalytic degradation of azo dyes in aqueous solution: kinetic and mechanistic investigations. A review," *Appl. Catal. B Environ.*, vol. 49, pp. 1–14, 2004.
- [11] J. L. Wang and L. J. Xu, "Advanced oxidation processes for wastewater treatment: Formation of hydroxyl radical and application," *Crit. Rev. Environ. Sci. Technol.*, vol. 42, no. 3, pp. 251–325, 2012.
- [12] L. Prieto-Rodriguez *et al.*, "Optimization of mild solar TiO<sub>2</sub> photocatalysis as a tertiary treatment for municipal wastewater treatment plant effluents," *Appl. Catal. B Environ.*, vol. 128, pp. 119–125, 2012.

- [13] A. Fujishima and K. Honda, "Electrochemical photolysis of water at a semiconductor electrode," *Nature*, vol. 238, pp. 37–38, 1972.
- [14] S. Chakrabarti and B. K. Dutta, "Photocatalytic degradation of model textile dyes in wastewater using ZnO as semiconductor catalyst," *J. Hazard. Mater.*, vol. B112, pp. 269–278, 2004.
- [15] S. K. Kansal, M. Singh, and D. Sud, "Studies on photodegradation of two commercial dyes in aqueous phase using different photocatalysts," *J. Hazard. Mater.*, vol. 141, pp. 581–590, 2007.
- [16] H. Zhang, G. Chen, and D. W. Bahnemann, "Photoelectrocatalytic materials for environmental applications," *J. Mater. Chem.*, vol. 19, pp. 5089–5121, 2009.
- [17] S. Malato, P. Fernández-Ibáñez, M. I. Maldonado, I. Oller, and M. I. Polo-López, "Solar photocatalytic pilot plants: Commercially available reactors," in *Photocatalysis and water purification: From fundamentals to recent applications*, P. Pichat, Ed. Weinheim: Wiley-VCH Verlag GmbH & Co. KGaA, 2013, pp. 377–397.
- [18] S. Malato, J. Blanco, A. Vidal, and C. Richter, "Photocatalysis with solar energy at a pilot-plant scale: an overview," *Appl. Catal. B Environ.*, vol. 37, pp. 1–15, 2002.
- [19] S. Malato Rodríguez *et al.*, "Engineering of solar photocatalytic collectors," *Sol. Energy*, vol. 77, pp. 513–524, 2004.
- [20] E. Boonen *et al.*, "Construction of a photocatalytic de-polluting field site in the Leopold II tunnel in Brussels," *J. Environ. Manage.*, vol. 155, pp. 136–144, 2015.
- [21] M. Gallus *et al.*, "Photocatalytic de-pollution in the Leopold II tunnel in Brussels: NO<sub>x</sub> abatement results," *Build. Environ.*, vol. 84, pp. 125–133, 2015.
- [22] D. Ollis, "Photocatalytic treatment of water: Irradiance influences," in *Photocatalysis and water purification: From fundamentals to recent applications*, P. Pichat, Ed. Weinheim: Wiley-VCH Verlag GmbH & Co. KGaA, 2013, pp. 313–333.
- [23] R. J. Braham and A. T. Harris, "Review of major design and scale-up considerations for solar photocatalytic reactors," *Ind. Eng. Chem. Res.*, vol. 48, pp. 8890–8905, 2009.
- [24] N. Xu, Z. Shi, Y. Fan, J. Dong, J. Shi, and M. Z.-C. Hu, "Effects of particle size of TiO<sub>2</sub> on photocatalytic degradation of methylene blue in aqueous suspensions," *Ind. Eng. Chem. Res.*, vol. 38, pp. 373–379, 1999.
- [25] A. Houas, H. Lachheb, M. Ksibi, E. Elaloui, C. Guillard, and J.-M. Herrmann, "Photocatalytic degradation pathway of methylene blue in water," *Appl. Catal. B Environ.*, vol. 31, pp. 145–157, 2001.
- [26] M. Bodzek and M. Rajca, "Photocatalysis in the treatment and disinfection of water. Part I. Theoretical backgrounds," *Ecol. Chem. Eng. S*, vol. 19, no. 4, pp. 489–512, 2012.

- [27] K. Ishibashi, A. Fujishima, T. Watanabe, and K. Hashimoto, "Quantum yields of active oxidative species formed on TiO<sub>2</sub> photocatalyst," *J. Photochem. Photobiol. A Chem.*, vol. 134, pp. 139–142, 2000.
- [28] A. L. Linsebigler, G. Lu, and J. T. Yates Jr., "Photocatalysis on TiO<sub>2</sub> surfaces: Principles, mechanisms, and selected results," *Chem. Rev.*, vol. 95, pp. 735–758, 1995.
- [29] C. Minero, V. Maurino, and D. Vione, "Photocatalytic mechanisms and reaction pathways drawn from kinetic and probe molecules," in *Photocatalysis and water purification: From fundamentals to recent applications*, P. Pichat, Ed. Weinheim: Wiley-VCH Verlag GmbH & Co. KGaA, 2013, pp. 53–72.
- [30] Y. Nosaka and A. Y. Nosaka, "Identification and roles of the active species generated on various photocatalysts," in *Photocatalysis and water purification: From fundamentals to recent applications*, P. Pichat, Ed. Weinheim: Wiley-VCH Verlag GmbH & Co. KGaA, 2013, pp. 3–24.
- [31] T. Ochiai and A. Fujishima, "Photoelectrochemical properties of TiO<sub>2</sub> photocatalyst and its applications for environmental purification," *J. Photochem. Photobiol. C Photochem. Rev.*, vol. 13, pp. 247–262, 2012.
- [32] H. Park, Y. Park, W. Kim, and W. Choi, "Surface modification of TiO<sub>2</sub> photocatalyst for environmental applications," *J. Photochem. Photobiol. C Photochem. Rev.*, vol. 15, pp. 1–20, 2013.
- [33] A. Fujishima, X. Zhang, and D. A. Tryk, "TiO<sub>2</sub> photocatalysis and related surface phenomena," *Surf. Sci. Rep.*, vol. 63, pp. 515–582, Dec. 2008.
- [34] Y. Sun and J. J. Pignatello, "Evidence for a surface dual hole-radical mechanism in the TiO<sub>2</sub> photocatalytic oxidation of 2,4-dichlorophenoxyacetic acid," *Environ. Sci. Technol.*, vol. 29, pp. 2065–2072, 1995.
- [35] S. Yang, L. Lou, K. Wang, and Y. Chen, "Shift of initial mechanism in TiO<sub>2</sub>-assisted photocatalytic process," *Appl. Catal. A Gen.*, vol. 301, pp. 152–157, 2006.
- [36] L. Yu *et al.*, "The degradation mechanism of methyl orange under photo-catalysis of TiO<sub>2</sub>," *Phys. Chem. Chem. Phys.*, vol. 14, pp. 3589–3595, 2012.
- [37] C. Kormann, D. W. Bahnemann, and M. R. Hoffmann, "Photolysis of chloroform and other organic molecules in aqueous TiO<sub>2</sub> suspensions," *Environ. Sci. Technol.*, vol. 25, pp. 494–500, 1991.
- [38] N. M. Mahmoodi, M. Arami, N. Y. Limaee, and N. S. Tabrizi, "Kinetics of heterogeneous photocatalytic degradation of reactive dyes in an immobilized TiO<sub>2</sub> photocatalytic reactor," *J. Colloid Interface Sci.*, vol. 295, pp. 159–164, 2006.
- [39] M. R. Hoffmann, S. T. Martin, W. Choi, and D. W. Bahnemann, "Environmental applications of semiconductor photocatalysis," *Chem. Rev.*, vol. 95, pp. 69–96, 1995.

- [40] E. Evgenidou, K. Fytianos, and I. Poullos, "Semiconductor-sensitized photodegradation of dichlorvos in water using TiO<sub>2</sub> and ZnO as catalysts," *Appl. Catal. B Environ.*, vol. 59, pp. 81–89, 2005.
- [41] J.-M. Herrmann, "Heterogeneous photocatalysis: state of the art and present applications," *Top. Catal.*, vol. 34, no. 1–4, pp. 49–65, 2005.
- [42] C. McCullagh, N. Skillen, M. Adams, and P. K. J. Robertson, "Photocatalytic reactors for environmental remediation: a review," *J. Chem. Technol. Biotechnol.*, vol. 86, pp. 1002–1017, 2011.
- [43] H. Arora *et al.*, "Titanium dioxide nanocomposites," in *Nanomaterials for the life sciences*, vol. 8, S. S. R. C. Kumar, Ed. Weinheim: Wiley-VCH Verlag GmbH & Co. KGaA, 2010, pp. 1–51.
- [44] N. Shaham-Waldmann and Y. Paz, "Modified photocatalysts," in *Photocatalysis and water purification: From fundamentals to recent applications*, P. Pichat, Ed. Weinheim: Wiley-VCH Verlag GmbH & Co. KGaA, 2013, pp. 103–143.
- [45] Thomson Reuters, "Web of Science," 2017. [Online]. Available: <http://apps.webofknowledge.com>. [Accessed: 10-Jun-2017].
- [46] R. Daghrir, P. Drogui, and D. Robert, "Modified TiO<sub>2</sub> for environmental photocatalytic applications: A review," *Ind. Eng. Chem. Res.*, vol. 52, pp. 3581–3599, 2013.
- [47] S. Rehman, R. Ullah, A. M. Butt, and N. D. Gohar, "Strategies of making TiO<sub>2</sub> and ZnO visible light active," *J. Hazard. Mater.*, vol. 170, pp. 560–569, 2009.
- [48] C. Di Valentin, G. Pacchioni, A. Selloni, S. Livraghi, and E. Giamello, "Characterization of paramagnetic species in N-doped TiO<sub>2</sub> powders by EPR spectroscopy and DFT calculations," *J. Phys. Chem. B*, vol. 109, no. 23, pp. 11414–11419, 2005.
- [49] J. Zhang, Y. Wu, M. Xing, S. A. K. Leghari, and S. Sajjad, "Development of modified N doped TiO<sub>2</sub> photocatalyst with metals, nonmetals and metal oxides," *Energy Environ. Sci.*, vol. 3, pp. 715–726, 2010.
- [50] M. Shen, Z. Wu, H. Huang, Y. Du, Z. Zou, and P. Yang, "Carbon-doped anatase TiO<sub>2</sub> obtained from TiC for photocatalysis under visible light irradiation," *Mater. Lett.*, vol. 60, pp. 693–697, 2006.
- [51] A. Kumar and N. Mathur, "Photocatalytic oxidation of aniline using Ag<sup>+</sup>-loaded TiO<sub>2</sub> suspensions," *Appl. Catal. A Gen.*, vol. 275, pp. 189–197, 2004.
- [52] P. V. Kamat, "Photophysical, photochemical and photocatalytic aspects of metal nanoparticles," *J. Phys. Chem. B*, vol. 106, pp. 7729–7744, 2002.
- [53] M. K. Seery, R. George, P. Floris, and S. C. Pillai, "Silver doped titanium dioxide nanomaterials for enhanced visible light photocatalysis," *J. Photochem. Photobiol. A Chem.*, vol. 189, pp. 258–263, 2007.

- [54] R. Georgekutty, M. K. Seery, and S. C. Pillai, "A highly efficient Ag-ZnO photocatalyst: synthesis, properties and mechanism," *J. Phys. Chem. C*, vol. 112, pp. 13563–13570, 2008.
- [55] F. B. Li and X. Z. Li, "The enhancement of photodegradation efficiency using Pt-TiO<sub>2</sub> catalyst," *Chemosphere*, vol. 48, pp. 1103–1111, 2002.
- [56] X. Z. Li and F. B. Li, "Study of Au/Au<sup>3+</sup>-TiO<sub>2</sub> photocatalysts toward visible photooxidation for water and wastewater treatment," *Environ. Sci. Technol.*, vol. 35, pp. 2381–2387, 2001.
- [57] C. Wang, C. Böttcher, D. W. Bahnemann, and J. K. Dohrmann, "A comparative study of nanometer sized Fe(III)-doped TiO<sub>2</sub> photocatalysts: synthesis, characterization and activity," *J. Mater. Chem.*, vol. 13, pp. 2322–2329, 2003.
- [58] G. Colón, M. Maicu, M. C. Hidalgo, and J. A. Navío, "Cu-doped TiO<sub>2</sub> systems with improved photocatalytic activity," *Appl. Catal. B Environ.*, vol. 67, pp. 41–51, 2006.
- [59] E. Borgarello, J. Kiwi, M. Grätzel, E. Pelizzetti, and M. Visca, "Visible light induced water cleavage in colloidal solutions of chromium-doped titanium dioxide particles," *J. Am. Chem. Soc.*, vol. 104, pp. 2996–3002, 1982.
- [60] R. Ullah and J. Dutta, "Photocatalytic degradation of organic dyes with manganese-doped ZnO nanoparticles," *J. Hazard. Mater.*, vol. 156, pp. 194–200, 2008.
- [61] E. Arpaç, F. Sayılkan, M. Asiltürk, P. Tatar, N. Kiraz, and H. Sayılkan, "Photocatalytic performance of Sn-doped and undoped TiO<sub>2</sub> nanostructured thin films under UV and vis-lights," *J. Hazard. Mater.*, vol. 140, pp. 69–74, 2007.
- [62] Z. M. El-Bahy, A. A. Ismail, and R. M. Mohamed, "Enhancement of titania by doping rare earth for photodegradation of organic dye (Direct Blue)," *J. Hazard. Mater.*, vol. 166, pp. 138–143, 2009.
- [63] X. Yan, J. He, D. G. Evans, X. Duan, and Y. Zhu, "Preparation, characterization and photocatalytic activity of Si-doped and rare earth-doped TiO<sub>2</sub> from mesoporous precursors," *Appl. Catal. B Environ.*, vol. 55, pp. 243–252, 2005.
- [64] M. S. Hassan, T. Amna, O.-B. Yang, H.-C. Kim, and M.-S. Khil, "TiO<sub>2</sub> nanofibers doped with rare earth elements and their photocatalytic activity," *Ceram. Int.*, vol. 38, pp. 5925–5930, 2012.
- [65] H. Shi, T. Zhang, T. An, B. Li, and X. Wang, "Enhancement of photocatalytic activity of nano-scale TiO<sub>2</sub> particles co-doped by rare earth elements and heteropolyacids," *J. Colloid Interface Sci.*, vol. 380, pp. 121–127, 2012.
- [66] V. Štengl, S. Bakardjieva, and N. Murafa, "Preparation and photocatalytic activity of rare earth doped TiO<sub>2</sub> nanoparticles," *Mater. Chem. Phys.*, vol. 114, pp. 217–226, 2009.

- [67] A.-W. Xu, Y. Gao, and H.-Q. Liu, "The preparation, characterization, and their photocatalytic activities of rare-earth-doped TiO<sub>2</sub> nanoparticles," *J. Catal.*, vol. 207, pp. 151–157, 2002.
- [68] T. Hirakawa and P. V. Kamat, "Charge separation and catalytic activity of Ag@TiO<sub>2</sub> core-shell composite clusters under UV-irradiation," *J. Am. Chem. Soc.*, vol. 127, pp. 3928–3934, 2005.
- [69] P. D. Cozzoli, E. Fanizza, R. Comparelli, M. L. Curri, A. Agostiano, and D. Laub, "Role of metal nanoparticles in TiO<sub>2</sub>/Ag nanocomposite-based microheterogeneous photocatalysis," *J. Phys. Chem. B*, vol. 108, pp. 9623–9630, 2004.
- [70] Y. Liu, L. Chen, J. Hu, J. Li, and R. Richards, "TiO<sub>2</sub> nanoflakes modified with gold nanoparticles as photocatalysts with high activity and durability under near UV irradiation," *J. Phys. Chem. C*, vol. 114, pp. 1641–1645, 2010.
- [71] S. G. Kumar and L. G. Devi, "Review on modified TiO<sub>2</sub> photocatalysis under UV/visible light: Selected results and related mechanisms on interfacial charge carrier transfer dynamics," *J. Phys. Chem. A*, vol. 115, pp. 13211–13241, 2011.
- [72] D. Zhao, G. Sheng, C. Chen, and X. Wang, "Enhanced photocatalytic degradation of methylene blue under visible irradiation on graphene@TiO<sub>2</sub> dyade structure," *Appl. Catal. B Environ.*, vol. 111–112, pp. 303–308, 2012.
- [73] S. Scalese *et al.*, "Photocatalytic properties of carbon nanotubes/titania nanoparticles composite layers deposited by electrophoresis," *Mater. Sci. Semicond. Process.*, vol. 42, pp. 45–49, 2016.
- [74] K. Vinodgopal and P. V. Kamat, "Enhanced rates of photocatalytic degradation of an azo dye using SnO<sub>2</sub>/TiO<sub>2</sub> coupled semiconductor thin films," *Environ. Sci. Technol.*, vol. 29, pp. 841–845, 1995.
- [75] S. Higashimoto, M. Sakiyama, and M. Azuma, "Photoelectrochemical properties of hybrid WO<sub>3</sub>/TiO<sub>2</sub> electrode. Effect of structures of WO<sub>3</sub> on charge separation behavior," *Thin Solid Films*, vol. 503, pp. 201–206, 2006.
- [76] N. Serpone, P. Maruthamuthu, P. Pichat, E. Pelizzetti, and H. Hidaka, "Exploiting the interparticle electron transfer process in the photocatalysed oxidation of phenol, 2-chlorophenol and pentachlorophenol: chemical evidence for electron and hole transfer between coupled semiconductors," *J. Photochem. Photobiol. A Chem.*, vol. 85, pp. 247–255, 1995.
- [77] X. Fu, L. A. Clark, Q. Yang, and M. A. Anderson, "Enhanced photocatalytic performance of titania-based binary metal oxides: TiO<sub>2</sub>/SiO<sub>2</sub> and TiO<sub>2</sub>/ZrO<sub>2</sub>," *Environ. Sci. Technol.*, vol. 30, no. 2, pp. 647–653, 1996.

- [78] J.-M. Herrmann, H. Tahiri, Y. Ait-Ichou, G. Lassaletta, A. R. González-Elípe, and A. Fernández, "Characterization and photocatalytic activity in aqueous medium of TiO<sub>2</sub> and Ag-TiO<sub>2</sub> coatings on quartz," *Appl. Catal. B Environ.*, vol. 13, pp. 219–228, 1997.
- [79] A. Goossens, E.-L. Maloney, and J. Schoonman, "Gas-phase synthesis of nanostructured anatase TiO<sub>2</sub>," *Chem. Vap. Depos.*, vol. 4, no. 3, pp. 109–114, 1998.
- [80] F. Di Fonzo, C. S. Casari, V. Russo, M. F. Brunella, A. Li Bassi, and C. E. Bottani, "Hierarchically organized nanostructured TiO<sub>2</sub> for photocatalysis applications," *Nanotechnology*, vol. 20, pp. 1–7, 2009.
- [81] S. Eiden-Assmann, J. Widoniak, and G. Maret, "Synthesis and characterization of hollow and non-hollow monodisperse colloidal TiO<sub>2</sub> particles," *J. Dispers. Sci. Technol.*, vol. 25, no. 4, pp. 535–545, 2005.
- [82] H. Uchida, S. Katoh, and M. Watanabe, "Photocatalytic degradation of trichlorobenzene using immobilized TiO<sub>2</sub> films containing poly(tetrafluoroethylene) and platinum metal catalyst," *Electrochim. Acta*, vol. 43, no. 14–15, pp. 2111–2116, 1998.
- [83] T. Ochiai and A. Fujishima, "Design and optimization of photocatalytic water purification reactors," in *Photocatalysis and water purification: From fundamentals to recent applications*, P. Pichat, Ed. Weinheim: Wiley-VCH Verlag GmbH & Co. KGaA, 2013, pp. 361–376.
- [84] N. A. Almeida *et al.*, "TiO<sub>2</sub>/graphene oxide immobilized in P(VDF-TrFE) electrospun membranes with enhanced visible-light-induced photocatalytic performance," *J. Mater. Sci.*, vol. 51, pp. 6974–6956, 2016.
- [85] M. Rochkind, S. Pasternak, and Y. Paz, "Using dyes for evaluating photocatalytic properties: A critical review," *Molecules*, vol. 20, pp. 88–110, 2015.
- [86] F. Benoit-Marquié, U. Wilkenhöner, V. Simon, A. M. Braun, E. Oliveros, and M.-T. Maurette, "VOC photodegradation at the gas–solid interface of a TiO<sub>2</sub> photocatalyst," *J. Photochem. Photobiol. A Chem.*, vol. 132, pp. 225–232, 2000.
- [87] T. Ochiai *et al.*, "Development of a hybrid environmental purification unit by using of excimer VUV lamps with TiO<sub>2</sub> coated titanium mesh filter," *Chem. Eng. J.*, vol. 218, pp. 327–332, 2013.
- [88] A. Abramowitz, "Units, symbols, and equations for radiometric and photometric quantities," in *CRC handbook of chemistry and physics*, 76th ed., D. R. Lide and H. P. R. Frederikse, Eds. Boca Raton: CRC Press, 1995, pp. 289–290.
- [89] C. Minero, E. Pelizzetti, S. Malato, and J. Blanco, "Large solar plant photocatalytic water decontamination: Effect of operational parameters," *Sol. Energy*, vol. 56, no. 5, pp. 421–428, 1996.
- [90] D. F. Ollis, "Kinetics of liquid phase photocatalyzed reactions: An illuminating approach," *J. Phys. Chem. B*, vol. 109, pp. 2439–2444, 2005.

- [91] A. V. Emeline, V. Ryabchuk, and N. Serpone, "Factors affecting the efficiency of a photocatalyzed process in aqueous metal-oxide dispersions: Prospect of distinguishing between two kinetic models," *J. Photochem. Photobiol. A Chem.*, vol. 133, pp. 89–97, 2000.
- [92] B. F. Abramović, N. D. Banić, and J. B. Krstić, "Degradation of thiacloprid by ZnO in a laminar falling film slurry photocatalytic reactor," *Ind. Eng. Chem. Res.*, vol. 52, no. 14, pp. 5040–5047, 2013.
- [93] A. J. Hoffman, H. Yee, G. Mills, and M. R. Hoffmann, "Photoinitiated polymerization of methyl methacrylate using Q-sized ZnO colloids," *J. Phys. Chem.*, vol. 96, pp. 5540–5546, 1992.
- [94] J.-M. Herrmann, "Heterogeneous photocatalysis: fundamentals and applications to the removal of various types of aqueous pollutants," *Catal. Today*, vol. 53, pp. 115–129, 1999.
- [95] M. de los M. Ballari, R. Brandi, O. Alfano, and A. Cassano, "Mass transfer limitations in photocatalytic reactors employing titanium dioxide suspensions. I. Concentration profiles in the bulk," *Chem. Eng. J.*, vol. 136, pp. 50–65, 2008.
- [96] M. de los M. Ballari, R. Brandi, O. Alfano, and A. Cassano, "Mass transfer limitations in photocatalytic reactors employing titanium dioxide suspensions. II. External and internal particle constrains for the reaction," *Chem. Eng. J.*, vol. 136, pp. 242–255, 2008.
- [97] M. de los M. Ballari, O. M. Alfano, and A. E. Cassano, "Mass transfer limitations in slurry photocatalytic reactors: Experimental validation," *Chem. Eng. Sci.*, vol. 65, pp. 4931–4942, Sep. 2010.
- [98] L. Erdei, N. Arecrachakul, and S. Vigneswaran, "A combined photocatalytic slurry reactor-immersed membrane module system for advanced wastewater treatment," *Sep. Purif. Technol.*, vol. 62, pp. 382–388, 2008.
- [99] D. F. Ollis, "Integrating photocatalysis and membrane technologies for water treatment," *Ann. N. Y. Acad. Sci.*, vol. 984, pp. 65–84, 2003.
- [100] W. M. Samhaber and M. T. Nguyen, "Applicability and costs of nanofiltration in combination with photocatalysis for the treatment of dye house effluents," *Beilstein J. Nanotechnol.*, vol. 5, pp. 476–484, 2014.
- [101] R. S. Thakur, R. Chaudhary, and C. Singh, "Fundamentals and applications of the photocatalytic treatment for the removal of industrial organic pollutants and effects of operational parameters: A review," *J. Renew. Sustain. Energy*, vol. 2, no. 042701, pp. 1–37, 2010.
- [102] A. E. Cassano and O. M. Alfano, "Reaction engineering of suspended solid heterogeneous photocatalytic reactors," *Catal. Today*, vol. 58, pp. 167–197, 2000.

- [103] M. N. Chong, S. Lei, B. Jin, C. Saint, and C. W. K. Chow, "Optimisation of an annular photoreactor process for degradation of Congo Red using a newly synthesized titania impregnated kaolinite nano-photocatalyst," *Sep. Purif. Technol.*, vol. 67, pp. 355–363, 2009.
- [104] Y. Boyjoo, M. Ang, and V. Pareek, "Light intensity distribution in multi-lamp photocatalytic reactors," *Chem. Eng. Sci.*, vol. 93, pp. 11–21, 2013.
- [105] B. Bayarri, J. Giménez, M. I. Maldonado, S. Malato, and S. Esplugas, "2,4-Dichlorophenol degradation by means of heterogeneous photocatalysis. Comparison between laboratory and pilot plant performance," *Chem. Eng. J.*, vol. 232, pp. 405–417, 2013.
- [106] "Solar treatment of water facilities." [Online]. Available: <http://www.psa.es/en/instalaciones/aguas.php>. [Accessed: 06-Jun-2016].
- [107] D. F. Ollis and C. Turchi, "Heterogeneous photocatalysis for water purification: Contaminant mineralization kinetics and elementary reactor analysis," *Environ. Prog.*, vol. 9, no. 4, pp. 229–234, 1990.
- [108] D. Robert, V. Keller, and N. Keller, "Immobilization of a semiconductor photocatalyst on solid supports: methods, materials, and applications," in *Photocatalysis and water purification: From fundamentals to recent applications*, P. Pichat, Ed. Weinheim: Wiley-VCH Verlag GmbH & Co. KGaA, 2013, pp. 145–178.
- [109] S. Fukahori, H. Ichiura, T. Kitaoka, and H. Tanaka, "Capturing of bisphenol A photodecomposition intermediates by composite TiO<sub>2</sub>-zeolite sheets," *Appl. Catal. B Environ.*, vol. 46, pp. 453–462, 2003.
- [110] S. Teixeira, P. M. Martins, S. Lanceros-Méndez, K. Kühn, and G. Cuniberti, "Reusability of photocatalytic TiO<sub>2</sub> and ZnO nanoparticles immobilized in poly(vinylidene difluoride)-co-trifluoroethylene," *Appl. Surf. Sci.*, vol. 384, pp. 497–504, 2016.
- [111] E. Bannier *et al.*, "Microstructure and photocatalytic activity of suspension plasma sprayed TiO<sub>2</sub> coatings on steel and glass substrates," *Surf. Coat. Technol.*, vol. 206, pp. 378–386, 2011.
- [112] S. Rodríguez Couto, A. Domínguez, and A. Sanromán, "Photocatalytic degradation of dyes in aqueous solution operating in a fluidised bed reactor," *Chemosphere*, vol. 46, pp. 83–86, 2002.
- [113] L. A. Dibble and G. B. Raupp, "Fluidized-bed photocatalytic oxidation of trichloroethylene in contaminated air streams," *Environ. Sci. Technol.*, vol. 26, pp. 492–495, 1992.
- [114] T. H. Lim and S. D. Kim, "Trichloroethylene degradation by photocatalysis in annular flow and annulus fluidized bed photoreactors," *Chemosphere*, vol. 54, pp. 305–312, 2004.
- [115] D.-D. Phan, F. Babick, M.-T. Nguyen, B. Wessely, and M. Stintz, "Modelling the influence of mass transfer on fixed-bed photocatalytic membrane reactor," *Chem. Eng. Sci.*, vol. 173, pp. 242–252, 2017.

- [116] G. S. Shephard, S. Stockenström, D. de Villiers, W. J. Engelbrecht, and G. F. S. Wessels, "Degradation of microcystin toxins in a falling film photocatalytic reactor with immobilized titanium dioxide catalyst," *Water Res.*, vol. 36, no. 1, pp. 140–146, 2002.
- [117] S. N. Hosseini, S. M. Borghei, M. Vossoughi, and N. Taghavinia, "Immobilization of TiO<sub>2</sub> on perlite granules for photocatalytic degradation of phenol," *Appl. Catal. B Environ.*, vol. 74, pp. 53–62, 2007.
- [118] E. Cossich *et al.*, "Development of electrospun photocatalytic TiO<sub>2</sub>-polyamide-12 nanocomposites," *Mater. Chem. Phys.*, vol. 164, pp. 91–97, 2015.
- [119] A. Vild, S. Teixeira, K. Kühn, G. Cuniberti, and V. Sencadas, "Orthogonal experimental design of titanium dioxide-Poly(methyl methacrylate) electrospun nanocomposite membranes for photocatalytic applications," *J. Environ. Chem. Eng.*, vol. 4, pp. 3151–3158, 2016.
- [120] A. R. Khataee, M. N. Pons, and O. Zahraa, "Photocatalytic degradation of three azo dyes using immobilized TiO<sub>2</sub> nanoparticles on glass plates activated by UV light irradiation: Influence of dye molecular structure," *J. Hazard. Mater.*, vol. 168, pp. 451–457, 2009.
- [121] A. K. Ray and A. A. C. M. Beenackers, "Novel swirl-flow reactor for kinetic studies of semiconductor photocatalysis," *AIChE J.*, vol. 43, no. 10, pp. 2571–2578, 1997.
- [122] D. Dixit, A. Verma, S. Gupta, and P. Bansal, "Assessment of solar photocatalytic degradation and mineralization of amoxicillin trihydrate (AMT) using slurry and fixed-bed batch reactor: efficacy of parabolic trough collector," *RSC Adv.*, vol. 6, pp. 36109–36117, 2016.
- [123] D. Beydoun, R. Amal, G. K.-C. Low, and S. McEvoy, "Novel photocatalyst: Titania-coated magnetite. Activity and photodissolution," *J. Phys. Chem. B*, vol. 104, pp. 4387–4396, 2000.
- [124] J. O. Carneiro *et al.*, "Synthesis of iron-doped TiO<sub>2</sub> nanoparticles by ball-milling process: The influence of process parameters on the structural, optical, magnetic, and photocatalytic properties," *J. Mater. Sci.*, vol. 49, pp. 7476–7488, 2014.
- [125] S. Teixeira *et al.*, "Photocatalytic degradation of recalcitrant micropollutants by reusable Fe<sub>3</sub>O<sub>4</sub>/SiO<sub>2</sub>/TiO<sub>2</sub> particles," *J. Photochem. Photobiol. A Chem.*, vol. 345, pp. 27–35, 2017.
- [126] S. Horikoshi, N. Watanabe, H. Onishi, H. Hidaka, and N. Serpone, "Photodecomposition of a nonylphenol polyethoxylate surfactant in a cylindrical photoreactor with TiO<sub>2</sub> immobilized fiberglass cloth," *Appl. Catal. B Environ.*, vol. 37, pp. 117–129, 2002.
- [127] H. Zangeneh, A. A. L. Zinatizadeh, and M. Feyzi, "Degradation of linear alkyl benzene using an immobilized nano TiO<sub>2</sub> photocatalytic reactor: Process analysis and modeling," *Clean - Soil, Air, Water*, vol. 44, pp. 78–88, 2016.

- [128] W. Wang and Y. Ku, "The light transmission and distribution in an optical fiber coated with TiO<sub>2</sub> particles," *Chemosphere*, vol. 50, pp. 999–1006, 2003.
- [129] K. Hofstadler, R. Bauer, S. Novalic, and G. Heisler, "New reactor design for photocatalytic waste-water treatment with TiO<sub>2</sub> immobilized on fused-silica glass-fibers: Photomineralization of 4-Chlorophenol," *Environ. Sci. Technol.*, vol. 28, pp. 670–674, 1994.
- [130] N. J. Peill and M. R. Hoffmann, "Development and optimization of a TiO<sub>2</sub>-coated fiber-optic cable reactor: photocatalytic degradation of 4-Chlorophenol," *Environ. Sci. Technol.*, vol. 29, no. 12, pp. 2974–2981, 1995.
- [131] M. Mohajerani, M. Mehrvar, and F. Ein-Mozaffari, "An overview of the integration of advanced oxidation technologies and other processes for water and wastewater treatment," *Int. J. Eng.*, vol. 3, no. 2, pp. 120–146, 2009.
- [132] V. Augugliaro, M. Litter, L. Palmisano, and J. Soria, "The combination of heterogeneous photocatalysis with chemical and physical operations: A tool for improving the photoprocess performance," *J. Photochem. Photobiol. C Photochem. Rev.*, vol. 7, pp. 127–144, 2006.
- [133] S. Mozia, "Photocatalytic membrane reactors (PMRs) in water and wastewater treatment. A review," *Sep. Purif. Technol.*, vol. 73, pp. 71–91, 2010.
- [134] S. Leong, A. Razmjou, K. Wang, K. Hapgood, X. Zhang, and H. Wang, "TiO<sub>2</sub> based photocatalytic membranes: A review," *J. Memb. Sci.*, vol. 472, pp. 167–184, 2014.
- [135] J. Fu, M. Ji, Z. Wang, L. Jin, and D. An, "A new submerged membrane photocatalysis reactor (SMPR) for fulvic acid removal using a nano-structured photocatalyst," *J. Hazard. Mater.*, vol. B131, pp. 238–242, 2006.
- [136] J. Ryu, W. Choi, and K.-H. Choo, "A pilot-scale photocatalyst-membrane hybrid reactor: performance and characterization," *Water Sci. Technol.*, vol. 51, no. 6–7, pp. 491–497, Jan. 2005.
- [137] U. G. Akpan and B. H. Hameed, "Parameters affecting the photocatalytic degradation of dyes using TiO<sub>2</sub>-based photocatalysts: A review," *J. Hazard. Mater.*, vol. 170, pp. 520–529, 2009.
- [138] M. Tanveer and G. Tezcanli Guyer, "Solar assisted photo degradation of wastewater by compound parabolic collectors: Review of design and operational parameters," *Renew. Sustain. Energy Rev.*, vol. 24, pp. 534–543, Aug. 2013.
- [139] R. J. Brandi, G. Rintoul, O. M. Alfano, and A. E. Cassano, "Photocatalytic reactors - Reaction kinetics in a flat plate solar simulator," *Catal. Today*, vol. 76, pp. 161–175, 2002.
- [140] T. Van Gerven, G. Mul, J. Moulijn, and A. Stankiewicz, "A review of intensification of photocatalytic processes," *Chem. Eng. Process. Process Intensif.*, vol. 46, pp. 781–789, 2007.

- [141] J. P. Knowles, L. D. Elliott, and K. I. Booker-Milburn, "Flow photochemistry: Old light through new windows," *Beilstein J. Org. Chem.*, vol. 8, pp. 2025–2052, 2012.
- [142] F. Amano, E. Ishinaga, and A. Yamakata, "Effect of particle size on the photocatalytic activity of WO<sub>3</sub> particles for water oxidation," *J. Phys. Chem. C*, vol. 117, pp. 22584–22590, 2013.
- [143] T. Zhang, T. Oyama, S. Horikoshi, H. Hidaka, J. Zhao, and N. Serpone, "Photocatalyzed N-demethylation and degradation of methylene blue in titania dispersions exposed to concentrated sunlight," *Sol. Energy Mater. Sol. Cells*, vol. 73, pp. 287–303, 2002.
- [144] I. Oller, S. Malato, and J. A. Sánchez-Pérez, "Combination of advanced oxidation processes and biological treatments for wastewater decontamination - A review," *Sci. Total Environ.*, vol. 409, pp. 4141–4166, 2011.
- [145] M. Bitenc, B. Horvat, B. Likozar, G. Dražić, and Z. C. Orel, "The impact of ZnO load, stability and morphology on the kinetics of the photocatalytic degradation of caffeine and resazurin," *Appl. Catal. B Environ.*, vol. 136–137, pp. 202–209, 2013.
- [146] R. W. Matthews, "Purification of water with near-U.V. illuminated suspensions of titanium dioxide," *Water Res.*, vol. 24, no. 5, pp. 653–660, 1990.
- [147] S. Sakthivel, B. Neppolian, M. V. Shankar, B. Arabindoo, M. Palanichamy, and V. Murugesan, "Solar photocatalytic degradation of azo dye: comparison of photocatalytic efficiency of ZnO and TiO<sub>2</sub>," *Sol. Energy Mater. Sol. Cells*, vol. 77, pp. 65–82, 2003.
- [148] M. A. Behnajady, N. Modirshahla, and R. Hamzavi, "Kinetic study on photocatalytic degradation of C.I. Acid Yellow 23 by ZnO photocatalyst," *J. Hazard. Mater.*, vol. B133, pp. 226–232, 2006.
- [149] L. Yang, L. E. Yu, and M. B. Ray, "Degradation of paracetamol in aqueous solutions by TiO<sub>2</sub> photocatalysis," *Water Res.*, vol. 42, pp. 3480–3488, 2008.
- [150] T. Soltani and M. H. Entezari, "Solar photocatalytic degradation of RB5 by ferrite bismuth nanoparticles synthesized via ultrasound," *Ultrason. Sonochem.*, vol. 20, pp. 1245–1253, 2013.
- [151] A. J. Hoffman, E. R. Carraway, and M. R. Hoffmann, "Photocatalytic production of H<sub>2</sub>O<sub>2</sub> and organic peroxides on quantum-sized semiconductor colloids," *Environ. Sci. Technol.*, vol. 28, pp. 776–785, 1994.
- [152] N. Serpone and A. Salinaro, "Terminology, relative photonic efficiencies and quantum yields in heterogeneous photocatalysis. Part I: Suggested protocol," *Pure Appl. Chem.*, vol. 71, no. 2, pp. 303–320, 1999.
- [153] B. Neppolian, H. C. Choi, S. Sakthivel, B. Arabindoo, and V. Murugesan, "Solar/UV-induced photocatalytic degradation of three commercial textile dyes," *J. Hazard. Mater.*, vol. B89, pp. 303–317, 2002.

- [154] C. Nickel *et al.*, "Dynamic light-scattering measurement comparability of nanomaterial suspensions," *J. Nanoparticle Res.*, vol. 16:2260, pp. 1–12, 2014.
- [155] H. Zhang, R. L. Penn, R. J. Hamers, and J. F. Banfield, "Enhanced adsorption of molecules on surfaces of nanocrystalline particles," *J. Phys. Chem. B*, vol. 103, pp. 4656–4662, 1999.
- [156] M. Anpo, T. Shima, S. Kodama, and Y. Kubokawa, "Photocatalytic hydrogenation of CH<sub>3</sub>CCH with H<sub>2</sub>O on small-particle TiO<sub>2</sub>: Size quantization and reaction intermediates," *J. Phys. Chem.*, vol. 91, pp. 4305–4310, 1987.
- [157] A. J. Maira, K. L. Yeung, C. Y. Lee, P. L. Yue, and C. K. Chan, "Size effects in gas-phase photo-oxidation of trichloroethylene using nanometer-sized TiO<sub>2</sub> catalysts," *J. Catal.*, vol. 192, pp. 185–196, 2000.
- [158] H. Lin, C. P. Huang, W. Li, C. Ni, S. Ismat Shah, and Y.-H. Tseng, "Size dependency of nanocrystalline TiO<sub>2</sub> on its optical property and photocatalytic reactivity exemplified by 2-chlorophenol," *Appl. Catal. B Environ.*, vol. 68, pp. 1–11, 2006.
- [159] K. Kočí *et al.*, "Effect of TiO<sub>2</sub> particle size on the photocatalytic reduction of CO<sub>2</sub>," *Appl. Catal. B Environ.*, vol. 89, pp. 494–502, 2009.
- [160] F. Babick, "Characterisation of colloidal suspensions," in *Suspensions of colloidal particles and aggregates*, J. M. V. Millán, Ed. Springer, 2016, pp. 7–74.
- [161] D. Jassby, J. F. Budarz, and M. Wiesner, "Impact of aggregate size and structure on the photocatalytic properties of TiO<sub>2</sub> and ZnO nanoparticles," *Environ. Sci. Technol.*, vol. 46, pp. 6934–6941, 2012.
- [162] R. Finsy and N. De Jaeger, "Particle sizing by photon correlation spectroscopy. Part II: average values," *Part. Part. Syst. Charact.*, vol. 8, pp. 187–193, 1991.
- [163] K. P. Hapgood, G. V. Franks, J. S. Curtis, and M. Rhodes, "Particle size analysis," in *Introduction to Particle Technology*, 2nd ed., M. Rhodes, Ed. Wes Sussex: Jon Wiley & Sons, Ltd, 2008, pp. 1–28.
- [164] H. Rumpf and Translated by F.A. Bull, "The characteristics of systems and their changes of states," in *Particle technology*, B. Scarlett, Ed. Chapman and Hall, 1990, pp. 8–55.
- [165] S. Malato, M. I. Maldonado, P. Fernández-Ibáñez, I. Oller, I. Polo, and R. Sánchez-Moreno, "Decontamination and disinfection of water by solar photocatalysis: The pilot plants of the Plataforma Solar de Almeria," *Mater. Sci. Semicond. Process.*, vol. 42, pp. 15–23, 2016.
- [166] S. Teixeira, R. Gurke, H. Eckert, K. Kühn, J. Fauler, and G. Cuniberti, "Photocatalytic degradation of pharmaceuticals present in conventional treated wastewater by nanoparticle suspensions," *J. Environ. Chem. Eng.*, vol. 4, pp. 287–292, 2016.

- [167] M. E. Davis and R. J. Davis, "Heterogeneous catalysis," in *Fundamentals of chemical reaction engineering*, 1st ed., E. D. Glandt, M. T. Klein, and T. F. Edgar, Eds. New York: McGraw-Hill Higher Education, 2003, pp. 133–183.
- [168] B. Neppolian, H. C. Choi, S. Sakthivel, B. Arabindoo, and V. Murugesan, "Solar light induced and TiO<sub>2</sub> assisted degradation of textile dye reactive blue 4," *Chemosphere*, vol. 46, pp. 1173–1181, 2002.
- [169] O. M. Alfano, A. E. Cassano, R. J. Brandi, and M. L. Satuf, "A methodology for modeling slurry photocatalytic reactors for degradation of an organic pollutant in water," in *Photocatalysis and water purification: From fundamentals to recent applications*, P. Pichat, Ed. Weinheim: Wiley-VCH Verlag GmbH & Co. KGaA, 2013, pp. 335–359.
- [170] J.-M. Herrmann, "Fundamentals and misconceptions in photocatalysis," *J. Photochem. Photobiol. A Chem.*, vol. 216, pp. 85–93, 2010.
- [171] X. Fu, L. A. Clark, W. A. Zeltner, and M. A. Anderson, "Effects of reaction temperature and water vapor content on the heterogeneous photocatalytic oxidation of ethylene," *J. Photochem. Photobiol. A Chem.*, vol. 97, pp. 181–186, 1996.
- [172] R. Jain, M. Mathur, S. Sikarwar, and A. Mittal, "Removal of the hazardous dye rhodamine B through photocatalytic and adsorption treatments," *J. Environ. Manage.*, vol. 85, pp. 956–964, 2007.
- [173] M. Kosmulski, "The significance of the difference in the point of zero charge between rutile and anatase," *Adv. Colloid Interface Sci.*, vol. 99, pp. 255–264, 2002.
- [174] K. C. Akratopulu, C. Kordulis, and A. Lycourghiotis, "Effect of temperature on the point of zero charge and surface charge of TiO<sub>2</sub>," *J. Chem. Soc. Faraday Trans.*, vol. 86, no. 20, pp. 3437–3440, 1990.
- [175] S. Malato, J. Blanco, D. C. Alarcón, M. I. Maldonado, P. Fernández-Ibáñez, and W. Gernjak, "Photocatalytic decontamination and disinfection of water with solar collectors," *Catal. Today*, vol. 122, pp. 137–149, 2007.
- [176] J. S. Noh and J. A. Schwarz, "Estimation of the point of zero charge of simple and mixed oxides by mass titration," *J. Colloid Interface Sci.*, vol. 130, no. 1, pp. 157–164, 1989.
- [177] R. Terzian and N. Serpone, "Heterogeneous photocatalyzed oxidation of creosote components: mineralization of xylenols by illuminated TiO<sub>2</sub> in oxygenated aqueous media," *J. Photochem. Photobiol. A Chem.*, vol. 89, pp. 163–175, 1995.
- [178] M. Fujihira, Y. Satoh, and T. Osa, "Heterogeneous photocatalytic reactions on semiconductor materials. III. Effect of pH and Cu<sup>2+</sup> ions on the photo-fenton type reaction," *Bull. Chem. Soc. Jpn.*, vol. 55, no. 3, pp. 666–671, 1982.
- [179] J. M. Bolts and M. S. Wrighton, "Correlation of photocurrent-voltage curves with flat-band potential for stable photoelectrodes for the photoelectrolysis of water," *J. Phys. Chem.*, vol. 80, no. 24, pp. 2641–2645, 1976.

- [180] C. Guillard, H. Lachheb, A. Houas, M. Ksibi, E. Elaloui, and J.-M. Herrmann, "Influence of chemical structure of dyes, of pH and of inorganic salts on their photocatalytic degradation by TiO<sub>2</sub> comparison of the efficiency of powder and supported TiO<sub>2</sub>," *J. Photochem. Photobiol. A Chem.*, vol. 158, pp. 27–36, 2003.
- [181] A. Mills, S. Morris, and R. Davies, "Photomineralisation of 4-chlorophenol sensitised by titanium dioxide: a study of the intermediates," *J. Photochem. Photobiol. A Chem.*, vol. 70, pp. 183–191, 1993.
- [182] W. Schmidt, "Molecular absorption spectroscopy," in *Optical spectroscopy in chemistry and life sciences*, Weinheim: Wiley-VCH Verlag GmbH & Co. KGaA, 2005, pp. 129–194.
- [183] M. I. Cabrera, O. M. Alfano, and A. E. Cassano, "Absorption and scattering coefficients of titanium dioxide particulate suspensions in water," *J. Phys. Chem.*, vol. 100, pp. 20043–20050, 1996.
- [184] S. E. Braslavsky *et al.*, "Glossary of terms used in photocatalysis and radiation catalysis (IUPAC recommendations 2011)," *Pure Appl. Chem.*, vol. 83, no. 4, pp. 931–1014, 2011.
- [185] J.-M. Herrmann, "Photocatalysis fundamentals revisited to avoid several misconceptions," *Appl. Catal. B Environ.*, vol. 99, pp. 461–468, 2010.
- [186] H. N. Le, F. Babick, K. Kühn, M. T. Nguyen, M. Stintz, and G. Cuniberti, "Impact of ultrasonic dispersion on the photocatalytic activity of titania aggregates," *Beilstein J. Nanotechnol.*, vol. 6, pp. 2423–2430, 2015.
- [187] Philips, "TL mini blacklight blue." [Online]. Available: [http://www.lighting.philips.com/main/prof/lamps/fluorescent-lamps-and-starters/tl-miniature/tl-mini-blacklight-blue/928001010803\\_EU/product](http://www.lighting.philips.com/main/prof/lamps/fluorescent-lamps-and-starters/tl-miniature/tl-mini-blacklight-blue/928001010803_EU/product). [Accessed: 28-Nov-2016].
- [188] SCHOTT Technical Glass Solutions GmbH, *Schott Borofloat 33*. Jena, 2009.
- [189] H. N. Le, F. Babick, K. Kühn, M. T. Nguyen, M. Stintz, and G. Cuniberti, "Impact of optical property on the photocatalytic activity of aggregates," in *Particle Technology*, 2016, pp. 1–4.
- [190] Y. A. Çengel and J. M. Cimbala, "Flow in pipes," in *Fluid mechanics: Fundamentals and applications*, S. Jeans, Ed. New York: McGraw-Hill, 2006, pp. 321–398.
- [191] J. N. Tilton, "Fluid and particle dynamics," in *Perry's chemical engineers' handbook*, 8th ed., D. W. Green and R. H. Perry, Eds. McGraw-Hill, 2008, pp. 1–56.
- [192] "Das Labor im Computer," *Dresdner Universitätsjournal*, Dresden, p. 9, Jan-2015.
- [193] U. Boehmer, S. H. Suhardi, and T. Bley, "Decolorizing reactive textile dyes with white-rot fungi by temporary immersion cultivation," *Eng. Life Sci.*, vol. 6, no. 4, pp. 417–420, 2006.

- [194] U. Böhmer, C. Kirsten, T. Bley, and M. Noack, "White-rot fungi combined with lignite granules and lignitic xylite to decolorize textile industry wastewater," *Eng. Life Sci.*, vol. 10, no. 1, pp. 26–34, 2010.
- [195] M. E. Davis and R. J. Davis, "The basics of reaction kinetics for chemical reaction engineering," in *Fundamentals of chemical reaction engineering*, 1st ed., E. D. Glandt, M. T. Klein, and T. F. Edgar, Eds. New York: McGraw-Hill Higher Education, 2003, pp. 1–52.
- [196] M. E. Davis and R. J. Davis, "Reactors for measuring reaction rates," in *Fundamentals of chemical reaction engineering*, 1st ed., E. D. Glandt, M. T. Klein, and T. F. Edgar, Eds. New York: McGraw-Hill Higher Education, 2003, pp. 64–99.
- [197] Evonik, "AEROXIDE®, AERODISP® and AEROPERL® titanium dioxide as photocatalyst," 2013. [Online]. Available: <https://www.aerosil.com/sites/lists/RE/DocumentsSI/TI-1243-Titanium-Dioxide-as-Photocatalyst-EN.pdf>. [Accessed: 20-Jan-2015].
- [198] W. R. Siah, H. O. Lintang, M. Shamsuddin, and L. Yuliaty, "High photocatalytic activity of mixed anatase-rutile phases on commercial TiO<sub>2</sub> nanoparticles," *IOP Conf. Ser. Mater. Sci. Eng.*, vol. 107, pp. 1–8, 2016.
- [199] R. López and R. Gómez, "Band-gap energy estimation from diffuse reflectance measurements on sol-gel and commercial TiO<sub>2</sub>: a comparative study," *J. Sol-Gel Sci. Technol.*, vol. 61, pp. 1–7, 2012.
- [200] M. Wu, Y. Li, Z. Deng, and B.-L. Su, "Three-dimensionally ordered macroporous titania with structural and photonic effects for enhanced photocatalytic efficiency," *ChemSusChem*, vol. 4, pp. 1481–1488, 2011.
- [201] M. Kosmulski, "The pH-dependent surface charging and the points of zero charge," *J. Colloid Interface Sci.*, vol. 253, pp. 77–87, 2002.
- [202] M. Kosmulski, J. Gustafsson, and J. B. Rosenholm, "Correlation between the zeta potential and rheological properties of anatase dispersions," *J. Colloid Interface Sci.*, vol. 209, pp. 200–206, 1999.
- [203] T. Preočanin and N. Kallay, "Point of zero charge and surface charge density of TiO<sub>2</sub> in aqueous electrolyte solution as obtained by potentiometric mass titration," *Croat. Chem. Acta*, vol. 79, no. 1, pp. 95–106, 2006.
- [204] J. Han, Y. Liu, N. Singhal, L. Wang, and W. Gao, "Comparative photocatalytic degradation of estrone in water by ZnO and TiO<sub>2</sub> under artificial UVA and solar irradiation," *Chem. Eng. J.*, vol. 213, pp. 150–162, 2012.
- [205] V. Srikant and D. R. Clarke, "On the optical band gap of zinc oxide," *J. Appl. Phys.*, vol. 83, no. 10, pp. 5447–5451, 1998.

- [206] H. Lachheb *et al.*, "Photocatalytic degradation of various types of dyes (Alizarin S, Crocein Orange G, Methyl Red, Congo Red, Methylene Blue) in water by UV-irradiated titania," *Appl. Catal. B Environ.*, vol. 39, pp. 75–90, 2002.
- [207] A. Mills, C. Hill, and P. K. J. Robertson, "Overview of the current ISO tests for photocatalytic materials," *J. Photochem. Photobiol. A Chem.*, vol. 237, pp. 7–23, 2012.
- [208] S. Bae, S. Kim, S. Lee, and W. Choi, "Dye decolorization test for the activity assessment of visible light photocatalysts: Realities and limitations," *Catal. Today*, vol. 224, pp. 21–28, 2014.
- [209] X. Yan, T. Ohno, K. Nishijima, R. Abe, and B. Ohtani, "Is methylene blue an appropriate substrate for a photocatalytic activity test? A study with visible-light responsive titania," *Chem. Phys. Lett.*, vol. 429, pp. 606–610, 2006.
- [210] H. Eckert, M. Bobeth, S. Teixeira, K. Kühn, and G. Cuniberti, "Modeling of photocatalytic degradation of organic components in water by nanoparticle suspension," *Chem. Eng. J.*, vol. 261, pp. 67–75, 2015.
- [211] P. T. Hang and G. W. Brindley, "Methylene blue absorption by clay minerals. Determination of surface areas and cation exchange capacities (clay-organic studies XVIII)," *Clays Clay Miner.*, vol. 18, pp. 203–212, 1970.
- [212] U. Neugebauer, A. Szeghalmi, M. Schmitt, W. Kiefer, J. Popp, and U. Holzgrabe, "Vibrational spectroscopic characterization of fluoroquinolones," *Spectrochim. Acta - Part A*, vol. 61, pp. 1505–1517, 2005.
- [213] P. A. Shahu, V. V. Potnis, P. V. Dangre, and L. T. Thote, "Development and validation of simultaneous estimation of ciprofloxacin hydrochloride and dexamethasone sodium phosphate in bulk drug and its formulation," *Indo Am. J. Pharm. Res.*, vol. 3, no. 9, pp. 7103–7113, 2013.
- [214] S. Te Lin, T.-H. You, and C.-H. Cheng, "Method for reactive dyeing of leather," US2012/0047663 A1, 2012.
- [215] A. Akyol, H. C. Yatmaz, and M. Bayramoglu, "Photocatalytic decolorization of Remazol Red RR in aqueous ZnO suspensions," *Appl. Catal. B Environ.*, vol. 54, pp. 19–24, 2004.
- [216] F. Gruy and M. Cournil, "On-line determination of aggregate size and morphology in suspensions," *Part. Part. Syst. Charact.*, vol. 21, pp. 197–204, Oct. 2004.
- [217] J. Gregory, "Monitoring particle aggregation processes," *Adv. Colloid Interface Sci.*, vol. 147–148, pp. 109–123, 2009.
- [218] H.-D. Dörfler, "Lichtstreuung an kolloiden und makromolekularen Systemen," in *Grenzflächen- und Kolloidchemie*, T. Kellersohn, Ed. Weinheim: VCH, 1994, pp. 412–451.
- [219] Deutsche Norm, "DIN 52980: Photocatalytic activity of surfaces – Determination of photocatalytic activity by degradation of methylene blue," Berlin, 2008.

- [220] International Standard, "ISO 10678:2010(E): Fine ceramics (advanced ceramics, advanced technical ceramics) - Determination of photocatalytic activity of surfaces in an aqueous medium by degradation of methylene blue," Geneva, 2010.
- [221] Shimadzu, "Measurements of band gap in compound semiconductors - Band gap determination from diffuse reflectance spectra," Tokyo.
- [222] J. Torrent and V. Barrón, "Diffuse reflectance spectroscopy," in *Methods of soil analysis. Part 5. Mineralogical methods.*, no. 5, A. L. Ulery and L. R. Drees, Eds. Madison: Soil Science Society of America Book Series, 2008, pp. 367–385.
- [223] N. De Jaeger *et al.*, "Particle sizing by photon correlation spectroscopy. Part I: Monodisperse latices: Influence of scattering angle and concentration of dispersed material," *Part. Part. Syst. Charact.*, vol. 8, pp. 179–186, 1991.
- [224] R. Finsy, N. De Jaeger, R. Sneyers, and E. Geladé, "Particle sizing by photon correlation spectroscopy. Part III: Mono and bimodal distributions and data analysis," *Part. Part. Syst. Charact.*, vol. 9, pp. 125–137, 1992.
- [225] R. Finsy *et al.*, "Particle sizing by photon correlation spectroscopy. Part IV: Resolution of bimodals and comparison with other particle sizing methods," *Part. Part. Syst. Charact.*, vol. 10, pp. 118–128, 1993.
- [226] Deutsche Norm, "DIN ISO 13321: Particle size analysis – Photon correlation spectroscopy," Berlin, 2004.
- [227] J. Hyeon-Lee, G. Beaucage, S. E. Pratsinis, and S. Vemury, "Fractal analysis of flame-synthesized nanostructured silica and titania powders using small-angle X-ray scattering," *Langmuir*, vol. 14, pp. 5751–5756, 1998.
- [228] W. J. Tseng and K.-C. Lin, "Rheology and colloidal structure of aqueous TiO<sub>2</sub> nanoparticle suspensions," *Mater. Sci. Eng. A*, vol. 355, pp. 186–192, 2003.
- [229] IKA German technology, "Dispersers. From invention to innovation." [Online]. Available: [http://www.ika.com/ika/pdf/flyer-catalog/Disperser\\_Brochure\\_IWS\\_EN\\_wop\\_screen.pdf](http://www.ika.com/ika/pdf/flyer-catalog/Disperser_Brochure_IWS_EN_wop_screen.pdf). [Accessed: 27-Feb-2017].
- [230] K. S. Suslick and G. J. Price, "Applications of Ultrasound To Materials Chemistry," *Annu. Rev. Mater. Sci.*, vol. 29, pp. 295–326, 1999.
- [231] M. Pohl, H. Schubert, and H. P. Schuchmann, "Herstellung stabiler Dispersionen aus pyrogener Kieselsäure," *Chemie Ing. Tech.*, vol. 77, no. 3, pp. 258–262, 2005.
- [232] M. Pohl and H. Schubert, "Untersuchungen zum Dispergierverhalten nanoskaliger Pulver," *Chemie Ing. Tech.*, vol. 75, pp. 1111–1112, 2003.
- [233] S. Teixeira, "Doctoral dissertation: Photocatalytic degradation of pharmaceuticals present in wastewater," Technische Universität Dresden, 2018.

- [234] M. L. Satuf, R. J. Brandi, A. E. Cassano, and O. M. Alfano, "Experimental method to evaluate the optical properties of aqueous titanium dioxide suspensions," *Ind. Eng. Chem. Res.*, vol. 44, pp. 6643–6649, 2005.
- [235] F. Babick, "Suspensions of colloidal aggregates," in *Suspensions of colloidal particles and aggregates*, vol. 20, J. M. V. Millán, Ed. Springer, 2016, pp. 119–220.
- [236] T. Zhang, T. Oyama, A. Aoshima, H. Hidaka, J. Zhao, and N. Serpone, "Photooxidative N-demethylation of methylene blue in aqueous TiO<sub>2</sub> dispersions under UV irradiation," *J. Photochem. Photobiol. A Chem.*, vol. 140, pp. 163–172, 2001.
- [237] S. Venkatraman, "Master thesis: Optical properties of TiO<sub>2</sub> photocatalyst applied for the degradation of environmental products in a flow photoreactor," Technische Universität Dresden, Department of Hydro Science, 2016.
- [238] H. Le, "Diploma thesis: Die Entfärbung von kommerziellen Textilfarbstoffen mittels Photokatalyse in einem Durchflussreaktor," Technische Universität Dresden, Chair of Materials Science and Nanotechnology, 2017.
- [239] O. Impert, A. Katafias, P. Kita, A. Mills, A. Pietkiewicz-graczyk, and G. Wrzeszcz, "Kinetics and mechanism of a fast leuco-Methylene Blue oxidation by copper (II)–halide species in acidic aqueous media," *Dalt. Trans.*, pp. 348–353, 2003.
- [240] B. H. Kaye, "An exploration of the physical significance of fractal structures in three-dimensional space," in *A random walk through fractal dimensions*, 1st ed., C. Dyllick-Brenzinger, Ed. Weinheim: VCH, 1989, pp. 297–325.
- [241] M. Styliadi, D. I. Kondarides, and X. E. Verykios, "Pathways of solar light-induced photocatalytic degradation of azo dyes in aqueous TiO<sub>2</sub> suspensions," *Appl. Catal. B Environ.*, vol. 40, pp. 271–286, 2003.
- [242] G. N. Lewis, O. Goldschmid, T. T. Magel, and J. Bigeleisen, "Dimeric and other forms of methylene blue: Absorption and fluorescence of the pure monomer," *J. Am. Chem. Soc.*, vol. 65, no. 6, pp. 1150–1154, 1943.
- [243] D. Heger, J. Jirkovský, and P. Klán, "Aggregation of methylene blue in frozen aqueous solutions studied by absorption spectroscopy," *J. Phys. Chem. A*, vol. 109, pp. 6702–6709, 2005.
- [244] A. R. Silva *et al.*, "Ciprofloxacin wastewater treated by UVA photocatalysis: contribution of irradiated TiO<sub>2</sub> and ZnO nanoparticles on the final toxicity as assessed by *Vibrio fischeri*," *RSC Adv.*, vol. 6, pp. 95494–95503, 2016.
- [245] Ministry of Natural Resources and Environment of Vietnam, "QCVN 13-MT:2015/BTNMT: National technical regulation on the effluent of textile industry," Hanoi, 2015.
- [246] U. Soltmann, "CLIENT Vietnam: Verbundprojekt Konzeptentwicklung für die Abwasserbehandlung von Textilunternehmen in Vietnam mittels photokatalytischer

Oxidation mit nanoskaligem Titandioxid als Photokatalysator: Entwicklung photoaktiver Oberflächenbeschichtungen," Gesellschaft zur Förderung von Medizin-, Bio- und Umwelttechnologien e.V., 2017.

- [247] G. Cuniberti, "CLIENT Vietnam - Navitex: Verbundprojekt Konzeptentwicklung für die Abwasserbehandlung von Textilunternehmen in Vietnam mittels photokatalytischer Oxidation mit nanoskaligem Titandioxid als Photokatalysator: Entwicklung Photokatalysatoren," Technische Universität Dresden, Institut für Werkstoffwissenschaft und Max-Bergmann-Zentrum für Biomaterialien, 2017.
- [248] A. Meyer, "NaViTex - Verbundprojekt Konzeptentwicklung für die Abwasserbehandlung von Textilunternehmen in Vietnam mittels photokatalytischer Oxidation mit nanoskaligem Titandioxid als Photokatalysator: Entwicklung Anlagenkonzept," UMEX GmbH Dresden, 2017.
- [249] Deutsche Norm, "DIN ISO 9276-2:2006-02: Representation of results of particle size analysis - Part 2: Calculation of average particle sizes/diameters and moments from particle size distributions," Berlin, 2006.

## APPENDIX

### A1. FUNDAMENTALS OF PARTICLE SIZE

#### Equivalent diameters

The shape of a particle can be spherical, non-spherical or even irregular. Geometrical measures of a particle can be stipulated such as the main dimensions, statistical lengths, or volume, surface area, projected area [163]. The measure is expressed in the term of “equivalent diameter” [164]. It varies depending on analytical methods. E.g., image analyses give the projection of particles, sieve analyses determine the diameter of circumscribing spheres, and sedimentation analyses handle the hydrodynamic equivalent diameter [163], [164].

#### Particle size distribution

Size and shape of particles are non-uniform, thus lead to the fact that size-dependent geometric and physical features are non-uniform. Particle size distribution is necessary to characterize particle populations.

Let  $x$  a size of particle measurement distributed from the minimum value  $x_{\min}$  to the maximum value  $x_{\max}$ . The proportion of the total population lying between  $x_{\min}$  and  $x$  is defined as the cumulative function  $Q_r(x)$  (Figure A 1). Since the number of particles in most practical assemblies is large,  $Q_r(x)$  can be regarded as continuous and can be differentiated to have the density function  $q_r(x)$  (Figure A 1)

$$q_r(x) = \frac{dQ_r(x)}{dx} \Leftrightarrow Q_r(x) = \int_{x_{\min}}^x q_r(x) dx. \quad (\text{A.1})$$

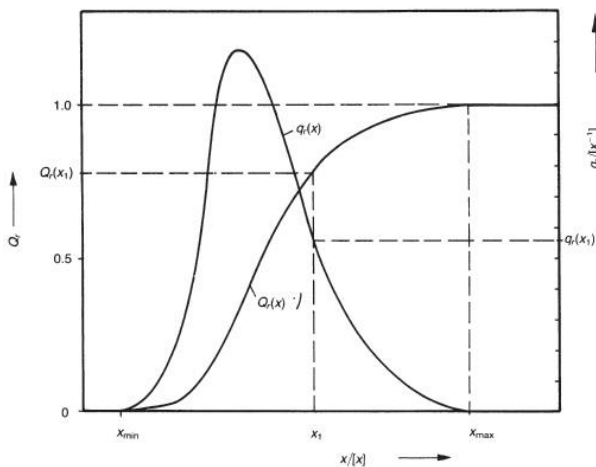


Figure A 1 Graphical representation of particle size distribution of an assemble [164].

The measure of the distribution can be number, length, surface area, or volume, corresponding to the subscript  $r$  of 0, 1, 2 or 3, respectively.

In particle size distribution, some specific statistical values may be considered [162], [163]: the mode  $x_{\text{mode},r}$  is the most frequently occurring size in the sample, where  $q_r(x_{\text{mode}})$  holds the maximum value; the median size  $x_{50,r}$  corresponds to the cumulative distribution as 50 % size, or  $Q_r(x_{50}) = 0.5$ , and the power mean size  $\bar{x}_{k,r}$  [249]

$$\bar{x}_{k,r} = \sqrt[k]{\int_{x_{\min}}^{x_{\max}} x^k dQ_r(x)}, \quad (\text{A.2})$$

where  $\int_{x_{\min}}^{x_{\max}} x^k dQ_r(x)$  is the moment of the size distribution. Corresponding to the exponent  $k$ , there are different means: arithmetic mean  $\bar{x}_{1,r}$  with  $k = 1$ , harmonic mean  $\bar{x}_{-1,r}$  with  $k = -1$ , geometric mean  $\bar{x}_{0,r}$  with  $k = 0$ , or quadratic mean  $\bar{x}_{2,r}$  with  $k = 2$ . E.g.,  $\bar{x}_{1,0}$  is the arithmetic mean of number weighted-size distribution, which is truly the average particle size. Note that the measure of distribution can be physical properties, such as extinction or scattering light intensity. For instance,  $\bar{x}_{-1,\text{int}}$  is the harmonic mean of intensity weighted-size distribution (section A2).

## A2. CHARACTERIZATION OF P25 COLLOIDAL SUSPENSIONS BY PHOTON CORRELATION SPECTROSCOPY

### A typical DLS correlogram

Photon correlation spectroscopy (or dynamic light scattering (DLS) method) was used to characterize the size of  $\text{TiO}_2$  P25 aggregates. P25 has the primary size of  $25 \pm 3$  nm [166], and the point of zero charge (PZC) at pH of approx. 6.4. Figure A 2 shows a typical correlogram of P25 samples measured by DLS instruments.

The data were analyzed by the Zetasizer software, version 7.02. The starting time of the decay gives information about the harmonic mean  $x_{\text{cum}}$ , whereas the angle of the decay  $\theta$  relates to the polydispersity *PDI* of the intensity-weighted size distribution (section A1). The baseline (shown in the inset of the figure) gives information of the presence of big aggregates.

### Effect of the particle concentrations on the DLS measurements

The quality of the DLS measurements can be influenced by the concentration of material. In this section, varied concentrations were tested to investigate the optimal concentration for the highest reliability of measurement. A rather strong ultrasonication was applied to disintegrate and homogenize the P25 suspension. The high power of 52 W by the ultrasonic processor Topas UDS751 was used. The dispersion lasted for 16 min. The prepared suspension was then diluted to have desired concentrations. The values  $x_{\text{cum}}$  and *PDI* were measured with the DLS Malvern Nano S90 instrument (Table A 1).

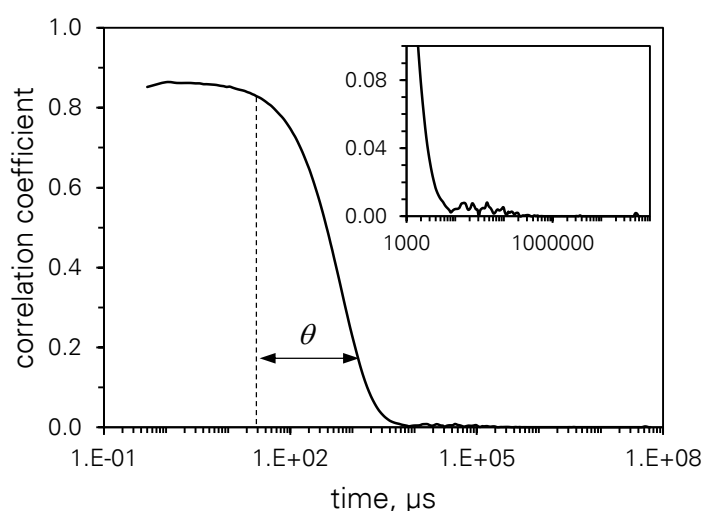


Figure A 2 Correlogram of a sample measured by dynamic light scattering. The inset shows the baseline of the correlation function.

Table A 1 Effect of particle concentration on the dynamic light scattering measurements.

No	concentration of particles g/l	mean count rate kcps	intercept -	attenuator -	$x_{cum}$ nm	$PDI$ -
1	1.000	209	0.742	9	74.3 $\pm$ 0.8	0.553 $\pm$ 0.027
2	0.333	339	0.903	8	217.3 $\pm$ 2.1	0.238 $\pm$ 0.013
3	0.167	468	0.906	8	220.9 $\pm$ 1.9	0.184 $\pm$ 0.015
4	0.100	431	0.915	8	221.2 $\pm$ 0.9	0.181 $\pm$ 0.010
5	0.067	367	0.924	8	220.6 $\pm$ 0.9	0.195 $\pm$ 0.021
6	0.033	225	0.945	8	238.6 $\pm$ 3.4	0.160 $\pm$ 0.020
7	0.017	334	0.936	9	626.1 $\pm$ 14.0	0.229 $\pm$ 0.028

The size  $x_{cum}$  of the 1 g/l particle concentration sample is too small compared to most of the other data, while  $PDI$  is too high. This suspension is too turbid, and light is extinguished through a short optical pathlength (see also section 5.2.3). The diluted sample of 0.017 g/l, on the contrary, has extremely big size. Probably the sample does not provide enough scattering signal for the detector. In both case, the attenuator is higher than the others. These two concentrations are not recommended for the DLS measurements.

Measurements at concentrations of 0.033–0.333 g/l suspensions give similar data. However, the  $PDI$  of the 0.333 g/l sample is a bit higher than the others, which can be attributed to the turbidity. Figure A 3 shows the transmittance of the suspensions with UV-VIS spectra. Accordingly, the suspension at 0.3 g/l induces a very low transmittance (2 %) at 633 nm which is the red laser wavelength of the nanosizer. Additionally, the 0.033 g/l sample has higher  $x_{cum}$  and lower  $PDI$ . For these reasons, a particle concentration of 0.067–0.167 g/l was chosen for further measurements.

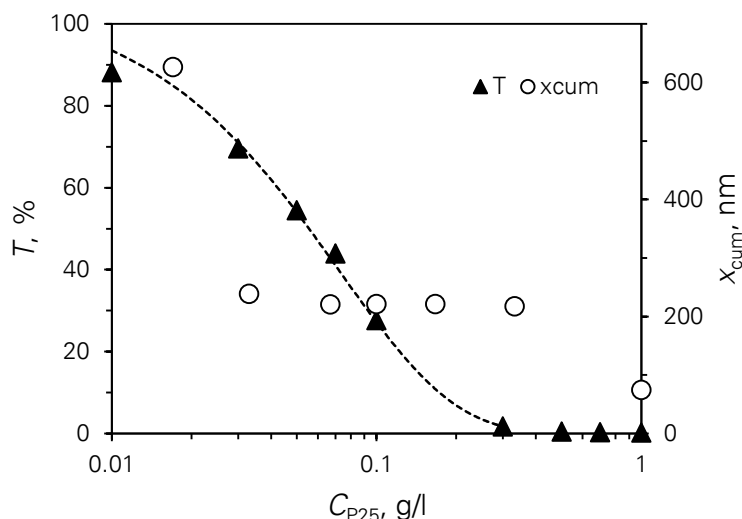


Figure A 3 Effect of the particle concentrations on the transmittance and dynamic light scattering measurements. Transmittances of P25 suspensions were measured by the UV-VIS spectroscopy, the 10 mm optical pathlength cuvette was used. The particle size  $x_{cum}$  was measured by the Nano S90 DLS instrument, the standard deviations of data are small and involved in the markers.

### Correlation of mean size measured by two DLS Malvern instruments: HPPS-ET and Nano S90

In this work, the harmonic intensity-weighted mean sizes of photocatalysts were measured by two DLS instruments, Malvern HPPS-ET and Nano S90. The HPPS-ET instrument was used in early studies: choosing a technique of dispersion and the energy concept of ultrasonic dispersion (sections 5.1.1 and A3) and the stability test of the suspensions (section A3). The other experiments were conducted with the Nano S90 instrument. Only one instrument was used throughout each series of experiments, thus the comparisons of the results were ensured. However, to have an overview for all data of this study, a correlation between data achieved by these two instruments is needed.

A 200 ml suspension of 1 g/l P25 was used as a standard suspension for the correlation function. The low ultrasonic power of 30 W by the ultrasonic processor Hielscher was used. The small decay rate of the integrated aggregate size (Figure A 4) helps to maximize the difference of the data achieved by the two instruments, thus increases the accuracy of the correlation. The time models of the ultrasonic dispersion were determined

$$x_{cum} = A \times t^{-\alpha}, \quad (A.3)$$

where  $A$  and  $\alpha$  are model parameters. For each instrument, they were found as in Table A 2. The size measured by these instruments is correlated to each other by the following equation

$$x_{cum(S90)} = x_{cum(HPPS)} \times 1.0055 \times t^{0.027}. \quad (A.4)$$

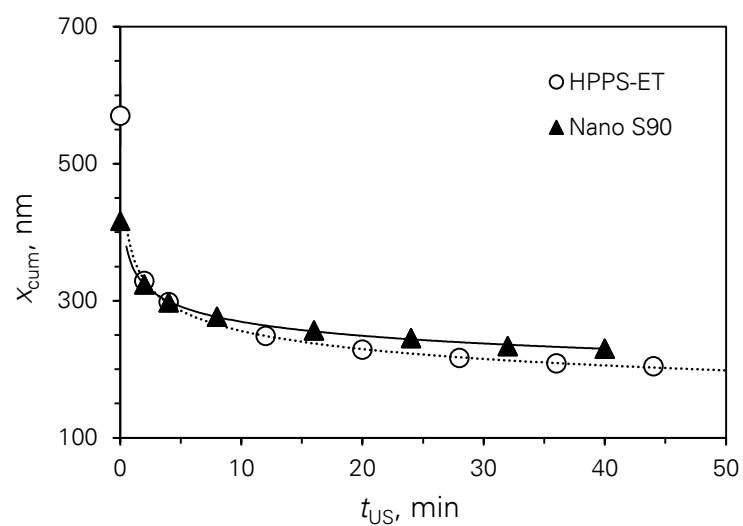


Figure A 4 Correlation of two dynamic light scattering instruments. A 200 ml P25 suspension of 1 g/l was dispersed with 30 W ultrasonication by the Hielscher processor for 40–50 min. Aggregate sizes of P25 measured by two dynamic light scattering instruments Malvern HPPS-ET and Nano S90 show a power function of dispersion time.

Table A 2 Correlation of two dynamic light scattering instruments Malvern HPPS-ET and Nano S90: Parameters of the time models.

Instrument	HPPS-ET	Nano S90
$A$	368.5	370.53
$\alpha$	0.158	0.131

### A3. DISPERSION OF P25

#### Dispersion with an ULTRA-TURRAX® device

ULTRA-TURRAX® dispersers are considered as a high-performance dispersing technique. A very high rotation speed of 21500 rpm (corresponding to 40 W) was applied to disperse 200 ml P25 suspension of 1 g/l. Within the dispersion period of 60 min, the aggregate size  $x_{cum}$  is in the sub-micron range of 495–586 nm (Figure A 5). Polydispersity index  $PDI$  fluctuates within the high range of 0.44–0.74 which is not precise when being measured by DLS technique (shown by large error bars). The results suggest that this technique is not efficient to disintegrate P25 aggregates. They are probably structured by tight bonds, which require another dispersion technique with a higher energy.

#### Dispersion with ultrasonication

A 200 ml volume of 1 g/l P25 suspension was dispersed within a period of 40 min. A rather low electric power of 30 W was applied by using the Hielscher device. Samples before and after ultrasonic dispersion were measured with the DLS Nano S90 instrument. Figure A 6 and Figure A 7 show the correlogram and the particle size distribution by intensity of samples, respectively.

Prior to the dispersion, the population is polydispersed, shown by the deviation of curves in Figure A 6a. Additionally, the baselines of the samples are high, evidencing the presence of big aggregates. The second peaks of thousands nm in Figure A 7a prove it as well. Note that with DLS method, the scattered light by large particles dominates that by small particles. For this reason, five measurements are dissimilar.

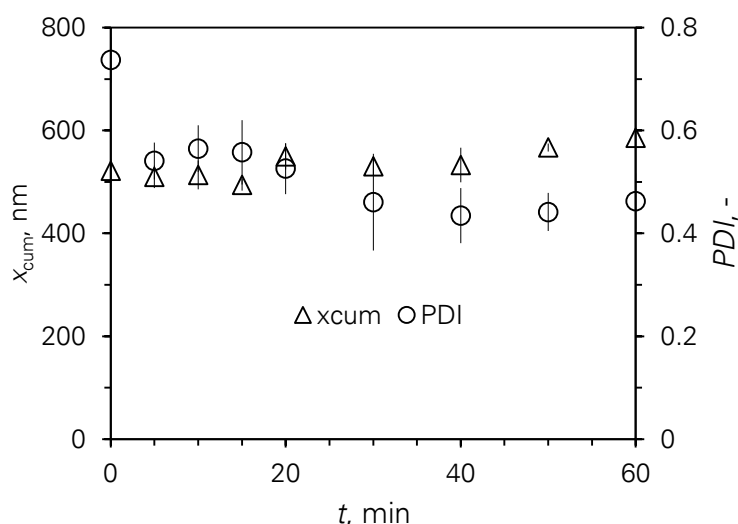


Figure A 5 ULTRA-TURRAX® dispersion of P25 suspension: Size characterization. A 200 ml P25 suspension of 1 g/l was dispersed by an ULTRA-TURRAX® dispenser for 60 min with the rotation speed of 21 500 rpm. Aggregate size and polydispersity index were measured by the Malvern HPPS-ET dynamic light scattering instrument and are shown along with the dispersion time.

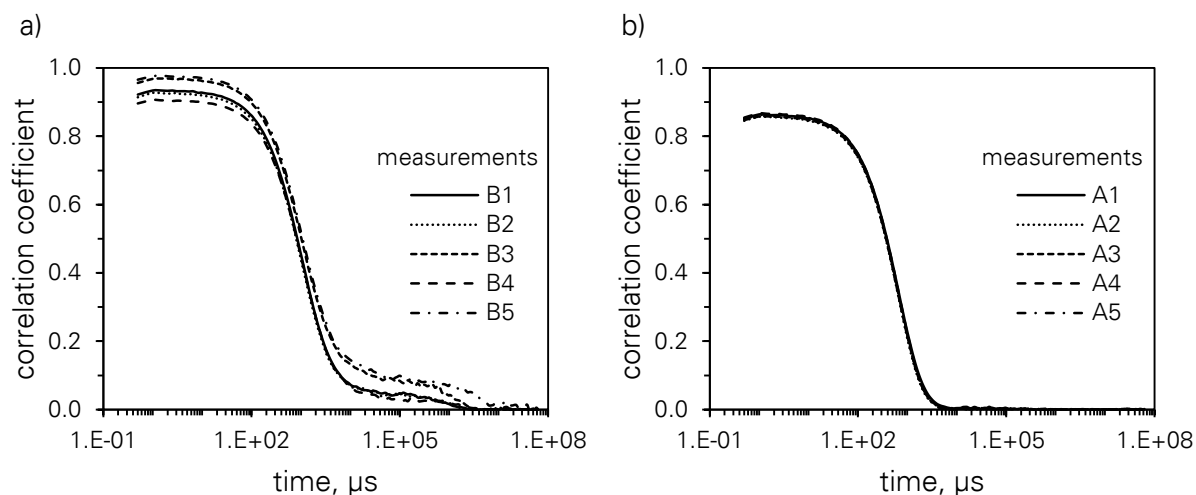


Figure A 6 Ultrasonic dispersion of P25 suspension: Size characterization (cont.) : Correlogram. A 200 ml P25 suspension of 1 g/l was dispersed with 30 W ultrasonication by the Hielscher processor for 40 min. Samples a) before, and b) after dispersion were measured by the Malvern Nano S90 dynamic light scattering instrument. Five measurements were operated for each sample.

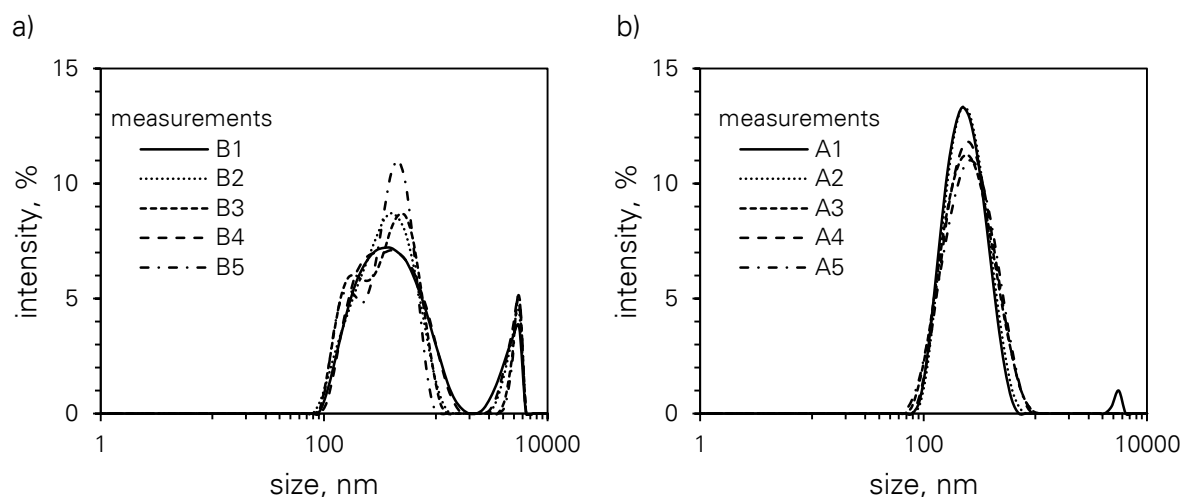


Figure A 7 Ultrasonic dispersion of P25 suspension: Size characterization (cont.): Particle size distribution by intensity. A 200 ml P25 suspension of 1 g/l was dispersed with 30 W ultrasonication by the Hielscher processor for 40 min. Samples a) before, and b) after dispersion were measured by the Malvern Nano S90 dynamic light scattering instrument. Five measurements were operated for each sample.

After the dispersion, big aggregates were well disintegrated, shown by the very low baseline (next to the horizontal axis of Figure A 6b). Also the decay of the correlation coefficient is steep, indicating the low polydispersity index. The repeated data of five measurements in Figure A 7b also confirms the result.

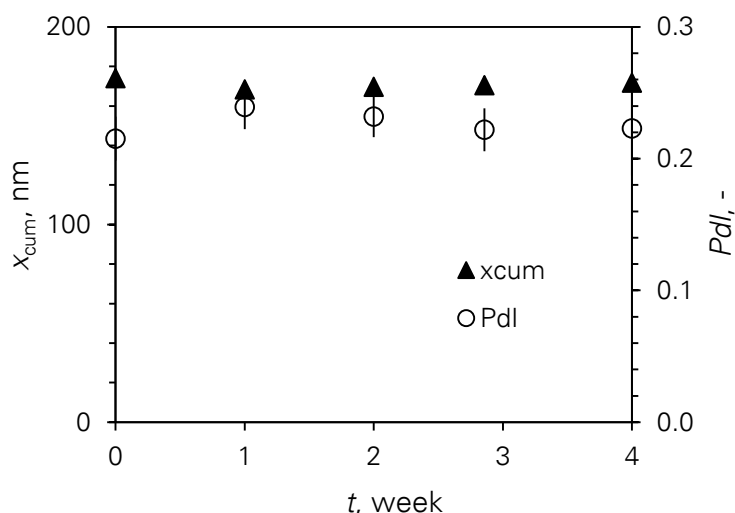


Figure A 8 Ultrasonic dispersion of P25 suspension: Stability test. 200 ml P25 suspension of 1 g/l (without methylene blue) was dispersed with 22 W ultrasonication by Topas UDS751 processor for 60 min. The stability test was then carried out over 4 weeks. Aggregates size were measured by the Malvern HPPS-ET dynamic light scattering instrument and the correlation with Malvern Nano S90 was done (Appendix A2).

#### Stability of dispersed P25 suspension

Prior to the stability test, a 200 ml P25 suspension of 1 g/l was dispersed with 22 W ultrasonication for 60 min. The aggregate size  $x_{cum}$  of  $174 \pm 1$  nm and the polydispersity index  $PDI$  of  $0.22 \pm 0.017$  were obtained. The suspension was then kept in ambient conditions for the stability test within 4 weeks. Conductivity remained approx. 12  $\mu\text{S}/\text{cm}$  during the test. The pH value of 3.8–3.9 was unchanged during the first 3 weeks, however the sample at week 4 has a higher pH of 4.4. Figure A 8 shows that  $x_{cum}$  has a minor change of 3 %, while  $PDI$  fluctuates within 11 %. The result shows the stability of the suspension over weeks.

## A4. UV-VIS ABSORBANCE OF METHYLENE BLUE

### Calibration curves

Methylene blue (MB) stock solution of 3.126 mM was prepared by mixing 0.1 g MB (Merck KGaA) powder in 100 ml ultrapure water. The MB concentrations in the range of 0.5–189.5  $\mu\text{M}$  were prepared from the stock solution. The MB absorbance through a 1, 2, 5 and 10 mm optical cuvette was scanned in the wavelength range of 200–800 nm with the UV-VIS spectrometer. The peak of the spectra was recorded at 664 nm.

When MB concentration exceeds 7  $\mu\text{M}$ , dimerization occurs [211]



where M and D stand for MB monomers and dimers, respectively. The dimerization equilibrium constant  $K$  can be written as

$$K = \frac{C_{n,D}}{C_{n,M}^2}, \quad (\text{A.6})$$

where  $C_n$  is the molar concentration of the molecules at equilibrium. The material balance gives the relation

$$C_{n,M,0} = C_{n,M} + 2C_{n,D}. \quad (\text{A.7})$$

where  $C_{n,0}$  is the total molar concentration of monomers and dimers. Solution of Eqs. (A.6) and (A.7) is

$$K = \frac{C_{n,M,0} - C_{n,M}}{2C_{n,M}^2}, \quad (\text{A.8})$$

$$2KC_{n,M}^2 + C_{n,M} - C_{n,M,0} = 0, \quad (\text{A.9})$$

$$C_{n,M} = \frac{(1 + 8KC_{n,M,0})^{0.5} - 1}{4K}, \quad (\text{A.10})$$

$$\frac{C_{n,M}}{C_{n,M,0}} = \frac{(1 + 8KC_{n,M,0})^{0.5} - 1}{4KC_{n,M,0}}. \quad (\text{A.11})$$

The Beer-Lambert law applied for a system of both monomers and dimers is

$$E_\lambda = \varepsilon_{\lambda,M}LC_{n,M} + \varepsilon_{\lambda,D}LC_{n,D}, \quad (\text{A.12})$$

where  $E_\lambda$  is the extinction of MB solution at the wavelength  $\lambda$  through an optical pathlength  $L$ ,  $\varepsilon_{M,\lambda}$  and  $\varepsilon_{D,\lambda}$  are the true molar extinction coefficients of monomers and dimers, respectively. At the wavelength of 664 nm, no dimer is detected, i.e.,  $\varepsilon_{D,664} = 0$ . Thus, the extinction  $E_{664}$  can be written as

$$E_{664} = \varepsilon_{664,M}LC_{n,M}, \quad (\text{A.13})$$

$$\frac{E_{664}}{L} = \varepsilon_{M,664} \frac{C_{n,M}}{C_{n,M,0}} C_{n,M,0} = \varepsilon_{app,664} C_{n,M,0}, \quad (\text{A.14})$$

where  $\varepsilon_{app,664}$  is the apparent molar extinction coefficient of MB. For a clearer display, the subscripts M and 664 are omitted. It can be derived as

$$\varepsilon_{app} = \varepsilon \frac{C_n}{C_{n,0}} = \varepsilon \frac{(1 + 8KC_{n,0})^{0.5} - 1}{4KC_{n,0}}. \quad (\text{A.15})$$

Put  $(1 + 8KC_{n,0})^{0.5} = x$ , we have

$$\varepsilon_{app} = \varepsilon \frac{2(x - 1)}{x^2 - 1}, \quad (\text{A.16})$$

$$\frac{2\varepsilon}{\varepsilon_{\text{app}}} - 1 = (1 + 8KC_{n,0})^{0.5}, \quad (\text{A.17})$$

$$\left( \frac{2\varepsilon}{\varepsilon_{\text{app}}} - 1 \right)^2 = 1 + 8KC_{n,0}, \quad (\text{A.18})$$

$$C_{n,0} = \frac{\varepsilon^2}{2K} \left( \frac{1}{\varepsilon_{\text{app}}} \right)^2 - \frac{\varepsilon}{2K} \frac{1}{\varepsilon_{\text{app}}}. \quad (\text{A.19})$$

In each measurement, the sample was prepared and the value  $C_{n,0}$  is known. Extinction coefficient at 664 nm was measured with a cuvette of optical pathlength  $L$ , thus the apparent extinction coefficient  $\varepsilon_{\text{app}}$  can be determined as Eq. (A.13) (Figure A 9). Least square regression was done from the known data set  $(1/\varepsilon_{\text{app},i}, C_{n,0,i})$ , the true extinction coefficient of monomer  $\varepsilon$  and the dimerization equilibrium constant  $K$  were found to be  $\varepsilon = 1.9 \times 10^4 \text{ m}^2/\text{mol}$  and  $K = 3.58 \text{ m}^3/\text{mol}$ .

It can be derived from Eqs. (A.14) and (A.19) as

$$\frac{E}{\varepsilon L} = \frac{(1 + 8KC_{n,0})^{0.5} - 1}{4K}, \quad (\text{A.20})$$

$$C_{n,0} = \frac{2K}{\varepsilon^2 L^2} E^2 + \frac{1}{\varepsilon L} E. \quad (\text{A.21})$$

Eq. (A.21) is the calibration formula of MB and it was used to determine MB concentration in the thesis. All graphical results of calibration are shown in Figure A 9.

### Influences of pH on the UV-VIS absorbance spectra

Methylene blue (MB) is a cationic dye. The acid dissociation of MB is described as



The acidity constant  $K_a$  is determined at the quotient of the equilibrium concentrations  $C_n$  as

$$K_a = \frac{C_{n,\text{MB-OH}}}{C_{n,\text{MB}^+} C_{n,\text{OH}^-}}, \quad (\text{A.24})$$

The total amount of MB  $C_{n,\text{MB}}$  is

$$C_{n,\text{MB}} = C_{\text{MB}^+} + C_{\text{MB-OH}}. \quad (\text{A.25})$$

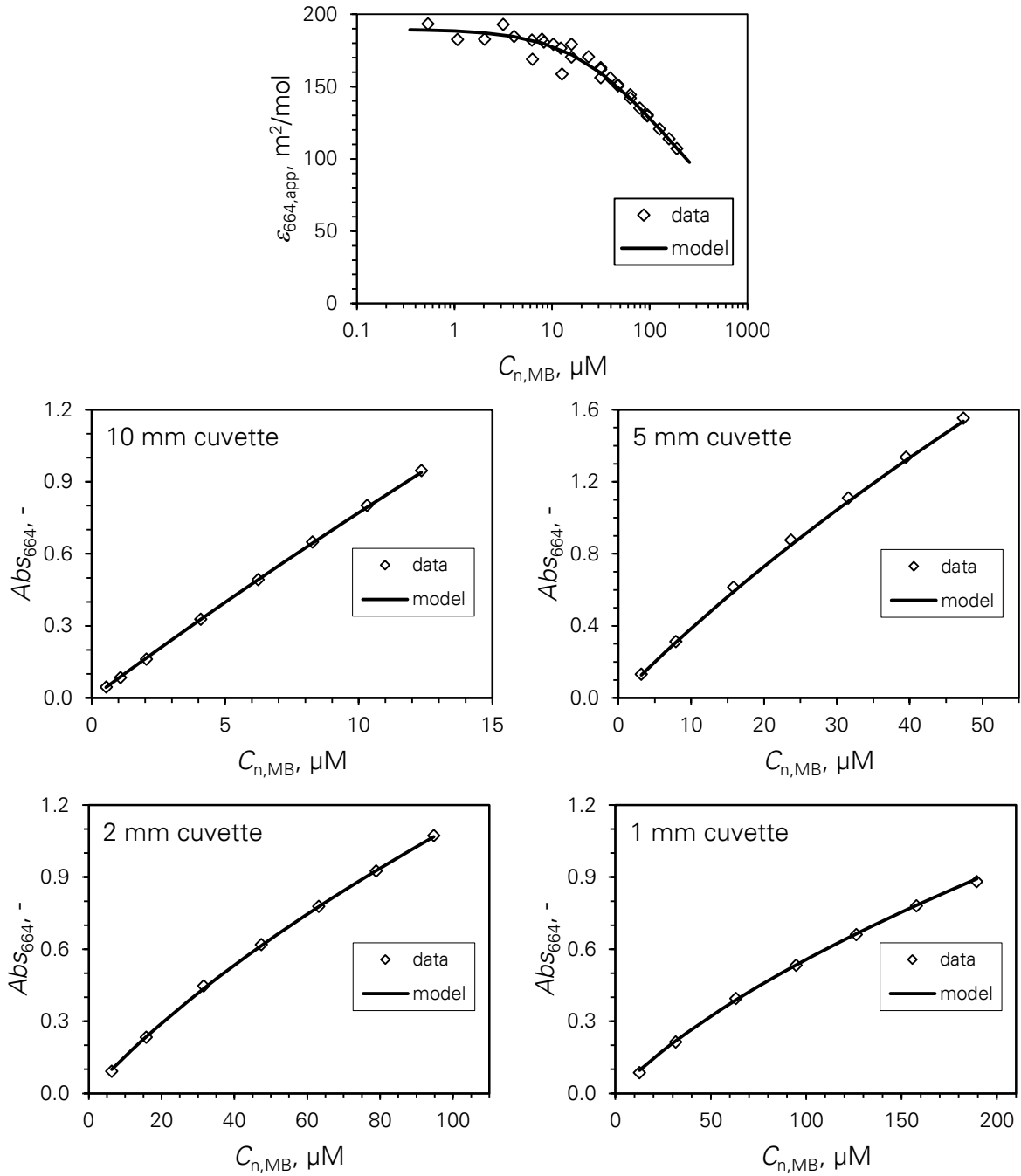


Figure A 9 Calibration of methylene blue (MB). Absorbance of MB solutions (0.5–189.5 μM) were measured by UV-VIS spectroscopy with 1, 2, 5 and 10 mm optical cuvettes: (Napierian) molar extinction coefficient and (decadic) absorbance at 664 nm vs. MB concentration. Measured data were compared with computation.

Mathematic conversions give

$$C_{n,MB^+} = C_{n,MB} \frac{1}{1 + K_a C_{n,OH^-}}, \quad (A.26)$$

$$C_{n,MB-OH} = C_{n,MB} \frac{K_a C_{n,OH^-}}{1 + K_a C_{n,OH^-}}. \quad (A.27)$$

The Beer-Lambert law written for MB solution including two species MB<sup>+</sup> and MB-OH is

$$E_\lambda = \varepsilon_{MB^+, \lambda} C_{n,MB^+} L + \varepsilon_{MB-OH, \lambda} C_{n,MB-OH} L, \quad (A.28)$$

where  $E_\lambda$  is the absorbance of a matrix of component at a certain wavelength  $\lambda$ ,  $\varepsilon_\lambda$  is the molar the extinction coefficients and  $L$  is the optical pathlength. The apparent molar extinction coefficient of the matrix can be defined as

$$\varepsilon_{\lambda,app} = \frac{E_\lambda}{C_{n,MB,ini} L} = \frac{1 + \frac{\varepsilon_{MB-OH, \lambda}}{\varepsilon_{MB^+, \lambda}} K_a C_{n,OH^-}}{1 + K_a C_{n,OH^-}}. \quad (A.29)$$

For MB,  $pK_a = 0$  [239], thus  $K_a = 1$ . In experiments, pH is in the range of 3–10, which means that  $K_a C_{n,OH^-} = C_{n,OH^-} = 10^{-(14-pH)} \ll 1$ . Eqs. (A.26), (A.27) and (A.29) are rewritten as

$$C_{n,MB^+} = C_{n,MB} \quad (A.30)$$

$$C_{n,MB-OH} = C_{n,MB} 10^{-(14-pH)}, \quad (A.31)$$

$$\varepsilon_{\lambda,app} = \frac{1 + \frac{\varepsilon_{MB-OH, \lambda}}{\varepsilon_{MB^+, \lambda}} 10^{14-pH}}{1 + 10^{14-pH}}. \quad (A.32)$$

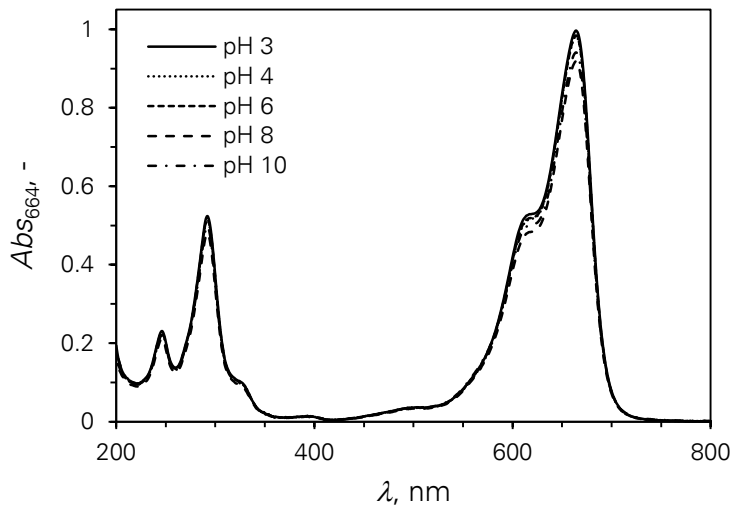


Figure A 10 Effect of pH on the UV-VIS absorption spectra of methylene blue. Absorbance of 13  $\mu$ M methylene blue solutions (pH = 3–10) were measured by UV-VIS spectroscopy with a 10 mm optical cuvettes.

Experimentally, almost no change of the absorption spectra is observed in the pH range of 3–10 (Figure A 10). At 664 nm, MB shows the peak of  $0.965 \pm 0.032$ , which means that the apparent extinction coefficient can be considered as a constant and that  $\frac{\epsilon_{\text{MB-OH},664}}{\epsilon_{\text{MB}^+,664}} = 1$ .

## A5. UV-VIS ABSORBANCE OF CIPROFLOXACIN

Ciprofloxacin (Cipro) was used in this study on the photocatalytic activity of the magnetic particles. The stock solution was prepared by dissolving 5 mg Cipro powder (Sigma-Aldrich, Inc.) in 1 l ultrapure water. The medium was adjusted to be acidic by adding a small amount of HCl 0.1 M, thus ensured the solubility of Cipro in water. The solution was then diluted to have the concentrations of 3.0–21.1  $\mu\text{M}$ . Samples were measured with the UV-VIS spectrometer. The maximum absorbance peak at 277 nm was used to determine the calibration curve.

This work addressed the cooperation with Sara Teixeira. The data were kindly provided. The relation between absorbance and concentration obeys the linear function (Figure A 11)

$$Abs_{277} = 0.0417C_{n,Cipro} - 0.0054. \quad (\text{A.33})$$

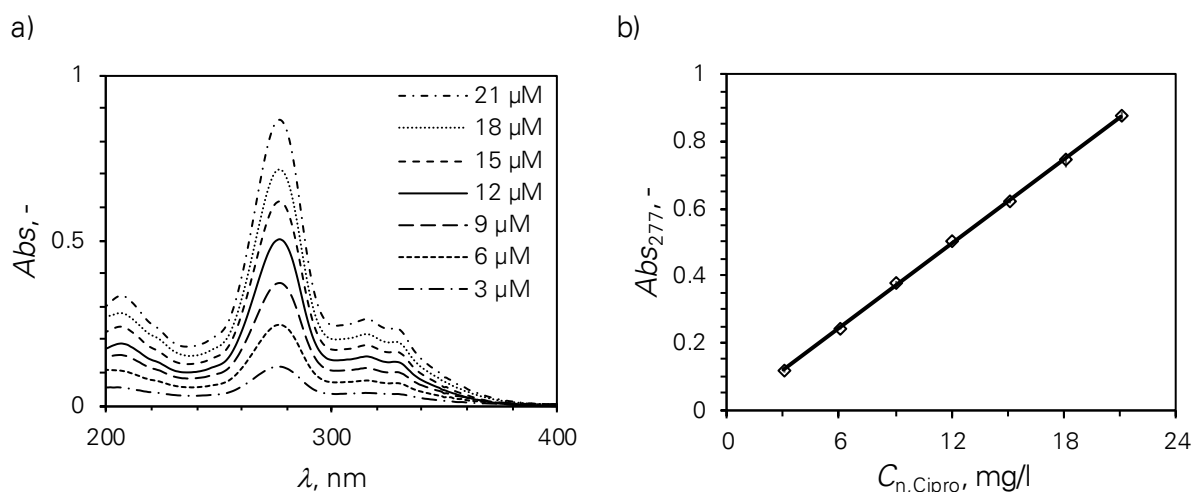


Figure A 11 Calibration of ciprofloxacin. Absorbance of ciprofloxacin (Cipro) solutions (3–21  $\mu\text{M}$ ) were measured by UV-VIS spectroscopy with a 10 mm optical cuvettes. a) The UV-VIS absorbance spectra, and b) The calibration curve at the wavelength of 277 nm.

## A6. UV-VIS ABSORBANCE OF WASTEWATER FROM HACHIBA COMPANY

Towards application of photocatalysis, color removal of two commercial dye solutions from March 29 Textile-Garment Joint Stock Company (Hachiba), Danang, Vietnam were tested. The highest concentration of the solution was chosen based on the color intensity of real wastewater (WW) from the company. Figure A 12 shows the UV-VIS absorbance spectra of four WW solutions collected and measured in October 2014 in the Department of Science and Technology, Danang, Vietnam. Different dilution factors were used.

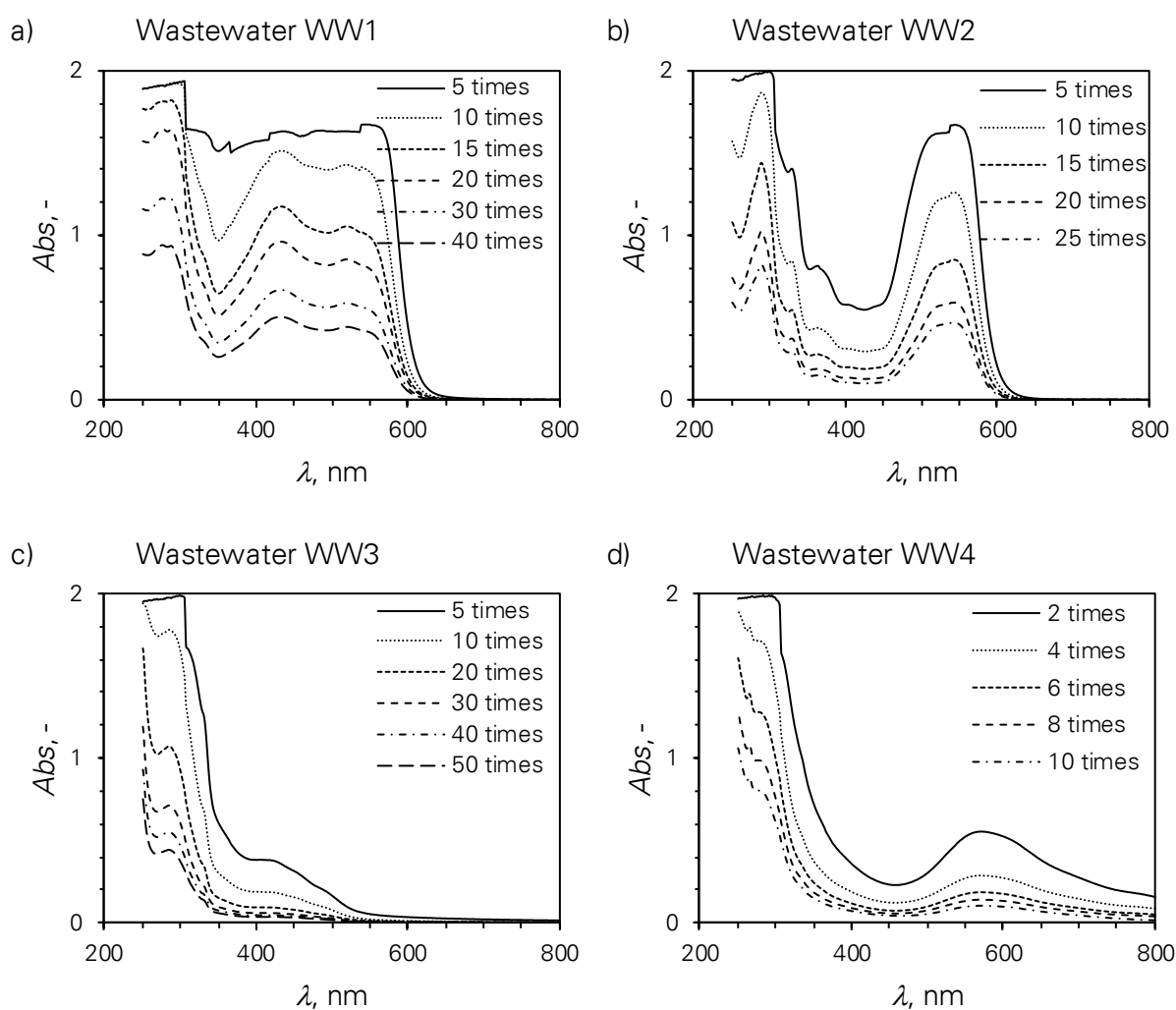


Figure A 12 UV-VIS absorbance of real wastewater from Hachiba Company (Danang, Vietnam). Wastewater (WW) was diluted from 5–50 times and analyzed by UV-VIS spectroscopy with a 10 mm optical cuvettes.

## SCIENTIFIC OUTPUT

### Publication and proceeding

1. **H.N. Le**, F. Babick, K. Kühn, M.T. Nguyen, M. Stintz, and G. Cuniberti. Impact of optical property on the photocatalytic activity of aggregates. In: *Particle Technology*. Nuremberg: Nürnberg Messe GmbH; 2016:1-4.
2. **H.N. Le**, F. Babick, K. Kühn, M.T. Nguyen, M. Stintz, and G. Cuniberti. Impact of ultrasonic dispersion on the photocatalytic activity of titania aggregates. *Beilstein J Nanotechnol.* 2015;6:2423-2430. doi:10.3762/bjnano.6.250.

### Selected conferences

1. May 22–26, 2017: **H. N. Le**, S. Venkatraman, F. Babick, K. Kühn, M. Stintz, and G. Cuniberti. "Optical penetration in a flow photocatalytic reactor". 2017 E-MRS Spring Meeting, Strasbourg, France. (Oral presentation)
2. Apr 09–12, 2017: P. M. Martins, S. Kappert, **H. N. Le**, K. Kühn, G. Cuniberti, V. Sebastian, and S. Lanceros-Méndez. "Gold nanoisland-decorated TiO<sub>2</sub> for enhanced photocatalysis". MATERIALS 2017, Aveiro, Portugal. (Oral presentation)
3. Apr 19–21, 2016: **H. N. Le**, F. Babick, K. Kühn, M. T. Nguyen, M. Stintz, and G. Cuniberti. "Impact of optical property on the photocatalytic activity of titania aggregates". PARTEC 2016, Nuremberg, Germany. (Oral presentation)
4. May 11–15, 2015: **H. N. Le**, F. Babick, K. Kühn, M. Stintz, and G. Cuniberti. "Impact of ultrasonic dispersion on photocatalytic activity of titania aggregates". 2015 E-MRS Spring Meeting, Lille, France. (Oral presentation)
5. Jul 01–03, 2014: **H. N. Le**, F. Babick, K. Kühn, M. Stintz, and G. Cuniberti. "Impact of photocatalyst size on the degradation of methylene blue". Nanofair 2014, Dresden, Germany. (Poster presentation)



# ***CURRICULUM VITAE***

**Lê, Hoài Nga**

lehoainga@gmail.com

Date of birth: 25.08.1986 | Nationality: Vietnam

## **Work experience**

09.2009–Present	Lecturer assistant at Hanoi University of Science and Technology (HUST), Hanoi (Vietnam)
06.2017–Present	Research assistant at Technische Universität Dresden (TU Dresden), Dresden (Germany)
02.2017–04.2017	Research assistant at Helmholtz-zentrum Dresden-Rossendorf, Dresden (Germany)
07.2015–04.2016	Research assistant at TU Dresden, Dresden (Germany)

## **Education and training**

07.2012–Present	Ph.D. candidate at TU Dresden, Dresden (Germany) Thesis title: A concept for nanoparticle-based photocatalytic treatment of wastewater from textile industry
08.2016–10.2016	Internship at University of Minho, Braga (Portugal) Research title: The development of novel photocatalytic materials for dye wastewater treatment
01.2012–03.2012	Staff exchange at Chiang Mai University, Chiang Mai (Thailand) Research title: Production of bioactive compounds from economical plants in the northern region of Thailand
10.2009–06.2011	Master of science at HUST, Hanoi (Vietnam) Thesis title: Establish dynamic model of crystallization to apply in curcumin isolation from <i>Curcuma Longa</i> Linn
09.2004–06.2009	Chemical engineer at HUST, Hanoi (Vietnam) Thesis title: Study on affecting parameters of ultrasonic extraction and concentration in curcumin isolation from <i>Curcuma Longa</i> Linn

## **Awards**

10.2016–01.2017	Completion grant awarded by the Graduate Academy, TU Dresden, Dresden (Germany)
08.2016–10.2016	Travel grant awarded by the Graduate Academy, TU Dresden, Dresden (Germany)
07.2012–06.2015	Mobility grant award by Erasmus Mundus (One More Step)
01.2012–03.2012	Awardee of the staff and student exchange program between Thailand and Great Mekong Sub-region countries
05.2009	Third prize for "Researching for Students" by HUST, Hanoi (Vietnam)
05.2008	First prize for "Researching for Students" by HUST, Hanoi (Vietnam)